

Thesis for the degree Doctor of Technology  
Sundsvall 2007

## **Design and characterization of 64K pixels chips working in single photon processing mode**

**Xavier Llopart Cudié**

Supervisors: Docent Christer Fröjd  
Doctor Michael Campbell

Electronics Design Division, in the  
Department of Information Technology and Media  
Mid Sweden University, SE-851 70 Sundsvall, Sweden

ISSN 1652-893X  
Mid Sweden University Doctoral Thesis 27

ISBN 978-91-85317-56-1

**ELECTRONICS**  
Design Division



**Mittuniversitetet**  
MID SWEDEN UNIVERSITY

Akademisk avhandling som med tillstånd av Mittuniversitetet i Sundsvall  
framläggs till offentlig granskning för avläggande av licentiatexamen i elektronik  
***fredagen den 25 maj 2007***, klockan ***10.15*** i sal ***M102***, Mittuniversitetet Sundsvall.  
Seminariet kommer att hållas på engelska.

## Design and characterization of 64K pixels chips working in single photon processing mode

Xavier Llopert Cudié

© Xavier Llopert Cudié, 2007

Electronics Design Division, in the  
Department of Information Technology and Media  
Mid Sweden University, SE-851 70 Sundsvall  
Sweden

Telephone: +46 (0)60 148889

Printed by Kopieringen Mittuniversitetet, Sundsvall, Sweden, 2007

**a la meva família,**



## ABSTRACT

Progress in CMOS technology and in fine pitch bump bonding has made possible the development of high granularity single photon counting detectors for X-ray imaging. This thesis studies the design and characterization of three pulse processing chips with 65536 square pixels of  $55\text{ }\mu\text{m} \times 55\text{ }\mu\text{m}$  designed in a commercial  $0.25\text{ }\mu\text{m}$  6-metal CMOS technology. The 3 chips share the same architecture and dimensions and are named *Medipix2*, *Mpix2MXR20* and *Timepix*.

The *Medipix2* chip is a pixel detector readout chip consisting of  $256 \times 256$  identical elements, each working in single photon counting mode for positive or negative input charge signals. The preamplifier feedback provides compensation for detector leakage current on a pixel by pixel basis. Two identical pulse height discriminators are used to define an energy window. Every event falling inside the energy window is counted with a 13-bit pseudo-random counter. The counter logic, based in a shift register, also behaves as the input/output register for the pixel. Each cell also has an 8-bit configuration register which allows masking, test-enabling and 3-bit individual threshold adjust for each discriminator. The chip can be configured in serial mode and readout either serially or in parallel. Measurements show an electronic noise  $\sim 160\text{ e}^-$  rms with a gain of  $\sim 9\text{ mV/ke}^-$ . The threshold spread after equalization of  $\sim 120\text{ e}^-$  rms brings the full chip minimum detectable charge to  $\sim 1100\text{ e}^-$ . The analog static power consumption is  $\sim 8\text{ }\mu\text{W}$  per pixel with  $V_{dd}=2.2\text{ V}$ .

The *Mpix2MXR20* is an upgraded version of the *Medipix2*. The main changes in the pixel consist of: an improved tolerance to radiation, improved pixel to pixel threshold uniformity, and a 14-bit counter with overflow control. The chip periphery includes new threshold DACs with smaller step size, improved linearity, and better temperature dependence.

*Timepix* is an evolution of the *Mpix2MXR20* which provides independently in each pixel information of arrival time, time-over-threshold or event counting. *Timepix* uses as a time reference an external clock (*Ref\_Clk*) up to 100 MHz which is distributed all over the pixel matrix during acquisition mode. The preamplifier is improved and there is a single discriminator with 4-bit threshold adjustment in order to reduce the minimum detectable charge limit. Measurements show an electrical noise  $\sim 100\text{ e}^-$  rms and a gain of  $\sim 16.5\text{ mV/ke}^-$ . The threshold spread after equalization of  $\sim 35\text{ e}^-$  rms brings the full chip minimum detectable charge either to  $\sim 650\text{ e}^-$  with a naked chip (i.e. gas detectors) or  $\sim 750\text{ e}^-$  when bump-bonded to a detector. The pixel static power consumption is  $\sim 13.5\text{ }\mu\text{W}$  per pixel with  $V_{dd}=2.2\text{ V}$  and *Ref\_Clk*=80 MHz.

This family of chips have been used for a wide variety of applications. During these studies a number of limitations have come to light. Among those are limited energy resolution and surface area. Future developments, such as *Medipix3*, will aim to address those limitations by carefully exploiting developments in microelectronics.



## SAMMANDRAG

Framstegen inom CMOS-teknologin och tekniken för bump bondning har möjliggjort utveckling av högupplösnande bilddetektorer för detektering av enskilda röntgenfotoner eller laddade partiklar. Denna avhandling behandlar design och karakterisering av tre pulsräknande utläsningskretsar med 65536 kvadratiska bildelement med storleken  $55 \times 55 \text{ }\mu\text{m}^2$ . De tre kretsarna, benämnda *Medipix2*, *Mpix2MXR20* och *Timepix*, delar samma arkitektur och dimensioner.

*Medipix2* är en utläsningskrets för avbildning med  $256 \times 256$  identiska bildelement som räknar enskilda fotoner utgående från positiva eller negativa laddningspulser. Förstärkarens återkoppling kompenseras individuellt för läckströmmen i varje bildelement. Ett energifönster kan definieras med hjälp av två identiska diskriminatorkretsar. Varje händelse som faller inom energifönstret räknas i en 13-bitars pseudo-random räknare. Räknaren, utformad som ett skiftregister, fungerar också som in/utregister för varje bildelement. Kretsen kan läsas ut antingen seriellt eller parallellt. Det elektroniska bruset har uppmätts till  $\sim 160 \text{ e}^- \text{ rms}$  vid en förstärkning av  $\sim 9 \text{ mV/ke}^-$ . Spridningen i tröskelspanning efter justering är  $\sim 120 \text{ e}^- \text{ rms}$  vilket ger en minsta detekterbar laddningspuls över hela kretsen på  $\sim 1100 \text{ e}^-$ . Den statiska effektförbrukningen i del analoga delen är  $\sim 8 \text{ mW}$  per bildelement vid  $V_{dd}=2,2 \text{ V}$ .

*Mpix2MXR20* är en uppdaterad version av *Medipix2*. De huvudsakliga förändringarna är: bättre strålningshärdighet, jämnare tröskelvärdet och en 14-bitsräknare med overflow. Periferin innehåller också nya DA-omvandlare med mindre steg, förbättrad linjäritet och mindre temperaturberoende.

*Timepix* är en vidareutveckling av *Mpix2MXR20* som medger detektering av ankomsttid, time-over-threshold eller pulsräkning individuellt i varje bildelement. *Timepix* utnyttjar en extern klocka (*Ref\_Clk*) med frekvenser upp till 100 MHz som distribueras över hela bildmatrisen. Förstärkaren är förbättrad och en enkel diskriminator med 4 bitars tröskeljustering används för att minimera längsta detekterbara laddningspuls. Mätningar visar ett elektroniskt brus på  $\sim 100 \text{ e}^- \text{ rms}$  och förstärkningen  $16,5 \text{ mV/ke}^-$ . Med en tröskelspridning på  $35 \text{ e}^- \text{ rms}$  blir minsta detekterbara laddning för den nakna kretsen (t.ex. i en gasfyllt detektor)  $\sim 650 \text{ e}^-$  och för en bondad detektor  $\sim 750 \text{ e}^-$ . Den statiska effektförbrukningen är  $\sim 13,5 \text{ mV}$  per bildelement vid  $V_{dd}=2,2 \text{ V}$  och *Ref\_Clk*= 80 MHz.

Den här kretsfamiljen har använts i ett antal olika applikationer. Under dessa studier har ett antal begränsningar konstaterats. Bland dessa märks begränsad energiupplösning och begränsad detektorarea. Framtida utvecklingsprojekt, t.ex. *Medipix3*, kommer att inriktas på att avhjälpa dessa begränsningar genom att utnyttja den senaste utvecklingen på mikroelektronikområdet.



## ACKNOWLEDGEMENTS

I came to CERN in May 1999 to help in the design of the *Medipix2* chip. Soon after my arrival, Michael Campbell offered me the possibility to start my doctoral studies in the Microelectronics group for the design and characterisation of the *Medipix2*. Eight years have passed and two other chips have been designed since then. I owe a lot to Michael, firstly for accepting with such patience the time it has taken me to complete this thesis, but mostly for always being an excellent supervisor and giving me good technical advice and encouragement.

This thesis would not have been possible without the support of Christer Fröjdh who immediately accepted me as a doctoral student at Mittuniversitetet, and Erik Heijne who has been a reference for my work and a continuous source of knowledge.

I would like to express my gratitude to all the members of the Medipix collaboration which have become my “scientific family” during all these past years. In particular the financial support of the collaboration is grateful acknowledged. IFAE [IFA] contributed financially to my first 8 months at CERN. PANalytical [PAN] has contributed financially to the project through the support of the *Medipix2* and *Mpix2MXR20* developments. The EUDET project [EUD] has provided financial support to the *Timepix* development. I specially acknowledge for their technical support in the project the groups from IEAP-CTU [IEA] led by Stanislav Pospisil (for the development of Pixelman and the USB readout boards), NIKHEF [NIK] led by Jan Visschers (for the development of the MUROSV2.x boards and the multi-chip carriers), and INFN-Napoli [INF] led by Paolo Russo (for the development of Medisoft4.x).

I also would like to thank the different office mates I have had during these years: Roberto Dinapoli and Bettina Mikulec with whom I shared a lot of interesting technical and non-technical discussions; Lukas Tlustos for always being available for lessons in semiconductor physics and applied German...and Rafael Ballabriga for helping me keep my catalan alive and who has already shown excellence as an engineer.

Many people are to be acknowledged for their help and availability. In the Microelectronics groups at CERN I would like to thank to Paul, Giovanni (Anelli and Cervelli), Paulo, Jan, Federico, Bert, Danielle, Winnie, Matthieu, Francois, Laura, Giulia, Walter, Francis, Alessandro, Pierre, Mike and many others... Special thanks to Ian McGill and Francoise Cossey for their “magic” bonding ability.

All my love goes to my family (mama, papa, Joan, Oriol, avis, tiets, cosins...) who have always given me their support and affection. My heart is with my wife, Katta, for her endless support, love, and for giving me, so far, one wonderful daughter, Mireia.

Working in an international place like CERN gives one the chance to make friends from different cultures and traditions. Many come, some leave, and some

stay but all of them have contributed to the completion of this thesis even if they don't know it. Thanks specially to Manel, Blanca, Matteo, Roger, Eva and JuanRa.

To conclude and to make sure I didn't forget anybody unintentionally, I also would like to thank all the people who, reading the acknowledgements, think that they have been forgotten...

## TABLE OF CONTENTS

<b>ABSTRACT .....</b>	<b>I</b>
<b>SAMMANDRAG .....</b>	<b>III</b>
<b>ACKNOWLEDGEMENTS .....</b>	<b>V</b>
<b>TABLE OF CONTENTS .....</b>	<b>VII</b>
<b>LIST OF FIGURES .....</b>	<b>XI</b>
<b>LIST OF PAPERS .....</b>	<b>1</b>
<b>INTRODUCTION.....</b>	<b>3</b>
<b>1 IMAGING WITH SEGMENTED DETECTORS .....</b>	<b>5</b>
1.1 DIGITAL X-RAY IMAGING.....	5
1.1.1 <i>Direct versus indirect detection systems</i> .....	5
1.1.2 <i>Counting versus integrating methods</i> .....	5
1.2 DETECTOR TECHNOLOGIES .....	6
1.2.1 <i>CCD</i> .....	6
1.2.2 <i>Flat Panel Imager</i> .....	7
1.2.3 <i>Monolithic Active Pixel Sensors (MAPS)</i> .....	8
1.2.4 <i>DEPFET</i> .....	10
1.2.5 <i>Silicon on Insulator (SOI)</i> .....	11
1.2.6 <i>Hybrid pixel detectors</i> .....	12
1.3 THE MEDIPIX PROJECT (A SHORT HISTORY).....	14
SUMMARY .....	16
<b>2 DESIGN OF THE MEDIPIX2 CHIP .....</b>	<b>17</b>
2.1 MOTIVATIONS AND REQUIREMENTS FOR THE NEW DESIGN.....	17
2.2 THE MEDIPIX2 CHIP .....	18
2.3 PIXEL CELL .....	18
2.3.1 <i>Analog block of the pixel</i> .....	20
2.3.2 <i>Digital block of the pixel</i> .....	34
2.3.3 <i>Pixel power distribution strategy</i> .....	39
2.3.4 <i>Pixel Layout</i> .....	41
2.4 MEDIPIX2 PERIPHERY .....	42
2.4.1 <i>Analog Periphery</i> .....	43
2.4.2 <i>Digital Periphery</i> .....	46
2.5 TILING OF LARGE AREAS .....	51
2.6 SUMMARY .....	52

<b>3</b>	<b>MEDIPIX2 MEASUREMENTS AND CALIBRATION .....</b>	<b>55</b>
3.1	<i>MEDIPIX2 READOUT SYSTEMS .....</i>	55
3.1.1	<i>Medipix2 chipboards and probe card .....</i>	55
3.1.2	<i>Readout hardware .....</i>	57
3.1.3	<i>Readout software .....</i>	58
3.1.4	<i>Other Medipix2 readout developments .....</i>	59
3.2	<i>WAFER PROBING .....</i>	59
3.2.1	<i>Communication Test (digital) .....</i>	60
3.2.2	<i>DAC scan test (analog) .....</i>	61
3.2.3	<i>Analog test .....</i>	63
3.3	<i>ELECTRICAL CHARACTERIZATION .....</i>	63
3.4	<i>BUMP BONDING .....</i>	64
3.5	<i>X-RAY IMAGING WITH THE MEDIPIX2 .....</i>	64
3.5.1	<i>Absolute pixel calibration .....</i>	66
3.5.2	<i>The Medipix2 Quad .....</i>	67
3.6	<i>RADIATION HARDNESS .....</i>	69
3.7	<i>SUMMARY .....</i>	70
<b>4</b>	<b>REDESIGN OF THE MEDIPIX2 (<i>MPIX2MXR20</i>) .....</b>	<b>73</b>
4.1	<i>MOTIVATION OF THE REDESIGN .....</i>	73
4.2	<i>PIXEL UPGRADES .....</i>	74
4.2.1	<i>Mpix2MXR20 CSA .....</i>	76
4.2.2	<i>Mpix2MXR20 discriminator .....</i>	78
4.2.3	<i>Shift Register and Counter (digital) .....</i>	79
4.3	<i>PERIPHERY UPGRADES .....</i>	80
4.3.1	<i>Mpix2MXR20 DACs .....</i>	80
4.3.2	<i>Mpix2MXR20 test pulse architecture .....</i>	83
4.3.3	<i>IO logic upgrade .....</i>	84
4.3.4	<i>Fuses .....</i>	85
4.3.5	<i>Other layout enhancements .....</i>	86
4.4	<i>ELECTRICAL CHARACTERIZATION .....</i>	86
4.4.1	<i>DAC Measurements .....</i>	87
4.4.2	<i>Electrical characterization of the pixel .....</i>	89
4.4.3	<i>Low threshold equalization .....</i>	93
4.4.4	<i>High threshold equalization .....</i>	95
4.5	<i>IMAGING WITH THE MPIX2MXR20 .....</i>	96
4.5.1	<i>Mpix2MXR20 overflow control .....</i>	96
4.5.2	<i>Absolute calibration .....</i>	97
4.6	<i>SUMMARY .....</i>	98
<b>5</b>	<b>TIMEPIX .....</b>	<b>99</b>
5.1	<i>GASEOUS DETECTORS: PIXEL AS A DIRECT ANODE .....</i>	99
5.2	<i>TIMEPIX PIXEL CELL .....</i>	99

5.2.1	<i>Modifications to the analog side of the pixel</i> .....	100
5.2.2	<i>Modifications of the digital side of the pixel</i> .....	104
5.2.3	<i>Pixel Layout</i> .....	107
5.2.4	<i>The reference counting clock (Ref_Clk)</i> .....	108
5.3	PERIPHERY DESIGN.....	109
5.4	ELECTRICAL CHARACTERIZATION .....	110
5.4.1	<i>Optimization of the operating point of the pixel</i> .....	110
5.4.2	<i>Electrical characterization of the pixel</i> .....	113
5.5	FIRST MEASUREMENTS WITH GAS DETECTORS .....	113
5.6	ABSOLUTE CALIBRATION .....	115
5.7	SUMMARY .....	117
<b>6</b>	<b>FUTURE DEVELOPMENTS IN PIXEL DETECTORS .....</b>	<b>119</b>
6.1	LIMITATION OF THE ACTUAL CHIP (CHARGE SHARING).....	119
6.1.1	<i>The Medipix3 Prototype chip</i> .....	119
6.2	FUTURE DEVELOPMENTS FOR TIMEPIX .....	122
6.3	THE SQUARE TILE .....	123
6.4	SUMMARY .....	125
<b>7</b>	<b>SUMMARY OF PUBLICATIONS .....</b>	<b>127</b>
7.1	PAPER I.....	127
7.2	PAPER II .....	127
7.3	PAPER III .....	127
7.4	PAPER IV .....	127
7.5	PAPER V .....	128
7.6	PAPER VI .....	128
7.7	PAPER VII .....	128
7.8	PAPER VIII AND PAPER IX .....	128
7.9	PAPER X .....	128
7.10	PAPER XI .....	129
<b>8</b>	<b>THESIS SUMMARY .....</b>	<b>131</b>
<b>9</b>	<b>REFERENCES.....</b>	<b>135</b>
<b>PAPER I.....</b>	<b>141</b>	
<b>PAPER II.....</b>	<b>149</b>	
<b>PAPER III .....</b>	<b>159</b>	
<b>PAPER IV.....</b>	<b>167</b>	
<b>PAPER V .....</b>	<b>177</b>	

PAPER VI.....	187
PAPER VII .....	195
PAPER VIII.....	211
PAPER IX.....	219
PAPER X .....	231
PAPER XI.....	249

## LIST OF FIGURES

Figure 1.1. Schematic diagram showing the concept of direct AMFPI [ZHA05].	7
Figure 1.2. The baseline architecture of CMOS imager [RIZ07]. Transistor M1 resets the photosite to reverse bias, transistor M2 is a row switch, while transistor M2 is the input of a source follower. Follower's current source (common to entire row) and column selection switch are located outside the pixel.	9
Figure 1.3. Cross-section of an annular pulsed clear DEPFET [ULR05]. The structure is symmetric around the source contact. The potential along the axis top gate-rear contact shows a minimum for electrons under the JFET channel.	11
Figure 1.4. Cross section of an SOI process using the substrate as sensitive detection volume [KUC04]. The layer of SiO <sub>2</sub> (buried oxide-BOX) insulates the CMOS readout electronics and the sensitive substrate (handle wafer).	11
Figure 1.5. Schematic of a hybrid pixel detector with the sensor chip and the electronics chip connected via bump bonds.	12
Figure 1.6. Transistor density per pixel versus CMOS process for the three chips of the Medipix project. The Medipix1 chip is in reality build in a 1 μm SACMOS technology but the component density achievable is comparable to a 0.6 μm standard CMOS process [MIK00].	13
Figure 1.7. The Medipix1 pixel cell schematic.	15
Figure 1.8 A picture of the Medipix1 chip without detector sensor.	16
Figure 2.1. On the left the <i>Medipix2</i> passivation openings. On the right the <i>Medipix2</i> floor plan: the sensitive area with 65536 square pixels of 55 μm <sup>2</sup> (top), and the non-sensitive area (dark green) are shown.	18
Figure 2.2. <i>Medipix2</i> pixel schematic. In red the analog side and in blue the digital side.	19
Figure 2.3. Analog schematic. In red are highlighted the 10 global biasing 8-bit DACs used in the analog side. In blue analog power supplies are split accordingly for each biasing branch.	20
Figure 2.4. CSA schematic.	21
Figure 2.5. CSA open loop response for Ipreamp=500 to 1000nA. The phase margin is always > 70°.	23
Figure 2.6. Closed loop transfer function simulation with Ikrum from 5 to 20 nA.	23
Figure 2.7. CSA output voltage simulation response for both collection polarities to an equivalent injected input charge of 1, 2, 3 and 4 ke <sup>-</sup> .	

On the left $I_{krum}=15\text{nA}$ on the right $I_{krum}=5\text{nA}$ . $I_{preamp}=750\text{nA}$ , $V_{FBK}=1105\text{mV}$ and $V_{GND}=1.1\text{V}$ .....	24
Figure 2.8. CSA output simulated gain versus $I_{krum}$ for both polarities. $I_{Preamp}=750 \text{ nA}$ and $C_{in}=40 \text{ fF}$ .....	24
Figure 2.9. Two simulations of the CSA output pulse width. On the left increasing input charges show a linear response due to the resistive feedback loop ( $I_{krum} = 10 \text{ nA}$ and $I_{Preamp} = 1 \mu\text{A}$ ). On the right increasing $I_{krum}$ bias settings show a shorter pulse width due to the faster return to baseline ( $I_{Preamp} = 1 \mu\text{A}$ and $Q_{in} = 10 \text{ ke}^-$ ) .....	25
Figure 2.10. Front-end linear range is 900 mV (0.6 to 1.5 V). This is composed from the CSA linear output range from 0.3 to 1.5 V with linearity above 99.9% and the discriminator input range from 0.6 to 2.2 V.....	25
Figure 2.11. CSA voltage and current sources of the critical nodes.....	26
Figure 2.12. ENC calculation using an analog simulator for different $I_{krum}$ an $I_{Preamp}$ bias settings. In these simulations the detector leakage current is zero and the input capacitance is 40fF .....	28
Figure 2.13. ENC calculation using an analog simulator for an increasing input capacitance. The CSA is biased at default settings of $I_{krum}=10\text{nA}$ and $I_{Preamp}=750\text{nA}$ . The ENC slope is $\sim 0.7\text{e}^-/\text{fF}$ .....	29
Figure 2.14. <i>Medipix2</i> CSA layout. In the center are placed the $C_{fb}$ and $C_{test}$ realized as a metal to metal capacitance .....	30
Figure 2.15. Discriminator block diagram .....	30
Figure 2.16. Preamplifier and discriminators simulation response to a $\pm 1 \text{ ke}^-$ input charge. $V_{FBK}=1.1\text{V}$ and $I_{krum}=10\text{nA}$ .....	31
Figure 2.17. Layout of 1 discriminator branch. Total area is $27.5 \mu\text{m} \times 13.4 \mu\text{m}$ and contains 22 transistors .....	32
Figure 2.18. Digital section schematic. The global control lines are in red .....	34
Figure 2.19. The layout of the pixel digital side .....	35
Figure 2.20. DDL schematic. The global line is displayed in red .....	35
Figure 2.21. Simulation example of two working modes of the DDL. Left: Energy window discrimination mode (1 count). Right: Single Discrimination mode (2 counts). The output pulse width is $\sim 300 \text{ ns}$ ( $IDelay=50 \text{ nA}$ ) .....	36
Figure 2.22. The <i>Medipix2</i> SR/C schematic. The global lines are displayed in red .....	37
Figure 2.23. The layout of one DFF. Each cell contains 22 minimum-sized transistors .....	38
Figure 2.24. PCR is formed by latching 8-bit of the 13-bit shift register .....	38
Figure 2.25. Power distribution schematic of one column and one critical branch	39
Figure 2.26. Worst case power supply voltage drop for a pixel at the top of the column for different metal widths and pixel biasing currents .....	40
Figure 2.27. <i>Medipix2</i> layout. 1) Preamplifier; 2) High Threshold Discriminator; 3) Low Threshold Discriminator; 4) 8-bit Pixel Configuration Register; 5) DDL; 6) SR/C (13-bit shift register and logic) .....	42

Figure 2.28. The <i>Medipix2</i> periphery floor plan. On blue the periphery blocks and IO lines using the analog power supply, on green the blocks and IO lines using digital power supply and on purple the blocks and IO lines using LVDS power supply.....	43
Figure 2.29. Binary weighted architecture implemented in the <i>Medipix2</i> DACs ..	44
Figure 2.30. Layout of a <i>Medipix2</i> 8-bit DAC.....	45
Figure 2.31. One Set-Reset flip flop from the <i>Medipix2</i> digital library.....	46
Figure 2.32. On the left: simplified diagram of LVDS Driver and receiver connected via $100\Omega$ differential impedance media. On the right: LVDS data rate vs Cable Length in meters [NAT98]. .....	47
Figure 2.33. On the left one LVDS receiver with the $100\Omega$ P+ diffusion. On the right the layout of one LVDS driver. The receivers are placed at the bottom left corner of <i>Medipix2</i> while the LVDS drivers are placed at the bottom right corner of <i>Medipix2</i> .....	48
Figure 2.34. The IO Logic schematic. ....	49
Figure 2.35. The <i>Medipix2</i> IO Logic. 1)IO Decoder; 2)Post counter logic; 3) 256 binary column counter; 4) 3328 binary row counter. ....	50
Figure 2.36. End-of-Column logic schematic for 4 pixel columns.....	51
Figure 2.37. End-of-Column logic layout. The image is rotated for printing purposes. The width of the EoC is $34\mu m$ to cope with the high density pitch column pitch.....	51
Figure 2.38. Distances from the last active pixels to the edge of the chip. The passivation openings are octagons of $20\mu m$ long.....	52
Figure 2.39. Schematic of two <i>Medipix2</i> chips connected in daisy chain. ....	52
Figure 3.1 The <i>Medipix2</i> probe card. The central hole is bigger than the <i>Medipix2</i> sensitive for the test of the assemblies with x-ray sources..	55
Figure 3.2. <i>Medipix2</i> CERN single chipboard coupled with the VHDCI cable. A naked <i>Medipix2</i> chip is mounted on the PCB.....	56
Figure 3.3. The <i>Medipix2</i> NIKHEF octet board [FOR03] can hold up to 8 chips. In the image a <i>Medipix2</i> Quad assembly is mounted on the board....	56
Figure 3.4. The <i>Medipix2</i> NIKHEF quad board with a mounted <i>Medipix2</i> quad.....	57
Figure 3.5. The Muros2.1 system. ....	58
Figure 3.6. The MedipixUSB system connected to a <i>Medipix2</i> CERN single chipboard [VYK06].....	58
Figure 3.7. Two <i>Medipix2</i> wafer maps from two different production runs. Each wafer contains 94 chips.....	60
Figure 3.8. Pixel error rate versus read clock ( $F_{clock}$ ) frequency for three different chips.....	61
Figure 3.9. <i>Medipix2</i> current DACs transfer functions.....	61
Figure 3.10. <i>Medipix2</i> voltage DACs transfer functions. ....	62
Figure 3.11. INL and DNL of the threshold DAC (V <sub>THL</sub> ) of one <i>Medipix2</i> chip. ....	63
Figure 3.12. Two SEM images before assembling. On the left the eutectic tin-lead solder bumps sitting on top of the <i>Medipix2</i> and on the right the Si sensor side. [Courtesy of A. Huffman, RTI]. .....	64

Figure 3.13. A leave inside capton tape: image taken with a <i>Medipix2</i> assembled to a high resistivity $300 \mu\text{m} \text{ p}^+$ on n Si sensor exposed to a $^{55}\text{Fe}$ X-ray source during 300 seconds. The images has been flatfield corrected.....	65
Figure 3.14. On the left pixel threshold scan with a $10 \times 10 \mu\text{m}^2$ 7.9 keV pencil beam with its harmonics focused at the center of one pixel. On the right pixel linearity and gain slope extracted from the threshold scan.....	67
Figure 3.15. Section and top view schematic of a <i>Medipix2</i> multi-chip structure ( <i>Medipix2 Quad</i> ).....	67
Figure 3.16. Threshold dispersion before equalization (step trace): Chip0 $\sigma=394 \text{ e}^-$ rms and Chip[1-3] $416 \text{ e}^-$ rms with a minimum detectable charge of $\sim 4400 \text{ e}^-$ . Threshold dispersion after equalization (solid bar trace): Chip [0-3] $\sigma=117 \text{ e}^-$ rms with a minimum detectable charge of $\sim 1200 \text{ e}^-$ .....	68
Figure 3.17. Image taken with a $^{109}\text{Cd}$ source using a 10 min acquisition time. On the left before equalization, and on the right after equalization. Note that the grey levels of the larger pixels have been normalized to their surface area.....	69
Figure 3.18. Images taken with an equalized <i>Medipix2 quad</i> : On the left 500 ms acquisition of an anchovy with a W X-ray tube at 15 kVp; on the right: A 100 ms acquisition of a wrist watch with a W X-ray tube at 50 kVp.....	69
Figure 3.19. Threshold shift as seen in the 3-bit low threshold equalization mask. After 10 krad of integrated dose a threshold shift is clearly visible in the irradiated area.....	70
Figure 4.1. The <i>Mpix2MXR20</i> pixel cell. On the left the analog side and on the right the digital side.....	75
Figure 4.2. The <i>Mpix2MXR20</i> pixel cell layout. 1) Preamplifier; 2) High Threshold Discriminator; 3) Low Threshold Discriminator; 4) 8-bit configuration latches; 5) DDL; 6) 14-bit Counter and overflow control. In yellow the passivation opening for bump bonding.....	75
Figure 4.3. Threshold shift as seen in the 3-bit low threshold equalization mask. After 200 krad of integrated dose a threshold shift is clearly visible in the irradiated area.....	76
Figure 4.4. On top the <i>Medipix2</i> CSA. On the bottom the <i>Mpix2MXR20</i> CSA using ELTs (at the bottom left). .....	77
Figure 4.5 On the left a typical <i>Medipix2</i> 3-bit equalization mask and on the right a <i>Mpix2MXR20</i> 3-bit equalization mask. The right picture has a better uniformity.....	78
Figure 4.6. The <i>Mpix2MXR20</i> SR/C schematic. The global lines are displayed in red.....	79
Figure 4.7. <i>Mpix2MXR20</i> PCR is formed by latching 8-bit of the 14-bit shift register.....	80

Figure 4.8. The <i>Mpix2MXR20</i> periphery floor plan. On blue the periphery blocks and IO lines using the analog power supply, on green the blocks and IO lines using digital power supply and on purple the blocks and IO lines using LVDS power supply. The dashed lines indicate the upgrades or new blocks compared to <i>Medipix2</i> .....	80
Figure 4.9. Circuit used to transform the temperature independent voltage ( $V_{bg}$ of 1.16V) into a temperature independent current to bias the DACs ( $I_2$ of 40nA). .....	81
Figure 4.10. A 14-bit voltage DAC layout. On the left: the regular structure of an 8-bit DAC is used to create a 4-bit DAC (coarse) by grounding the less significant bits. On the right: current source array and output stage of the 10-bit DAC. ....	82
Figure 4.11. On the left simulated linearity and gain response of the unitary gain buffers. The unitary gain dynamic range extends from ~0.4 to 2.2 V. On the right a simulation of the test pulse at the input and output of the buffer which is loaded with an extracted column equivalent impedance of $3\text{ k}\Omega$ and 3 pF. The symmetrical rise and fall time are below 50 ns for an input charge of 400 mV (20 ke $^-$ ). ....	83
Figure 4.12. <i>Mpix2MXR20</i> fuses EoC register. ....	85
Figure 4.13. On the left the <i>Medipix2</i> bond pads and on the right the <i>Mpix2MXR20</i> bond pads. New pads are 100 $\mu\text{m}$ longer for wire bonding robustness. ....	86
Figure 4.14. Two typical <i>Mpix2MXR20</i> wafer maps obtained after selection process. Each <i>Mpix2MXR20</i> wafer contains 107 dies. ....	87
Figure 4.15. Measured Current DACs from chip G6 of wafer XX4ISST (23).....	87
Figure 4.16. Measured voltage DACs from chip G6 of wafer XX4ISST (23). ....	88
Figure 4.17. Measured threshold voltage DACs from chip G6 of wafer XX4ISST (23). ....	88
Figure 4.18. INL and DNL for the THL DAC of one <i>Mpix2MXR20</i> chip.....	89
Figure 4.19. Pixel characterization using the injection test pulse. The noise, gain, effective threshold and linearity can be extracted for all pixels using this technique. ....	90
Figure 4.20. On the left: normalized gain variation versus IPreamp DAC. On the right: ENC assuming Ctest 8 fF. Measurements realized over 8 pixels from chip G6 of wafer XX4ISST(23). The ENC measurements show a non continuous curve due to quantization errors.....	90
Figure 4.21. Measured gain vs Preamp DAC with error bars showing the top-down pixel gain variation. ....	91
Figure 4.22 On the left: normalized gain variation versus Ikrum DAC. On the right: ENC assuming Ctest 8fF. Measurements realized over 8 pixels from chip G6 of wafer XX4ISST(23). The ENC measurements show a non continuous curve due to quantization errors.....	91

Figure 4.23. Test pulse linearity for both polarities with a linear fit in 16 pixels across the matrix.....	92
Figure 4.24. Measured effective charge of 3 different pixels across the matrix during 28 consecutive hours. A new frame is taken every minute. Top: mean = 2469 e <sup>-</sup> and sigma=18.3 e <sup>-</sup> ; Middle: mean = 2514 e <sup>-</sup> and sigma=16.5 e <sup>-</sup> ; Bottom: mean = 2493 e <sup>-</sup> and sigma=17.1 e <sup>-</sup> .....	93
Figure 4.25. Low threshold equalization using the noise floor for both collection polarities. Before equalization (step traces) the threshold variation is ~400 e <sup>-</sup> for both polarities. After equalization (solid bar traces) the measured threshold variation is ~95 e <sup>-</sup> for both polarities. Chip used J2-W15.....	94
Figure 4.26. Row average threshold before (top and bottom curves) and after equalization (middle curve) for chip G6-W23. ....	94
Figure 4.27. Threshold adjustment DAC linearity.....	95
Figure 4.28. On the left: high threshold equalization distributions before (step traces) and after (solid bar trace) equalization. On the right the THL and THH equalization mask comparison. ....	96
Figure 4.29. Image taken with a <i>Mpix2MXR20</i> bonded to a 300 $\mu\text{m}$ Si sensor of a <sup>90</sup> Sr $\beta$ -source with 60 s exposure time. On the left the 2D image on the right the profile image. The pixel counter overflow control is stopped at 11810 counts. ....	97
Figure 4.30. Energy calibration of a <i>Mpix2MXR20</i> bonded to a 300 $\mu\text{m}$ thick Si sensor. Several materials have been put in front of a X-ray tube in order to use the fluorescence lines K $\alpha$ and K $\beta$ as calibration references: Cd (23.1 / 26.1 keV) Pd (21.2 / 23.8 keV) In (24.2 / 27.3 keV) Cu (8.05 / 8.9 keV). The measured gain slope is ~145 eV per THL DAC step and a minimum detectable energy of ~3.8 keV. ....	98
Figure 5.1. The <i>Timepix</i> pixel cell. ....	100
Figure 5.2. <i>Timepix</i> simulated CSA output gain versus Ikrum. The addition of the cascode in the differential pair of the preamplifier improves the gain by ~30% in both polarities. The dotted curve corresponds to the <i>Medipix2</i> gain shown in Figure 2.8. ....	102
Figure 5.3. Preamplifier voltage output linearity and dynamic range versus input charge. ....	102
Figure 5.4. <i>Timepix</i> simulated CSA output ENC versus Ikrum and Ipreamp. The dotted curve corresponds to the <i>Medipix2</i> ENC for Ipreamp=750nA shown in Figure 2.12. ....	102
Figure 5.5. Simulated peaking time of the CSA output pulse. The cascode in the preamplifier reduces the CSA input capacitance and reducing the rise time for the same bias conditions as for <i>Medipix2</i> and <i>Mpix2MXR20</i> .....	103
Figure 5.6. Discriminator block diagram.....	104
Figure 5.7. The TSL schematic. In red are displayed the global signals applied to all pixels simultaneously and in black the internal lines in each pixel.....	106

Figure 5.8. Simulated output of a pixel configured in arrival time mode (left)	106
and in TOT mode (right). ....	
Figure 5.9. <i>Timepix</i> PCR is formed by latching 8 bits of the 14-bit shift register.	106
Figure 5.10. <i>Timepix</i> pixel cell layout: 1) CSA, 2) Discriminator with 4-bit	
threshold equalization, 3) 8-bit PCR, 4) <i>Ref_Clk</i> buffer and TSL	
and 5) 14-bit shift register and overflow control. ....	107
Figure 5.11. Digital power distribution simulation on a column of pixels during	
<i>Ref_Clk</i> startup taking into account the parasitic capacitances and	
stray resistance at <i>Ref_Clk</i> =100 MHz. Once the <i>Ref_Clk</i> is fully	
propagated to all the column ( $\sim 50$ ns) the digital power	
consumption is quasi-static. This effect reduces the coupling to	
neighboring analog lines.....	108
Figure 5.12. Analog wafer test for chip D10-W15 (class C chip). 100 pulses are	
sent in each acquisition. On the left all the pixels are in event	
counting mode: there is only information of number of dead	
columns. On the right all the pixels are in TOT mode: It can be seen	
the two dead columns and the pixel to pixel gain variations.....	110
Figure 5.13. Gain (in red) and ENC (in blue) versus Preamp DAC measured in	
event counting mode. The non-monotonic behavior is due to a	
digital problem in the DACs registers which affect only certain	
binary codes in some DACs. ....	111
Figure 5.14. Measured peaking time variation for three Preamp DAC settings.	
The measurement is done by setting the matrix in arrival time mode	
and sending one test pulse of 18.75 ke <sup>-</sup> while scanning the global	
threshold. As expected the time-walk and gain maximizes for high	
preamp currents. ....	112
Figure 5.15. Gain (in red) and electrical noise (in blue) versus Ikrum biasing	
current measured in event counting mode.....	112
Figure 5.16 On the left: TOT mode measurement of a single cosmic background	
particle interacting on a gas volume of a triple GEM detector. The	
maximum number pixel value of 1929 counts corresponds after	
calibration to $\sim 120$ ke <sup>-</sup> . On the right: Arrival time measurement of a	
cosmic background particle obtained with a Micromegas gas gain	
grid coupled to the <i>Timepix</i> chip with a time resolution of $\sim 20$ ns.	
Both 2D images are made with raw data. The green background on	
the left image displays pixels with no counts. ....	114
Figure 5.17. The full pixel matrix is in mixed-mode: every two pixels one is	
configured in TOT mode and the other in arrival time mode. After	
readout two images are generated from the same event using	
interpolation: On the left a TOT measurement, and on the right the	
arrival time measurement. Data taken during a test beam in DESY	
(Hamburg, November 2006). Green background shows pixels with	
no counts.....	114
Figure 5.18. Energy calibration of a <i>Timepix</i> bonded to a 300 $\mu$ m high	
resistivity Si sensor. <sup>109</sup> Cd ( with 22.1 and 24.9 keV emission lines)	

and $^{55}\text{Fe}$ (with a main 5.9 keV emission line) X-ray sources are used as energy references. The measured gain slope, on the right figure, is $\sim 87$ eV per THL DAC step with a full chip minimum detectable charge of $\sim 2.7$ keV.....	115
Figure 5.19. S-curve response of a pixel in the center of the matrix before and after bump-bonding for two different chips but under the same bias conditions. The injected test pulse is 4.7 keV. The ENC is extracted from s-curve slope. After detector bump-bonding the measured ENC is $\sim 16\%$ higher than with a <i>naked</i> chip.....	116
Figure 5.20. On the left is shown TOT raw data for the full chip exposed to a $^{241}\text{Am}$ radioactive source with 100 ms <i>Shutter</i> time. The large pixel clusters are the result of the charge deposition by single $\alpha$ particles (above 5 MeV). Three $\alpha$ clusters are shown in the 3D plot revealing the energy information. The single hits are due to the $^{241}\text{Am}$ $\gamma$ radiation (mainly 13.9 and 59.5 keV). The threshold is set $\sim 3.1$ keV, and $\text{Ref\_Clk} = 47.3$ MHz. The 2D images on the right and on the top left the green color indicates pixels with no counts.....	117
Figure 6.1. CSA output pulse of a 4 pixel cluster after detecting a 59.5 keV photon from a $^{241}\text{Am}$ radioactive source. The event is split amongst the 4 pixels generating a distortion in the measured spectrum. Data taken using the Medipix2 3x3 analog output with 4 channels connected to a 1Gs/s digital oscilloscope. X= 200 ns/div and Y= 10 mV/div.....	119
Figure 6.2. The <i>Medipix3</i> prototype. The 8 x 8 pixel matrix is at the centre of the chip. The top and bottom bon pads are used for analog power, transistor biasing, and seven injection test pads. The lateral pads are used for digital power and digital communication.....	120
Figure 6.3. The <i>Medipix3</i> pixel cell schematic.....	121
Figure 6.4. The <i>Medipix3</i> prototype pixel layout: 1) CSA, 2) Shaper and replica currents, 3) Discriminators with 5-bit threshold adjustment, 4) Control logic, 5) Two 15-bit shift register/counters, 6) 19-bit PCR and 7) Arbitration circuit.....	122
Figure 6.5. Drawing of the proposed RELAXD tile. The sensor (blue) is connected to 4 <i>Mpix2MXR20</i> chips by (red) flip-chip solder balls. The <i>Mpix2MXR20</i> chips (red) are connected to the printed circuit board (green) by etching holes through the chips, while on their backside contact is made via Ball-Grid-Array technology (white balls). [Vis06].....	124
Figure 6.6. The square tile. Wafer thinning and thorough-wafer vias are built in order to interconnect the sensor material, the pixel matrix chip and the IO chip.....	125

## LIST OF PAPERS

This thesis is based on the following papers, herein referred to by their Roman numerals:

- Paper I     ***Medipix2, a 64k pixel readout chip with 55 $\mu$ m square elements working in single photon counting mode***  
X. Llopert, M. Campbell, R. Dinapoli, D. San Segundo, and E. Pernigotti, *IEEE Trans. Nucl. Sci.*, vol. 49, pp: 2279-2283, 2002
- Paper II    ***First test measurements of a 64k pixel readout chip working in single photon counting mode***  
X. Llopert and M. Campbell, Nuclear Instruments and Methods in Physics Research A 509, pp: 157–163, 2003.
- Paper III   ***X-ray imaging using single photon processing with semiconductor pixel detectors***  
B. Mikulec, M. Campbell, E. Heijne, X. Llopert and L. Tlustos, Nuclear Instruments and Methods in Physics Research A 511, pp: 282-286, 2003.
- Paper IV   ***First Experimental Tests with a CdTe Photon Counting Pixel Detector Hybridized with a Medipix2 Readout Chip***  
M. Chmeissani, C. Frojdh, O. Gal, X. Llopert, J. Ludwig, M. Maiorino, E. Manach, G. Mettivier, M. C. Montesi, C. Ponchut, P. Russo , L. Tlustos and A.Zwerger, *IEEE Trans. Nucl. Sci.*, vol. 51, pp: 2379 – 2385, 2004.
- Paper V    ***Signal variations in high-granularity Si pixel detectors***  
L. Tlustos, M. Campbell, E.H.M. Heijne and X. Llopert, *IEEE Trans. Nucl. Sci.*, vol. 51, pp: 3006-3012, 2004.
- Paper VI   ***Imaging properties of the Medipix2 system exploiting single and dual energy thresholds***  
L. Tlustos, R. Ballabriga, M. Campbell, E.H.M Heijne, K. Kincade, X. Llopert and P. Stejskal, “”, *IEEE Trans. Nucl. Sci.*, vol. 53, pp: 367-372, 2006.
- Paper VII   ***Electron imaging with Medipix2 hybrid pixel detector***  
G. McMullan, D.M. Cattermole, S. Chen, R. Henderson, X. Llopert, C. Summerfield, L. Tlustos and A.R. Faruqi, *Ultramicroscopy*, vol. 107, pp: 401-413, 2007.

- Paper VIII    **The readout of a GEM or Micromegas-equipped TPC by means of the *Medipix2* CMOS sensor as direct anode**  
 P. Colas, A.P. Colijn, A. Fornaini, Y. Giomataris, H. van der Graaf, E.H.M. Heijne, X. Llopart, J. Schmitz, J. Timmermans and J.L. Visschers, Nuclear Instruments and Methods in Physics Research A 535, pp: 506–510, 2004.
- Paper IX    **Detection of single electrons by means of a Micromegas-covered *Medipix2* pixel CMOS readout circuit**  
 M. Campbell, M. Chefdeville, P. Colas, A.P. Colijn, A. Fornaini, Y. Giomataris, H. van der Graaf, E.H.M. Heijne, P. Kluit, X. Llopart, J. Schmitz, J. Timmermans, J.L. Visschers, Nuclear Instruments and Methods in Physics Research A 540, pp: 295–304, 2005.
- Paper X    ***Timepix*, a 65k programmable pixel readout chip for arrival time, energy and/or photon counting measurements**  
 X. Llopart, R. Ballabriga, M. Campbell, L. Tlustos and W. Wong, proceedings of the 11<sup>th</sup> International Vienna Conference on Instrumentation, February 2007.
- Paper XI    **The *Medipix3* Prototype, a Pixel Readout Chip Working in Single Photon Counting Mode with Improved Spectrometric Performance**  
 R. Ballabriga, M. Campbell, E.H.M. Heijne, X. Llopart and L. Tlustos, proceedings of Nuclear Science Symposium IEEE 2006, October 2006, San Diego, USA, published on CDROM.

## INTRODUCTION

Hybrid semiconductor detectors have become important tools for particle tracking in high multiplicity environments in high-energy physics experiments. Silicon pixel detectors were introduced at the beginning of the 1990s [ANG92] as a substitution of silicon strip detectors in environments requiring high granularity due to the large density of particle tracks. Silicon sensors have improved since then, but the continuing popularity of semiconductor detectors can be accredited mainly to progress in microelectronics. According to Moore's Law [MOO65], the number of transistors on a chip roughly doubles every two years. As transistor counts climb so does the functionality per unit area providing more sophisticated readout or reduced pixel size.

Small pixel sizes together with high electronic component densities allowed pulse processing electronics to be applied to imaging applications for the first time. Using pulse processing a particle signal can be distinguished from background noise with the help of a noise reducing preamplifier shaper circuit if a discriminator is used. The discrimination level can be safely set above the noise level for applications requiring low-dose or low-rate imaging.

This thesis summarizes the design and characterization of three pulse processing chips for X-ray imaging with a square pixel size of 55  $\mu\text{m}$  organized as a matrix of 256 x 256 pixels realized with a commercial 0.25  $\mu\text{m}$  6-metal CMOS technology. The three chips, named *Medipix2*, *Mpix2MXR20* and *Timepix*, share the same floor plan and dimensions (14111  $\mu\text{m}$  x 16280  $\mu\text{m}$ ).

A description of the contents of the thesis, chapter by chapter, follows:

- Chapter 1: The field of X-ray imaging with segmented detectors is introduced. A short overview of the advantages of digital imaging systems compared to analog systems is presented. Emphasis is placed on the distinction between direct and indirect detection systems and integrating and counting methods. Different detector technologies are overviewed but concentrating on the potential of the direct detection photon counting hybrid pixel chips.
- Chapter 2: The requirements of the *Medipix2* chip are outlined. The *Medipix2* is designed in a commercial 0.25  $\mu\text{m}$  CMOS technology which contains 256 x 256 square pixels. The *Medipix2* pixel cell and the chip periphery architecture are described. Also the design actions taken to tile multi-chip structures using the *Medipix2* are explained.
- Chapter 3: After an overview of the available chip carriers, readout boards and software for *Medipix2* the wafer probing selection criteria is presented as an important step to select good dies before detector mounting. First electrical measurements show a good performance of the chip, which is confirmed by an absolute calibration using the *Medipix2* connected to a 300  $\mu\text{m}$  silicon detector.

- Chapter 4: The *Mpix2MXR20* is an upgrade of the *Medipix2*. In this chapter the pixel and periphery modifications are described in detail together with the first electrical characterisation of the chip. After detector bonding an absolute calibration reveals that the chip performs according to the design specifications.
- Chapter 5: Successful tests with the *Medipix2* and *Mpix2MXR20* as readout anodes for Micro-Patterned Gas Detectors (MPGD) lead to the major modification of the *Mpix2MXR20* to provide arrival time, time-over-threshold or event counting in every pixel. The main design modifications of the new chip, named *Timepix*, are analysed. Pixel electrical characterisation, first images when coupled to gas gain grids, and an absolute calibration using X-ray sources are also reported
- Chapter 6: The effects on the measured energy spectrum of high granularity pixel detectors due to charge sharing are analysed. The *Medipix3* collaboration has been set to build a new prototype chip designed at CERN and manufactured in a commercial  $0.13\text{ }\mu\text{m}$  8-metal CMOS technology. The chip architecture and first electrical results are reported. Some new ideas for future pixel detector developments are described.
- Thesis summary: This final chapter deals with the conclusions which can be drawn from this work. The main results and their significance are discussed.

# 1 IMAGING WITH SEGMENTED DETECTORS

This chapter introduces the concept of digital X-ray imaging using pixel detectors. First the advantages of digital X-ray imaging over classic analog systems are discussed in section 1.1. In the same section digital X-ray systems are categorized as a function of their photon detection system and by the way their information is processed. Section 1.2 describes different pixel readout technologies for X-ray imaging. The readout chips described in this thesis are the latest in a line of development which originated in High Energy Physics (HEP). This historical perspective is presented in section 1.3.

## 1.1 DIGITAL X-RAY IMAGING

The development of digital detectors for X-ray imaging in general is motivated by the many advantages of digital imaging over analog screen film images:

- Data storage and archiving.
- Image post-processing can be applied for image enhancement.
- Fast data transfer through computer networks.
- Real time imaging.
- Dose reduction: the dose can be optimized to the required signal-to-noise level for a specific setup.
- Higher dynamic range.

Practically all digital x-ray imaging technologies can be categorized by their photon detection system (direct versus indirect) and by the particle or photon recording method (integrating versus counting)

### 1.1.1 Direct versus indirect detection systems

In the direct photon detection systems the X-rays convert in the sensor itself whereas in indirect systems they typically use an intermediate layer to convert the X-rays into light which is then detected in the sensor. In the indirect detection systems the light spread in the conversion layer leads to a reduction of contrast and spatial resolution. The most common indirect detector systems use a scintillator connected with a CCD or AMFPI. These are normally used in radiology where a lower spatial resolution is accepted as a trade-off with improved sensitivity. Direct detection systems offer higher spatial resolution and higher energy resolution. CMOS imagers, charged coupled devices (CCD) or flat panel imagers (AMFPI) are common direct detection systems.

### 1.1.2 Counting versus integrating methods

In an integrating system the collected current pulse produced by each X-ray interaction is added to a potential well (CCD) or a capacitor without any further

treatment (MAPS). Currents originating from other sources than the detected signal, such as detector leakage currents, are also added and introduce noise to the accumulated signal. Especially in low count rate applications, where long acquisition times are required, the contribution of integrated noise becomes more pronounced.

The number of charges generated when a photon is completely absorbed in a sensor is directly proportional to its energy. Therefore the contribution of the converted photons in an integrating system is weighted by their energy. Image contrast is generated by the absorption of photons in the object. Low energy photons which are transmitted through an object are more strongly attenuated and therefore they carry more information. By weighting the photon by its energy, image contrast carried by low energy photons has a weaker weight and the Poisson noise contribution from high energy photons is enhanced. The result is a decrease in image SNR.

In the case of photon counting the collected charge produced by each X-ray interaction is compared to a threshold. If the detected charge is above the threshold the counter is incremented. The effect of having a threshold eliminates the contribution of detector leakage and low rate imaging can be then performed. Photon counting removes the weighting of photons and only registers the validity of an event, thereby increasing the SNR. Counting systems exhibit a perfectly linear and theoretically unlimited dynamic range [MIK00]. The setting of a threshold makes it possible to discriminate not only noise from signal, but also lower from higher energies or even multi-threshold discrimination is possible [Paper XI].

## 1.2 DETECTOR TECHNOLOGIES

In this section a brief overview is provided of a selection of pixel readout technologies used for X-ray imaging. This should help in better understanding the difficulties related to this field and the advantages a hybrid photon counting chip system could bring.

### 1.2.1 CCD

A charge coupled device imager (CCD) consists of an array of potential wells in a metaloxide-semiconductor chip. Gate electrodes are built on top of an insulating oxide layer and when charged create a depleted zone in the semiconductor underneath the oxide. The pixels are organized in parallel columns by implanted potential barriers [GRU02 and LUT99]. Photo-charges generated in the semiconductor are accumulated in the potential wells. The readout is accomplished by clocking the gate potentials in such a way that the accumulated charge packets are shifted down the pixel columns. At the end of the columns an analog output shift register transports the charge packets to an on-chip preamplifier. The main advantage of this structure is the very low input capacitance presented to the preamplifier, which allows for noise figures down to a few electrons rms in devices cooled below  $\sim 130$  K. The main disadvantages are that the detector

is still sensitive to radiation and leakage currents during the readout charge transport from pixel to pixel and that the pixel values have to be processed serially by the preamplifier. This limits the achievable readout speed and also links the noise performance to the readout speed. Furthermore the dynamic range is limited by the potential well, usually is in the order of  $10^5$  e<sup>-</sup> [GRU02] and the minimal charge signal of ~100 e<sup>-</sup>.

The CCD itself is weakly sensitive to X-rays, since the depletion is only several  $\mu\text{m}$ . Therefore most X-ray imaging CCDs are coupled to scintillating materials like CsI(Tl) or Gd<sup>2</sup>O<sup>2</sup>S. As already described, in this indirect detection scheme the achievable spatial resolution is limited by the light spread of the scintillator layer. Although pixel sizes for CCD systems in medical applications may be as small as 25  $\mu\text{m}$ , the spatial resolution is in the order of ~5 lp/mm [EVA02].

### 1.2.2 Flat Panel Imager

Active matrix flat panel imagers (AMFPI) use thin film transistor (TFT) or thin film diode (TFD) arrays as readout electronics. In such devices each pixel element contains a converter, a charge storage node, and readout switch (see Figure 1.1). Flat panel imagers are based on amorphous silicon and use a similar manufacturing process as liquid crystal displays, allowing for large areas to be covered. Typically the readout electronics is deposited onto a glass substrate. Pixel sizes range from 100 to 400  $\mu\text{m}$  [HUN04, LEP05 and PAR02]. In the case of a direct detection system, the converter layer, e.g. amorphous Se [HUN04], is deposited directly on the readout. In indirect systems a layer of light sensitive photodiode is deposited on top of the TFT, followed by the scintillator. The necessity to implement the photodiode leads to a reduced fill factor, i.e. a reduction in sensitive area per pixel cell. The readout switches connect a row of pixels to charge amplifiers located at the bottom of the columns. In this way the readout time can be significantly improved with respect to CCD systems. The main advantage of AMFPI over CCDs is that large areas can be covered. The biggest drawback is the high electronic noise of ~700 e<sup>-</sup> [ZHA05] per pixel even with pixel amplification, without pixel amplification is a factor 2-4 higher, which makes this technology not suitable for low X-ray energy detection.

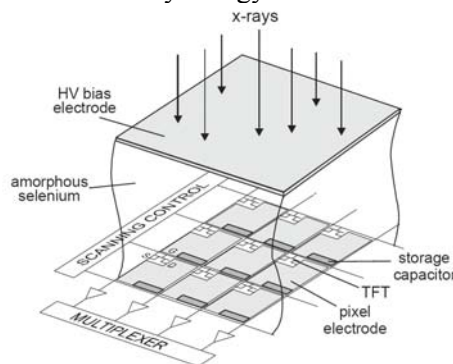


Figure 1.1. Schematic diagram showing the concept of direct AMFPI [ZHA05].

### 1.2.3 Monolithic Active Pixel Sensors (MAPS)

CMOS MAPS technology, developed for visible light imaging in the early '90s [FOS97], and now widely applied in commercial digital cameras and for scientific applications, seems very promising for application in future tracking detectors. These monolithic devices incorporate in the same substrate a very thin sensor (only a few tens of microns thick) and the readout electronics. The use of commercial CMOS technology for the readout results in high functional density, low power consumption and low fabrication costs. The first MAPS prototype sensors for particle tracking have been realized [TUR01] with an extremely simple sequential readout scheme, as generally used for imaging applications.

In CMOS active pixels the signal generated by a particle crossing the detector is collected by a diode formed between the n-well and a lightly doped, thin p-type epitaxial layer present in several CMOS technologies between the low resistivity bulk substrate and the CMOS processing layers. A typical MAPS pixel is schematically shown in Figure 1.2. Several differences are present with respect to high resistivity sensors. The charge generated moves by thermal diffusion in the p-epitaxial layer, since full depletion is not an option with a doping of about  $10^{15} \text{ cm}^{-3}$  and CMOS voltage restrictions. The potential wells at the boundaries of the epi layer, due to the high doping of the neighboring p-type substrate and p-wells, confine the generated electrons in the epitaxial layer until they reach the collecting electrodes, within a typical collection time of the order of a few tens of ns to 100 ns. Due to the relatively low carrier lifetime in the epitaxial layer (of order 10  $\mu\text{s}$ ) the diffusion distance is limited, and even with a thick p-epitaxial layer, the typical signal collected for a minimum ionizing particle (MIP) ranges from several hundreds to a thousand electrons, depending on the thickness of the active epi layer and on the size of the collecting electrode.

The basic readout principle of CMOS MAPS is based on only three transistors (3T) inside the pixel cell (Figure 1.2): one used to select the pixel (M3), a source follower to buffer the collected charge (M2), and a reset used periodically to compensate the diode leakage current integration and to remove the collected charge from the previous event (M1). Two main design rules need to be followed in the design of the baseline 3T CMOS MAPS: the collecting electrode should be as small as possible, since charge to voltage conversion is performed using the sensor capacitance and only NMOS transistors are allowed inside the active sensor area; one should avoid the presence of an additional n-well region, which could otherwise subtract charge from the collecting n-well electrode causing an efficiency loss when detecting MIPs. The small size of the collecting electrode further reduces the single pixel signal to about 300  $e^-$ , for the seed pixel in the cluster, even with a thick epi-layer of about 14  $\mu\text{m}$  [DEP02].

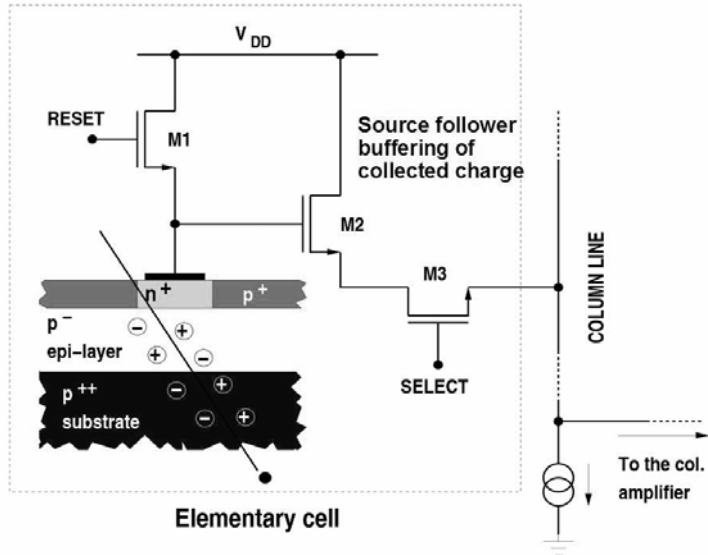


Figure 1.2. The baseline architecture of CMOS imager [RIZ07]. Transistor M1 resets the photosite to reverse bias, transistor M2 is a row switch, while transistor M2 is the input of a source follower. Follower's current source (common to entire row) and column selection switch are located outside the pixel.

Even though these prototypes have shown successful results they still suffer from three major drawbacks:

- Large charge spreading over many pixels and a relative *slow* charge collection (~100ns) due to the poor charge collection and thermal diffusion in the n-well/p-epi diode.
- Since only NMOS transistors can be used the charge transfer outside the pixel is slow and only possible in an analog approach.
- The need of a thick epi-layer makes the choice of appropriate standard CMOS technologies very small and only useable for detection off photons with few keV (limit set by epi-layer thickness).

A new approach in the design of CMOS MAPS sensors has been proposed in [BET07], exploiting the triple well option available in several commercially available technologies, to improve the readout speed potential of MAPS devices and at the same time to increase the sensitive element area. This addresses two of the major limitations of the baseline 3T MAPS design described before. In triple well commercial CMOS processes an n-well with a deep junction is available to ensure better insulation of the analog n-channel devices from the substrate and the neighbouring digital devices. In the pixel design the deep n-well is used as a charge collecting electrode and also contains part of the front-end stage. This was possible since part of the n-channel devices of the analog readout electronics are located in the p-type well, physically overlapped with the area of the sensitive element. In this way the collecting electrode can cover a large fraction of the elementary cell,

maximizing the fill factor, and at the same time more room is available to develop more complex readout electronics at the pixel level. The signal processing chain implemented in-pixel includes a charge preamplifier, a shaper, a discriminator and some elementary logic functionality. With the use of a charge preamplifier as a front-end element the charge sensitivity is independent of the capacitance of the charge collecting electrode, whose area can thus be extended. With the large sensing electrode area (about  $1000 \mu\text{m}^2$ ) made possible with this new approach, charge collection could be very efficient, increasing by more than a factor of three the single pixel signal collected with respect to a typical 3T MAPS device with the same epitaxial layer thickness. A further advantage of the new design proposed is that the readout scheme is easily compatible with already available architectures performing data sparsification at the elementary cell level.

Even though with the recent MAPS developments where full CMOS circuitry can be built, overcoming one of the major limitations in the past, this detection technology still suffers from two weak points:

- Only few processing technologies are suited since the thickness of the epi-layer varies from different CMOS technologies.
- The slow charge collection is still an issue even with the increased collection area, due to the due to thermal diffusion.

#### 1.2.4 DEPFET

Based on the sideward depletion principle [GAT84], the Depleted Field Effect Transistor (DEPFET) detector–amplifier structure has been invented in 1985 by Kemmer and Lutz [KEM87]. A p-channel field effect transistor is placed on a fully depleted bulk (Figure 1.3). By suitable doping, a potential maximum (internal gate or IG) is created below the transistor channel. Electrons created anywhere in the depleted bulk are collected in the IG, inducing a mirror charge within the channel, thus increasing its conductivity. The unique properties of this device, as for example, combined detector and amplification properties signal charge storage and non-destructive readout make it useful for many applications. Of particular interest is its use as a building block of a pixel detector with very low noise, due to the small capacitance of the internal gate, and power consumption. Different DEPFET structures (linear and circular) are being studied for biomedical autoradiography [ULR05], imaging of low energy X-rays from astronomical sources [HOL00] and particle detection at a future linear collider [KOH03].

The DEPFET sensor technology is non-standard. The operation of pixel detectors requires separate steering and amplification ICs which might become the biggest contribution of power consumption and noise in large systems.

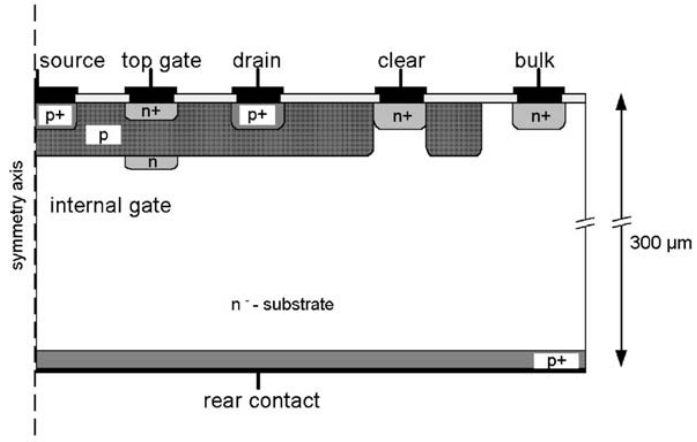


**Figure 1.3.** Cross-section of an annular pulsed clear DEPFET [ULR05]. The structure is symmetric around the source contact. The potential along the axis top gate-rear contact shows a minimum for electrons under the JFET channel.

### 1.2.5 Silicon on Insulator (SOI)

A silicon on insulator (SOI) wafer consists of a monocrystalline Si film (device layer) over an insulating layer of  $\text{SiO}_2$  (buried oxide-BOX) on a Si substrate (handle wafer). In the standard SOI technologies, the handle wafer serves as a mechanical support for the device layer with the integrated circuits. In SOI pixel detectors (see Figure 1.4), the high-resistivity handle wafer is used for the fabrication of the sensor (a matrix of fully depleted diodes) monolithically coupled to the read-out electronics integrated in the device layer. That idea was published by [DIE93] and several pixel prototypes has been produced [PEN96, XU01, ZHE03 and KUC04] using different wafer processing techniques. These monolithic detector designs requires non-standard processing (double-sided processing, p-implants underneath the oxide layer of the SOI wafer) which can make it very expensive.

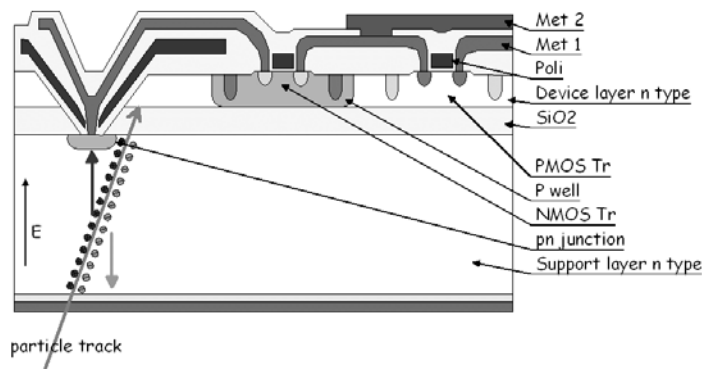


**Figure 1.4.** Cross section of an SOI process using the substrate as sensitive detection volume [KUC04]. The layer of  $\text{SiO}_2$  (buried oxide-BOX) insulates the CMOS readout electronics and the sensitive substrate (handle wafer).

### 1.2.6 Hybrid pixel detectors

In the hybrid pixel detector architecture, Figure 1.5, the radiation sensor element and the readout are processed separately. The sensor is segmented with the same geometry as the readout chip and detector and readout cells are connected using standard flip-chip technology. The separation in processing allows for independent optimisation of readout and sensor and different sensor materials can be used with the same readout.

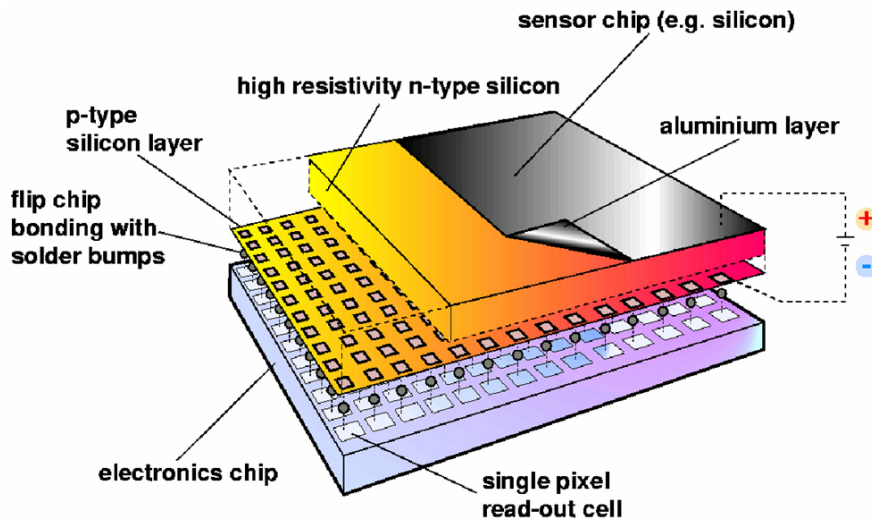
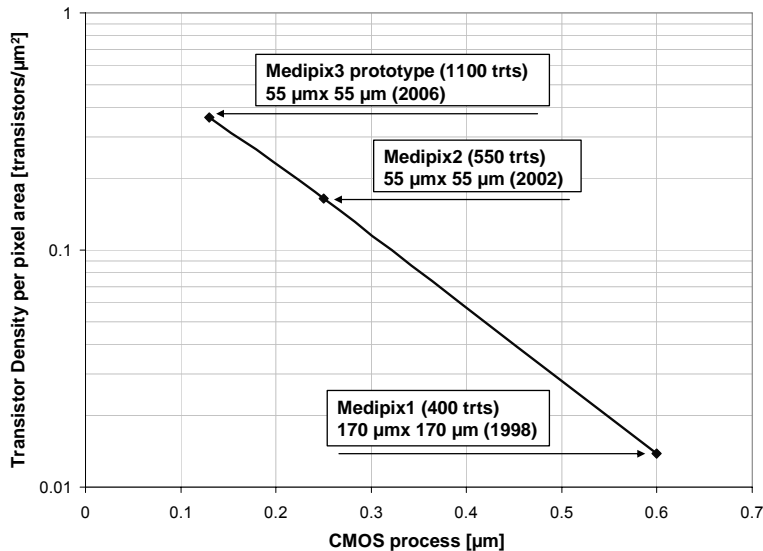


Figure 1.5. Schematic of a hybrid pixel detector with the sensor chip and the electronics chip connected via bump bonds.

By developing the readout electronics using standard CMOS technology the increase in component density can be fully exploited and advanced signal processing such as energy discrimination and digitalization can be performed on the pixel level. This is of great advantage as the photolithographic techniques are quickly evolving [MOO65] allowing either smaller pixel sizes (with inherent low noise because of smaller input capacitance [KRU91]) or more pixel functionality for the same space and power budgets (see Figure 1.6).



**Figure 1.6.** Transistor density per pixel versus CMOS process for the three chips of the Medipix project. The Medipix1 chip is in reality build in a 1 $\mu\text{m}$  SACMOS technology but the component density achievable is comparable to a 0.6  $\mu\text{m}$  standard CMOS process [MIK00].

Several groups [ROE96, COL97, and FIS99] use the direct detection photon counting hybrid pixel system approach for many different imaging applications. Two of the most active groups developing CMOS pixel chips as active readouts, apart from the Medipix project described later, are:

*The Pilatus project*, located at the Swiss Light Source (SLS), has built a large system for X-ray crystallography. Several versions of the PILATUS chip have been designed [PIL06]. The latest ASIC PILATUSII chip was designed in a commercial CMOS 0.25  $\mu\text{m}$  technology. It is arranged as a matrix of 60 columns and 97 rows of square pixels measuring 172  $\mu\text{m}$  on the side. The threshold can be tuned with 6 bits and the pixel counters have a depth of 20 bits with a maximum count rate  $\sim$ 1.5 MHz/pixel/s. The PILATUS 100K detector consists of a single module (each module has 2x8 PILATUSII chips) and has 487 x 195 pixels. The active area covers over 84 x 34 mm<sup>2</sup>. Such a detector is in use at the X04SA materials science beam line at the SLS for surface diffraction experiments since 2006. The PILATUS 6M (composed of 5 x 12 modules with 2463 x 2527 pixels and a total active area of 424 x 435 mm<sup>2</sup>) and the PILATUS 2M (composed of 3 x 7 modules with 1475 x 1467 pixels and a total active area of 254 x 252 mm<sup>2</sup>) are under construction at present.

*The XPAD project*, located in the ESRF (Grenoble) has the same aims as the Pilatus project but their applications range extend also to medical with their new XPAD3 series [PAN07] (XPAD3S and XPAD3C). The new chip [PAN07] uses a 0.25  $\mu\text{m}$  CMOS technology to achieve a square pixel measuring 130  $\mu\text{m}$  on the

side with 9600 pixels (80 x 120). Two different chips have been designed with different analog front-ends for either hole collection (with one threshold XPA3S) or electron collection (with two thresholds XPA3C).

### 1.3 THE MEDIPIX PROJECT (A SHORT HISTORY)

The Omega series [ANG92] were the first hybrid pixel detectors assembled at CERN under the RD19 collaboration [HEI90] at the beginning of the 90s. This collaboration was set to develop hybrid and monolithic pixel detectors for the future LHC experiments. Other chips followed (see summary in [ROP00]) allowing the collaboration to gain experience in the design and test of hybrid pixel detectors. Large area pixel detectors were also successfully assembled [CAM94] for the WA97 heavy-ion experiment. This experiment showed that hybrid pixel detectors were excellent devices in tracking systems especially in high multiplicity environments where excellent spatial resolution is combined with extremely high signal to noise ratios allowing physicists to find traces of rare particle tracks in very complicated events [DIB97].

The idea of using the single photon counting principle with hybrid pixel detectors for X-ray imaging dated back to late 80s [HEI89]. This technology enables the counting of particles which are deposited in each pixel. The Medipix collaboration was formed to exploit the knowledge gained in the design and fabrication of hybrid pixel detectors to make a single photon counting system for X-ray radiography. Partners of the collaboration were CERN, the University of Freiburg (Germany), the University of Glasgow (Scotland) and the INFN of Pisa and Napoli (both Italy).

The *Medipix1* (or PCC) [CAM98] is a hybrid photon counting pixel detector with a 4096 (64 x 64) square pixels designed in the SACMOS1 process with 2 metal layers. The *Medipix1* pixel cell (see the schematic in Figure 1.7) dimensions are 170  $\mu\text{m}$  x 170  $\mu\text{m}$  and contained: one charge sensitive amplifier with column leakage current compensation and one test capacitance, one threshold discriminator with a 3-bit current DAC for threshold adjustment, one delay line and a 15-bit shift register that behave as a counter or as a shift register depending on the Shutter line state.

A picture of the *Medipix1* is shown in Figure 1.8. The PCC measured 12250  $\mu\text{m}$  x 14000  $\mu\text{m}$  yielding a total area of  $\sim 1.7 \text{ cm}^2$ . About 70% ( $\sim 1.18 \text{ cm}^2$ ) of the total area were sensitive. The insensitive area contained the guard-ring and power supply lines on three sides. The largest insensitive area is at the bottom of the chip. It is due a dummy row of pixels for the leakage current sensing plus to a 66<sup>th</sup> row of bump-bonding contacts used for grounding the guard-ring of the sensor. As well as this there is the peripheral control logic and two rows of wire bonding pads.

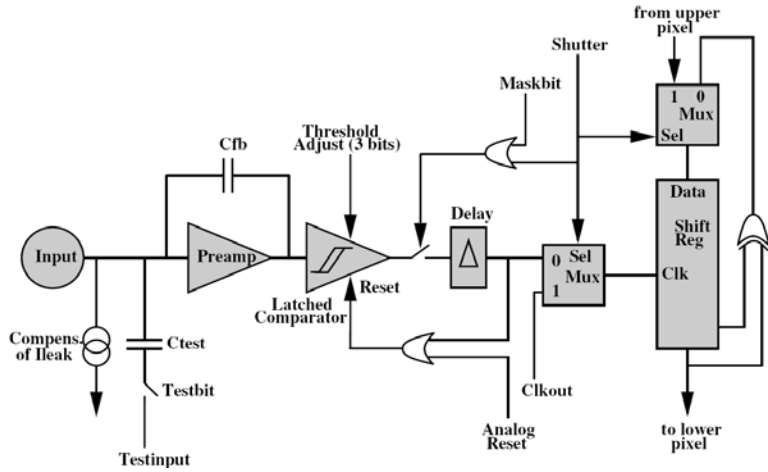
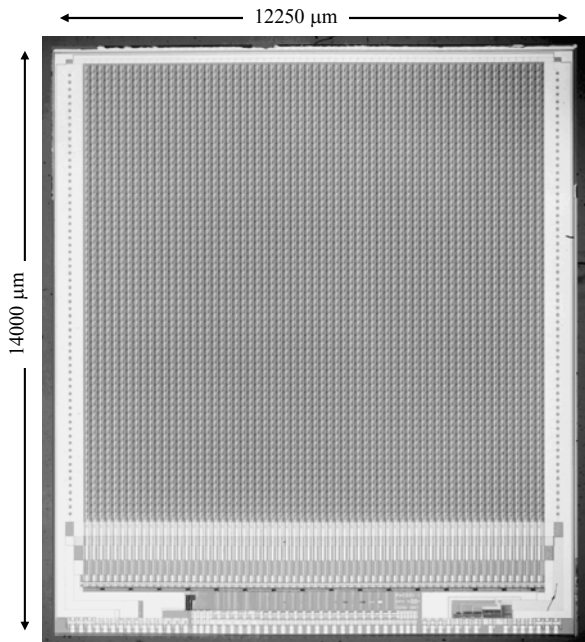


Figure 1.7. The Medipix1 pixel cell schematic.

The chip could be read out through a 16-bit bidirectional data bus using a 10 MHz clock in 384  $\mu$ s. There were two readout systems available:

- The MRS (Laben Medipix Readout System) based on a VME system [AME99].
- Muros1 (*Medipix1* re-Usable Rear-Out System) [BAR00].

The *Medipix1* was successfully assembled to 200 $\mu$ m thick semi-insulating GaAs and 300 $\mu$ m thick high resistivity silicon detectors. The equivalent noise charge of the full front-end chain was measured  $\sim$ 250 e $^-$ . The threshold spread before adjustment was  $\sim$ 500 e $^-$  and after equalization  $\sim$ 100 e $^-$ . The measured full chip minimum detectable charge was  $\sim$ 2000 e $^-$ . More detailed measurements are summarized in [MIK00, SCH01 and TLU05].



**Figure 1.8 A picture of the Medipix1 chip without detector sensor.**

## SUMMARY

In this first chapter different methods and systems to detect X-rays with high spatial resolution (pixels) have been briefly overviewed. The advantages of digital over analog detection systems have been briefly summarized. These systems can be categorized depending on the photon detection system and by the particle or photon recording method.

Several monolithic detector technologies, in which detector and readout ultimately are one entity, have been presented. MAPS are cheap if commercial CMOS technologies with thick epi-layers, used for charge collection, are available. Moreover the charge transport towards the collection anode is very slow since the bulk cannot be fully depleted. SOI and DEPFET technologies use a fully depleted bulk as charge collection sensor but both processes use non-standard technologies which can make them very expensive.

The hybrid pixel detectors fully exploit the use of standard commercial CMOS technologies without compromising the sensor detection performances. Moreover the sensor material can be optimized independently giving great design flexibility to this technology. The *Medipix1* has been described as the predecessor of the series of hybrid pixel detector chips presented in this thesis.

## 2 DESIGN OF THE MEDIPIX2 CHIP

In the previous chapter several digital x-ray imaging devices have been studied. The potential of the direct detection photon counting hybrid pixel detectors as a chip was exploited by the successful *Medipix1* chip. The *Medipix1* limitations as an x-ray imaging system are briefly summarized in section 2.1 together with the requirements for a new chip. The *Medipix2* (section 2.2) is designed in a commercial 0.25  $\mu\text{m}$  CMOS technology which contains 65536 square pixels of 55  $\mu\text{m}^2$ . The analog and digital blocks of the pixel cell (section 2.3) and the architecture of the chip periphery are described in section 2.4. Section 2.5 details the design actions taken to tile multi-chip structures using the *Medipix2*.

The pixel cell and chip architecture of the *Medipix2* are described in paper I. This chapter goes into more detail in the design of the pixel cell and chip periphery which were never published.

### 2.1 MOTIVATIONS AND REQUIREMENTS FOR THE NEW DESIGN

Even though the *Medipix1* demonstrated that the photon counting approach provides images with excellent dynamic range which are practically free of non-photonic noise the chip showed limitations for a full x-ray imaging system:

- The spatial resolution of the system was limited by the size of the pixel (170  $\mu\text{m}$  x 170  $\mu\text{m}$ ) which was determined by the component density of the 1  $\mu\text{m}$  SACMOS process used.
- The preamplifier was only sensitive to positive input charges.
- The leakage current compensation was done only at the column level. Some detectors have very non-uniform leakage current distribution [TLU0].
- Tiling was not possible since the minimum dead area around the sensitive area was  $\sim$ 500  $\mu\text{m}$ .
- The system was difficult to operate since the analog biasing was done externally.
- The chip could only be accessed through a 16-bit parallel port.

Knowing the *Medipix1* performance and limitations a complete redesign of the readout chip was undertaken in the microelectronics group at CERN within the framework of the *Medipix2* collaboration. The new design benefited from the availability of a much more advanced 0.25  $\mu\text{m}$  6-metal CMOS technology. The main requirements for the *Medipix2* chip are listed below:

- Square pixel cell of  $\sim$ 50  $\mu\text{m}$  to have a spatial resolution compatible with the film screen radiographic systems.
- Maximum pixel count rate above 100 kHz.
- Front end sensitive to both polarities.

- DC leakage current compensation in each pixel.
- On-chip DACs used to bias the chip to avoid external analog biasing noise.
- Very fast readout (through a parallel port), or very flexible and portable (readout through a serial port).
- The distance from the last pixels to the chip edge should be kept as low as possible to minimize the dead areas and allowing tiling.

## 2.2 THE *MEDIPIX2* CHIP

The chip dimensions are 16120  $\mu\text{m}$  x 14111  $\mu\text{m}$  (see Figure 2.1). The sensitive area is organized as a 256 x 256 pixel matrix of 55  $\mu\text{m}$  x 55  $\mu\text{m}$  (see section 2.3) with a total active area of 1.982  $\text{cm}^2$  (87.35% of the total chip). The non sensitive area at the bottom of the chip is 2040  $\mu\text{m}$  x 14111  $\mu\text{m}$  which is 12.65% of the total chip. It includes 117 wire-bonding pads, biasing DACs and control logic (see section 2.4). The chip has three independent power supplies at 2.2V: VDDA, VDD and VDDLVDS. The chip static power consumption is  $\sim$ 550mW.

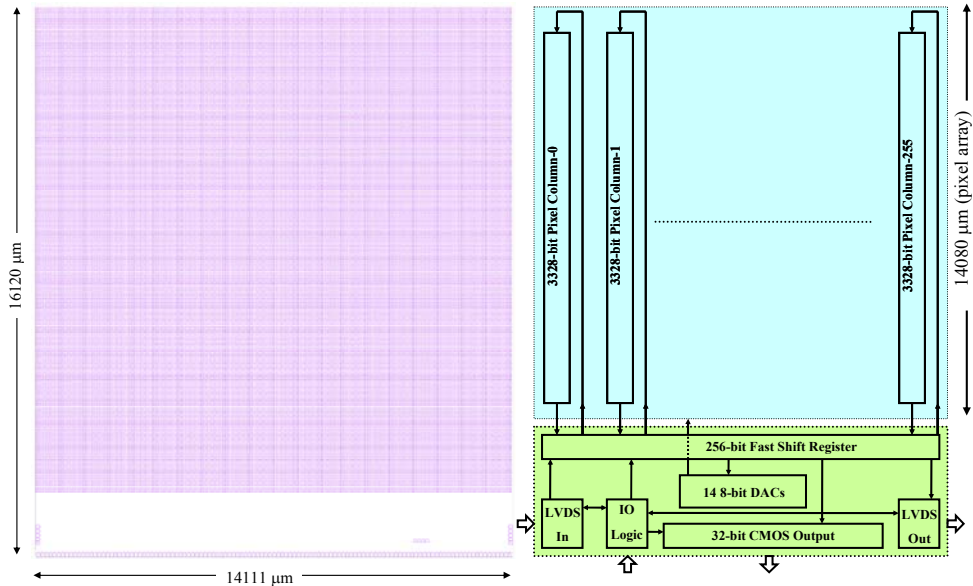


Figure 2.1. On the left the *Medipix2* passivation openings. On the right the *Medipix2* floor plan: the sensitive area with 65536 square pixels of 55  $\mu\text{m}^2$  (top), and the non-sensitive area (dark green) are shown.

## 2.3 PIXEL CELL

When a charged particle or a photon interacts in a detector material electron-hole pairs are generated and are drifted towards the collection electrode in the presence of a high electric field. Since the collection time is very short, being in the order of several ns [GAT86] and [KNO79], the detector output signal can be

represented as a Dirac current impulse, the integral of which equals the total generated charge  $Q$ . The generated charge  $Q$  is integrated onto a small feedback capacitor  $C_f$  by means of a low noise charge sensitive amplifier (CSA) giving rise, ideally, to a voltage step at the CSA output with an amplitude  $Q/C_f$  [CHA91]. The output pulse is then compared with two different thresholds that form an energy window. If the detected charge falls inside this energy window the digital counter is incremented.

The schematic of the pixel cell is shown in Figure 2.2. The analog side of the pixel (in red) contains a CSA (see section 2.3.1.1) with DC leakage current compensation, an injection test capacitance, and two branches of identical discriminators (see section 2.3.1.2) with 3-bit threshold adjustment current DACs. The digital side (in blue) contains the Double Discriminator Logic (DDL, see section 2.3.2.1), a 13-bit shift register (see section 2.3.2.2) plus CMOS logic for the counter and data shifting, and an 8-bit configuration register (see section 2.3.2.3). The dimensions of the cell are  $55 \times 55 \mu\text{m}^2$ . Each pixel has 504 transistors and a static analog power consumption of  $\sim 8 \mu\text{W}$ .

The pixel has two working modes depending on the CMOS input *Shutter* state. When the *Shutter* signal is low the pixel is in acquisition mode and the 13-bit shift register behaves as a linear feedback shift register counter with a single XOR tap with a dynamic range of 8001 counts [HOR80]. In this case, the output of the DDL is used as the clock of the counter. When the Shutter is high an external clock (*Clk\_Read*) is used to shift the data from pixel to pixel. Each pixel has eight independent configuration bits (*PCR*, see section 2.3.2.3). Six of them are used for the fine threshold adjustment (three bits for each discriminator), one for masking noisy pixels, and one to enable the input charge test through the 8 FF on-pixel test capacitance.

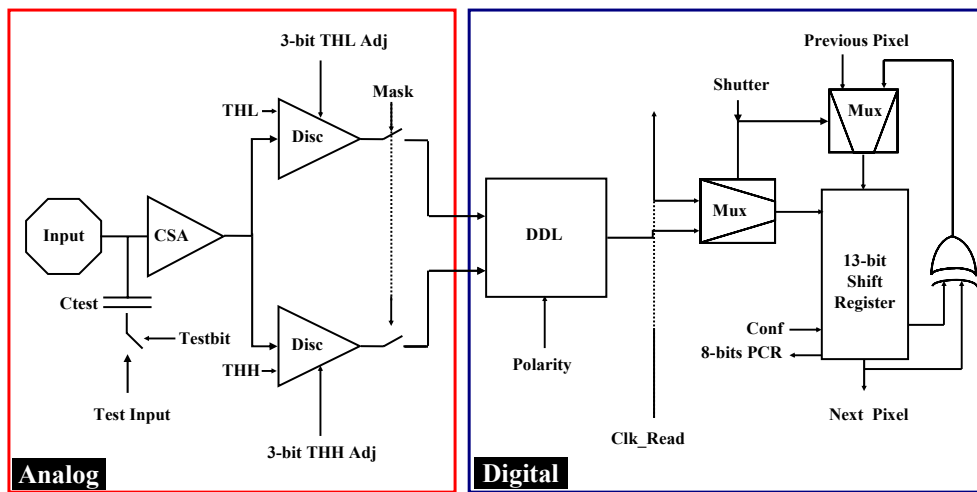


Figure 2.2. *Medipix2* pixel schematic. In red the analog side and in blue the digital side.

### 2.3.1 Analog block of the pixel

The *Medipix2* CSA integrates and shapes the charge collected in the input pad, and compensates for the detector DC leakage currents. The CSA output voltage is DC connected to two identical input branches which form the energy window. Figure 2.3 shows the schematic of the analog side of the *Medipix2* pixel. In red are highlighted the 10 global biasing 8-bit DACs (see section 2.4.1.1) used in the analog side. There are 5 current DACs (current is linear to the DAC settings) and 5 voltage DACs (output voltage is linear to the DAC settings). The analog power supplies (VDDA and VSSA) are split accordingly (in blue) for each biasing branch providing control of bottom-top column voltage drops (see section 2.3.3).

The analog block area is  $33 \mu\text{m} \times 55 \mu\text{m}$  and contains 54 transistors. The total static power consumption of the pixel analog section at the default DAC settings is  $\sim 8 \mu\text{W}$ .

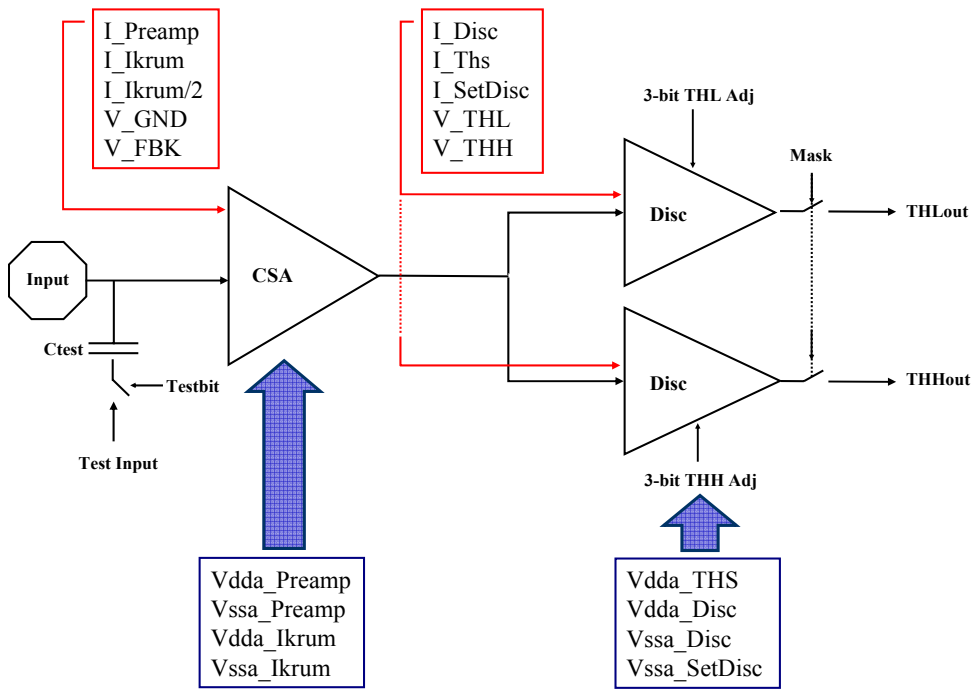


Figure 2.3. Analog schematic. In red are highlighted the 10 global biasing 8-bit DACs used in the analog side. In blue analog power supplies are split accordingly for each biasing branch.

#### 2.3.1.1 The Charge Sensitive Amplifier (CSA)

The CSA is based in a scheme proposed in [KRU91] shown in Figure 2.4. This configuration integrates and shapes the input charge and compensates for positive or negative input DC leakage currents. One output of the PMOS differential pair is connected to the amplifier input: this first feedback is equivalent to a resistor of value  $R_f = 2/g_m$  in parallel with  $C_f$ . The current of the second

differential pair output (drain of M<sub>lb</sub>) is integrated onto capacitor C and the resulting voltage controls the gate of the NMOS transistor M<sub>2</sub>. The action of this second feedback path is equivalent to an inductor connected in parallel with C<sub>f</sub> and therefore the detector DC leakage current flows into M<sub>2</sub> rather than into the equivalent feedback resistance R<sub>f</sub>. The main advantage of this configuration is that since M<sub>2</sub> can sink a total positive current, in hole collection mode, which is not limited by the value of the bias current I<sub>KRUM</sub> if equation 2.3 is satisfied, the leakage current of the detector may largely exceed the value of I<sub>KRUM</sub> without compromising the circuit operation. The same configuration compensates for negative DC leakage currents (in electron collection mode) up to I<sub>KRUM</sub>/2.

Given the pixel power and area restrictions the CSA is also used as a shaper by properly tuning the I<sub>KRUM</sub> bias current and the compensation capacitance. This solution reduces considerably the pixel power consumption and the transistor count yielding a small pixel size of 55  $\mu\text{m}$  square. In the other hand, the gain is not only sensitive to the feedback capacitance but also to variations of I<sub>KRUM</sub> and I<sub>Preamp</sub>. The DC preamplifier output voltage shift due to transistor matching, where baseline is set by M<sub>1a</sub> gate voltage (V<sub>FBK</sub>), has to be properly studied since the CSA output voltage is DC coupled to the discriminator input (see section 2.3.1.3). The CSA output noise needs also to be studied carefully because no further shaping is used to reduce the bandwidth of the system. In the other hand is demonstrated by [KRU91] that in addition to improving the spatial resolution, increasing the segmentation (reducing the pixel size) yields a higher sensitivity (gain) and a lower noise for the same power dissipation or equivalently a lower power consumption for the same noise performance. This means that detector segmentation is a key design issue for low-noise/low-power front end.

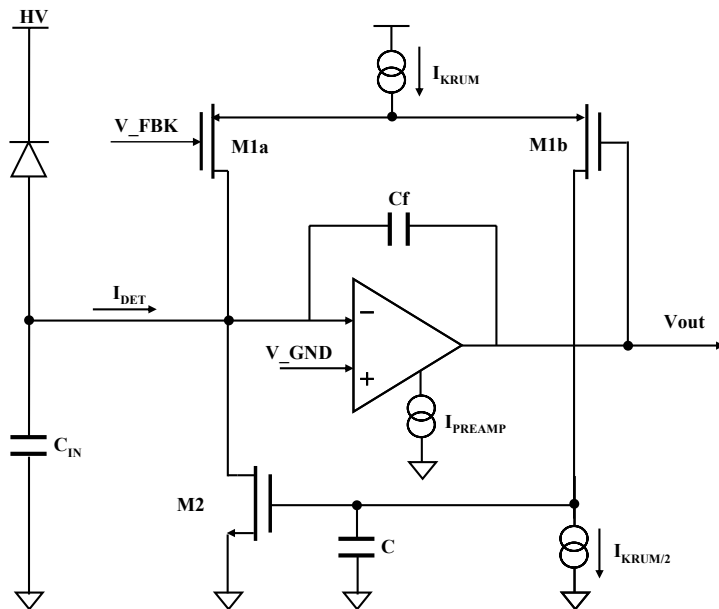


Figure 2.4. CSA schematic.

The CSA preamplifier consists of a transconductance amplifier implemented with NMOS input transistors. This configuration minimizes the substrate coupling to the input transistors due to the good common mode rejection of differential amplifiers, and minimizes the thermal serial noise of the input transistors. With such architecture the input node DC voltage is set through the 8-bit global voltage DAC V\_GND. The CSA baseline output is fixed by the 8-bit global voltage DAC V\_FBK in order to maximize the dynamic range in both collection polarities.

The small signal analysis shows that the CSA closed loop transfer function forms a band pass filter with 1 zero and 3 poles.

$$z_1 = \frac{gds_{Ikrum/2}}{2\pi \cdot C} \quad \text{and} \quad p_1 = \frac{gm_1 + gm_2}{4\pi \cdot C} \quad (2.1)$$

$$p_2 = \frac{gm_1}{4\pi \cdot Cf} \quad \text{and} \quad p3 = \frac{gm \cdot Cf}{2\pi \cdot (Cin + Cf) \cdot (Cl + Cf)} \quad (2.2)$$

Where  $gds_{Ikrum/2}$  is the output conductance of the Ikrum/2 voltage controlled current source,  $C$  is the compensation capacitance ( $\sim 1$  pF),  $gm_1$  is transconductance of the feedback transistors (M1a and M1b),  $gm_2$  is the transconductance of transistor M2,  $Cf$  is the feedback capacitance ( $\sim 8$  fF),  $gm$  is the transconductance of the preamplifier,  $Cin$  is the input capacitance and  $Cl$  the output capacitance. These three poles and the zero define the closed loop transfer function of the CSA where  $p3$  is the time constant of the CSA peaking time and  $p2$  is the time constant of the return to baseline. The discharge time constant of the compensation capacitance  $C$  is defined by  $z1$  and  $p1$ . To ensure a correct damping of the feedback loop, the compensation capacitance  $C$  must then be chosen so that:

$$\frac{C}{gm_2} > \frac{2 \cdot Cf}{gm_1} \quad (2.3)$$

This condition is satisfied because: first  $C$ , implemented as a PMOS gate capacitance of value  $\sim 1$  pF, is much bigger than  $Cf$ , realized as a metal to metal capacitance of value 8 fF; and second the increase of the transconductance of M2 ( $gm_2$ ) depends on positive DC detector leakage current, only hole collection mode, which limited to a small percentage of the feedback current (Ikrum) due to the small pixel size. Figure 2.5 shows the open loop response with a phase margin above  $70^\circ$ . Figure 2.6 shows the closed loop response of the CSA for different Ikrum biasing currents.

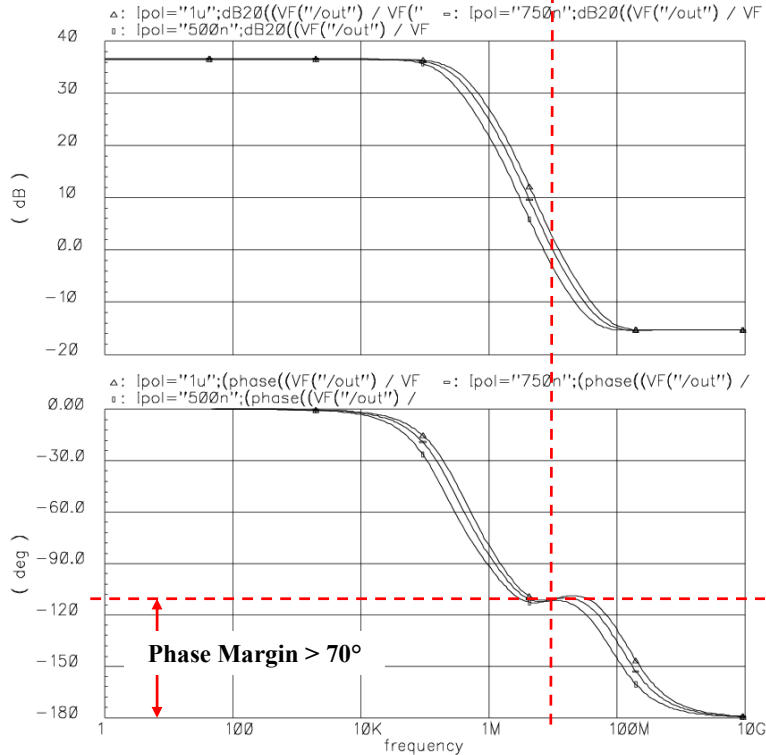


Figure 2.5. CSA open loop response for Ipreamp=500 to 1000nA. The phase margin is always  $> 70^\circ$ .

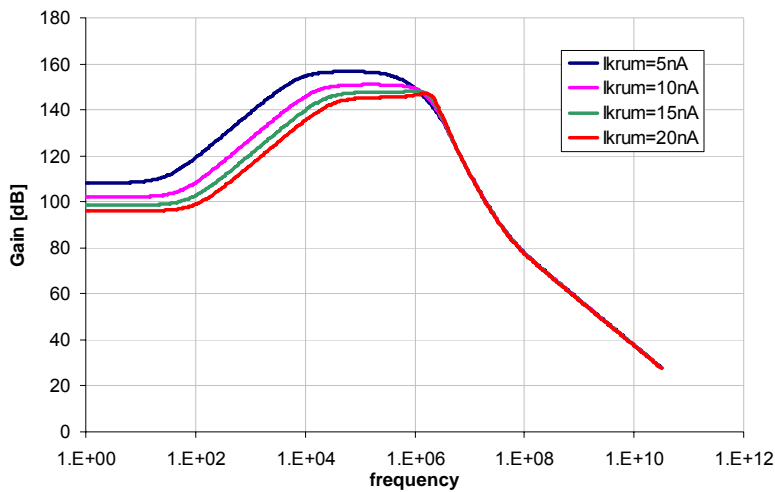
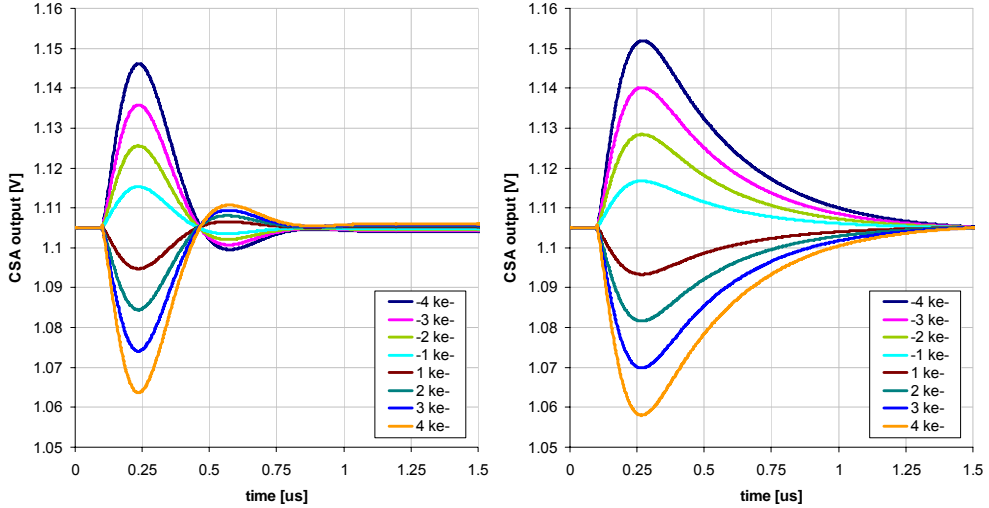


Figure 2.6. Closed loop transfer function simulation with Ikrum from 5 to 20 nA.

The CSA output time response has been checked with a series of simulations in order to validate equations 2.1 and 2.2. The extracted parasitic capacitances of the front-end layout, which include the feedback and injection test capacitances,

have been added to the simulation. Figure 2.7 shows a typical CSA output pulse response simulation for an increasing injected charge for two different Ikrum bias settings. As shown in equation 2.2 the increase of the transconductance of the feedback transistors decreases the equivalent feedback resistance reducing the return to baseline time but also the gain as seen in Figure 2.8.



**Figure 2.7.** CSA output voltage simulation response for both collection polarities to an equivalent injected input charge of 1, 2, 3 and 4 ke-. On the left Ikrum=15nA on the right Ikrum=5nA. Ipreamp= 750nA, V\_FBK=1105mV and V\_GND=1.1V.

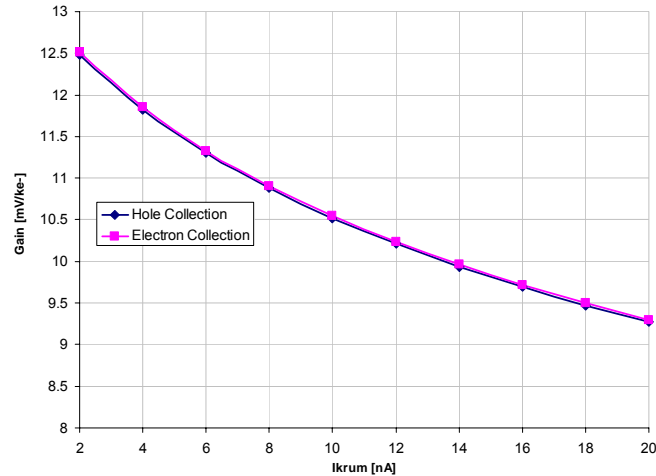


**Figure 2.8.** CSA output simulated gain versus Ikrum for both polarities. IPreamp=750 nA and Cin=40 fF.

In pulse processing front-ends an important parameter is the maximum pulse frequency that the front-end can process without losses. Since the CSA output pulse is DC coupled to the discriminator input the CSA output must be completely restored to baseline before processing another incoming pulse correctly. Figure 2.9 shows on the left the CSA output pulse width for an increasing input charge where

the plotted linear response is a consequence of the resistive behaviour of the feedback loop. The CSA output pulse width with an increasing Ikrum bias current for a fixed input charge of  $10 \text{ ke}^-$  is shown on the right of Figure 2.9.

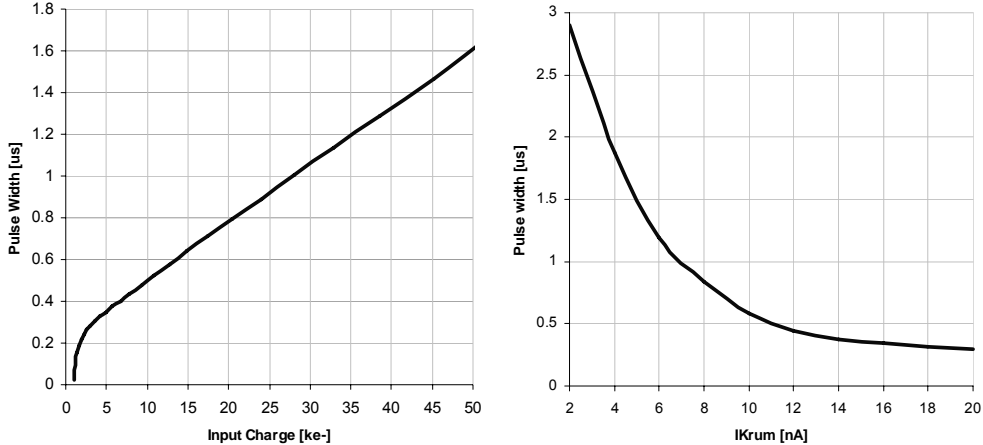


Figure 2.9. Two simulations of the CSA output pulse width. On the left increasing input charges show a linear response due to the resistive feedback loop ( $I_{\text{krum}} = 10 \text{ nA}$  and  $I_{\text{Preamp}} = 1 \mu\text{A}$ ). On the right increasing  $I_{\text{krum}}$  bias settings show a shorter pulse width due to the faster return to baseline ( $I_{\text{Preamp}} = 1 \mu\text{A}$  and  $Q_{\text{in}} = 10 \text{ ke}^-$ ).

The linearity of the CSA output, shown in Figure 2.10, is better than 99.9% with a 1.2 V range. The discriminator transconductance amplifier with NMOS input transistors has a common mode threshold  $\sim 600\text{mV}$  which limits the total front-end linear dynamic range to 0.6 to 1.5 V. At a nominal gain of  $10.5 \text{ mV/ke}^-$  the dynamic range of the CSA for both collection modes is  $\sim 85 \text{ ke}^-$  if the full 900 mV range is explored by setting the global DAC VFBK to 1.5 V in hole collection mode and to 0.6 V in electron collection mode.

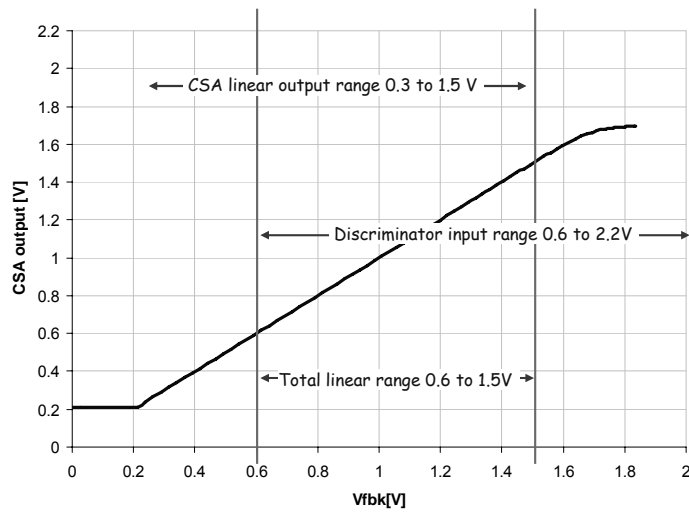


Figure 2.10. Front-end linear range is 900 mV (0.6 to 1.5 V). This is composed from the CSA linear output range from 0.3 to 1.5 V with linearity above 99.9% and the discriminator input range from 0.6 to 2.2 V.

The noise performance of a two port network can be represented by two equivalent input noise generators: a series voltage source usually named as series noise, and a parallel current source usually named as parallel noise [CHA91]. Figure 2.11 shows the noise voltage and current sources associated to the critical nodes of the *Medipix2* CSA. The different transistor noise sources (i.e. channel thermal noise, flicker noise, bulk resistance thermal noise, and gate resistance thermal noise) for the CMOS technology used in the design have been already deeply studied in [ANE01], therefore, will not be explained in this thesis.

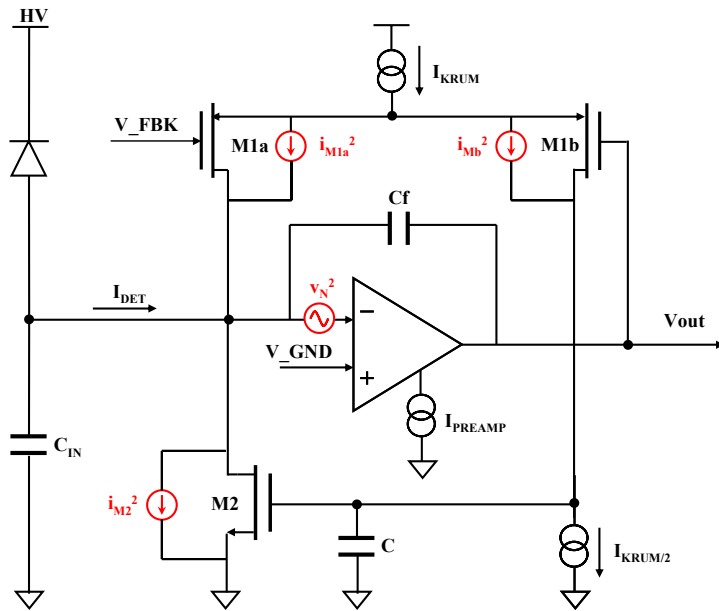


Figure 2.11. CSA voltage and current sources of the critical nodes.

The input series noise refers to the preamplifier input noise transistor and can be expressed as:

$$\frac{\bar{V}_{series}^2}{\Delta f} = 4kTn\gamma \frac{1}{gm} + \frac{K_a}{C_{ox}^2 WL} \frac{1}{f^\alpha} \quad \left[ \frac{V^2}{Hz} \right] \quad (2.4)$$

Where  $k$  is the Boltzmann constant ( $k=1.38 \cdot 10^{-23}$  J/K),  $T$  is the temperature in °K,  $n$  is the slope factor,  $\gamma$  varies from 1/2 to 2/3 from weak to strong inversion for an ideal device,  $gm$  is the preamplifier transconductance,  $\alpha$  is a parameter close to 1,  $K_a$  is a technology dependent parameter which expresses the noise characteristic of the process (typical values for the 0.25 μm process used are between 0.5 and  $4 \cdot 10^{27}$  C<sup>2</sup>/m<sup>2</sup>),  $W$  and  $L$  are the input transistor width and length, and  $C_{ox}$  is the gate oxide capacitance per unit area. The first term of equation 2.4

represents the channel thermal noise and the second the flicker or 1/f noise. The contribution of the bulk resistance thermal noise and gate resistance thermal noise are not taken into account if special care is taken during layout [CHA91]. The parallel input noise refers to the feedback loop resistance and the detector leakage current as:

$$\frac{\bar{V}_{parallel}^2}{\Delta f} = \frac{4kT}{R_F} + 2qI_{det} \quad \left[ \frac{V^2}{Hz} \right] \quad (2.5)$$

Where  $R_F$  is the equivalent feedback loop resistance,  $q$  is the electron charge ( $q=1.6 \cdot 10^{-19}$  C), and  $I_{det}$  is the detector leakage current.

The total integrated rms noise at the CSA output is given by:

$$v_{out} = \sqrt{\int_0^{\infty} |VoA(2\pi f)|^2 df} \quad [V_{rms}] \quad (2.6)$$

Where  $|VoA(2\pi f)|^2$  is the total noise power spectrum at the output of the CSA which is calculated by the transfer function of all individual noise sources from the noise source to the output of the CSA. The Equivalent Noise Charge, ENC, can be calculated as the total integrated rms noise divided by the CSA amplitude output corresponding to an input charge of 1 electron. It can be calculated that the series thermal and flicker contributions to the ENC are proportional to:

$$ENC_{Thermal}^2 \propto \frac{C_T^2}{gm \cdot \tau} \quad \text{and} \quad ENC_{1/f}^2 \propto \frac{C_T^2 \cdot K_a}{C_{ox}^2 \cdot W \cdot L} \quad (2.7)$$

Therefore, the thermal and 1/f noise can be minimized using big input transistors in weak inversion (i.e. weak inversion is the transistor operating zone with higher gain or transconductance per unit of drain current), with smaller input capacitance ( $C_T$ ) which is an inherent feature in pixel detectors, and with slow shaping times ( $\tau$ ) (i.e. limited bandwidth).

The parallel noise contributions to the ENC can be found as:

$$ENC_{parallel}^2 \propto \left( \frac{4kT}{R_F} + 2qI_{det} \right) \cdot \tau \quad (2.8)$$

This shows that the parallel ENC can be minimized for slow return to baseline (i.e.  $R_F$  is inversely proportional to the Ikrum bias current) and low detector leakage current but is increased for slow shaping times.

The CSA noise performance has been further studied with an analog simulator using foundry transistor models which included transistor thermal and

flicker noise sources. The CSA Equivalent Noise Charge is calculated as the simulated CSA total integrated rms output noise, as in equation 2.6, divided by the simulated output gain of the CSA for a known input charge. The simulated ENC has been studied for different CSA bias settings and input capacitances. The simulation netlist includes the extracted metal to metal parasitic capacitances including the feedback and injection test pulse capacitances.

Figure 2.12 shows the ENC at different I<sub>Krum</sub> and I<sub>Preamp</sub> settings. The simulated curves show the same trend depicted in equations 2.7 and 2.8 validating the methodology to estimate the ENC. The input capacitance is set to 40 fF which corresponds to the extracted metal to metal capacitance of the bump-bonding input pad. The ENC has been also simulated for different input capacitance as shown in Figure 2.13. The ENC slope is  $\sim 0.7 \text{ e}^-/\text{fF}$ .

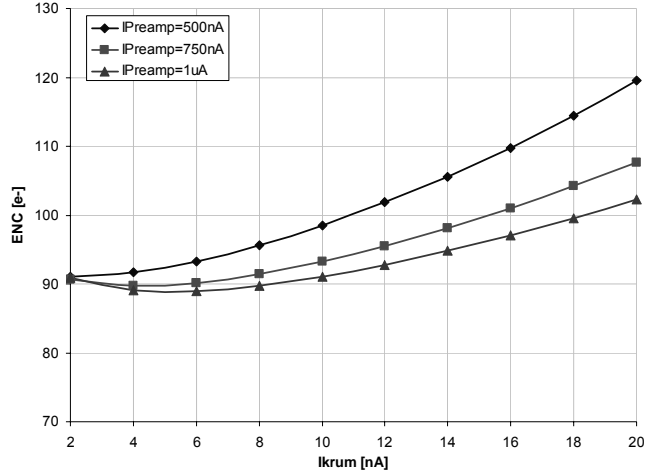


**Figure 2.12.** ENC calculation using an analog simulator for different I<sub>Krum</sub> and I<sub>Preamp</sub> bias settings. In these simulations the detector leakage current is zero and the input capacitance is 40fF.

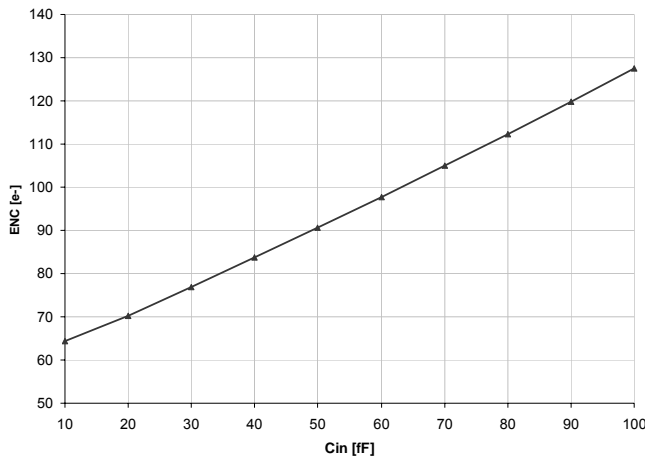


Figure 2.13. ENC calculation using an analog simulator for an increasing input capacitance. The CSA is biased at default settings of  $I_{k\text{rum}}=10\text{nA}$  and  $I_{\text{Preamp}}=750\text{nA}$ . The ENC slope is  $\sim 0.7\text{e}/\text{fF}$ .

Using the default DAC settings (i.e.  $I_{k\text{rum}}=10\text{nA}$  and  $I_{\text{Preamp}}=750\text{nA}$ ) the CSA performance is detailed in Table 2.1.

Preamplifier Gain	$\sim 10.5 \text{ mV/ke}^- [\text{h}^+/\text{e}^-]$ (see Figure 2.8)
Peaking time	$210$ to $150 \text{ ns}$ [ $I_{\text{Preamp}} = 500$ to $1000 \text{nA}$ ]
Dynamic Range	$\pm 85 \text{ ke}^- (V_{fbk} \text{ from } 300\text{mV} \text{ to } 1.5\text{V})$ (see Figure 2.10)
Linearity	$>99.9\%$ (see Figure 2.10)
Dead Time	$<0.6 \mu\text{s}$ if $Q_{in} < 10 \text{ ke}^- (I_{k\text{rum}} = 10 \text{nA})$ Figure 2.9)
Leakage current compensation	Electron collection: -10 to 0 nA/pixel (-330 to 0 $\mu\text{A/cm}^2$ ) Holes collection: 0 to $\sim 20 \text{ nA/pixel}$ (0 to $\sim 660 \mu\text{A/cm}^2$ ) $\sim 95 \text{ e}^- \text{ rms}$
Output Noise	$\sim 210 \text{ e}^- \text{ rms}$ (see equation 2.14)
Output mismatch	$\sim 1.8 \mu\text{W}$ with $V_{dd\text{a}} = 2.2 \text{ V}$
CSA power consumption	

Table 2.1. CSA performance summary table. All values given are simulations and they should be used as a trend.

Figure 2.14 shows the final layout of one CSA. The total area is  $55 \mu\text{m} \times 16 \mu\text{m}$  and contains 12 transistors with a maximum current consumption below 800 nA in the default DAC settings.

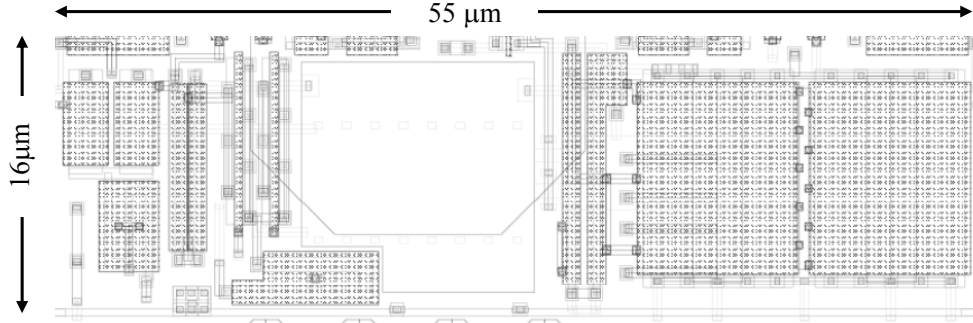


**Figure 2.14. Medipix2 CSA layout.** In the center are placed the Cfb and Ctest realized as a metal to metal capacitance.

### 2.3.1.2 Discriminator

The two discriminators shown in Figure 2.2 form an energy window. If the collected input charge falls inside the window, defined by the two discriminators, the counter will be incremented. As both discriminator branches are identical only one will be further studied.

An 8-bit DAC sets a global threshold across the full pixel matrix independently in the discriminator. As shown in Figure 2.15 there are three main blocks: a transconductance amplifier (OTA), a 3-bit current DAC for threshold adjustment, and a zero-crossing discriminator circuitry (Zx) whose output is gated with the mask bit.

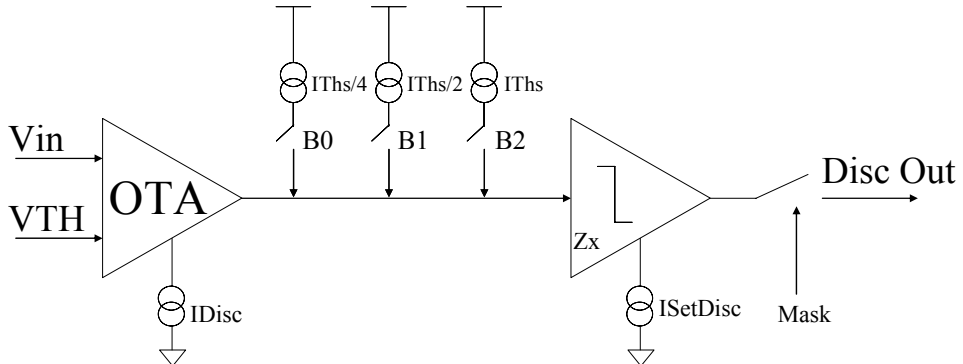


**Figure 2.15. Discriminator block diagram**

The discriminator input stage is a transconductance amplifier (OTA) with NMOS input transistors. The operational input range is limited from 0.6 to 2.2 V. If the input common mode is below 600 mV the voltage controlled current source of the OTA is in deep triode region and the circuit is incapable of signal amplification. In the operational input range the output current of the OTA can be approximated to:

$$I_{OTA} \cong (V_{IN} - V_{TH}) \cdot gmN_{OTA} \quad (2.9)$$

Where  $gmN_{OTA}$  is the transconductance of the NMOS input transistors. The output current is zero if the voltage input pulse,  $V_{IN}$  (the CSA output), is at threshold,  $V_{TH}$ . This means that when  $VFBK = VTH$  the discriminator operation point is “at the noise”. If  $V_{TH}$  is higher than  $V_{IN}$  the output current is negative and positive the contrary. The gain ( $gmN_{OTA}$ ) of this stage is controlled by IDisc (8-bit global current DAC).

The zero-crossing current discriminator is based in a scheme proposed by [TRA92] modified to provide a gain stage whose bias current is controlled by ISetDisc (8-bit global current DAC) and with a current starved output to limit the pixel power consumption. The output of the discriminator, DiscOut, is low if  $V_{IN} > V_{TH}$  and high if  $V_{IN} < V_{TH}$  giving an output pulse width equal to the time the CSA output pulse has been over threshold. Since the CSA output pulse width is proportional to the input charge, as already seen in Figure 2.9, the discriminator output pulse width contains information of the collected input charge. Figure 2.16 shows a typical full front-end response for both collection modes. With such an architecture the discriminator output pulse width is used by the DDL, described in section 2.3.2.1, to perform the energy window discrimination.

Each discriminator branch has three independent selectable current sources used to minimize the pixel to pixel threshold variation due to local transistor mismatch (section 2.3.1.3) and power distribution voltage drops (section 2.3.3.1). The current generated by these sources is added at the OTA output current before the zero-crossing detector. By properly tuning these 3-bit DAC the pixel to pixel threshold variation can be minimized (see Paper II).

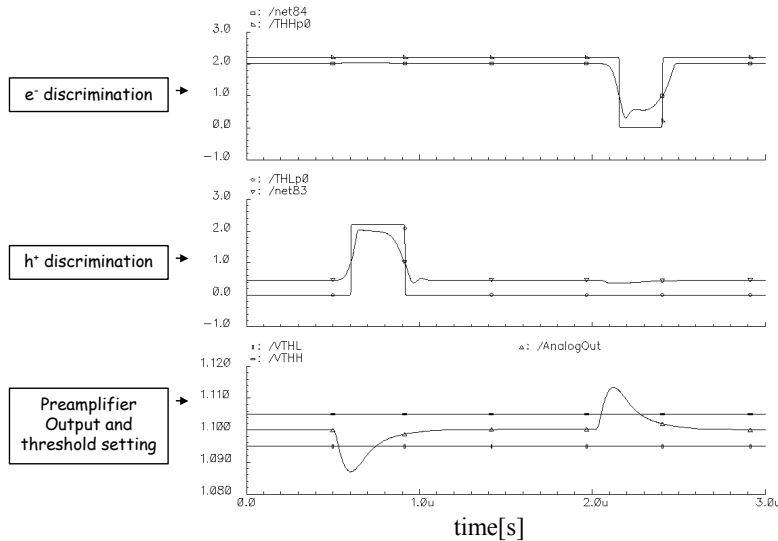


Figure 2.16. Preamplifier and discriminators simulation response to a  $\pm 1$  ke $^-$  input charge.  $VFBK=1.1$  V and  $I_{kum}=10$  nA

Figure 2.17 shows the final layout of one discriminator branch. The total area is  $27.5 \mu\text{m} \times 13.4 \mu\text{m}$  and contains 22 transistors with a maximum current consumption of

$$ITOT_{Disc} \leq 2 \cdot IDisc + ISetDisc + 7 \cdot IThs \quad (2.10)$$

In the default DAC settings  $ITOT_{Disc}$  is below  $1.5 \mu\text{A}$  per branch.

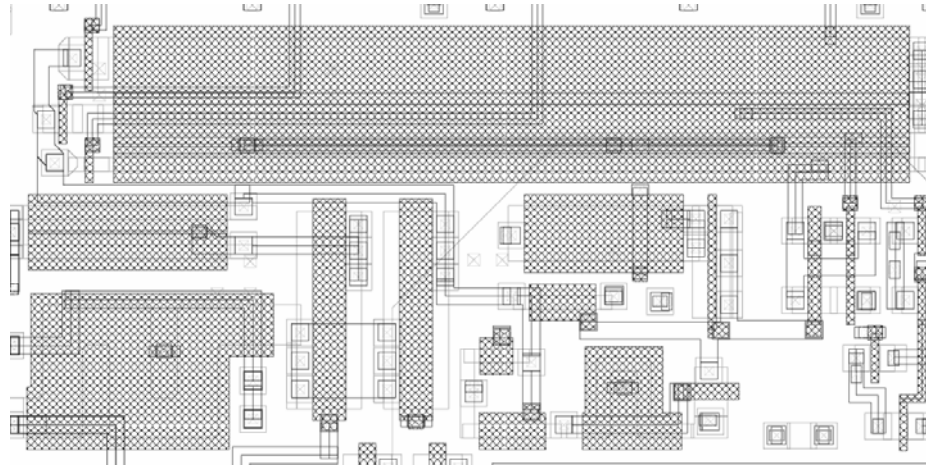


Figure 2.17. Layout of 1 discriminator branch. Total area is  $27.5 \mu\text{m} \times 13.4 \mu\text{m}$  and contains 22 transistors.

### 2.3.1.3 Analog chain mismatch

The sources of transistors mismatch between two identically laid out components can be either systematic and environmental effects or stochastic effects [ANE00]. The first class includes all the technological and geometrical effects (topography, metal coverage, packaging, etc) and can be solved by careful engineering during the layout phase. Transistors in a differential pair should for example be laid out close together in the same orientation, with the same metal coverage and with the same periphery. The second class of mismatch sources includes all the stochastic effects, such as dopant fluctuations, local mobility fluctuations, polysilicon gate granularity, oxide charges and interface states fluctuations. It can be shown [PEL89] that the variance of a  $\Delta P^1$  distribution can be approximated by

$$\sigma_{\Delta P}^2 = \frac{A_p^2}{W \cdot L} \quad (2.11)$$

Where W and L are the effective gate width and length and  $A_p$  is a constant which indicates the matching performance of the given technology.

---

<sup>1</sup> The mismatch of a parameter P is caused by many single microscopical events of the given mismatch-generating process. The random mismatch amplitudes  $\Delta P$  of the parameter P will therefore be normally distributed (Gaussian distribution).

The mismatch in the gate voltage of two transistors of a differential pair biased at the same current is

$$\sigma_{VG} = \sqrt{\sigma_{Vth}^2 + \left(\frac{I_D}{g_m}\right)^2 \sigma_\beta^2} \quad (2.12)$$

Where  $\sigma_{Vth}$  is the threshold voltage matching and  $\sigma_\beta$  is the current factor matching expressed as

$$\sigma_{Vth}^2 = \frac{A_{Vth}^2}{W \cdot L} \quad \sigma_\beta^2 = \frac{A_\beta^2}{W \cdot L} \quad (2.13)$$

The parameter  $A_{Vth}$  [V·m] represents the quadratic sum effects of doping fluctuations and interface charge<sup>2</sup>, and the parameter  $A_\beta$  [%·m] indicates the current factor performance due to the mobility and oxide capacitance fluctuations of the technology<sup>3</sup>.

The total mismatch of the front-end chain is found by translating the gate voltage mismatch, from equation 2.12, of the critical nodes as a mismatch current at the output of the discriminator OTA. In order to compensate the front-end mismatch in the full matrix the 3-bit threshold adjustment current is added at the OTA discriminator output node. The output voltage mismatch at the output of the CSA can be calculated as:

$$\sigma_{PREAMP} = \sqrt{\sigma_{FB}^2 + \left(\frac{gm_{IK2}}{gm_{FB}}\right)^2 \cdot \sigma_{IK2}^2 + \left(\frac{gm_{IK}}{2 \cdot gm_{FB}}\right) \cdot \sigma_{IK}^2} \quad [V] \quad (2.14)$$

Where  $\sigma_{FB}$ ,  $\sigma_{IK2}$  and  $\sigma_{IK}$  are the total gate voltage mismatches for the PMOS feed-back, the Ikrum/2 current source, and the Ikrum current source of the CSA (see Figure 2.4). The total voltage mismatch at the output at the default DAC biasing settings is  $\sigma_{PREAMP} = 2.2$  mV rms which corresponds to  $\sim 210$  e<sup>-</sup> rms with 10.5 mV/ke<sup>-</sup> gain.

The total output current mismatch at the output of the discriminator OTA is

$$\sigma_{OTA} = \sqrt{(gmN_{OTA} \cdot \sigma_{PREAMP})^2 + (2 \cdot gmN_{OTA} \cdot \sigma_{OTAN})^2 + (gmP_{OTA} \cdot \sigma_{OTAP})^2} \quad [A] \quad (2.15)$$

Where  $\sigma_{OTAN}$  and  $\sigma_{OTAP}$  are the total gate voltage mismatches for the NMOS and PMOS differential pair of the discriminator OTA. The total current mismatch at the output of the OTA is  $\sigma_{OTA} = 28$  nA rms which is less than 5% of the total output current of the OTA. In order to properly equalize the pixel to pixel variations the 3-bit current DAC dynamic range should cover completely the OTA output mismatch range. The total current range due to mismatch, assuming a Gaussian distribution, is  $\pm 3 \cdot \sigma_{OTA}$  which corresponds to  $\sim 168$  nA. This value sets the LSB of the pixel adjustment DAC to be  $\sim 20$ nA to fully compensate the

<sup>2</sup> The parameter  $A_{Vth}$  has been measured for the 0.25  $\mu$ m CMOS technology used in the design of 4 mV· $\mu$ m por NMOS transistors and 3.7 mV· $\mu$ m por PMOS transistors.

<sup>3</sup> The parameter  $A_\beta$  has been measured to be around 2 %· $\mu$ m (from 1 to 3) for many different process [TUI98].

mismatch introduced in the front-end chain. The LSB can be tuned using the global 8-bit current DAC THS between 0 and 50 nA.

### 2.3.2 Digital block of the pixel

Figure 2.18 shows schematic diagram of the digital block of the pixel. The two analog outputs from the discriminators are buffered at the input of the DDL (see section 2.3.2.1). The DDL is an asynchronous logic that uses the time-over-threshold pulse from the two discriminator branches to generate an output pulse if the detected input charge is inside the energy window defined by the global DACs THH and THL. The output of the DDL is used as clock to increment the counter in the Shift Register Counter block (SR/C, see section 2.3.2.2) if the global *Shutter* is opened. The SR/C behaves as 13-bit shift register when the *Shutter* is closed and as 13-bit pseudo-random counter with a dynamic range up to 8001 counts when the *Shutter* is closed. In shift register configuration the SR/C block uses a global clock (*Clk\_Read*) to shift the data from the previous pixel to the next pixel. When *Conf* is active the pixel configuration register (PCR) is loaded by latching 8 bits of the shift register into a static on-pixel memory (see section 2.3.2.3), otherwise the pixel matrix is read out.

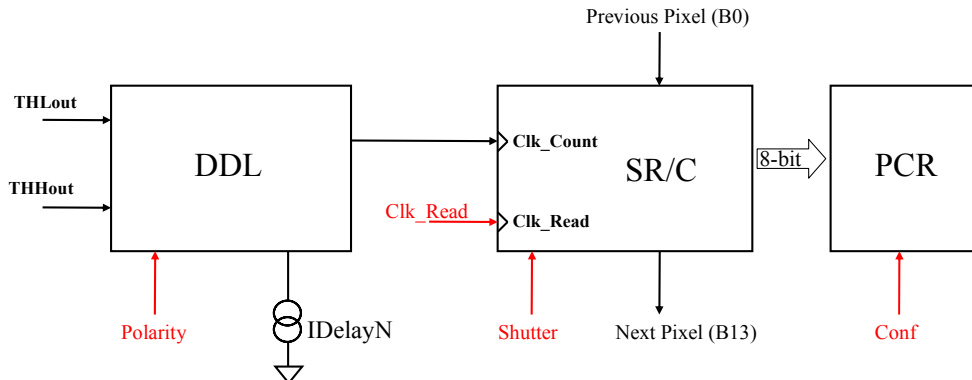


Figure 2.18. Digital section schematic. The global control lines are in red.

Given the small pixel size all the transistors (NMOS and PMOS) used in the digital section are minimum size. This choice produces unbalanced rise and fall times due to the difference of channel mobility between NMOS and PMOS transistors<sup>4</sup>. Special care has been put in the design of the digital block to avoid problems induced by this timing difference. On the other hand having slower rise times limits the total digital power consumption. The digital section has its own power supply (VDD, VSS and VDDWELL) to maximize the power supply rejection ratio (PSRR) towards the analog side.

<sup>4</sup> In the selected 0.25 μm CMOS technology the NMOS channel mobility is ~3 times higher than for a PMOS transistor. This means that in a digital CMOS logic rise times are ~3 times slower than fall times.

Figure 2.19 shows the layout of the digital section of the pixel cell. The total area of this block is  $32 \mu\text{m} \times 55 \mu\text{m}$  and contains 450 minimum-sized transistors.

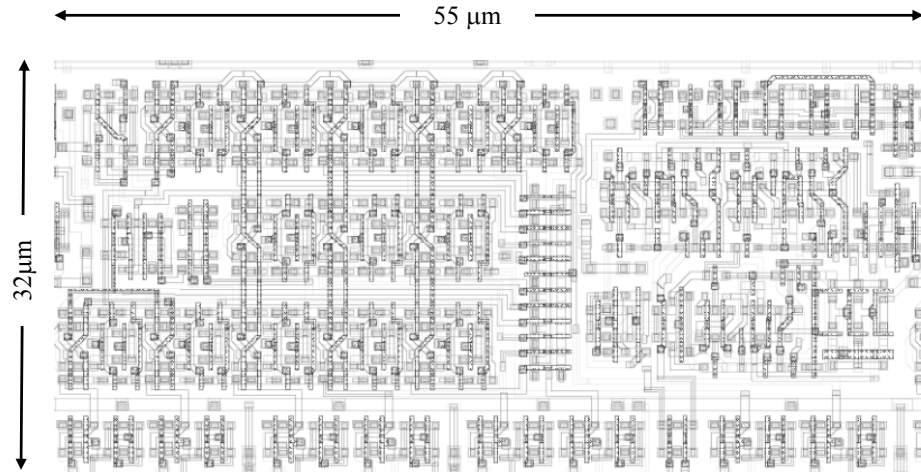


Figure 2.19. The layout of the pixel digital side.

### 2.3.2.1 Double Discrimination Logic

The DDL schematic is shown in Figure 2.20. The DDL is an asynchronous logic that uses the time-over-threshold pulse (*Hit*) from the two discriminator branches to generate and output pulse if the input charge is either inside the energy window defined by  $\text{THH-THL}$  (if  $\text{THH} > \text{THL}$ ) or when the input charge is above the low threshold (if  $\text{THH} < \text{THL}$ ). The global *Polarity* signal is used to multiplex the discriminator output pulses into the right polarity depending in the collection mode for correct functioning of the logic.

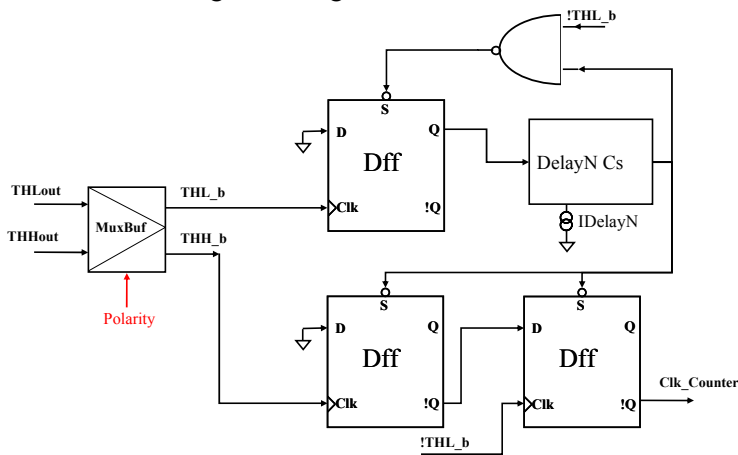


Figure 2.20. DDL schematic. The global line is displayed in red.

There are two main working modes depending on the *Polarity* signal and the *THL* and *THH* settings:

- **Energy window mode:** In this mode the THL and THH global thresholds form a window of discrimination and only the pulses falling inside it will be counted. At the end of the THL discrimination pulse an incrementing width controlled pulse is generated.
- **Single mode:** Setting the THH threshold lower than the THL sets the window discriminator in single threshold mode.

Table 2.2 summarizes all the above working modes. In Figure 2.21 shows a simulation in energy window mode and in fast single mode.

<b>Shutter</b>	<b>Polarity</b>	<b>Threshold</b>	<b>Working mode</b>
OFF	X	X	OFF
ON	LOW ( $e^-$ )	$THH > THL$	Energy window mode
ON	LOW ( $e^-$ )	$THH < THL$	Single mode
ON	HIGH ( $h^+$ )	$THH > THL$	Energy window mode
ON	HIGH ( $h^+$ )	$THH < THL$	Single mode

Table 2.2. DDL working modes

The output pulse width is controlled by a current starving circuit which is set through the 8-bit current global DAC IDelayN. In the example of Figure 2.21 the IDelayN is set to 50 nA which corresponds to an output width of  $\sim 300$  ns. The front-end pulse processing time before pile-up can be approximated as the CSA output pulse width, below 0.6  $\mu$ s if  $Q_{in} < 10 \text{ ke}^-$  in Table 2.1, plus the  $\sim 300$  ns counting pulse width. The front-end dead time is less than 1  $\mu$ s if the input charge ( $Q_{in}$ ) is below 10  $\text{ke}^-$ .

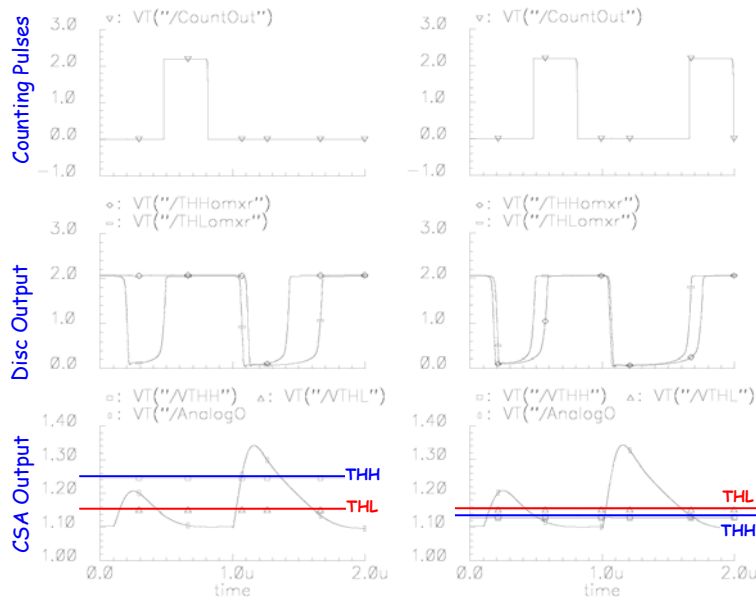


Figure 2.21. Simulation example of two working modes of the DDL. Left: Energy window discrimination mode (1 count). Right: Single Discrimination mode (2 counts). The output pulse width is  $\sim 300$  ns (IDelay=50 nA).

### 2.3.2.2 Shift Register and Counter (SR/C)

The Medipix2 SR/C schematic is shown in Figure 2.22 and contains: a 13-bit shift register made out of thirteen master-slave minimum size D flip-flops (see Figure 2.23), a 2-bit exclusive-OR, and a simple multiplexing logic controlled with the global *Shutter* signal. The global *Shutter* signal controls the behaviour of the logic:

- **Counter (*Shutter* opened):** In counting mode the system works as a linear feedback shift register with one 2-bit XOR tap between bits 13 and 10. With such configuration the maximum dynamic range is 8001 counts. In order to get to the full scale of a 13-bit counter (8192 counts) it is necessary to use with this scheme one 4-bit XOR [GEO01] which is too big to implement in such small available area. To avoid the lock state, when all bits in the counter are low, the shift register should be set to High before starting any counting operation using a *RESET MATRIX* command (see Table 2.7). The read out process resets automatically the counters, and therefore, no reset is needed.
- **Shift Register (*Shutter* closed):** In this mode the SR/C behaves as a shift register to either read out the pixel matrix (after an acquisition) or to set the 8-bit PCR when *Conf* is active. In this mode all the pixels of one column form a 3328-bit shift register with a common clock (*Clk\_Read*) generated in the periphery of the chip (see section 2.4.2.3).

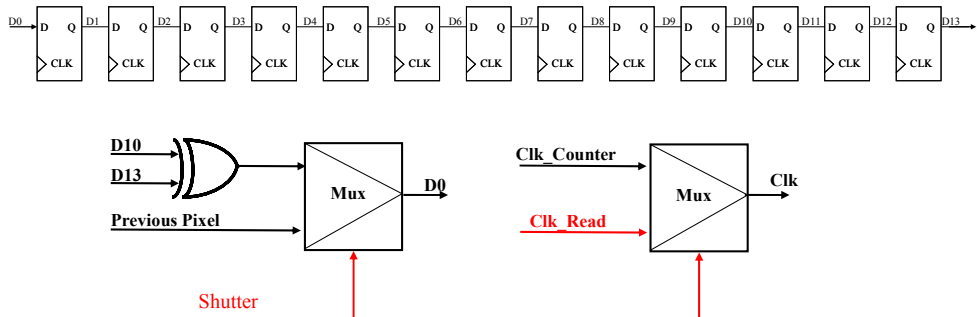


Figure 2.22. The Medipix2 SR/C schematic. The global lines are displayed in red.

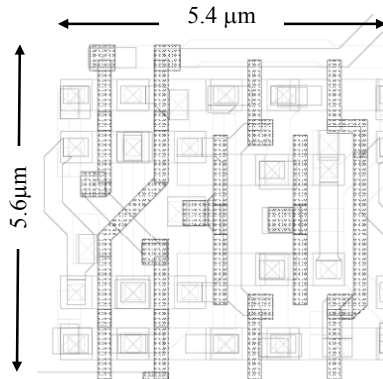


Figure 2.23. The layout of one DFF. Each cell contains 22 minimum-sized transistors.

### 2.3.2.3 Pixel Configuration Register (PCR)

The Pixel Configuration Register is a 8-bit static memory which stores the pixel information. This register stores the 3 bit low threshold equalization, the 3 bit high threshold equalization, one mask bit and one test bit. Each register cell is realized with static logic, which means that the data stored is kept until new data is loaded or the chip is powered off. After chip power up the PCR has to be loaded to ensure correct pixel operation. Table 2.3 shows the PCR bit functionality. The PCR data is latched from the pixel shift register at the falling edge of *Conf* signal. Figure 2.24 shows the bit tapping on the 13-bit shift register which are latched into the PCR.

3-Bit Low threshold adjust (Bit0L (LSB), Bit1L and Bit2L)	<i>I: off 0: on</i>
3-Bit High threshold adjust (Bit0H (LSB), Bit1H and Bit2H)	<i>I: off 0: on</i>
Test_Bit: Enables the external testing of the pixel	<i>I: Test bit off 0: Test bit on</i>
Mask_Bit: Masks out the pixel cell	<i>I: Unmasked 0: Masked</i>

Table 2.3. The Medipix2 PCR bit functionality.

b1	b2	b3	b4	b5	b6	b7	b8	b9	b10	b11	b12	b13
X	X	X	X		Bit2 High		X		Bit 1 Low	Bit 0 Low	Test Bit	Bit 0 High

Figure 2.24. PCR is formed by latching 8-bit of the 13-bit shift register.

### 2.3.3 Pixel power distribution strategy

The *Medipix2* bond pads are placed only at the bottom side of the chip to allow tiling of several chips at the three bond-free edges with a minimal loss of sensitive area. As all the analog and digital power supplies are placed at one edge of *Medipix2* the power distribution strategy has to be carefully studied. Top-down non-uniformities can appear if proper solutions are not foreseen in the analog and digital part of each pixel. In the analog side power consumption is *static* which means that current is continuous, while in the digital side the power supply is *dynamic*<sup>5</sup> which means that current only flows when there is a logic change.

#### 2.3.3.1 Analog pixel power distribution

On the analog side six voltage controlled current sources are used to bias the front end (CSA and discriminators). Each current source needs a stable reference voltage ( $V_{GS}$ ) to generate a stable output current. These reference voltages are made of the difference between one global DAC output as gate voltage, and a power supply as source voltage (either VDDA or VSSA depending on the target transistor). In order to uniformly generate the same biasing currents in all pixels the power supplies for each critical branch has been split at the column level. All the pixels of the same column share the same power connections for each critical branch. By doing this the problem for each critical branch and column is isolated and the worst case power distribution can be seen as a series of 256 pixel resistances ( $R_{pix}$ ) with a constant current source as seen in Figure 2.25. The resistance of each pixel depends on the CMOS technology metal resistance ( $R_{square}$ ) and the metal line width:

$$R_{pix} = \frac{55 \mu m}{MetalWidth} \cdot R_{square} \quad (2.16)$$

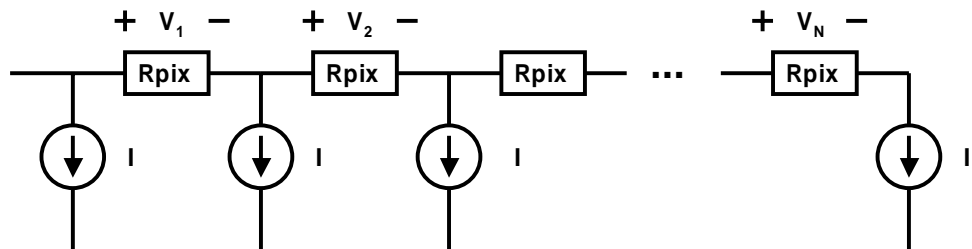


Figure 2.25. Power distribution schematic of one column and one critical branch

With such arrangement the worst case is the voltage drop seen by the pixel at the top of the column compared with the pixel at the bottom. This can be calculated as the following quadratic sum:

---

<sup>5</sup> If transistors leakage current are not taken into account.

$$\begin{aligned}
V_{drop} &= V_1 + V_2 + K + V_N = R_{pix} \cdot I \cdot (N + (N-1) + (N-2) + K + 1) = \\
R_{pix} \cdot I \cdot \frac{N}{2} \cdot (N+1) &= R_{pix} \cdot I \cdot \frac{N^2}{2}
\end{aligned} \tag{2.17}$$

In Figure 2.26 is shown the worst case power supply voltage drop for a pixel at the top of the column with different metal widths and biasing pixel currents.

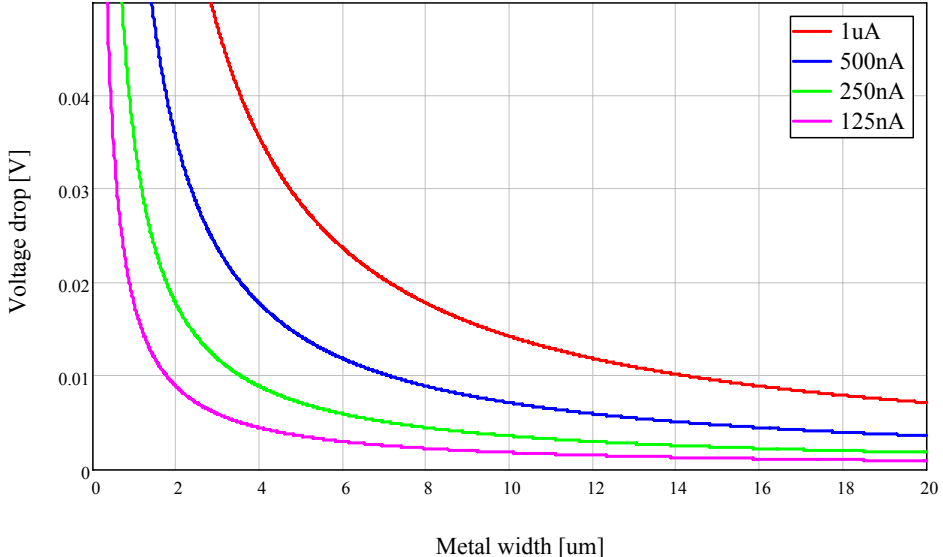


Figure 2.26. Worst case power supply voltage drop for a pixel at the top of the column for different metal widths and pixel biasing currents.

Each critical branch has its own power (VDDA) and ground (VSSA) laid out depending on the biasing current and the respective power voltage drops achieved are shown in Table 2.4. The preamplifier and discriminator power lines have the worst voltage drops due to the high currents they have to drive. In the discriminator there is a known top down non-uniformity that is corrected with the on-pixel equalization DAC.

Power line	Nominal Current	Voltage drop [mV]	Metal width [μm]
Vdda_Preamp	750 nA	61	1.88 (M4)
Vssa_Preamp	750 nA	20	5.64 (M4)
Vdda_Ikrum	15 nA	4.5	0.48 (M4)
Vssa_Ikrum	15 nA	2.2	1 (M5)
Vdda_Disc	3 μA	71	6 (M4)
Vssa_Disc	3 μA	40	10.68 (M5)
Vdda_THS	350 nA	4	13.3 (M4+M5)
Vssa_SetDisc	400 nA	9.5	6 (M5)

Table 2.4. Metal widths for the different static power supplies of the analog side.

The analog side has also independent biasing for PMOS transistor wells (VDDAWELL) to decouple as much as possible analog to digital, and a full P+ guard-ring all around the analog side.

### 2.3.3.2 *Digital pixel power distribution*

All the pixels of the same column share the same power (VDD) and ground (VSS) digital nets. VDD is 12.2  $\mu\text{m}$  wide with a column resistance of  $92 \Omega$  and VSS is 10.2  $\mu\text{m}$  wide with a column resistance of  $109 \Omega$ . At the top of the columns the digital power supplies are connected to a common 10  $\mu\text{m}$  wide metal line to uniformly distribute the digital power horizontally.

### 2.3.4 Pixel Layout

In Figure 2.27 the layout of the pixel cell is shown where the most important blocks are indicated. The octagonal bump bond opening, with a diameter of 20  $\mu\text{m}$ , is placed on top of the analog side and is the input node of the CSA using the top metal.

The pixel layout uses 6 metal layers:

- Metal 1-2 are used for local routing inside the pixel
- Metal 3 is mainly used for the global routing: analog column biasing and digital control lines.
- Metal 4-5 are used for the analog/digital power distribution
- Metal 6 is used for the bump-bonding connection.

The injection and feedback capacitances of the CSA are realized as metal-to-metal parasitic capacitors and are laid out as a “sandwich structure” between metal layers 1, 2 and 3. This structure gives a sufficient capacitance density while minimizing the input capacitance and coupling to neighbouring lines. The preamplifier compensation capacity (C in Figure 2.4) is realized as two PMOS gate capacitances in parallel with a total capacitance of  $\sim 1\text{pF}$ .

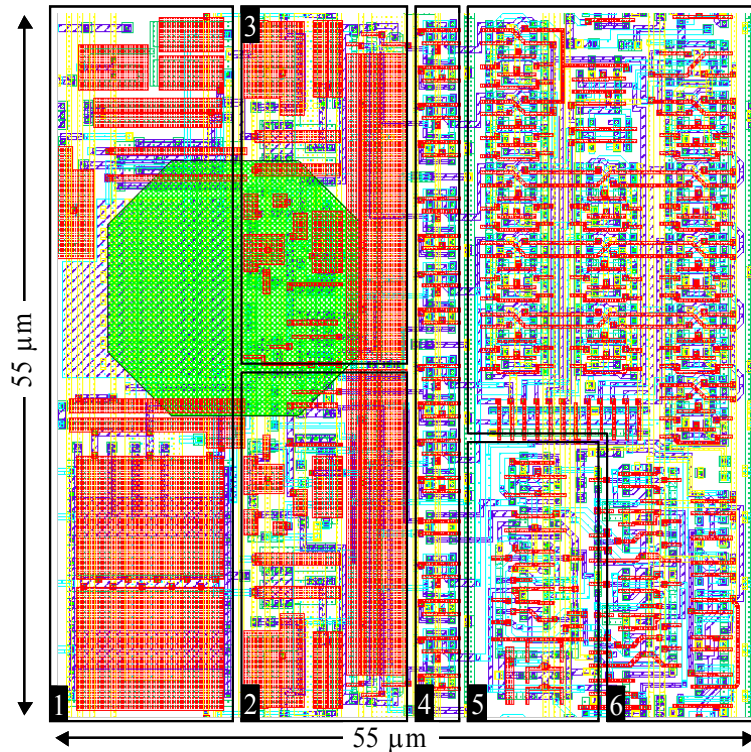
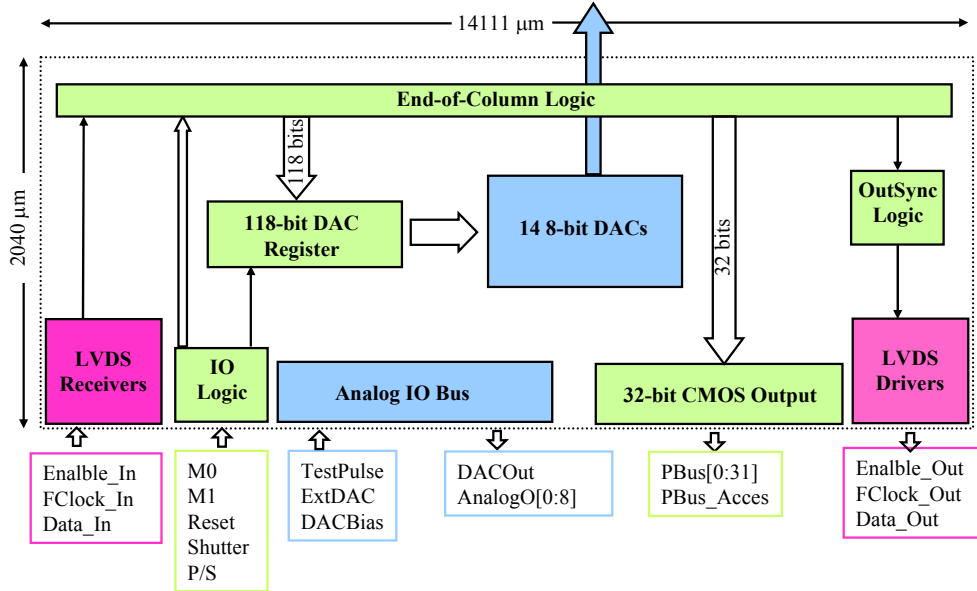


Figure 2.27. *Medipix2* layout. 1) Preamplifier; 2) High Threshold Discriminator; 3) Low Threshold Discriminator; 4) 8-bit Pixel Configuration Register; 5) DDL; 6) SR/C (13-bit shift register and logic).

## 2.4 MEDIPIX2 PERIPHERY

The *Medipix2* periphery is used to provide the analog biasing and generate the digital control signals to the pixel matrix. Figure 2.28 shows and schematic floor plan of the *Medipix2* periphery. The different colour indicates the power supply each periphery block is attached to: Analog (blue), Digital (green) and LVDS (pink). The periphery width dimension is 14111  $\mu\text{m}$  which is basically defined by the pixel matrix width ( $256 \times 55 = 14080 \mu\text{m}$ ). The height is mainly limited by the sensor non-sensitive guard-ring area needed to provide a uniform electrical field on the detector side (typically  $\sim 500 \mu\text{m}$ ), and to provide enough clearance in the mounting stage with the wire-bonding machine head ( $\sim 1 \text{ mm}$ ).



**Figure 2.28.** The *Medipix2* periphery floor plan. On blue the periphery blocks and IO lines using the analog power supply, on green the blocks and IO lines using digital power supply and on purple the blocks and IO lines using LVDS power supply.

For further study the periphery has been divided into the analog periphery block (powered by VDDA) which contains the DACs and the Analog IO Bus, and a digital periphery block that groups all the blocks powered by the supplies VDD and VDDLVDS which contains the LVDS drivers and receivers, the IO logic, the End-of-Column Logic and the 32-bit CMOS output buffers.

### 2.4.1 Analog Periphery

The *Medipix2* analog periphery includes the 13 8-bit DACs, injection test pulse bus architecture, and some IO analog buffers. For simplicity the same analog bufferes used for the internal buffering of the injection test pulse are used at the bond pad for buffering data into or out of the chip.

#### 2.4.1.1 DACs

There are 13 8-bit DACs included in the chip. Their role is to provide bias (voltages and currents) to the analogue and digital circuitry within the pixel cells. The DAC register is written via the LVDS serial port. All the DACs use the same binary weighted current architecture (see Figure 2.29 for schematic and Figure 2.30 for the layout). Two external supplies are used to generate the reference current for the DAC LSB (VDDA and DACbias). To avoid nonlinearity errors in the DAC due to transistor parameter gradients on the chip (mismatch), attention was paid to having the same centre of gravity for the current sources of all the bits. The output stage of each DAC has been tuned so that it provides a sensible nominal setting

following a chip *Reset* (the digital setting of each DAC after reset is its mid range value =  $10000000_b$ ).

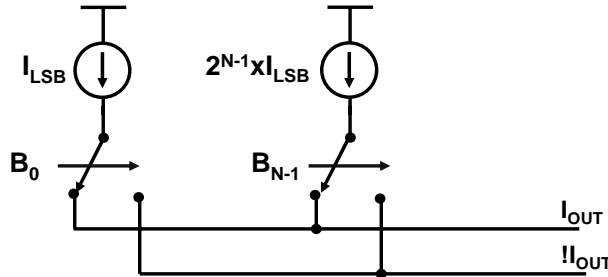


Figure 2.29. Binary weighted architecture implemented in the *Medipix2* DACs.

The 13 *Medipix2* DACs are listed in Table 2.5. All the DACs can be programmed independently by selecting an 8-bit code. The output range covers from the low 8-bit code ( $00_h$ ) to the high 8-bit code ( $FF_h$ ). The DAC code is used to select one of the *Medipix2* DACs. Moreover one can monitor the output voltage of a selected DAC through the *DACOut* output pin or impose an external DAC value for the selected DAC through the *ExtDAC* input pin. To maximize the CSA output voltage dynamic range the threshold DACs (*VTHL* and *V\_THH*) outputs are controlled by the *Polarity* input signal.

Each of the DAC output gate voltages is directly connected to one of the target transistor gates. The advantage of this approach is to provide a better mismatch and stability due to the large capacitance seen at the DAC output. The disadvantage is that any broken gate in the pixel array will make the chip non-operational limiting the yield performance.

	<b>DAC NAME</b>	<b>Type</b>	<b>DAC CODE</b>	<b>Polarity</b>	<b>Range</b>
<b>CSA</b>	<i>Preamp</i>	<i>I</i>	0011	<i>L,H</i>	0-1.4 $\mu A$
	<i>Ikrum</i>	<i>I</i>	0111	<i>L,H</i>	0-30 nA
	<i>FBK</i>	<i>V</i>	1010	<i>L</i>	0.4-0.85 V
				<i>H</i>	1.3-1.9 V
<b>Discriminator</b>	<i>GND</i>	<i>V</i>	1101	<i>L,H</i>	0.9-1.3 V
	<i>Disc</i>	<i>I</i>	0010	<i>L,H</i>	0-1.67 $\mu A$
	<i>THS</i>	<i>I</i>	0101	<i>L,H</i>	0-51.8 nA
	<i>SetDisc</i>	<i>I</i>	0100	<i>L,H</i>	0-400 nA
	<i>THL</i>	<i>V</i>	1011	<i>L</i>	0.6-0.85 V
				<i>H</i>	1.2-1.6 V
	<i>THH</i>	<i>V</i>	1100	<i>L</i>	0.6-0.85 V
				<i>H</i>	1.2-1.6 V
<b>DDL</b>	<i>DelayN</i>	<i>I</i>	0001	<i>L,H</i>	0-50 nA
<b>Analog Buff</b>	<i>Abuffer</i>	<i>V</i>	1110	<i>L,H</i>	0.7-1.1 V
<b>LVDS Driver</b>	<i>LVDS<sub>tx</sub></i>	<i>I</i>	0110	<i>L,H</i>	0-580 $\mu A$
	<i>RefLVDS<sub>tx</sub></i>	<i>V</i>	1001	<i>L,H</i>	0-1.1 V

Table 2.5. *Medipix2* DACs

Figure 2.30 shows the layout of a *Medipix2* 8-bit DAC. All the DACs have the same binary weighted block while the output and decoding logic is different.

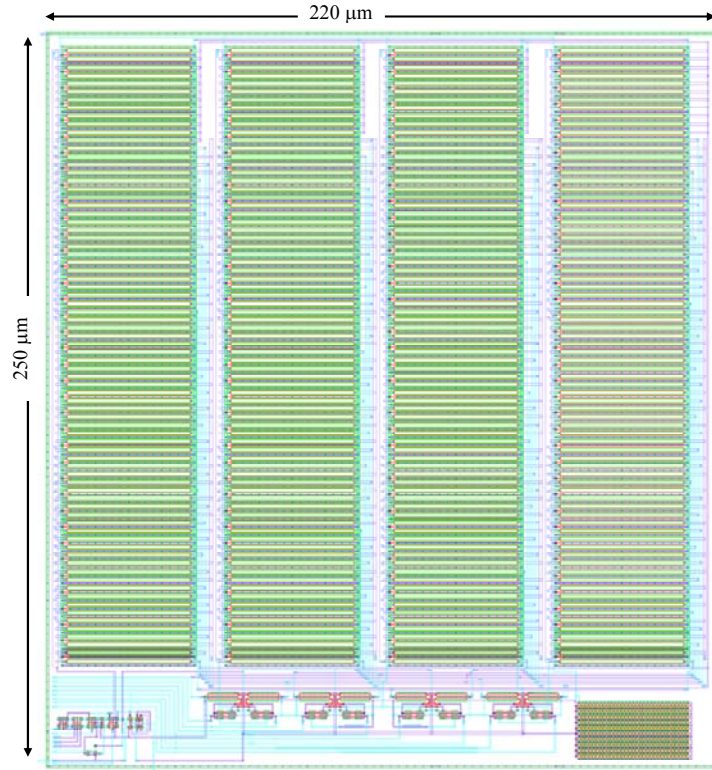


Figure 2.30. Layout of a *Medipix2* 8-bit DAC

#### 2.4.1.2 *Injection test pulse*

Each pixel contains an 8 fF injection capacitance connected in series with the CSA input (see Figure 2.2) to allow each pixel to be tested using an external voltage pulse. To simulate a charge injection from the detector a test pulse of known amplitude is stepped onto the injection capacitance  $C_{\text{test}}$ , which acts as a differentiator injecting into the preamplifier an equivalent charge of

$$Q_{\text{test}} = \frac{\alpha_{\text{BUF}} \cdot V_{\text{TP}} \cdot C_{\text{TEST}}}{q} \quad [\text{e}^-] \quad (2.18)$$

Where  $\alpha_{\text{BUF}}$  is the gain of the injection test pulse buffers ( $\sim 0.825$ ),  $V_{\text{TP}}$  is the injection test pulse voltage amplitude (0.8 to 2.2 V),  $C_{\text{TEST}}$  is the on-pixel injection test capacitance ( $\sim 8$  fF), and  $q$  is the electron charge ( $1.6 \cdot 10^{-19}$ ). At the bottom of every pixel column and at the *TESTPUSLE* bond pad two analog buffers are used to cope with the large capacitance and stray resistance of the internal electrical connections. These two buffers limit the maximum input test charge due to their dynamic range, linearity (0.8 to 2.2 V) and gain (0.825). The rise and fall time of

the input voltage step should be similar than the collection time of a charge collected in the detector in order to stimulate properly the front end chain.

### 2.4.2 Digital Periphery

The digital periphery is shown in Figure 2.28 and contains the LVDS receivers and drivers, the IO logic, the End-of-Column logic, the DAC registers and the synchronization output logic. Depending on the state of the CMOS input control lines (*Reset*, *Shutter*, *P\_S*, *M0* and *M1* and the LVDS signal *Enable\_IN*), the pixel matrix can be either written or read out and the DAC digital codes can be loaded. The data loading (matrix Reset, matrix PCR and DAC loading) is always done serially through the LVDS serial link. The read out can be either done serially through the LVDS link or in parallel through a 32-bit CMOS parallel bus (selectable via *P\_S* bond pad). The design target read out clock frequency is 100 MHz. With this clock frequency the pixel matrix should be written or read out in less than 9 ms using the serial LVDS port and in less than 300  $\mu$ s using the parallel port.

The digital blocks of the periphery use a full custom digital library which fully exploits the 6 metal layers available in the 0.25  $\mu$ m CMOS technology achieving a high gate density needed at the end-of-column logic due to the 55  $\mu$ m pixel pitch. The digital library has been fully designed and characterized using an analog simulator (HSPICE) and later verified with the digital simulator (VERILOG). The *Medipix2* digital library contains the following cells: *INVERTER*, *NAND*, *NOR*, *MUX2*, *SWITCH2*, *DFF*, *DFFSR*, *DFFS*, *DFFR* and different buffer sizes. Figure 2.31 shows one full custom designed Set-Reset D flip flop cell (*DFFSR*) of the *Medipix2* digital library.

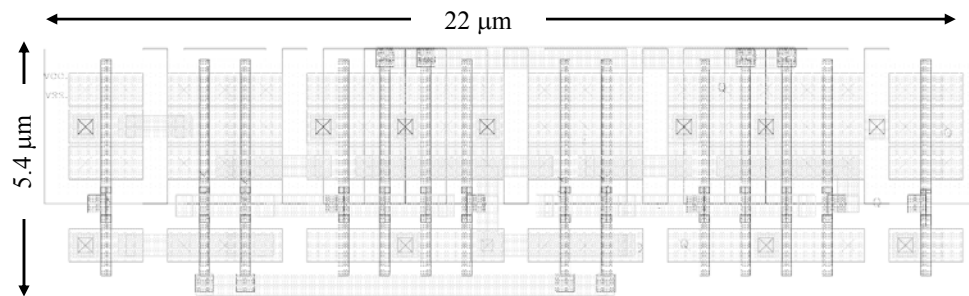


Figure 2.31. One Set-Reset flip flop from the *Medipix2* digital library.

#### 2.4.2.1 LVDS Driver and Receiver

The LVDS (Low Voltage Differential Signaling) is a low swing differential technology which allows single channel data transmission at very high speeds. LVDS delivers high data rates while consuming significantly less power than other technologies. In addition, it brings many other benefits, which include:

- Low-voltage power supply compatibility

- Low noise generation
- High noise rejection
- Robust transmission signals
- Ability to be integrated at chip system level

*Medipix2* uses the LVDS receivers and drivers for the serial communication link. The drivers and receivers use independent power supplies (VDDLVDS and VSSLVDS) to minimize the digital high frequency noise coupling to other parts of the chip. Table 2.6 shows the main characteristics of this technology and Figure 2.32 shows a schematic of the LVDS driver and receiver and the expected data rate versus cable length.

Parameter	Description	Min	Max	Units
$V_{OD}$	Differential Output Voltage	247	454	mV
$V_{OS}$	Offset Voltage	1.125	1.375	V
$\Delta V_{OD}$	$ Change in V_{OD} $	50	50	mV
$\Delta V_{OS}$	$ Change in V_{OS} $	50	50	mV
$I_{SC}$	Short Circuit Current	24	24	mA
$tr/tf$	Output Rise/Fall Times (>200 Mbps)	0.26	1.5	ns

Table 2.6. LVDS characteristics [NAT98].

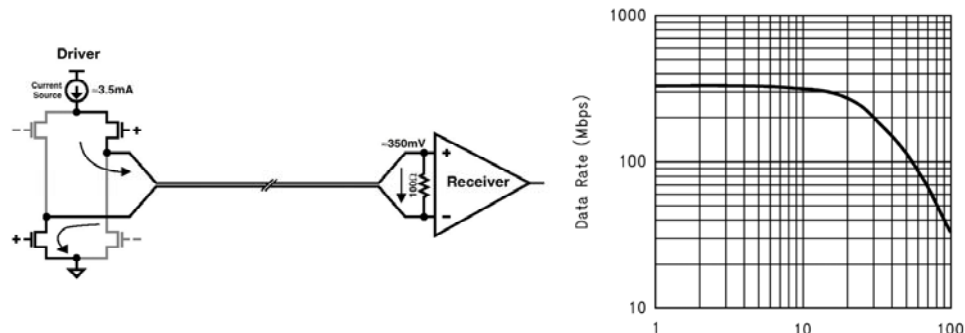


Figure 2.32. On the left: simplified diagram of LVDS Driver and receiver connected via  $100\Omega$  differential impedance media. On the right: LVDS data rate vs Cable Length in meters [NAT98].

As shown in Figure 2.28 the LVDS receivers are placed at the bottom left corner of the chip and the LVDS drivers are placed in the bottom right corner of the chip. The position of the LVDS drivers and receivers in the chip allows a daisy chain connection between different chips minimizing the dead area between them (see section 2.5).

There are three LVDS pairs at the input and output of the chip:

- $Fclock\_In$ : Is the master clock for all the chip IO operations.
- $Fclock\_Out$ : Given the internal delay of  $Fclock\_In$  (typically  $\sim 6$ ns) the  $Fclock\_Out$  is used to synchronize the  $Data\_Out$ .

- *Data\_In* and *Data\_Out*: Medipix2 samples *Data\_In* at the *Fclock\_In* rising edge and sets *Data\_Out* at the rising edge of *Fclock\_Out*.
- *Enable\_In* and *Enable\_Out*: When *Enable\_In* goes down the selected command is started, when *Enable\_Out* goes down the selected command is finished.

The LVDS receivers are based in a self-biased rail to rail differential amplifier scheme with CMOS buffered outputs.  $100\ \Omega$  P+ diffusion resistances are included on-chip at each receiver input. The LVDS drivers use a typical bridge switched topology with four zero-VT NMOS transistors. The bias current is controlled through the 8-bit current DAC  $I_{LVDSx}$  while the output common mode is set by the 8-bit voltage DAC  $V_{RefLVDSx}$ . Figure 2.33 shows the layout of one LVDS receiver and one LVDS driver.

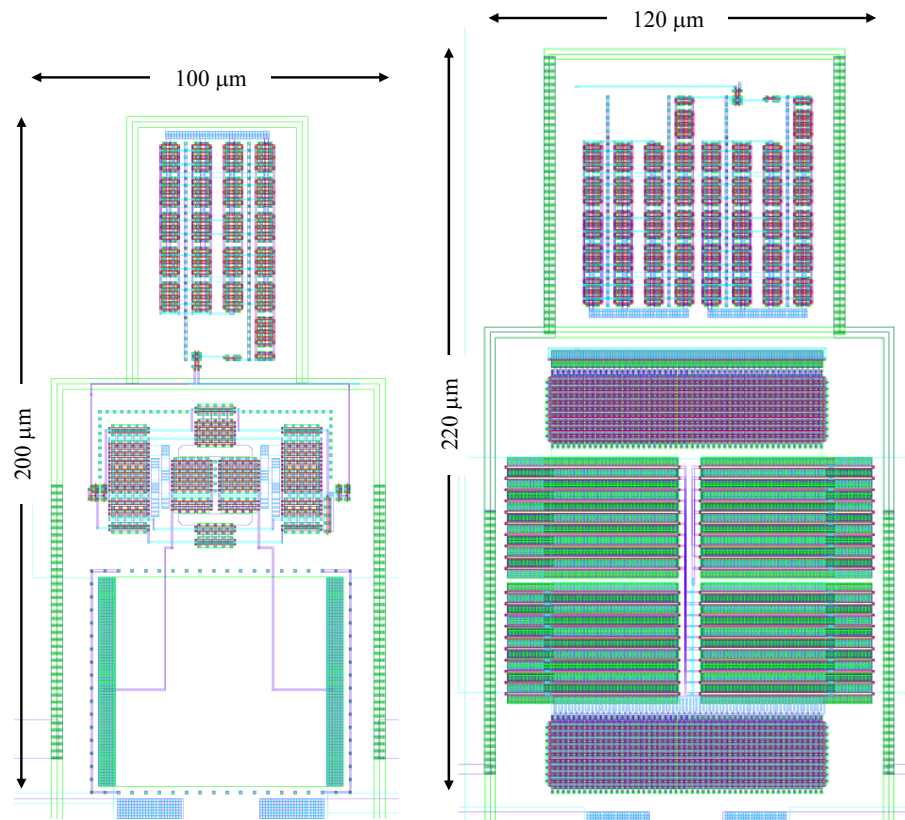


Figure 2.33. On the left one LVDS receiver with the  $100\ \Omega$  P+ diffusion. On the right the layout of one LVDS driver. The receivers are placed at the bottom left corner of Medipix2 while the LVDS drivers are placed at the bottom right corner of Medipix2.

#### 2.4.2.2 Medipix2 IO Logic

The chip is controlled by means of the CMOS input signals: *Reset*, *Shutter*, *P\_S*, *M0* and *M1* and the LVDS signal *Enable\_IN*. Table 2.7 summarizes the

different operation modes of the *Medipix2* chip depending on the control signals. The logic is designed using the full custom *Medipix2* digital cell library.

<i>M0</i>	<i>M1</i>	<i>Enable_IN</i>	<i>P_S</i>	<i>Shutter</i>	<i>Reset</i>	<i>Operation</i>
<i>X</i>	<i>X</i>	<i>X</i>	<i>X</i>	<i>X</i>	0	General reset of the chip
<i>X</i>	<i>X</i>	<i>X</i>	<i>X</i>	0	1	Acquisition
0	0	0	0	1	1	Read out the matrix (Serial)
0	0	0	1	1	1	Read out the matrix (Parallel)
0	1	0	<i>X</i>	1	1	Write the matrix PCR
1	0	0	<i>X</i>	1	1	Write DAC registers
1	1	<i>X</i>	<i>X</i>	1	1	Reset the matrix
0	1	<i>X</i>	<i>X</i>	0	1	Testing the FSR

Table 2.7. *Medipix2* operation modes.

A schematic view of the IO logic is shown in Figure 2.34. The IO Decoder is a simple combinatorial logic which translates the control lines into the chip generating the appropriate internal signals used by the Post Counter Logic and the End-of-Column Logic. The IO logic matrix commands see the pixel matrix as memory bank of 851968 bits formed by 256 columns and 3328 rows of bits. The logic has one binary column counter (up to 256) used as readout clock of the pixel matrix (*Clk\_Read*, see Figure 2.18) and one binary row counter (up to 3328 counts), clocked by the output of the column counter, used to indicate the end of operation (*Enable\_Out* low) in write matrix, reset matrix and read matrix commands. The same logic is used to load the DAC binary input stream where the output of the column counter indicates the end of operation. Figure 2.35 shows the layout of the complete IO logic.

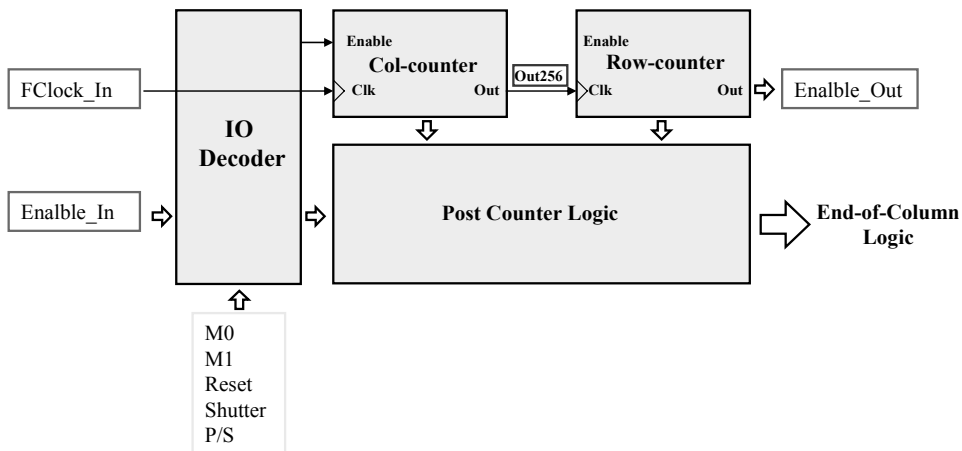


Figure 2.34. The IO Logic schematic.

At chip *Reset* the LVDS Drivers are not active, the IO control logic is reset to the initial condition, all DACS are set to the mid-range value and the 32-bit DOUT bus is in high impedance.

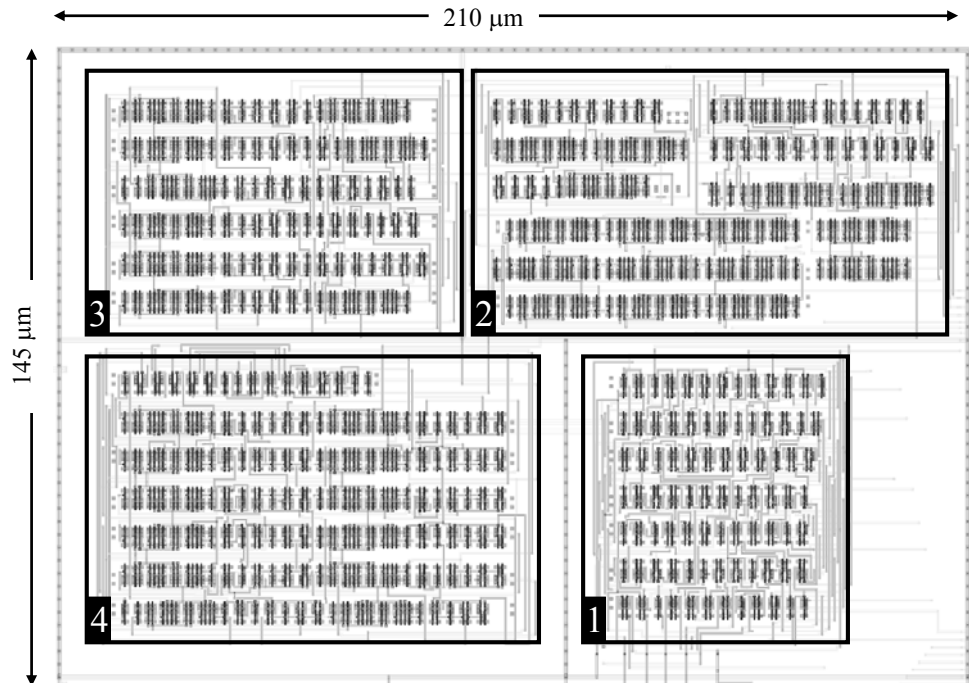


Figure 2.35. The *Medipix2* IO Logic. 1)IO Decoder; 2)Post counter logic; 3) 256 binary column counter; 4) 3328 binary row counter.

#### 2.4.2.3 End-of-Column Logic (EoC)

The End-of-Column logic provides the link between the pixel matrix and the periphery. The EoC includes sequential logic composed of a flip-flop with control logic (EoC in Figure 2.36) and a digital buffer block (Buffer in Figure 2.36) which is used because of the stray resistance and parasitic capacitance of the metal lines that bring the global control signals to the matrix. *Clk\_Read*, *Conf* and *Shutter* are global signals to the whole pixel matrix while *Data\_to\_matrix* and *Data\_from\_matrix* are column specific. There is an EoC block at the end of each pixel column, therefore there are 256 EoC blocks with a pitch of 55 μm. The flip flops form a 256-bit EoC shift register.

The selected operation mode (see Table 2.7) determines whether data is loaded to the matrix (through *Data\_to\_matrix*) or read out of the matrix (through *Data\_from\_Matrix*). The *Clk\_Read* frequency is 256 times slower than the *Fclock\_In* when data is transferred serially, and 8 times slower when either resetting or reading out the matrix in parallel. While reading out in parallel the 256 EoC column blocks are split into 32 subsections of 8 columns width where each subsection is connected to one of the 32 lines that form the parallel CMOS output bus.

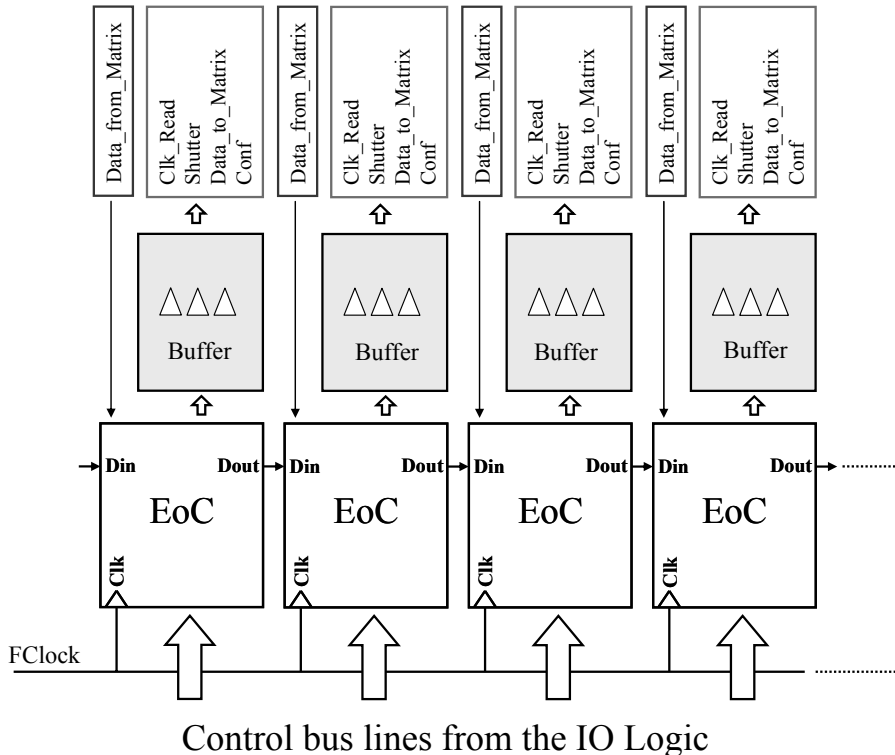


Figure 2.36. End-of-Column logic schematic for 4 pixel columns.

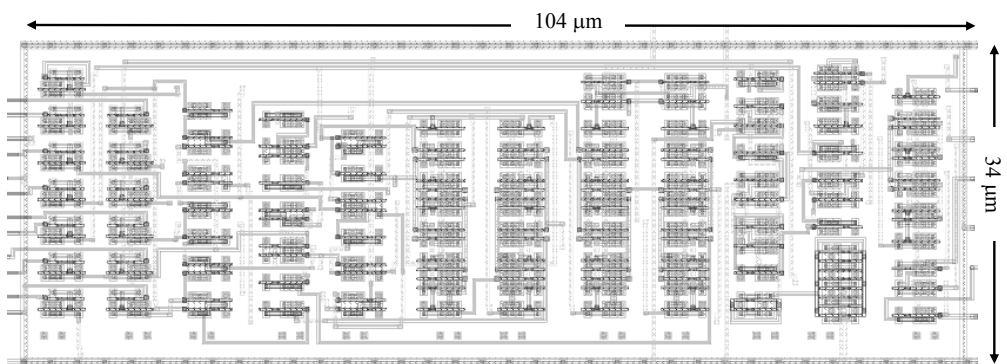


Figure 2.37. End-of-Column logic layout. The image is rotated for printing purposes. The width of the EoC is 34  $\mu\text{m}$  to cope with the high density pitch column pitch.

## 2.5 TILING OF LARGE AREAS

The ability to tile large areas has been a design priority. Allocating the chip periphery to the bottom of the chip and fully using the 6 metal layers available in the CMOS technology the non sensitive area in the left, right and top edges of the chip is reduced to less than 60  $\mu\text{m}$  (see Figure 2.38). By dicing as close as possible

to the chip edges it is possible to build multi-chip structures by placing N chips side by side and/or 2 chips top to top achieving any 2 x N combination.

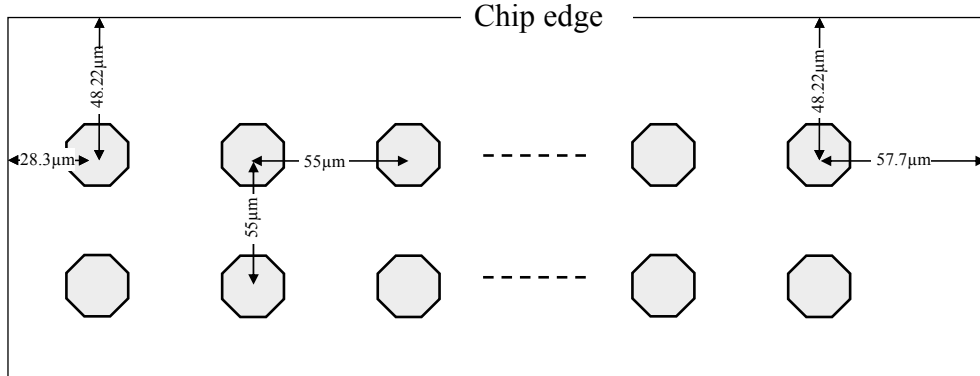


Figure 2.38. Distances from the last active pixels to the edge of the chip. The passivation openings are octagons of 20  $\mu\text{m}$  long.

The chips can be daisy chained through the LVDS serial link by connecting *Enable\_Out*, *Data\_Out* and *Fclock\_Out* of one chip to *Enable\_In*, *Data\_In* and *Fclock\_In* of the next chip in the chain (see Figure 2.39). With such a scheme the same readout system can be used for one single chip or any multi-chip daisy chained structure. The only penalty is the read out time.

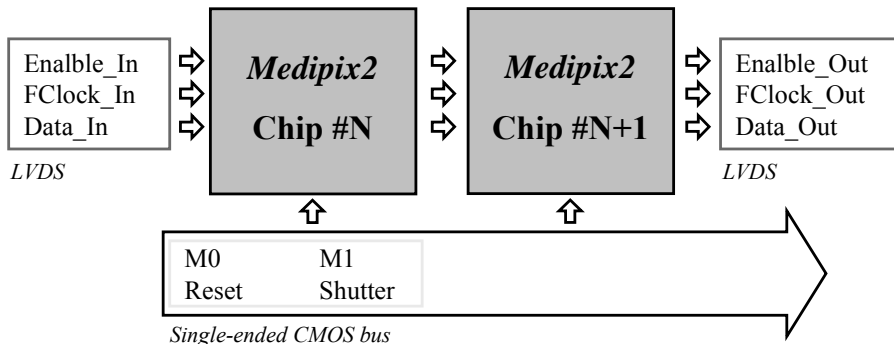


Figure 2.39. Schematic of two *Medipix2* chips connected in daisy chain.

## 2.6 SUMMARY

The motivations and requirements for the *Medipix2* design have been presented and the solutions chosen have been detailed and explained.

The *Medipix2* has 65536 pixels of 55  $\mu\text{m}$  x 55  $\mu\text{m}$ . Each pixel has a CSA whose output is DC coupled to two identical discriminator branches that form an energy window discriminator. The total analog power consumption per pixel is less than 8  $\mu\text{W}$ . The digital part of the pixel contains an 8-bit register, the energy window discrimination stage and a 13-bit counter.

The *Medipix2* periphery contains 117 IO pads, 13 8-bit DACs, LVDS drivers/receivers and the combinatorial and sequential logic for either reading from or writing to the chip. The chip can be daisy chained to form large multi-chip structures. A full custom digital library has been developed to fully exploit the 6 metal interconnecting layers available in the submicron technology used. Moreover, the design was heavily constrained by the need to bring all I/O and power lines from one edge of the chip.

In the next chapter the chip is electrically characterized using the injection test pulse and after bump bonding to a detector the X-ray imaging capabilities of the *Medipix2* chip are discussed.



### 3 MEDIPIX2 MEASUREMENTS AND CALIBRATION

In this chapter the electrical characterization (section 3.3) and first X-ray images (section 3.5) of the *Medipix2* chip bump bonded to a detector are presented. Section 3.1 gives an overview of the different chip carriers, readout boards and software available. Wafer probing (section 3.2) allows to select good dies before bump-bonding (section 3.4) to a detector. Section 3.6 studies the effects of radiation on the chip.

#### 3.1 MEDIPIX2 READOUT SYSTEMS

Several readout systems have been developed since the *Medipix2* chip became available in 2002. As an exercise of completeness the *Medipix2* collaboration common readout systems are briefly explained.

##### 3.1.1 *Medipix2* chipboards and probe card

The *Medipix2* probe card (see Figure 3.1) is used for wafer probing that classifies the chips according to their performances prior the assembling of the detector though bump bonding. Only good chips will be mounted to sensors reducing the cost of flip-chip assembling. The probe card is also used to characterize the *Medipix2* assemblies before mounting to the chipboard. The probe card is coupled through a 68-pin VHDCI<sup>6</sup> connector to either the Muros2 or the MedipixUSB serial readout systems (see 3.1.2). The board contains decoupling capacitance for the three power supplies (VDDA, VDD and VDDLVDS) and an analog multiplexer (MAX4634) used to generate the injection test pulse.

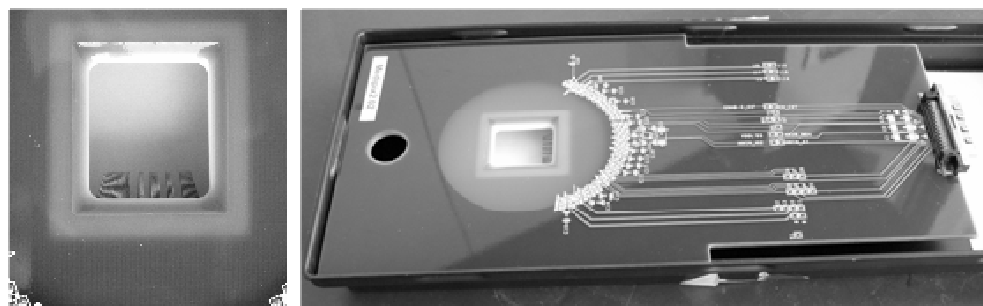


Figure 3.1 The *Medipix2* probe card. The central hole is bigger than the *Medipix2* sensitive for the test of the assemblies with x-ray sources.

The *Medipix2* CERN single chipboard is shown in Figure 3.2. The board schematic is identical to the probe card but adds a LEMO connector and a low pass filter used to provide a bias voltage for the detector. The *Medipix2* is directly glued

---

<sup>6</sup> Very High Density Cable Interconnect

to the ground plane and connected to the chipboard through 25  $\mu\text{m}$  thick aluminium wires using ultrasonic wedge bonding.

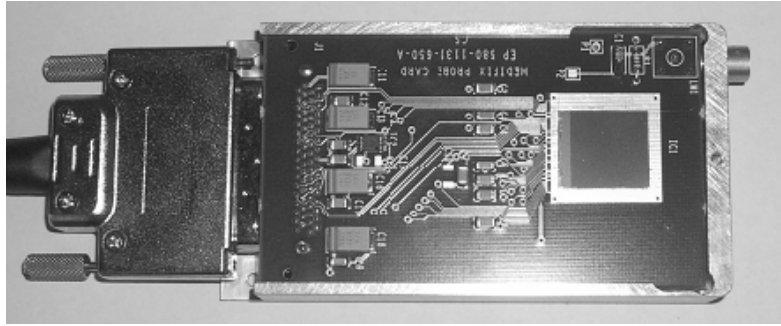


Figure 3.2. *Medipix2* CERN single chipboard coupled with the VHDCI cable. A naked *Medipix2* chip is mounted on the PCB.

The *Medipix2* octet board has been designed at Nikhef [FOR03]. This board can fit up to 8 chips in a 4x2 module. The card can be connected to the same readout systems as for the single chip chipboards (Muros2.1 and Medipix USB) using the daisy chain serial link. Figure 3.3 shows a picture of this board which has been used extensively in the measurements reported in Paper VII.

A more compact board has been recently developed by the same group at Nikhef to fit only a 2x2 multi-chip (*Medipix2* quad) with the same readout schematic as for the octet board but minimizing the non-sensitive PCB areas as shown in Figure 3.4.

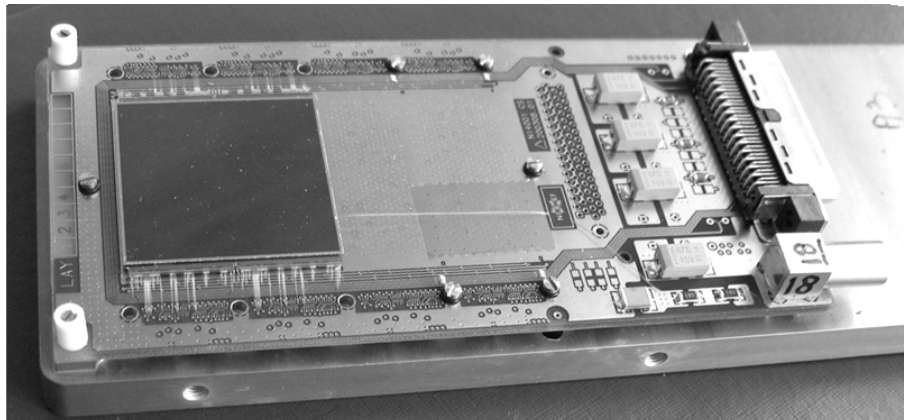


Figure 3.3. The *Medipix2* NIKHEF octet board [FOR03] can hold up to 8 chips. In the image a *Medipix2* Quad assembly is mounted on the board.

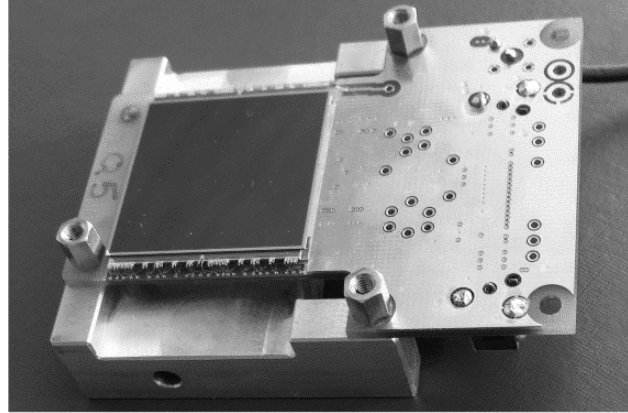


Figure 3.4. The *Medipix2 NIKHEF* quad board with a mounted *Medipix2* quad.

### 3.1.2 Readout hardware

Even though there are several readout systems for the *Medipix2* the Muros2 [SAN03] and the *MedipixUSB* [VYK06] are the *Medipix2* collaboration official readout boards. Other readout boards are briefly overviewed in section 3.1.4. Both boards have been used throughout the different measurements reported in Paper II-X.

*The Muros2 readout system* acts as an interface between any *Medipix2* chipboard (see section 3.1.1) and a commercial data acquisition system (National Instruments PCI-6533). The readout clock can be easily tuned from 30 to 200 MHz and can perform real-time acquisition at a maximum frame rate of  $\sim$ 30 Hz. The Muros2.1 is a second generation board that includes the possibility of using an internal power supply. The Muros2.1 is compatible with *Medipix2* (see Paper I, chapter 2), *Mpix2MXR20* (see chapter 4) and *Timepix* (see chapter 5) chips. It can be controlled either by the Pixelman or the Medisoft readout software (see 3.1.3). A photo of the system is shown in Figure 3.5.

*The MedipixUSB readout system* is an interface between any *Medipix2* chipboard (see section 3.1.1) and a PC through a USB1.1 connection. The readout clock is limited to 20 MHz and it can perform real-time acquisition at a maximum frame rate of  $\sim$ 5 Hz. The full system with one single chip can be powered through the 5 V 500 mA USB port allowing a high degree of portability. If multi-chip cards are used an external 5 V power supply is needed. The detector bias voltage supply up to 100V is internally generated and can be remotely controlled. The readout system is compatible with the *Medipix2* and *Mpix2MXR20* chips. It is controlled via the Pixelman software. A photo of a *MedipixUSB* system connected to the *Medipix2* single chip is shown in Figure 3.6. More detailed information can be found in [UTE07a].

The main common features of both readout systems are:

- On board power regulator.

- Generation of a stable calibration test pulse through software programmable DACs.
- On board 14-bit ADC for the *Medipix2* DAC monitoring.
- Generation of the *Medipix2* control commands as described in Table 2.7.



Figure 3.5. The Muros2.1 system.

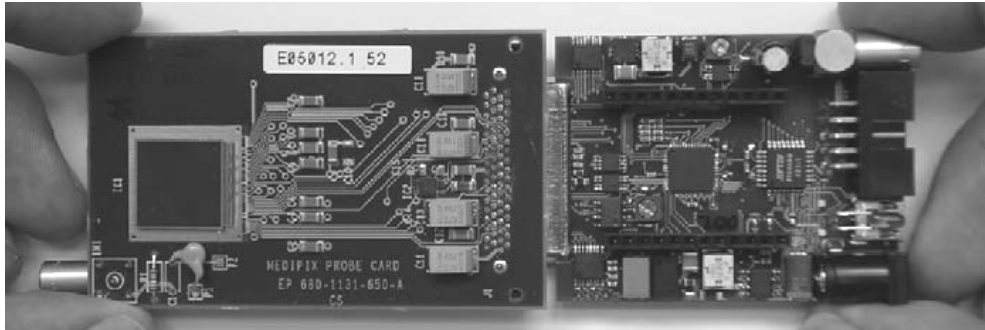


Figure 3.6. The MedipixUSB system connected to a *Medipix2* CERN single chipboard [VYK06].

### 3.1.3 Readout software

Two software programs are available for readout of the chip: the Medisoft4.0 developed at the University of Napoli (Italy) [MAI03] and the Pixelman software developed at the IEAP/UTEF (Prague, The Czech Republic) [HOL06].

The Medisoft program can operate with the *Medipix2* single chip and the *Medipix2* quad with the Muros2 readout system. The Pixelman can operate with all the single chip or multi-chip structures versions (*Medipix2*, *Mpix2MXR20* and *Timepix*) connected to any of the readout boards. It is also possible to run the

various readout systems on the same PC simultaneously. More information about the Pixelman software can be found in [UTE07b].

### 3.1.4 Other *Medipix2* readout developments

There are several other developments tailored to specific applications which demand either the fast readout (through the parallel bus) and/or the tiling of large areas.

The PRIAM board (ESRF, Grenoble-FR): An ultra fast readout system which uses the parallel bus is able to readout up to 5 chips simultaneously. This development is targeted for synchrotron applications [PON07] and adaptative optics for ground based telescopes [MIK06]. This system is reported to readout continuous frames from one chip at 1.4 kHz with an exposure time of 400  $\mu$ s (44% of dead time).

The Dear-Mamma project (IFAE, Barcelona-ES): A first demonstrator of a digital X-ray mammographic system has been built based on parallel readout [CHM06]. The readout system reports a measured frame rate of 500 Hz.

Some INFN groups (Cagliari, Napoli, Bologna, Pisa and Rome, IT) are currently developing an optical link based readout system for the *Medipix2* quad with a target frame rate of 25 Hz aimed at fast computed tomography scanning [MAR07].

## 3.2 WAFER PROBING

Wafer probing is the process of electrically testing each die on a wafer. A wafer is placed on a probe station and chips are tested by sequentially connecting a set of precision point needles on designated probe pads on a die (probe card, section 3.1.1). The *Medipix2* probe station is connected via one VHDCI cable to a Muros2 readout board using Medisoft or Pixelman software.

The needles provide the electrical contacts needed to test the die properly. Wire bond pads are also used as probe pads. Probing is done to select the good die before sensor bump bonding, thereby saving assembly and test costs.

The *Medipix2* is laid out in a shared reticle with other two small dies. The total reticle size is 18055  $\mu$ m x 14111  $\mu$ m and there are 94 units in an 8 inch wafer. The electrical tests employed by probing the *Medipix2* die consist of a communication test, a DAC scan and an analog front-end test using the calibration test pulse.

The selection criteria is based in the number of defective columns and DACs of the tested die as described in Table 3.1. Two wafer maps drawn after electrical tests from two different production lots are shown in Figure 3.7.

	<i>Selection criteria</i>
<b>A</b>	<i>No dead columns</i>
<b>B</b>	<i>1 dead column</i>
<b>C</b>	<i>2 dead columns</i>
<b>D</b>	<i>&gt; 2 dead columns</i>
<b>E</b>	<i>Bad DACs</i>
<b>F</b>	<i>Bad communication – High Analog current</i>

Table 3.1. The selection criterion for the *Medipix2* dies during wafer probing.

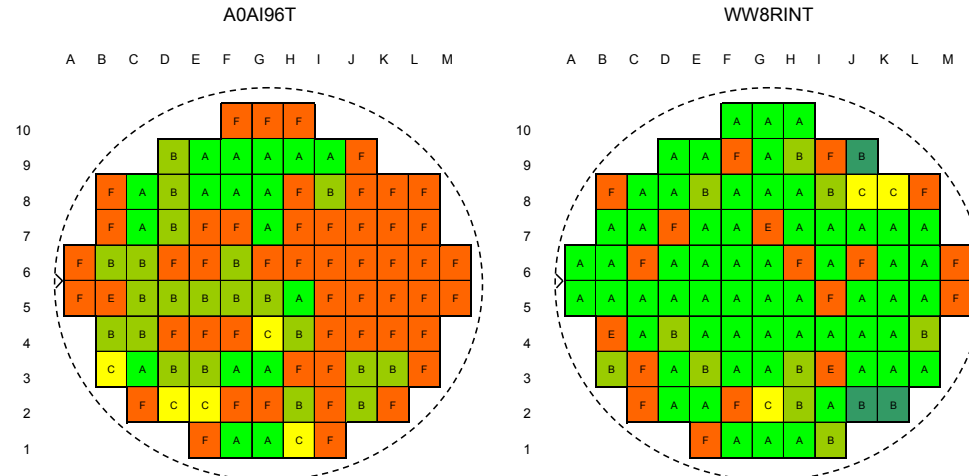


Figure 3.7. Two *Medipix2* wafer maps from two different production runs. Each wafer contains 94 chips.

### 3.2.1 Communication Test (digital)

A random bit pattern is written into the matrix and read out. The data sent and received are compared highlighting the communication errors. Given the *Medipix2* 3328-bit column shift register readout architecture the communication errors are displayed as number of dead columns per chip.

Scanning the *Fclock* clock frequency while doing the communication test the pixel error rate [%] can be plotted as shown in Figure 3.8. Below ~85 MHz the pixel error rate displays the number of failing columns due to yield. Above ~85 MHz the pixel error rate increases due to an internal delay between *Fclock\_Out* and *Data\_Out*. If the delay is corrected via software the maximum readout clock frequency for the *Medipix2* was measured to be ~130 MHz.

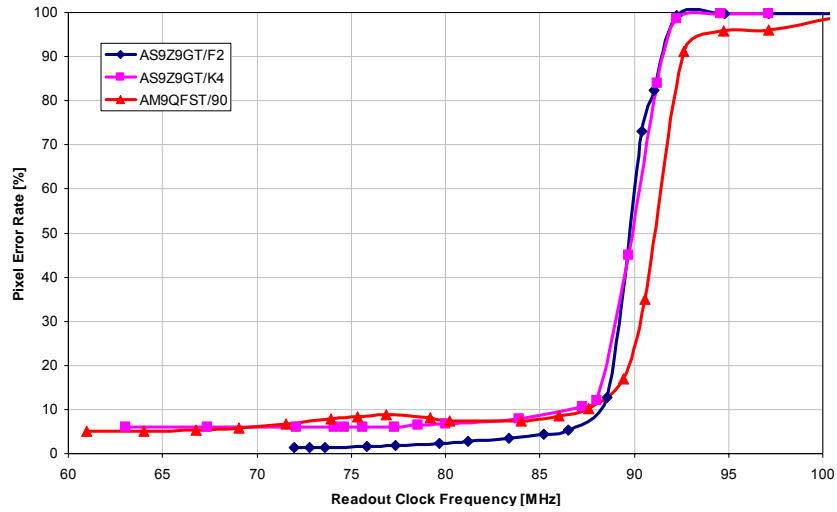


Figure 3.8. Pixel error rate versus read clock ( $F_{clock}$ ) frequency for three different chips.

### 3.2.2 DAC scan test (analog)

The 13 on-chip 8-bit DACs are monitored through one buffered analog output available at a wire bonding pad. A 14-bit ADC on the Muros2 readout board reads sequentially the output analog voltage of each DAC by scanning its 8-bit digital code. The DAC transfer functions of one *Medipix2* chip are shown in Figure 3.9 for the current DACs and in Figure 3.10 for the voltage DACs.

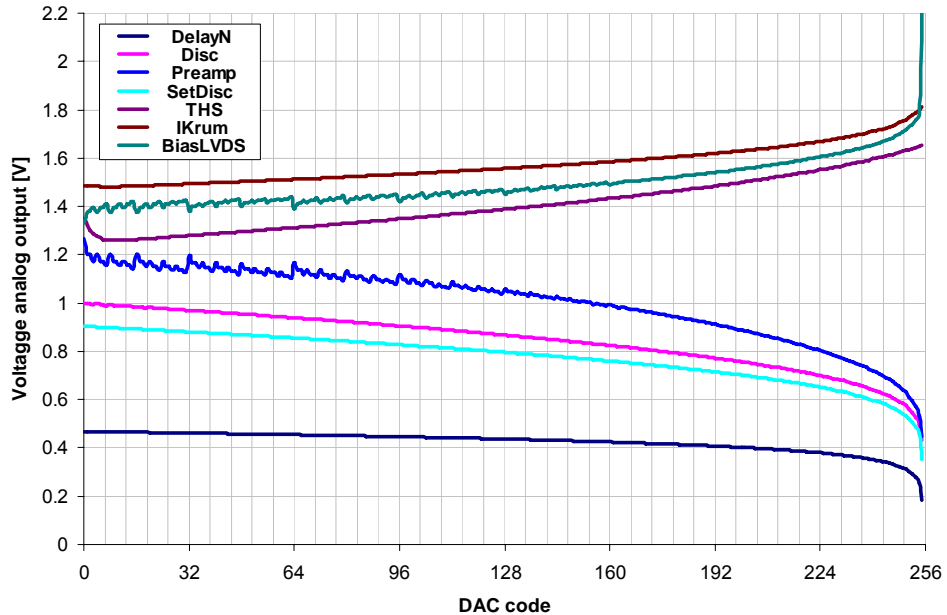


Figure 3.9. *Medipix2* current DACs transfer functions.

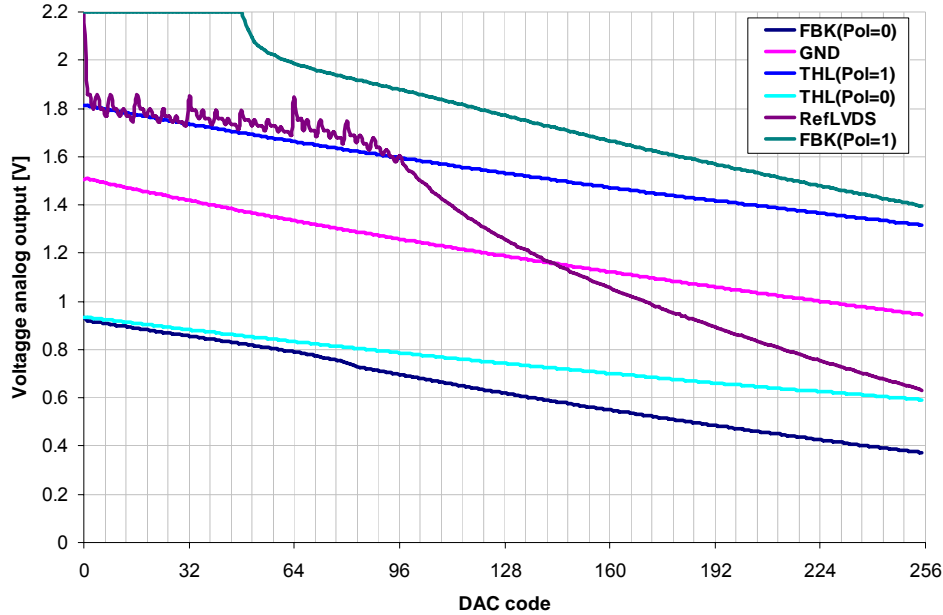


Figure 3.10. *Medipix2* voltage DACs transfer functions.

The *Medipix2* DACs transfer function analysis showed two undesired defects due to the DACs design:

- Non-Monotonicity: DACs BiasLVDS, Preamp and Ref\_LVDS showed a non-monotonic output behaviour due to a badly biased switch network in the binary weighted current block as shown in Figure 3.9 and Figure 3.10.
- Temperature dependence and linearity: All voltage DACs were realized with a NMOS target transistors working in linear region. This type of architecture showed high temperature dependence ( $1\text{mV}/^\circ\text{C}$ ) and poor linearity. Figure 3.11 shows the DNL<sup>7</sup> and INL<sup>8</sup> of the threshold DAC of one chip (V\_THL).

In spite of these two defects the chip could be operated normally with a good DAC calibration and in a temperature controlled environment.

---

<sup>7</sup> Differential non linearity (DNL) is defined as the difference between an actual step width and the ideal value of 1LSB.

<sup>8</sup> Integral non linearity (INL) is described as the deviation, in LSB or percent of full-scale range (FSR), of an actual transfer function from a straight line.

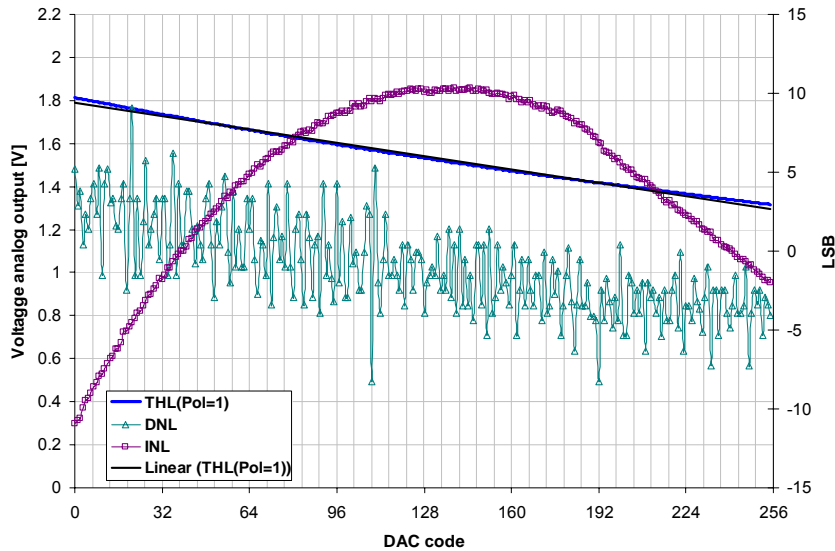


Figure 3.11. INL and DNL of the threshold DAC ( $V_{\text{THL}}$ ) of one *Medipix2* chip.

### 3.2.3 Analog test

A known number of injection test pulses are sent to every pixel with an equivalent input charge well above the low threshold. After acquisition and readout the counter value of all good pixels should be equal to the number of test pulses sent. The bad pixels are easily identified if they have either no counts or a noisy behaviour.

## 3.3 ELECTRICAL CHARACTERIZATION

First *Medipix2* electrical characterization has been done using a *naked* (without sensor) *Medipix2* chip mounted on the CERN single chipboard and using the Muros2 system and the Medisoft4 software as readout system. The details of the electrical characterization are described in Paper II and Table 3.2 summarizes the results.

	<i>Holes [h<sup>+</sup>]</i>	<i>Electrons [e<sup>-</sup>]</i>
Linearity [0-12 ke <sup>-</sup> ]	Not measured	>97%
ENC (at default settings)	~100 e <sup>-</sup> rms	~100 e <sup>-</sup> rms
Threshold variation before adjustment	~250 e <sup>-</sup> rms <sup>9</sup>	~450 e <sup>-</sup> rms
Threshold variation after adjustment	~120 e <sup>-</sup> rms	~120 e <sup>-</sup> rms
Minimum detectable charge	~1000 e <sup>-</sup>	~1000 e <sup>-</sup>

Table 3.2. *Medipix* electrical characterization summary from Paper II.

<sup>9</sup> The reported threshold variation before adjustment in positive published in paper II was found to be erroneous, after the publication of the article, due to an error on the gain calibration. The correct value is ~450 e<sup>-</sup> rms for both polarities.

The electrical test results reported in paper II are not fully accurate due to the non-linear behaviour of the injection test pulse. Moreover the pixel injection test capacitance was extracted from simulations which made absolute measurements like ENC, gain and threshold dispersion inexact. An absolute calibration of the chip was performed later with a *Medipix2* bump bonded to a 300  $\mu\text{m}$  thick high resistivity p<sup>+</sup> on n Si sensor using a monochromatic X-ray source (section 3.5.1).

### 3.4 BUMP BONDING

IBM introduced flip chip interconnection in the early sixties for their mainframe computers and it has evolved greatly in the last decades. Nowadays most electronic watches, and a growing percentage of cellular phones, pagers, and high speed microprocessors are assembled with flip chip.

Hybrid pixel detectors use flip chip technology to connect the pixel readout chip to the sensor material. The *Medipix2* has been bonded to 300  $\mu\text{m}$  and 700  $\mu\text{m}$  Si assemblies using a eutectic tin-lead solder process. Papers III, V, VI and VII used such assemblies for the reported measurements. During dicing of the sensor wafers is protected by photoresist to minimize the damage to the edge of the silicon sensor which would increase the leakage current. The bump deposition is done by electroplating while the final flip chip bonding happens in a fluxless environment [RTI and VTT]. Figure 3.12 shows two images taken with an electron microscope (SEM) of the readout and sensor side before flip chip bonding.

An indium bump bonding process has been used to bond a *Medipix2* to 1mm thick CdTe sensor as described in Paper IV because of the low temperature and pressure bonding requirements of the sensor material.

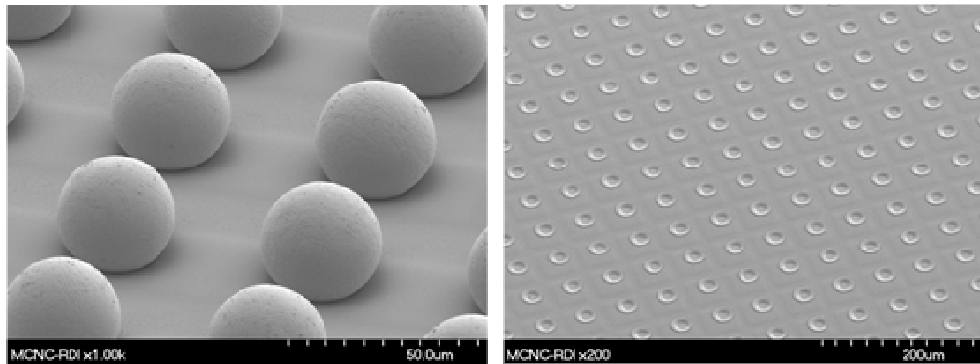
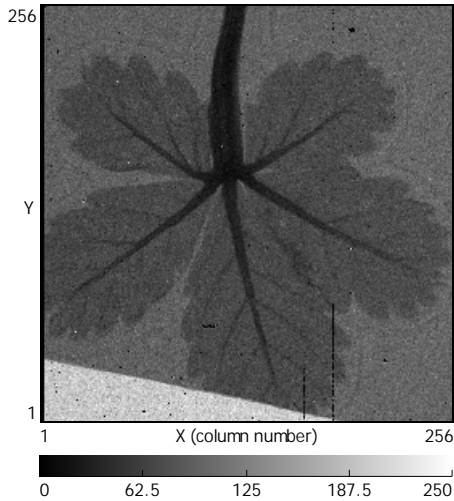


Figure 3.12. Two SEM images before assembling: On the left the eutectic tin-lead solder bumps sitting on top of the *Medipix2* and on the right the Si sensor side. [Courtesy of A. Huffman, RTI].

### 3.5 X-RAY IMAGING WITH THE *MEDIPIX2*

First X-ray images taken with *Medipix2* bonded to a high resistivity 300  $\mu\text{m}$  p<sup>+</sup> on n Si sensor (see paper III, Figure 3.13) demonstrated the *Medipix2* potential in various applications requiring high granularity single photon counting. Since

then many groups have used the *Medipix2* in different ways. Table 3.3 summarizes some of these applications including the number of *Medipix2* tiled chips, type of detector, and collection mode.



**Figure 3.13.** A leave inside captor tape: image taken with a *Medipix2* assembled to a high resistivity 300  $\mu\text{m}$   $\text{p}^+$  on n Si sensor exposed to a  $^{55}\text{Fe}$  X-ray source during 300 seconds. The images has been flatfield corrected.

<i>Applications</i>	<i>Medipix2</i>	<i>Detector</i>	<i>Publications</i>
<i>Adaptative optics</i>	1	<i>Micro channel plate (MCP)</i> [ $e^-$ ]	[VAL04]
<i>X-ray diffraction</i>	1	300 $\mu\text{m}$ Si [ $h^+$ ] 700 $\mu\text{m}$ Si [ $h^+$ ]	[VRI07] [MIT05]
<i>Micro-radiography</i>	1	300 $\mu\text{m}$ Si [ $h^+$ ]	[VAV05]
<i>Neutron imaging</i>	1	300 $\mu\text{m}$ Si + $^6\text{LiF}$ converter [ $h^+$ ] Neutron sensitive MCP [ $e^-$ ]	[JAK04], [JAK05] [SIE07]
<i>Autoradiography</i>	1	300 $\mu\text{m}$ Si [ $h^+$ ]	[MET04]
<i>Gamma imaging</i>	1	1mm CdTe [ $e^-$ ]	[MAN04] and paper IV
<i>Electron microscopy</i>	1	300 $\mu\text{m}$ Si [ $h^+$ ]	[FAR05]
	2x2	300 $\mu\text{m}$ Si [ $h^+$ ]	Paper VII
<i>Energy weighting</i>	1	300 $\mu\text{m}$ Si [ $h^+$ ]	[KAR05]
<i>In vivo optical and radionuclide imaging</i>	1	300 $\mu\text{m}$ Si [ $h^+$ ] 1mm CdTe [ $e^-$ ]	[AUT05]
<i>MPGD</i> <sup>10</sup>	1	<i>GEM and Micromegas</i> [ $e^-$ ]	Paper VIII and IX
<i>Mammography</i>	25 x 19 cm	700 $\mu\text{m}$ Si [ $h^+$ ] 800 $\mu\text{m}$ CdTe [ $e^-$ ]	[CHM06]

**Table 3.3.** Summary of applications using the *Medipix2* chip with different detector types and front-end collection modes.

<sup>10</sup> Micro-Patterned Gas Detectors

The imaging performance of the *Medipix2* readout chip bump bonded to a 300  $\mu\text{m}$  thick Si detector as a function of the global threshold DAC is presented in paper VI. The modulation transfer function (MTF) describing the spatial resolution properties, the noise power spectrum (NPS) describing the image noise, and the detective quantum efficiency (DQE) giving a measure for image quality with respect to the incoming photonic signal have been measured as a function of the single energy threshold. Measurements were carried out using a Seifert FK-61-04x12 X-ray tube with a W-target, a 2.5 mm thick Al filter and a tube voltage of 25 kVp. The MTF was measured using the angulated slit technique described in [FUJ92]. The spatial resolution has been measured using the MTF and it varies between 8.2 line-pairs/mm and 11.0 line pairs/mm at an MTF value of 70%. An associated measurement of NPS permits us to derive the DQE which can be as high as 25.5% for a broadband incoming spectrum.

### 3.5.1 Absolute pixel calibration

An absolute pixel characterization was realized using a  $10 \times 10 \mu\text{m}^2$  monochromatic pencil beam focused at the centre of one pixel at ESRF<sup>11</sup>. The monochromator was set to 7.9 keV, leaving the second monochromator crystal weakly detuned. In this way contaminations from higher harmonics could pass the monochromator, providing a set of well defined X-ray lines that were used in a single experiment to calibrate the DAC value-energy correlation. The harmonics placed at 23.7, 32.6 and 39.5 keV permitted a simple calibration at a pixel level. The external DAC input (EXT\_DAC) was used as global low threshold to have a larger dynamic range avoiding the non-linearity behaviour of the internal threshold DACs. Figure 3.14 shows on the left the resulting s-curve and on the right the energy calibration. The pixel linearity and gain can be obtained by fitting the measured effective threshold to the known input beam energy. The pixel ENC can be extracted by the s-curve method. The measured noise is  $\sim 167 \text{ e}^- \text{ rms}$ , with a gain of 8.7 mV/ke $^-$  or 416 eV/mV, and linearity better than 99.9% in the measured range (0 to 11 ke $^-$ ). The pixel minimum detectable charge is  $\sim 4 \text{ keV}$  or  $\sim 1100 \text{ e}^-$ . During the measurements at ESRF the Ikrum bias current was set to 15 nA, which corresponds to the default value after chip Reset, limiting the measured gain and ENC as shown in Figure 2.8.

---

<sup>11</sup> European Synchrotron Radiation Facility at Grenoble, France.

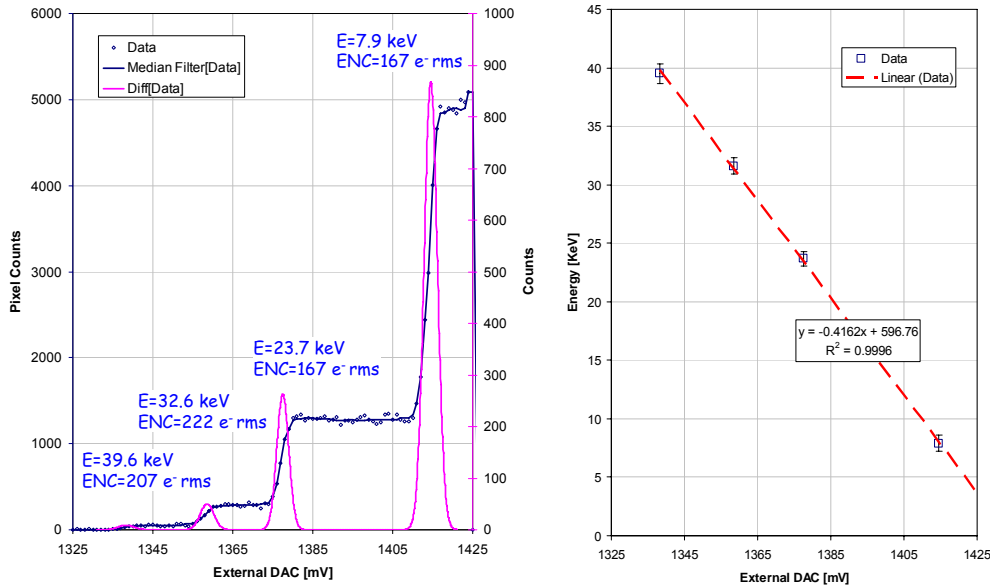


Figure 3.14. On the left pixel threshold scan with a  $10 \times 10 \mu\text{m}^2$  7.9 keV pencil beam with its harmonics focused at the center of one pixel. On the right pixel linearity and gain slope extracted from the threshold scan.

### 3.5.2 The Medipix2 Quad

Using this scheme four *Medipix2* chips have been successfully assembled to the same  $300 \mu\text{m}$  high resistivity Si sensor using solder bump-bonding. The total sensitive area achieved covers more than  $8 \text{ cm}^2$  with 262144 pixels. The pixels placed at the edge between 2 chips are 3 times wider to cope with the distance between diced chips. The inner corners are covered by pixels which are 9 times larger than the rest as shown in Figure 3.15. The *Medipix2* quad was mounted in the dedicated 9-layer PCB shown in Figure 3.3.

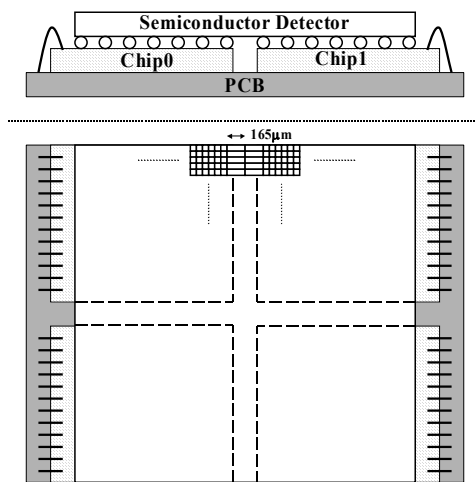


Figure 3.15. Section and top view schematic of a *Medipix2* multi-chip structure (*Medipix2 Quad*).

The *Medipix2* quad is equalized to allow correct global threshold setting for the four chips simultaneously. In a *Medipix2* quad the threshold variations are dominated basically by two components: the chip to chip DAC variations, and the pixel to pixel threshold variations in each chip due to electronic mismatch.

A new software algorithm was written to first equalize the chip to chip global threshold variation, and secondly to equalize each chip by using a noise equalization algorithm. The noise equalization procedure records the threshold at which each pixel hits the noise floor as described in paper X. Figure 3.16 and Figure 3.17 show an example of a quad equalization where Chip0 has a significant shift in its global low threshold DAC compared with the Chip[1:3]. After equalization a minimum threshold of  $\sim 1200$  e $^-$  is achieved. Figure 3.18 shows two images taken with the *Medipix2* quad using a W X-ray tube at different tube settings. The X-ray beam diameter is smaller than the quad length resulting in the black corners of the images (low counts). The counts of the larger pixels between chips had been normalized to its area.

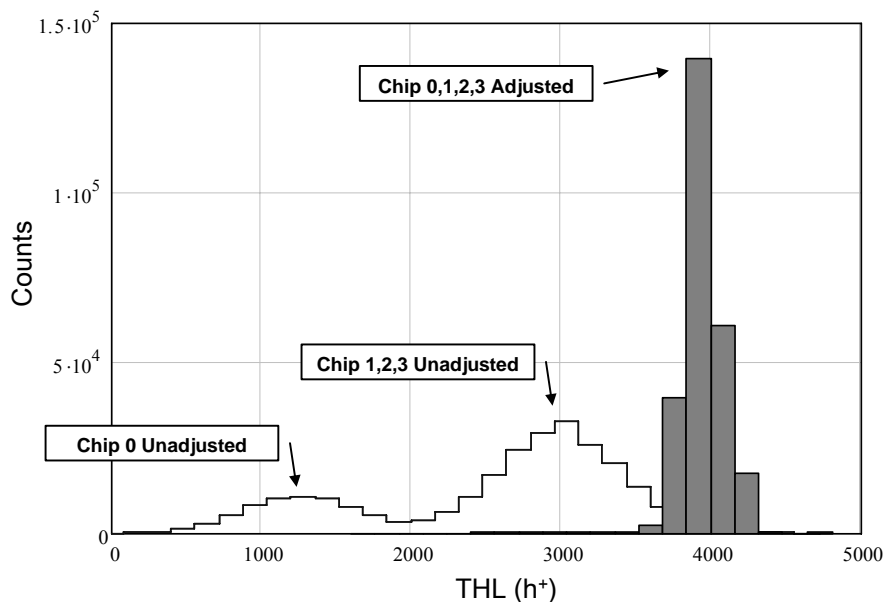


Figure 3.16. Threshold dispersion before equalization (step trace): Chip0  $\sigma=394$  e $^-$  rms and Chip[1-3] 416 e $^-$  rms with a minimum detectable charge of  $\sim 4400$  e $^-$ . Threshold dispersion after equalization (solid bar trace): Chip [0-3]  $\sigma=117$  e $^-$  rms with a minimum detectable charge of  $\sim 1200$  e $^-$ .

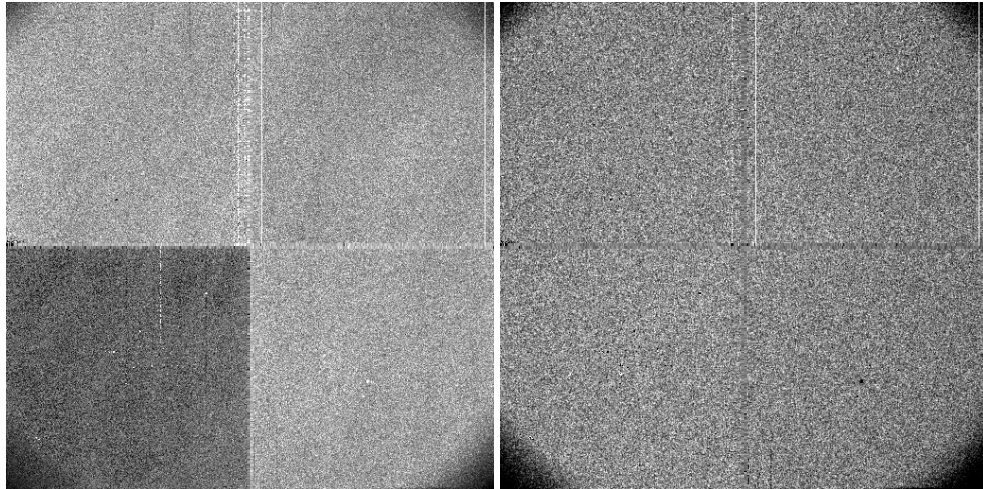


Figure 3.17. Image taken with a  $^{109}\text{Cd}$  source using a 10 min acquisition time. On the left before equalization, and on the right after equalization. Note that the grey levels of the larger pixels have been normalized to their surface area.

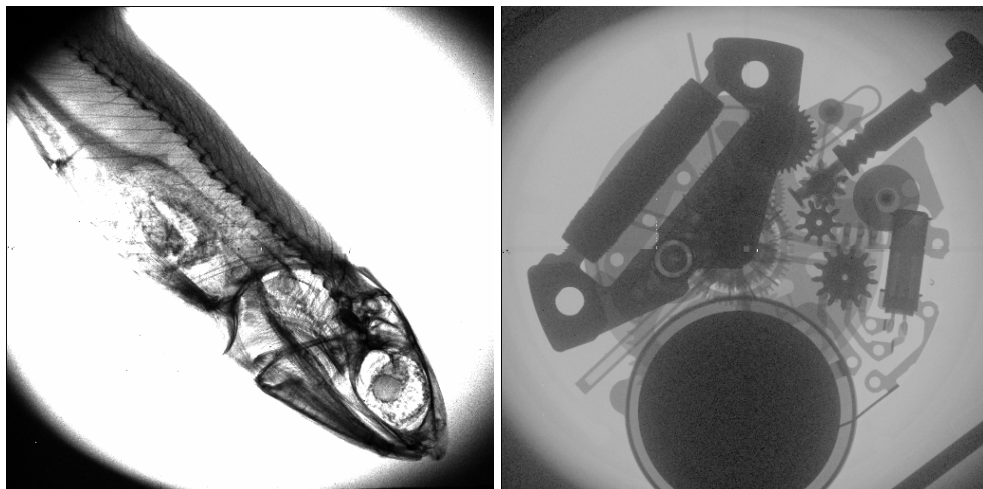


Figure 3.18. Images taken with an equalized *Medipix2 quad*: On the left 500 ms acquisition of an anchovy with a W X-ray tube at 15 kVp; on the right: A 100 ms acquisition of a wrist watch with a W X-ray tube at 50 kVp.

### 3.6 RADIATION HARDNESS

Radiation tolerance is an important issue for an X-ray imaging hybrid pixel readout chip. When ionizing radiation goes through a MOSFET, electron-hole pairs are generated. Due to the little resistance of the gate interconnect material (metal or polysilicon) and substrate the electron-hole pairs quickly disappear. On the contrary in the oxides, which is an insulator, electrons and holes have different behaviours, as their mobilities differ from five to twelve orders of magnitude

[ANE00]. The thin gate oxide is in fact practically immune from radiation while the thick oxide on the lateral isolations is a problem due to charge and interface states trapping. The leakage current increase and threshold voltage shift of NMOS transistors are clearly an issue due to the positive sign of the trapped charges.

As published in Paper I a first radiation tests were carried out using a dedicated X-ray machine (*Seifert RP149*). First results showed an increase of the analog and digital power consumption  $\sim 200$  krad<sup>12</sup> but the chip still could be operated digitally above 500 krad. For those test only power consumption shifts and basic functionality could be tested since the *Medipix2* readout systems were not available.

Some time later, using the Muros2 readout system another radiation campaign was organized using a *naked Medipix2* on the same radiation facility at CERN. The X-ray tube spot size was defined to be smaller than the *Medipix2* sensitive area. Threshold equalization masks were repeated at different integrated doses to find any threshold shift in the analog front-end. Figure 3.19 shows the results. After only  $\sim 10$  krad the threshold of the irradiated area had clearly shifted. Even though the equalization procedure was able to compensate the threshold shift after that integrated dose, and *Medipix2* still worked above 500 krad, this radiation damage at low doses set a practical limit for many applications.

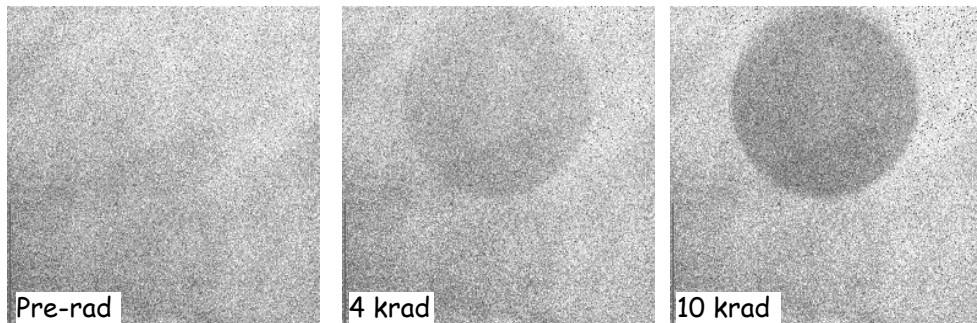


Figure 3.19. Threshold shift as seen in the 3-bit low threshold equalization mask. After 10 krad of integrated dose a threshold shift is clearly visible in the irradiated area.

### 3.7 SUMMARY

In this chapter the available *Medipix2* readout systems have been described. The overall performance of the *Medipix2* is very good and many applications with low noise high granularity single photon counting requirements have used it successfully. Measurements show an electronic noise  $\sim 160$  e<sup>-</sup> rms with a gain of  $\sim 9$  mV/ke<sup>-</sup>. The threshold spread after equalization of  $\sim 120$  e<sup>-</sup> rms brings the full

---

<sup>12</sup> One gray is the absorption of one joule of radiation energy by one kilogram of matter (1 Gy = 1 Joule/Kg). In High Energy Physics community (and also in this thesis) the *rad* is used (100 rad = 1 Gy).

chip minimum detectable charge to  $\sim 1100$  e $^-$ . The measured MTF at 70% varies between 8.2 line-pairs/mm and 11.0 line-pairs/mm. The DQE at 0 line-pairs/mm is measured to be as high as 25.5% for a broadband incoming spectrum.

Even though these encouraging results, the chip showed several weak points:

- The test pulse could not be used as a calibration tool due to the gain non-linearity of the analog buffers and parasitic coupling.
- The voltage DACs (i.e. the threshold DAC) show a significant non-linearity and temperature dependence.
- The chip radiation hardness was below the intrinsic limit of the CMOS technology used.

In next chapter a full chip redesign is undertaken in order to correct for these chip limitations.



## 4 REDESIGN OF THE *MEDIPIX2 (MPIX2MXR20)*

In this chapter the full redesign of the *Medipix2* is described. The new chip is called *Mpix2MXR20* and has the same physical dimensions as *Medipix2*. Section 4.1 discusses the motivation for the new design and presents the solutions chosen. Considerable changes have been made in the pixel cell (section 4.2) and in the periphery (section 4.3). The electrical characterisation of pixel and chip is reported in section 4.4. Section 4.5 explores the imaging performance of the new chip.

### 4.1 MOTIVATION OF THE REDESIGN

The *Medipix2* chip demonstrated the feasibility of high granularity direct detection photon counting hybrid pixel detectors. This was possible due to the availability of a well characterized 0.25  $\mu\text{m}$  commercial CMOS technology. Small pixels have the great advantage of having a very small input capacitance making the pixel power budget affordable (i.e. less than 8  $\mu\text{W}/\text{pixel}$ ). Tiling was also achieved with the *Medipix2* quad, as shown in Paper VII, where a sensitive area larger than 8  $\text{cm}^2$  with more than 256K pixels was completed. Fast readouts and portable systems were developed and successfully tested.

In spite of this success the chip was not fully robust due to some limitations of the design (already mentioned throughout chapter 3). Also some new ideas were generated while testing the *Medipix2*. The main reasons of the redesign in order of importance were:

- The voltage DACs showed a relatively high temperature dependence and a non-optimal linearity (INL = 8 LSB, see section 3.2.2).
- The analog buffers didn't have a unitary gain response as shown in section 2.4.1.2 (i.e. it was not possible to do an absolute calibration using injection test pulse).
- The pixel counter was reinitialized when the end of scale was reached (8001 counts). This was a problem if the counter registered value had to be used as an absolute measurement.
- The measured pixel radiation hardness ( $\sim 10$  krad) was at least one order of magnitude lower than expected by the technology used [ANE00].

These were the stronger motivations that lead to a full redesign of the chip but other changes bringing more functionality and robustness to the chip were added. The following list summarizes all the changes made to the *Medipix2* chip in the pixel cell and in the periphery.

On the pixel side:

- Improve the radiation hardness by using NMOS enclosed layout transistors in the sensitive nodes.

- Improved threshold dispersion in the front end by adding a local current mirror to generate  $I_{Krum}/2$
- Simplify the discriminator block while changing the masking gate to the digital side.
- Add an overflow bit

On the periphery side:

- Add an internal reference circuitry (band-gap circuitry).
- Improve the linearity and minimize the temperature dependence of the voltage DACs.
- Upgrade the analog buffers to be unitary gain buffers and minimize coupling.
- Increase the serial readout bandwidth of the system to  $\sim 200$  MHz.
- Add a 24-bit fused blown register for unique chip identification.
- Larger IO pads to facilitate wafer probing and improve the wire bonding robustness.

The chip is called *Mpix2MXR20* and uses the same commercial  $0.25\mu m$  CMOS technology used by the *Medipix2*. The pixel pitch, floor plan and chip dimensions of the *Mpix2MXR20* are identical than the *Medipix2* to avoid redesign of sensor and bump bonding masks. Given that several readout systems existed the chip readout architecture was kept unchanged.

## 4.2 PIXEL UPGRADES

Figure 4.1 shows the schematic of the *Mpix2MXR20* pixel cell. The pixel analog side (in red) contains a charge sensitive amplifier with and upgraded DC leakage current compensation and a local  $I_{Krum}$  current mirror, a test capacitance, and two branches of identical discriminators with 3-bit threshold adjustment current DACs. The digital side (in blue) contains the pixel masking inside the Double Discriminator Logic, a 14-bit shift register which doubles as a counter with overflow control and as a shift register, and a 8-bit register.

The pixel architecture concept is very much as the *Medipix2* pixel cell (see Figure 2.2). The main functional difference comes from the counter depth and the overflow control logic. The 14-bit shift register in acquisition mode (*Shutter* low) has a dynamic range up to 11810 counts with an overflow control logic that stops the pixel counter, by acting on the pixel *Shutter* signal, if the counter value gets to the end of scale.

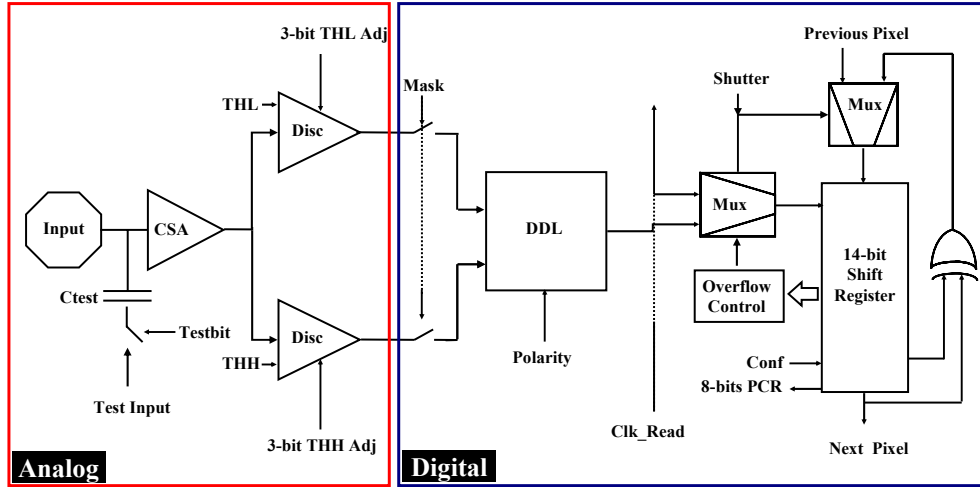


Figure 4.1. The *Mpix2MXR20* pixel cell. On the left the analog side and on the right the digital side.

The dimensions of the cell are unchanged. Each pixel has 529 transistors and a static analog power consumption comparable to *Medipix2* ( $\sim 8 \mu\text{W}$ ). The layout of the *Mpix2MXR20* pixel cell is shown in Figure 4.2.

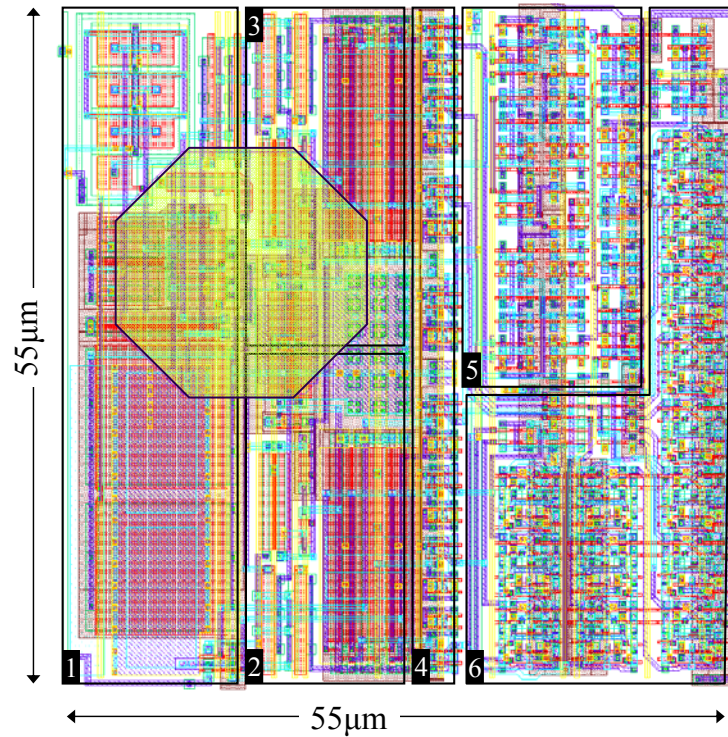


Figure 4.2. The *Mpix2MXR20* pixel cell layout. 1) Preamplifier; 2) High Threshold Discriminator; 3) Low Threshold Discriminator; 4) 8-bit configuration latches; 5) DDL; 6) 14-bit Counter and overflow control. In yellow the passivation opening for bump bonding.

## 4.2.1 *Mpix2MXR20* CSA

The CSA architecture is almost identical as the one described in section 2.3.1.1. The *MpixMXR20* upgrades in the CSA are: first to enhance the radiation hardness the CSA and second and second to generate internally the *Ikrum/2* current from the *Ikrum* by means of a local current mirror. This helps to minimize the pixel to pixel output voltage offset. These improvements in the CSA have no impact on its basic electrical performance, therefore, the CSA gain and noise studies realized in section 2.3.1.1 are valid.

### 4.2.1.1 *CSA radiation enhancement*

The radiation tolerance achieved by the *Medipix2* was lower than expected (see section 3.6). One of the consequences of radiation damage in NMOS transistors is the leakage current increase due to charge trapping in the thick isolation oxide and in the interface states [ANE00]. The CSA feedback architecture uses very low currents ( $\sim nA$ ) two bias the feedback loop. Any parasitic leakage current in the *Ikrum/2* branch will unbalance the PMOS differential pair and generate a DC output voltage. To harden this sensitive node of the design enclosed layout transistors (ELTs) have been used to eliminate such parasitic leakage currents. The effective W/L of the NMOS ELTs [GIR00] is calculated as 4.72/1.

Figure 4.4 shows the layout of the both designs were the ELTs are clearly visible at the bottom left corner of the *Mpix2MXR20* CSA. Measurements of the new CSA at the chip level are shown in Figure 4.3. Under the same experimental conditions as in section 3.6 the radiation tolerance is enhanced a factor  $\sim 20$ .

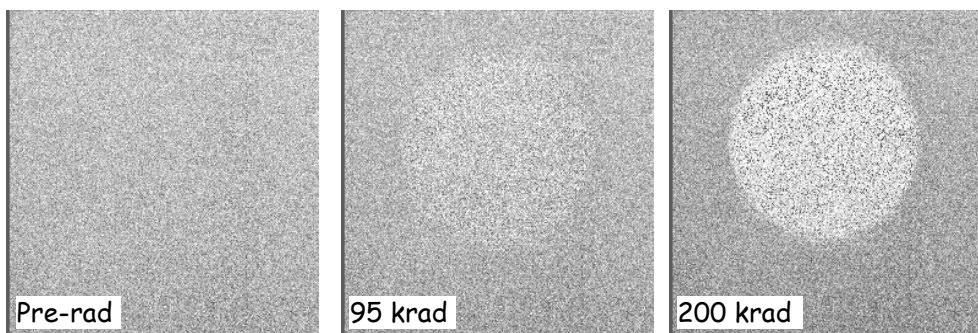


Figure 4.3. Threshold shift as seen in the 3-bit low threshold equalization mask. After 200 krad of integrated dose a threshold shift is clearly visible in the irradiated area.

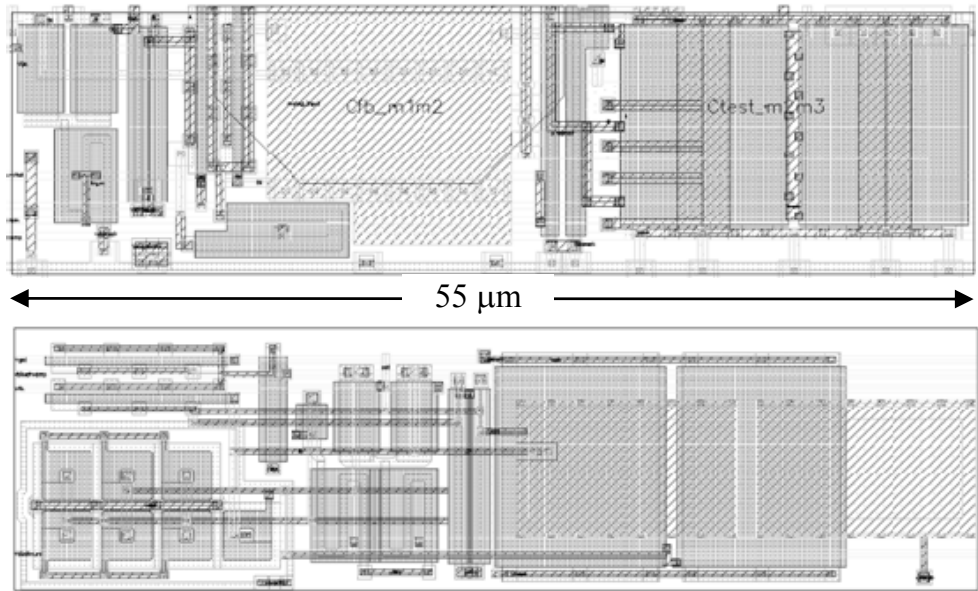


Figure 4.4. On top the *Medipix2* CSA. On the bottom the *Mpix2MXR20* CSA using ELTs (at the bottom left).

#### 4.2.1.2 *Ikrum local mirroring*

The *Medipix2* used two outputs from the same global DAC to generate Ikrum and Ikrum/2. These two gate voltages were connected to all pixels to generate the local copies of Ikrum and Ikrum/2 respectively. The transistor matching studies (see section 2.3.1.3) for these two current sources supposed that the source (at the output of the DAC) and target transistors (at every pixel) were placed at small distances (10 to 100  $\mu\text{m}$ ). In reality they were placed at distance as far as  $\sim 15000 \mu\text{m}$  (for pixels at the top of the matrix) and matching was not well controlled.

In *Mpix2MXR20* Ikrum current is copied in a secondary branch and divided by means of a 2:1 NMOS current mirror to the Ikrum/2 branch. As seen in section 4.2.1.1 the NMOS transistors of the feedback loop are radiation hard by design. Several experimental matching studies have revealed that threshold and current factor matching of ELTs don't have a straight response but curved. This reason is still under investigation [ANE00]. The threshold voltage matching and current factor matching for ELTs can be written as

$$\sigma_{V_{th}}^2 = \frac{A_{V_{th}}^2}{W \cdot L} + \sigma_o \quad \sigma_{\beta}^2 = \frac{A_{\beta}^2}{W \cdot L} + \sigma_o \quad (4.1)$$

Where  $\sigma_{V_{th}}=4.3 \text{ mV}\cdot\mu\text{m}$ ,  $\sigma_o=1 \text{ mV}\cdot\mu\text{m}$ ,  $\sigma_{\beta}=1.3 \% \cdot \mu\text{m}$  and  $\sigma_o=0.3 \%$  were found experimentally for the  $0.25\mu\text{m}$  technology used. The CSA DC output variation can be now precisely calculated as

$$\sigma_{PREAMP} = \sqrt{\sigma_{FB}^2 + \left( \frac{2}{3} \cdot \frac{gm_{IK2}}{gm_{FB}} \right)^2 \cdot \sigma_{IK2}^2 + \left( \frac{gm_{IK}}{2 \cdot gm_{FB}} \right) \cdot \sigma_{IK}^2} \quad [V] \quad (4.2)$$

Where  $\sigma_{FB}$ ,  $\sigma_{IK2}$  and  $\sigma_{IK}$  are the total gate voltage mismatches for the PMOS feed-back, the Ikrum/2 current source and the Ikrum current source of the preamplifier respectively (see Figure 2.4). Notice that the contribution from the Ikrum/2 branch is reduced by a factor 2/3 compared to equation 2.14. The total mismatch at the output at the default DAC biasing settings is  $\sigma_{PREAMP} = 2$  mV rms this is 10 % less than in *Medipix2* cell.

To better see the effects of the local mirroring at full chip scale a typical threshold equalization mask from a *Medipix2* and a *Mpix2MXR20* is shown in Figure 4.5. The *Mpix2MXR20* equalization mask is much uniform compared to the old chip.

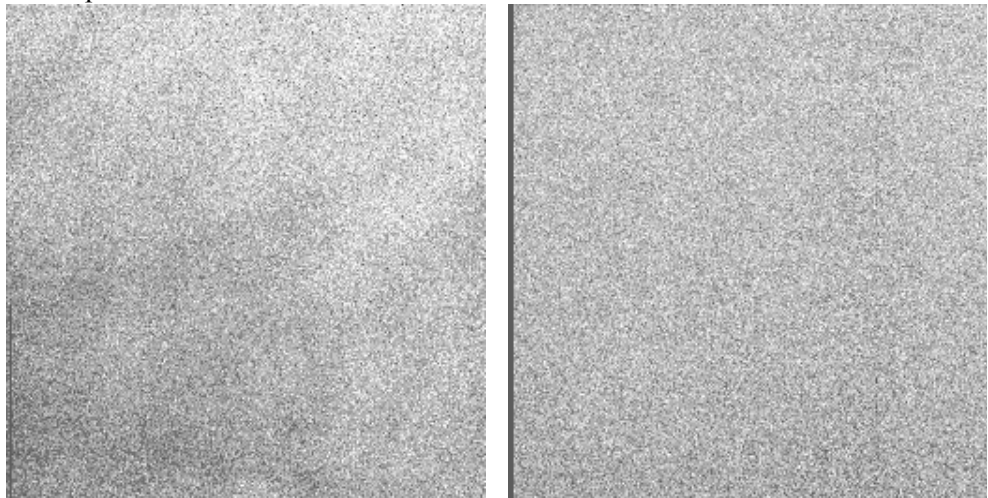


Figure 4.5 On the left a typical *Medipix2* 3-bit equalization mask and on the right a *Mpix2MXR20* 3-bit equalization mask. The right picture has a better uniformity.

#### 4.2.2 *Mpix2MXR20* discriminator

The *Medipix2* discriminator performed well. The discriminator architecture is similar to the one shown in Figure 2.15. is the same as in upgrades are in the 3-bit current DAC for threshold adjustment was slightly modified, and the masking NAND gate was moved to the digital side.

The *Medipix2* 3-bit DAC current sources were designed with different target transistors for each bit. This had an impact in the DAC linearity due to poor transistor matching. In the new design all the current sources are designed with the same target transistor (0.42/16). BO, B1 and B2 use 1, 2 and 4 target transistors in parallel respectively.

The new zero-crossing circuit uses the same scheme as in *Medipix2* [TRA92]. The IsetDisc DAC used as gain control stage has been removed since the

benefit in the circuit performance was minimal. The suppression of this DAC simplifies the global routing.

The *Medipix2* pixel mask bit was realized at the zero crossing output of each discriminator branch by means of a NAND gate which was powered from the analog power supply. The effect of that gate pulling current when switching (i.e. whenever there was a hit) was that injected switching noise was added to the analog power supply. When many pixels were hit simultaneously (i.e. threshold set close to the noise level) the added switching noise had a feedback effect to other pixels and the full matrix became noisy. In the *Mpix2MXR20* the gating of the mask bit is done at the input of the DDL which is powered by the digital supply.

#### 4.2.3 Shift Register and Counter (digital)

The block diagram of the digital side shown in Figure 2.18 is the same for the *Mpix2MXR20* digital side. The only changes are in the Shift Register/ Counter block (SR/C) and in the PCR register.

##### 4.2.3.1 *Mpix2MXR20* SR/C

The *Mpix2MXR20* schematic of the shift register and counter block is shown in Figure 4.6. The new pixel adds an extra shift register bit and a 14-input NAND gate. In acquisition mode (*Shutter* low) the counter has a dynamic range up to 11810 counts. The overflow control logic stops the counter by toggling the internal *Shutter* to a high state if the counter value is 1111111111110b.

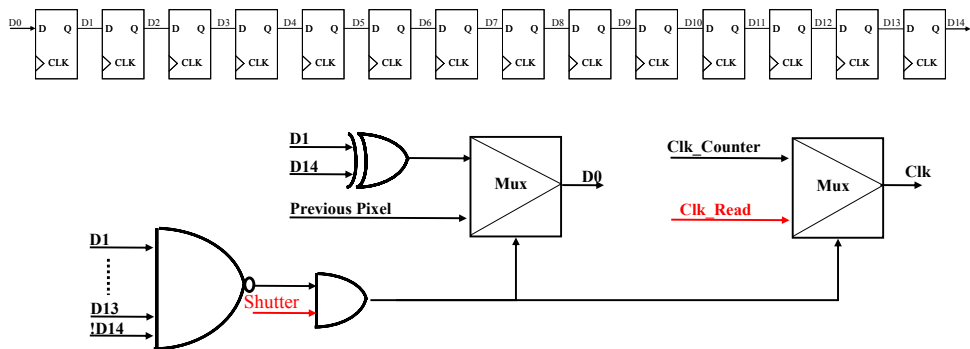


Figure 4.6. The *Mpix2MXR20* SR/C schematic. The global lines are displayed in red.

##### 4.2.3.2 *Mpix2MXR20* Pixel Configuration Register (PCR)

The layout of the digital block has been completely rebuilt to add an extra bit in the shift register. The configuration bits have the same functionality as for *Medipix2* (see Table 2.3) and Figure 4.7 shows which bits are latched into the PCR.

b0	b1	b2	b3	b4	b5	b6	b7	b8	b9	b10	b11	b12	b13
Mask Bit	X	X	X	X	X		Bit 1 Low	Bit 0 Low	Test Bit	Bit 1 High	Bit 0 High		X

Figure 4.7. *Mpix2MXR20* PCR is formed by latching 8-bit of the 14-bit shift register.

### 4.3 PERIPHERY UPGRADES

The *Mpix2MXR20* upgrades in the periphery aim to improve the chip temperature dependence, linearity, testability, readout speed and robustness. The new periphery has the same dimensions as in *Medipix2*. The schematic is shown in Figure 4.8 where the dashed blocks have been upgraded or added compared to *Medipix2*.

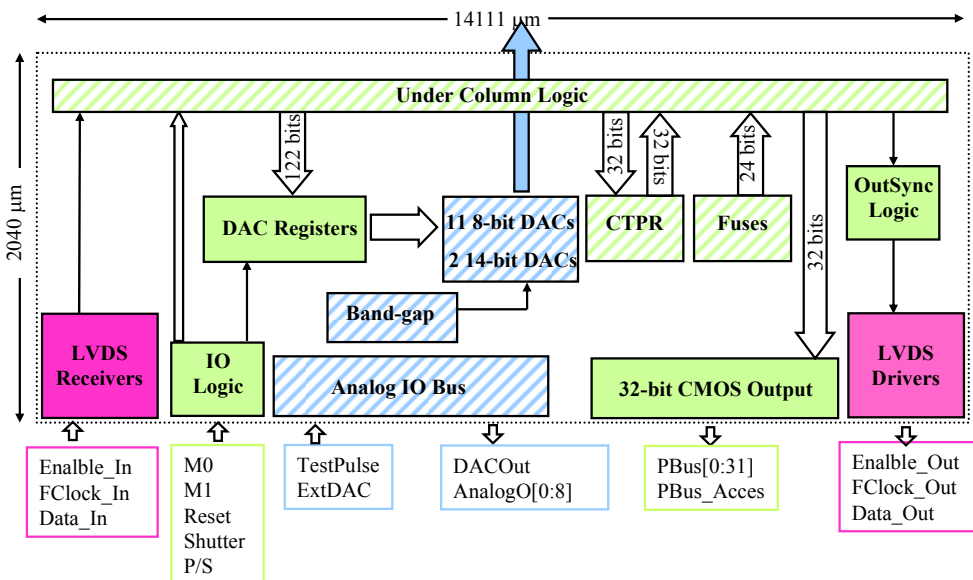


Figure 4.8. The *Mpix2MXR20* periphery floor plan. On blue the periphery blocks and IO lines using the analog power supply, on green the blocks and IO lines using digital power supply and on purple the blocks and IO lines using LVDS power supply. The dashed lines indicate the upgrades or new blocks compared to *Medipix2*.

#### 4.3.1 *Mpix2MXR20* DACs

The main design target for the new *Mpix2MXR20* DACs [BAL07] was the improvement of the stability of the DAC output values to temperature and DC power supply variations.

Temperature stability was achieved using an internal band-gap reference circuitry [KUI73] as a bias circuit to obtain a temperature stable voltage  $\sim 1.16V$ .

The output band-gap voltage ( $V_{bg}$  in Figure 4.9) shows measured temperature sensitivity of  $-0.22 \text{ mV}^{\circ}\text{C}$  and a power supply sensitivity of less than  $1 \text{ mV/V}$ . This DC voltage is converted into a temperature stable current to be copied in the array of current sources of each DAC, by means of an operational amplifier in a closed loop. A schematic of the circuit to obtain a temperature independent current source is shown in Figure 4.9.

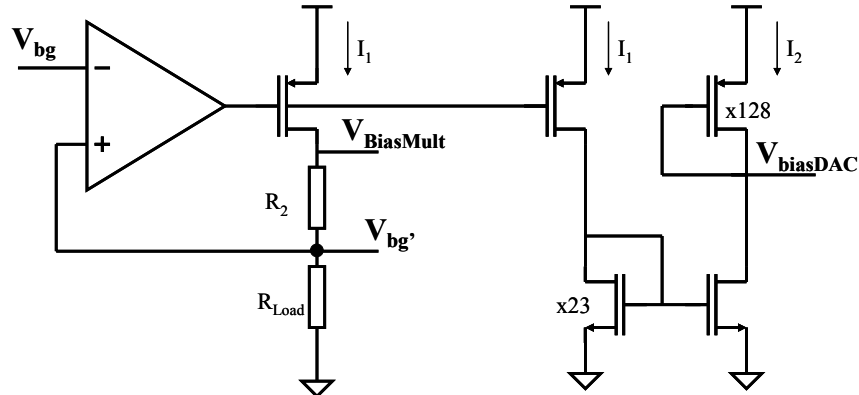


Figure 4.9. Circuit used to transform the temperature independent voltage ( $V_{bg}$  of  $1.16\text{V}$ ) into a temperature independent current to bias the DACs ( $I_2$  of  $40\text{nA}$ ).

The current source array has been implemented with  $2^N - 1$  transistors<sup>13</sup>, each delivering the LSB (least significant bit) current, in a binary-weighted current architecture as in *Medipix2*. In the new design dummy structures are responsible that the DAC current consumption keeps independent of the digital word.

The output stage of each DAC is either a transistor (a PMOS or a NMOS depending of the target current source) for linear current DACs or a polysilicon resistor for linear voltage DACs. There are two 14-bit voltage DACs for precise setting of the threshold and 11 8-bit current and voltage DACs. The 14-bit DACs are made of a high linearity 10-bit DAC (fine) and a 4-bit DAC (coarse) whose current outputs are summed into the same resistor to create the output voltage (see Figure 4.10). Table 4.1 summarizes the *Mpix2MXR20* DACs displaying type, number of bits and output range for each one.

---

<sup>13</sup> Where N is the DAC's number of bits.

	<b>DAC NAME</b>	<b>Type</b>	<b>Bits</b>	<b>DAC CODE</b>	<b>Range</b>
<b>CSA</b>	<i>I</i> Preamp	<i>I</i>	8	0111	0-2 $\mu A$
	<i>I</i> Ikrum	<i>I</i>	8	1111	0-40 nA
	<i>V</i> FBK	<i>V</i>	8	1010	0-2.2 V
	<i>V</i> GND	<i>V</i>	8	1101	0-2.2 V
<b>Discriminator</b>	<i>I</i> Disc	<i>I</i>	8	1011	0-1.67 $\mu A$
	<i>I</i> THS	<i>I</i>	8	0001	0-51.8 nA
	<i>V</i> THL	<i>V</i>	14	0110	0-2.2 V
	<i>V</i> THH	<i>V</i>	14	1100	0-2.2 V
<b>DDL</b>	<i>I</i> DelayN	<i>I</i>	8	1001	0-500 nA
<b>Analog Driver</b>	<i>I</i> BuffA	<i>I</i>	8	0011	0-10.2 $\mu A$
	<i>I</i> BuffB	<i>I</i>	8	0100	0-391 $\mu A$
<b>LVDS Driver</b>	<i>I</i> LVDS <sub>tx</sub>	<i>I</i>	8	0010	0-392 $\mu A$
	<i>V</i> RefLVDS <sub>tx</sub>	<i>V</i>	8	1110	0-817 mV

Table 4.1. MipxMXR20 DACs.

The output voltages of each DAC can be monitored through the output analog pad *DACOut* or externally forced through the input *ExtDAC* as in *Medipix2*. for debugging purposes three internal voltages from the band-gap biasing circuitry that can be monitored through *DACOut* as shown in Table 4.2.

<b>Internal Signal</b>	<b>DAC CODE</b>	<b>Expected Value</b>	<b>Signal description</b>
<i>BiasDAC</i>	0000	1.373 V	Voltage to be send to the gates of the transistors in the DAC array
<i>BiasOutStage</i>	0101	1.28 V	Voltage to bias the high swing output stage of some voltage DACs
<i>VbgOnChip</i>	1000	1.16 V	Internally generated reference voltage

Table 4.2. Internal nodes which can be monitored from the Band-gap biasing circuitry.

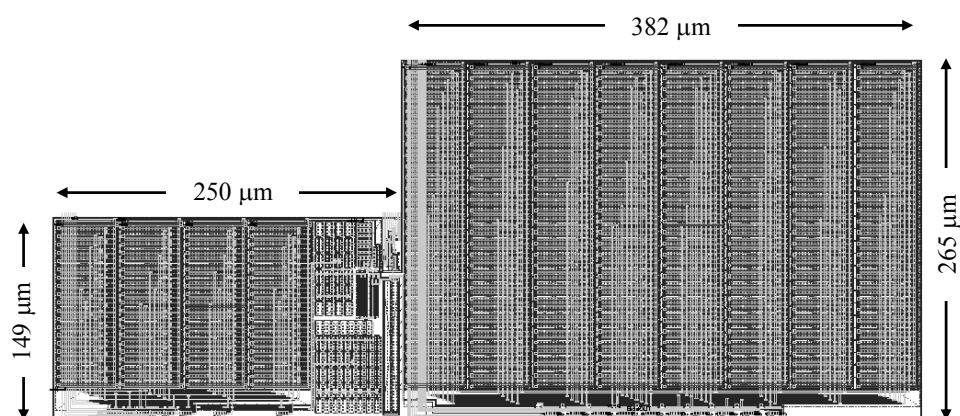


Figure 4.10. A 14-bit voltage DAC layout. On the left: the regular structure of an 8-bit DAC is used to create a 4-bit DAC (coarse) by grounding the less significant bits. On the right: current source array and output stage of the 10-bit DAC.

### 4.3.2 *Mpix2MXR20* test pulse architecture

The *Medipix2* test pulse could only be used to inject a badly defined input charge at the CSA input because of the gain variation of the analog buffers and the coupling of the calibration test pulse to the neighbouring circuitry. The *Mpix2MXR20* includes unitary gain buffers and a 32-bit register (CTPR) that selects individually the pixel columns to test.

#### 4.3.2.1 *Unitary gain analog buffers*

The analog buffers are used in several analog blocks of the chip: for the internal calibration test pulse, for the DACOut output, for the ExtDAC input and for the 9 special analog outputs. It is of great importance for global DAC and pixel calibration (linearity, noise and gain) that these buffers have a unitary gain, are fast, and can drive large capacitances.

The new analog buffers follow a Miller amplifier scheme [LAK94] made of a two-stage operational amplifier with a feedback capacitor. Figure 4.11 shows the simulated linearity and gain response of the analog buffer. The buffers show a unitary gain dynamic range of 1.8V and typical fall and rise times below 50 ns. The buffer biasing is controlled by means of two current DACs ( $I_{BuffA}$  and  $I_{BuffB}$ ). Each buffer can be switched off by means of a control signal applied to a multiplexer with the biasing lines as inputs.

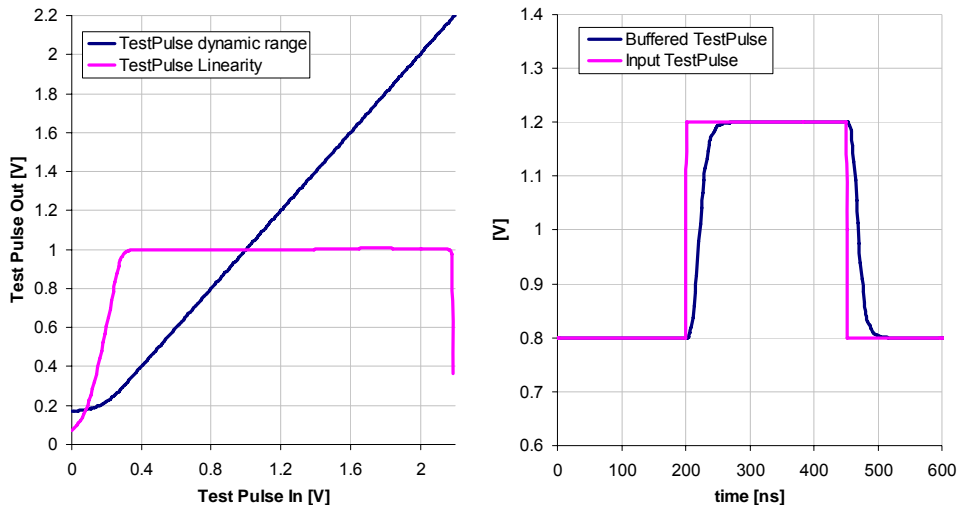


Figure 4.11. On the left simulated linearity and gain response of the unitary gain buffers. The unitary gain dynamic range extends from  $\sim 0.4$  to 2.2 V. On the right a simulation of the test pulse at the input and output of the buffer which is loaded with an extracted column equivalent impedance of  $3\text{ k}\Omega$  and  $3\text{ pF}$ . The symmetrical rise and fall time are below 50 ns for an input charge of 400 mV ( $20\text{ ke}^-$ ).

The voltage to charge conversion at the pixel input node can be found as:

$$Q_{test} = \Delta V_{in} [\text{Volts}] \cdot 50000 \text{ [e]} \quad (4.3)$$

#### 4.3.2.2 Column test pulse register (CTPR)

The *Medipix2* calibration voltage test pulse was sent to all the pixels simultaneously regardless of the number of pixels selected to be tested (Test bit active). The capacitance between the test pulse metal line and other neighbouring global lines (i.e global DACs, power supplies and digital control lines) was quite large inducing a measurable crosstalk between those global lines and the calibration test pulse bus. Therefore, whenever a calibration pulse was sent to the chip the resulting calibration measurements were imprecise (i.e. linearity, gain, noise).

The *Mpix2MXR20* includes a 32-bit register (CTPR) to select which columns are tested simultaneously. Every bit selects 8 columns distributed uniformly every 32 columns (i.e. if bit 0 is active then pixel columns 0, 32, 64, 96, 128, 160, 192 and 224 are selected). With this architecture the total coupling capacitance of the test pulse line can be reduced by a factor 32 if only one bit in the CTPR is selected. When all the CTPR bits are active the *Mpix2MXR20* has the same behaviour as the *Medipix2*. The CTPR is loaded simultaneously with the DACs at EoC [143:174].

#### 4.3.3 IO logic upgrade

The *Mpix2MXR20* IO logic architecture is very similar to the one in *Medipix2*. The main differences are:

- Longer row-counter (see Figure 2.34) to cope with the extra bit per pixel. The row-counter in *Mpix2MXR20* is  $256 \cdot 14 = 3584$  counts. The total chip memory is 917504 bits (7.1% larger than *Medipix2*).
- Sequential pixel matrix read out clock (*Read\_Clk*). In *Medipix2* the pixel matrix read out clock was generated simultaneously for all the columns generating error readouts due to digital power drops at frequencies higher than 90 MHz. In the new chip the clock sent to each column is offset by one clock pulse from its neighbour thus avoiding to clock all columns simultaneously with the attendant limitations. This new architecture puts less stress on the digital power supply as only one column at a time is active. The implementation of this architecture has required changes in the End-of-Column Logic (EoC) and in the IO Logic.
- Simplified operation modes (see Table 4.3). The Reset Matrix command is eliminated because the matrix can be reset by a dummy parallel or serial readout. At chip *Reset* the LVDS Drivers are not active, the 24 bit Chip ID is latched into the End-of-Column logic (EoC), the IO control

logic is reset to the initial condition, all DACS are set to the mid-range value and the 32-bit DOUT bus is in HiZ.

- Modified EoC and IO logic to either read the fuses or write CTPR simultaneously.
- The input data (Data\_In) to the *Mpix2MXR20* is latched at the rising edge of Fclock\_In while the output data from the *Mpix2MXR20* is set at the falling edge of the chip. The previous chip both input and output data were latched and set at the rising edge of Fclock. In multi-chip daisy chained structures the output clock had to be inverted for correct functioning.

<i>M0</i>	<i>M1</i>	<i>Enable_IN</i>	<i>P_S</i>	<i>Shutter</i>	<i>Reset</i>	<i>Operation</i>
<i>X</i>	<i>X</i>	<i>X</i>	<i>X</i>	<i>X</i>	0	General reset of the chip
<i>X</i>	<i>X</i>	<i>X</i>	<i>X</i>	0	1	Acquisition
0	0	0	0	1	1	Read out the matrix (Serial)
0	0	0	1	1	1	Read out the matrix (Parallel)
0	1	0	<i>X</i>	1	1	Write the matrix PCR
1	0	0	<i>X</i>	1	1	Write/Read EoC register

Table 4.3. *Mpix2MXR20* operation modes.

#### 4.3.4 Fuses

A laser-blown 24-bit register placed in the periphery identifies uniquely each *Mpix2MXR20* chip. The 24-bit register contains 12 bits to identify the wafer number, 4 bits for the in-wafer horizontal coordinate (X), 4 bits for the in-wafer vertical coordinate (Y), and 4 dummy bits (see Figure 4.12). After a chip reset (*RESET* pin is set low) the contents of the 24-bit register are loaded into the EoC[195:218] register and read out with the read EoC register command as indicated in Table 4.3.

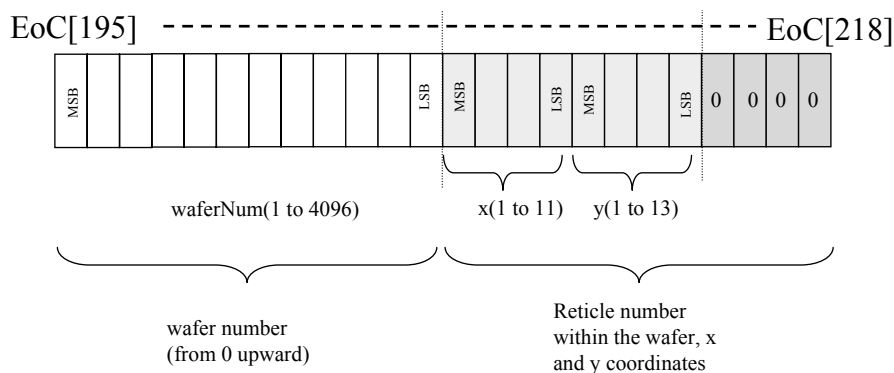


Figure 4.12. *Mpix2MXR20* fuses EoC register.

### 4.3.5 Other layout enhancements

For mechanical robustness the *Mpix2MXR20* bond pads have been enlarged as seen in Figure 4.13. Such a pad geometry provides better mechanical matching between the bond pad and the ultrasonic wedge-bonding tool and permits more aggressive (or repeated) probing.

New alignment marks used during the bump-bonding process are place at the bottom right and left of the chip.

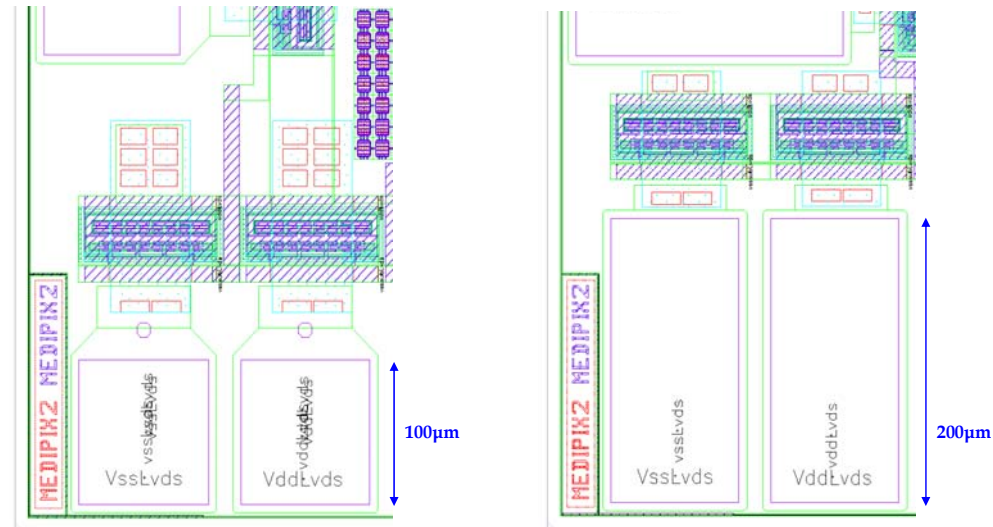


Figure 4.13. On the left the *Medipix2* bond pads and on the right the *Mpix2MXR20* bond pads. New pads are 100  $\mu\text{m}$  longer for wire bonding robustness.

## 4.4 ELECTRICAL CHARACTERIZATION

The *Mpix2MXR20* electrical characterization have been done at wafer level on the CERN probe station using the *Medipix2* probe card the Muros2.1 readout system and an upgraded version of the Medisoft4.1 program.

The *Mpix2MXR20* 8 inch wafers contain 107 dies. Figure 4.14 shows a typical *Mpix2MXR20* wafer map following the selection criteria described in Table 3.1. After testing of the first 30 wafers the achieved yield is ~62% if summing the categories A, B, and C.

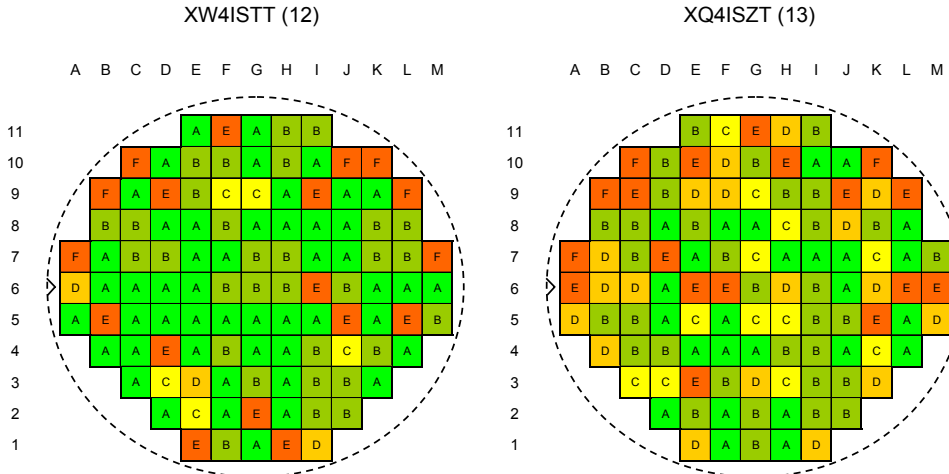


Figure 4.14. Two typical *Mpix2MXR20* wafer maps obtained after selection process. Each *Mpix2MXR20* wafer contains 107 dies.

#### 4.4.1 DAC Measurements

The *Mpix2MXR20* DACs can be monitored through the DACOut analog output. By scanning the full digital input range the transfer curve for each DAC is found. Figure 4.15 shows the eight 8-bit current DACs transfer curves, Figure 4.16 shows the three 8-bit voltage DACs transfer curves, and Figure 4.17 shows the two 14-bit threshold voltage DACs transfer curves of one chip.

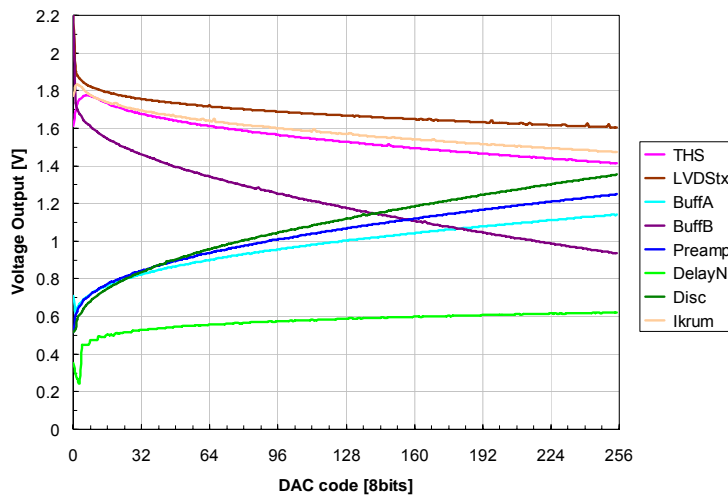


Figure 4.15. Measured Current DACs from chip G6 of wafer XX4ISST (23).

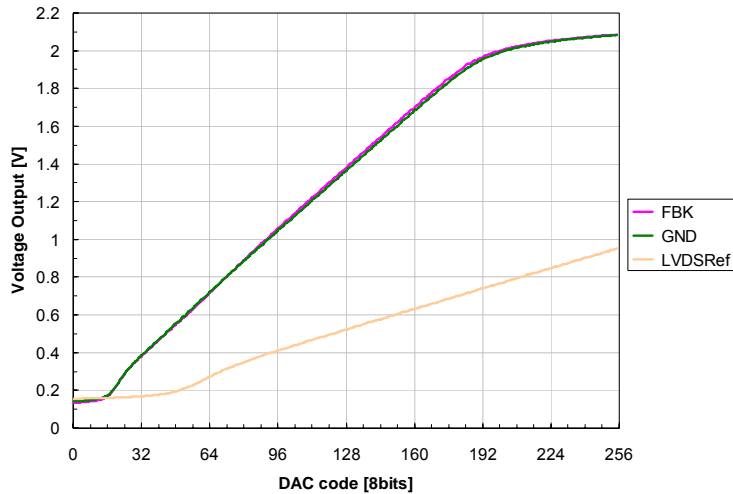


Figure 4.16. Measured voltage DACs from chip G6 of wafer XX4ISST (23).

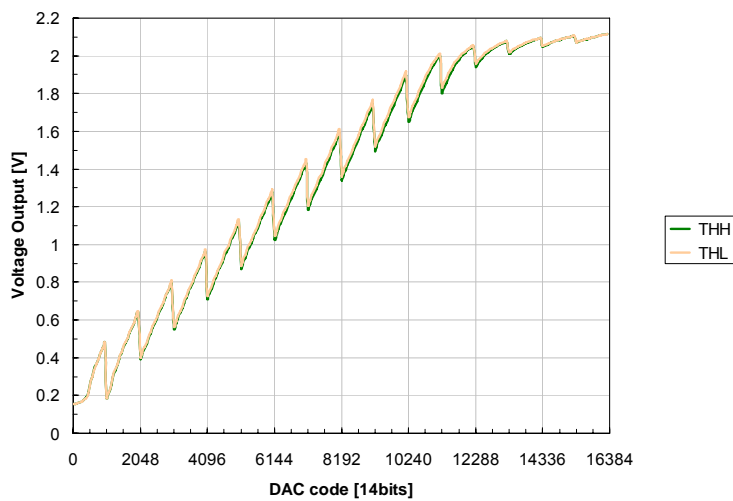


Figure 4.17. Measured threshold voltage DACs from chip G6 of wafer XX4ISST (23).

The INL and DNL of one threshold DAC is shown in Figure 4.18. The LSB is measured to be  $\sim 413 \mu\text{V}$  ( $38.6 \text{ e}^-$  with a gain  $\sim 10.7 \text{ mV/ke}^-$ ) as designed, with a measured INL for the full range of the 10-bit DAC below  $\pm 2$  LSB and DNL below  $\pm 1$  LSB. Compared to the *Medipix2* the INL and DNL are almost 25 times better in the new chip. The dynamic range of the 10-bit fine DAC is  $\sim 422 \text{ mV}$  this is energy  $\sim 45 \text{ ke}^-$ . To obtain a higher linear dynamic range either a full range calibration of the THL and THH DACs is realized, to overcome the mismatch introduced by the coarse 4-bit DAC, or the *EXTDAC* input is used.

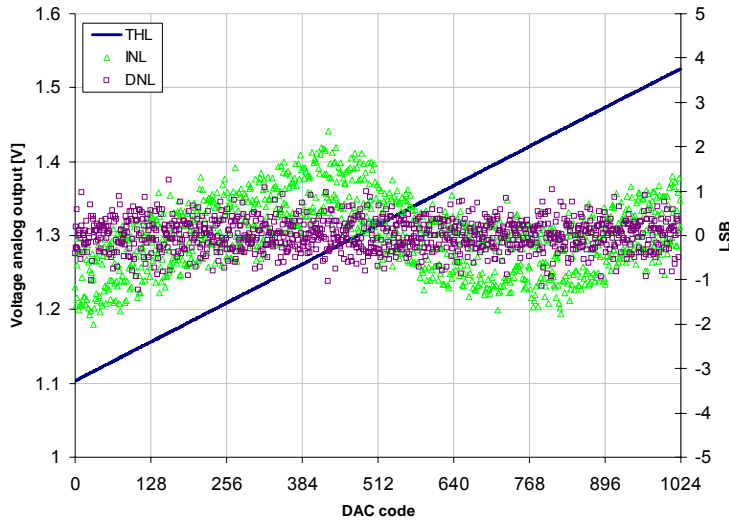


Figure 4.18. INL and DNL for the THL DAC of one *Mpix2MXR20* chip.

#### 4.4.2 Electrical characterization of the pixel

The *Mpix2MXR20* electrical characterization is realized using the injection test pulse circuitry. In order to get precise results only 8 pixels distributed uniformly in diagonal across the matrix are tested simultaneously to minimize the pixel to pixel crosstalk. Only 1 bit of the CTPR is active to reduce the test pulse coupling to the biasing lines. A fixed test pulse of 100 mV amplitude ( $\sim 5 \text{ ke}^-$ ) is used to characterize the analog pixel behaviour. Scanning the THL DAC over the test pulse and towards the DC noise floor the effective threshold, linearity, gain and noise can be extracted. The THL is set at half the test pulse height while 4000 test pulses are sent for each shutter opening. Figure 4.19 shows an example of such a measurement. The equivalent noise charge (ENC) and the effective threshold can be extracted by using the s-curve method described already in Paper II and Paper X. The gain can be calculated as the distance between the effective threshold and the noise floor. The linearity can be measured by consecutive scans at different injection input charge amplitudes.

The IPreamp and Ikrum DACs have been scanned in order to find the optimum operating conditions of the front-end chain.

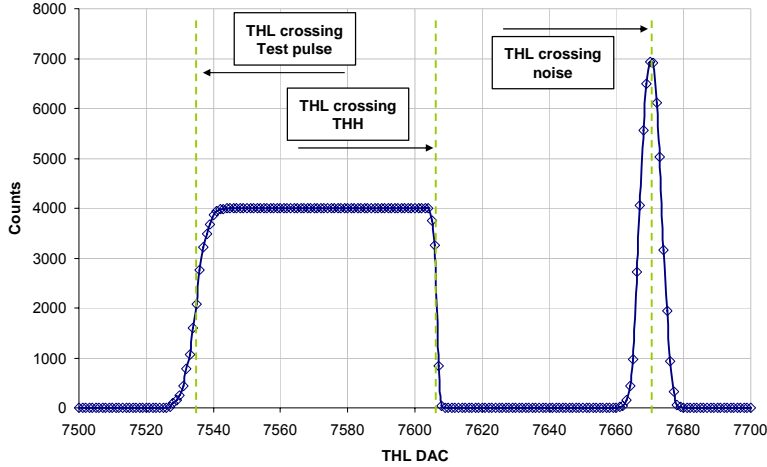


Figure 4.19. Pixel characterization using the injection test pulse. The noise, gain, effective threshold and linearity can be extracted for all pixels using this technique.

#### 4.4.2.1 Preamp DAC scan

Using the previous setup the Preamp DAC is scanned over its full range, from 0 (Ipreamp=0 $\mu$ A) up to 255 (Ipreamp=2 $\mu$ A) in 8 different pixels across the matrix. On the left of Figure 4.20 is shown the normalized gain and on the right the measured ENC. The effective gain is computed as the difference from the crossing of THL over the Test pulse to the THL crossing of the noise. The ENC is computed by measuring the slope of the THL crossing the test pulse while assuming an 8 fF injection test capacitance per pixel. The maximum gain and the minimum noise peaks between 140 and 170 which corresponds to preamplifier biasing current between 1.1 and 1.3  $\mu$ A.

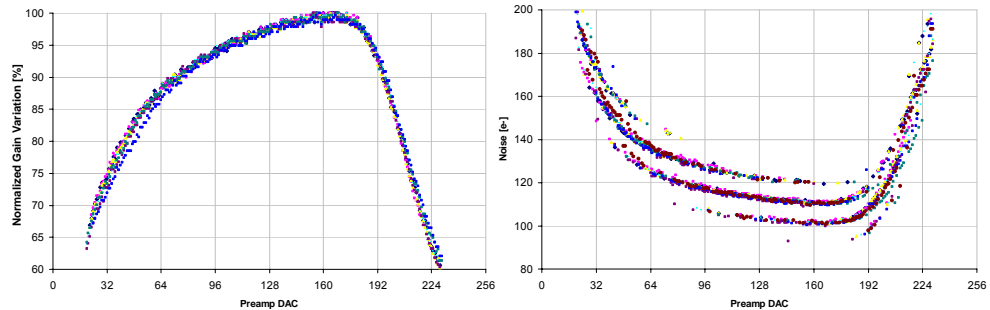
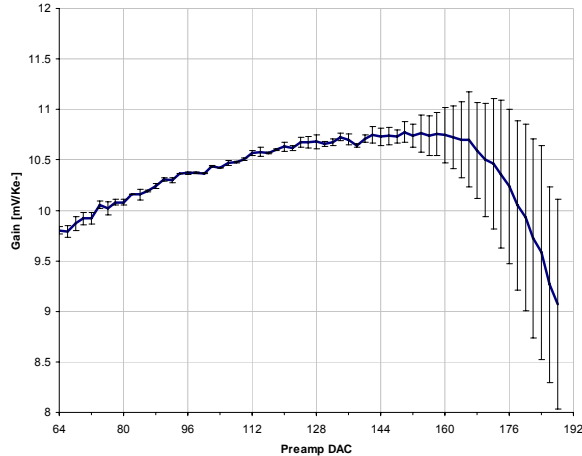


Figure 4.20. On the left: normalized gain variation versus IPreamp DAC. On the right: ENC assuming Ctest 8 fF. Measurements realized over 8 pixels from chip G6 of wafer XX4ISST(23). The ENC measurements show a non continuous curve due to quantization errors.

Figure 4.21 shows the mean and standard variation of the gain for the eight pixels across the matrix. Above Preamp DAC set tot 140 there is a big increase in

the pixel to pixel gain variation due to a top-down power supply voltage drop. This result fits with the static power distribution strategy discussed in section 2.3.3.1.



**Figure 4.21. Measured gain vs Preamp DAC with error bars showing the top-down pixel gain variation.**

Given the measured noise, gain and pixel to pixel variation the optimum working point of the Preamp DAC is set to the default value (i.e.  $I_{\text{preamp}} = 80\text{h}$ ) which results with a  $\text{ENC} \sim 110 \text{ e}^-$  and a pixel gain  $\sim 10.7 \text{ mV/ke}^-$ .

#### 4.4.2.2 Ikrum DAC scan

The Ikrum DAC was scanned over its full range, from 0 (Ikrum= 0nA) up to 255 (Ikrum= 40nA) in 8 different pixels across the matrix. On the left of Figure 4.22 is shown the normalized gain and on the right the ENC of the measured pixels for the studied Ikrum DAC range.

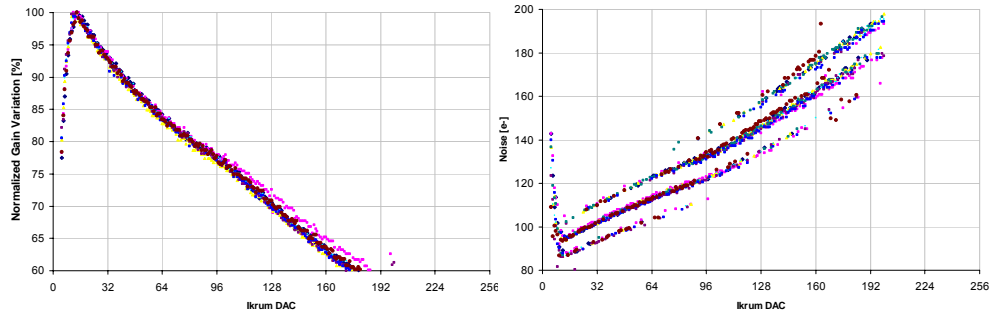


**Figure 4.22 On the left: normalized gain variation versus Ikrum DAC. On the right: ENC assuming Ctest 8FF. Measurements realized over 8 pixels from chip G6 of wafer XX4ISST(23). The ENC measurements show a non continuous curve due to quantization errors.**

The setting of the Ikrum biasing current determines the front-end gain as already shown in Figure 2.8. The pixel gain and ENC are optimal around  $\text{Ikrum}_{\text{DAC}}=10$  which corresponds to an Ikrum current of  $\sim 1.5 \text{ nA}$ . If Ikrum DAC is

below 10 the front end piles up, as shown on the right of Figure 2.9, since the return to zero is slower ( $>10 \mu\text{s}$ ) than the injection test pulse period for these measurements. As an optimum compromise between gain, noise and count rate (return to baseline) the Ikrum DAC default setting is set to 20 which corresponds to  $= 3 \text{ nA}$ .

#### 4.4.2.3 Pixel Linearity

The linearity is calculated by measuring the difference of the effective threshold and the noise floor for different injection input charges. To minimize the inter pixel coupling only 16 pixels uniformly distributed in diagonal across the matrix from bottom to top were used. The studied range was from 0 to  $20 \text{ ke}^-$  for both collection polarities. Figure 4.23 shows the measured data with a linear fit. The linearity is better than 99.9 % in the studied range. The slope in each polarity mode gives the gain of the front end analog chain. The measured gain slope corresponds to  $11.8 \text{ mV/ke}^-$  for electron collection and  $12.53 \text{ mV/ke}^-$  for hole collection. These measurements were done with lower Ikrum current ( $\text{Ikrum}_{\text{DAC}}=10$ ) which explains the higher gain obtained.

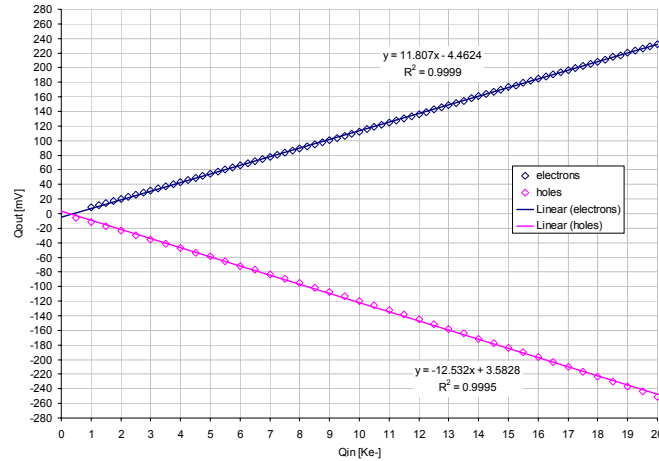
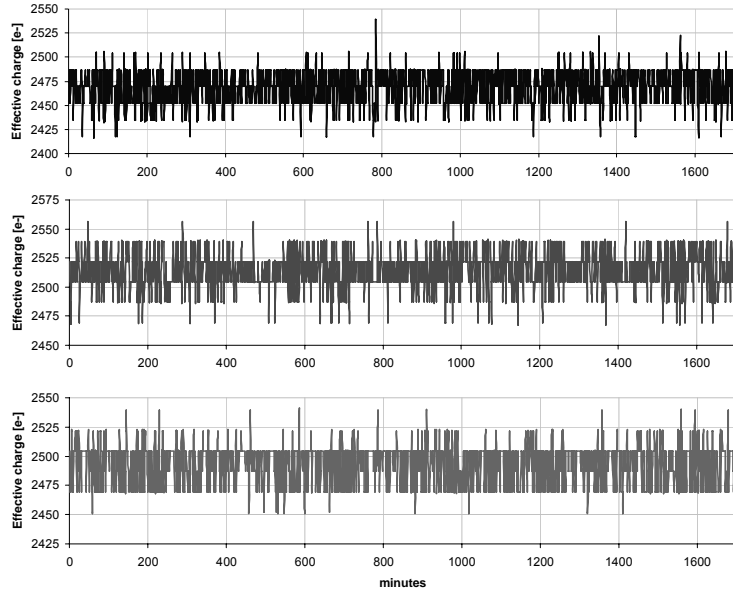


Figure 4.23. Test pulse linearity for both polarities with a linear fit in 16 pixels across the matrix.

#### 4.4.2.4 Long term stability

The threshold setting stability has been measured by repeating a threshold scan over a  $2.5 \text{ ke}^-$  equivalent injection test pulse every minute during 28 hours at room temperature for three different pixels. In Figure 4.24 the measured effective charge of three different pixels across the matrix is shown for the entire acquisition interval. The standard deviation during the full measurement time is below  $20 \text{ e}^-$  which is less than 1% of the injected charge.



**Figure 4.24.** Measured effective charge of 3 different pixels across the matrix during 28 consecutive hours. A new frame is taken every minute. Top: mean = 2469 e<sup>-</sup> and sigma=18.3 e<sup>-</sup>; Middle: mean = 2514 e<sup>-</sup> and sigma=16.5 e<sup>-</sup>; Bottom: mean = 2493 e<sup>-</sup> and sigma=17.1 e<sup>-</sup>;

#### 4.4.3 Low threshold equalization

Using the noise equalization procedure (see Paper X) the low threshold has been tuned. On Figure 4.25 an example of such equalization is shown with the threshold distributions before equalization with the 3-bit current DAC set to 111 and to 000. The threshold variation when all the bits are set to 000 (3-bit DAC on) is slightly bigger because of a top-down voltage drop at the 3-bit current DAC power supply. The width of the final distribution is exactly 1/7<sup>th</sup> of the adjustment range, this is, the distance between the 000-distribution and the 111-distribution. The final threshold variation is then:

$$\sigma_{adj} = \frac{LSB}{\sqrt{12}} \quad (4.4)$$

LSB is the 3-bit DAC current Least Significant Bit. The minimum detectable charge for all the pixels of the matrix can be estimated as:

$$MinDetectableQ = 6 \cdot \sqrt{ENC^2 + \sigma_{dist}^2} \quad (4.5)$$

The threshold variation before equalization is ~380 e<sup>-</sup> rms at code=111 and ~400 e<sup>-</sup> rms at code=000. Assuming ENC=110 e<sup>-</sup> rms (see 4.4.2) the minimum detectable charge before equalization is ~2400 e<sup>-</sup>. After equalization the achieved threshold variation is ~95e<sup>-</sup> rms and the minimum detectable charge is therefore ~900 e<sup>-</sup>.

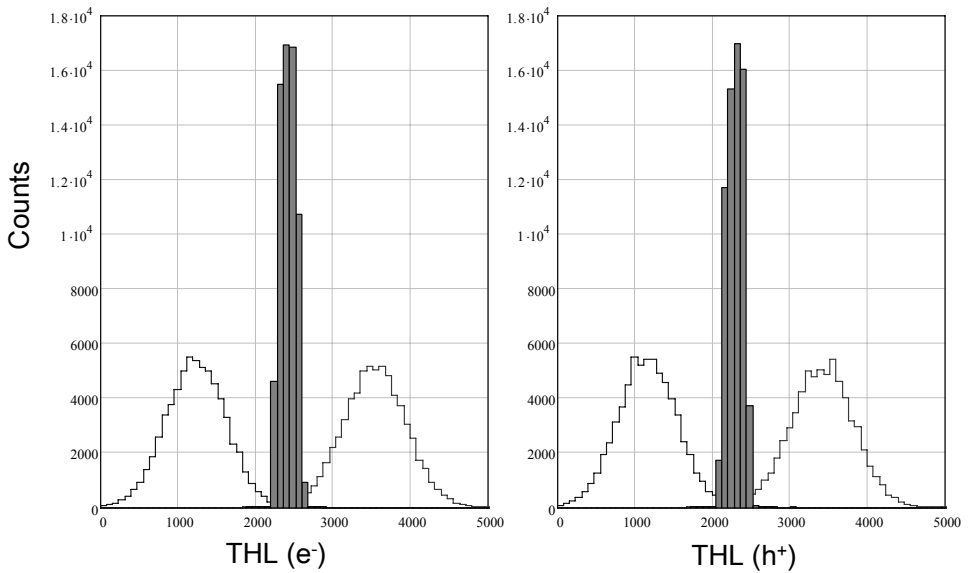


**Figure 4.25.** Low threshold equalization using the noise floor for both collection polarities. Before equalization (step traces) the threshold variation is  $\sim 400$  e for both polarities. After equalization (solid bar traces) the measured threshold variation is  $\sim 95$  e for both polarities. Chip used J2-W15.

Figure 4.26 shows the row average measured threshold before equalization (top with DAC code 111 and bottom with DAC code 000) and after equalization (middle curve). Figure 4.27 shows the linearity of the 3-bit threshold adjustment current DAC. To speed up the equalization process interpolation can be used due to the high DAC linearity.

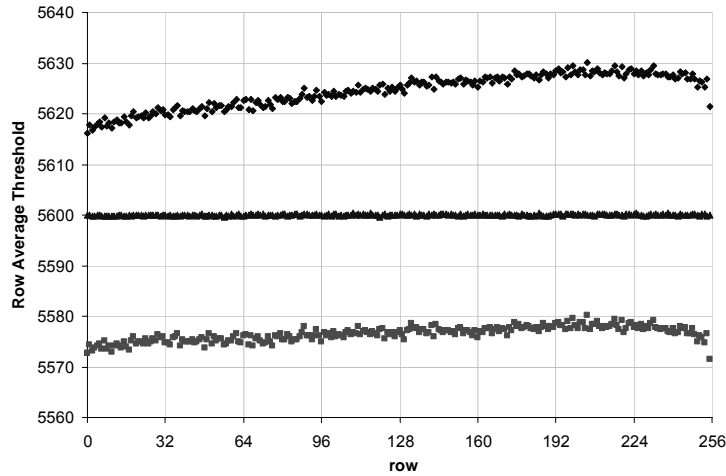


**Figure 4.26.** Row average threshold before (top and bottom curves) and after equalization (middle curve) for chip G6-W23.

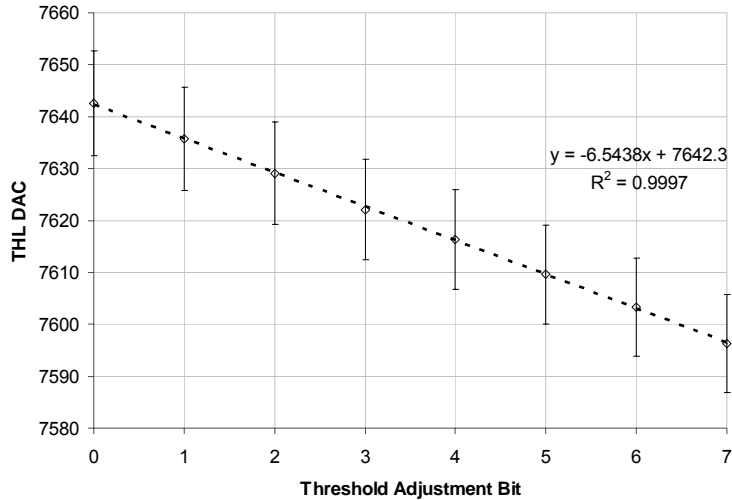


Figure 4.27. Threshold adjustment DAC linearity

#### 4.4.4 High threshold equalization

A method to equalize the high threshold eliminating the systematic errors from the injection test pulse is explained in paper VI. It uses the combination of two working modes of the double discriminator logic described in Table 2.2. Using a large enough injection test pulse, the THH is scanned through the already equalized low threshold from a region where there are no counts (window mode but the input charge is higher than the window range) until the THH crosses the THL (single threshold mode).

Using this method the effective energy window for each pixel is expected to be constant since the THH equalization takes as a reference the already calculated effective pixel low threshold. The resulting threshold distribution variations of such procedure are the convolution of the low threshold distribution after equalization with the high threshold distribution. The result is then the quadratic sum of the low and high threshold variation. On the left of Figure 4.28 is shown the result of a high threshold equalization where the adjusted uniform distribution is  $\sim 140$  e<sup>-</sup> rms. Knowing the low threshold distribution variation the non-convoluted high threshold distribution can be extracted as:

$$\sigma_{THH} = \sqrt{\sigma_{measured}^2 - \sigma_{THL}^2} \quad (4.6)$$

For the example of Figure 4.28 the  $\sigma_{THH} = 103$  e<sup>-</sup> rms if  $\sigma_{THL} = 95$  e<sup>-</sup> rms. On the right of Figure 4.28 is shown the comparison of the THH and THL equalization mask for the full chip as the histogram of the pixel code difference between the two masks. More than half of the pixels have the same equalization code for both masks showing that the one source of threshold mismatch is at the preamplifier

output which is shared for both discriminating branches, but also the local mismatch in each discriminator is also significant as it was seen in the design phase in section 2.3.1.3. This result also shows that a reasonable equalization mask for the THH can be obtained by copying the THL equalization.

The full chip minimum energy window is limited by the threshold dispersion. At a full chip level the best energy window achievable is  $\sim 900$  e $^-$ . At a pixel level the energy window is only limited by the local matching between both discriminators since the same input node is shared (i.e. the CSA output is DC coupled to the input of both discriminator branches). Furthermore, since the high threshold equalization uses as a reference the pixel low threshold the minimum energy window in each pixel is then the LSB of the 3-bit adjustment DAC. Paper VI reveals a measured minimum window of  $\sim 390$  e $^-$  for *Medipix2* which corresponds to the LSB of the pixel adjustment DAC.

#### 4.5 IMAGING WITH THE *MPIX2MXR20*

Given that the *Mpix2MXR20* has identical pixel size, and sensor material properties the imaging performances (i.e. MTF and DQE) with respect of the *Medipix2* are unchanged. Therefore, in this section only the overflow control and an absolute calibration using X-ray sources are presented.

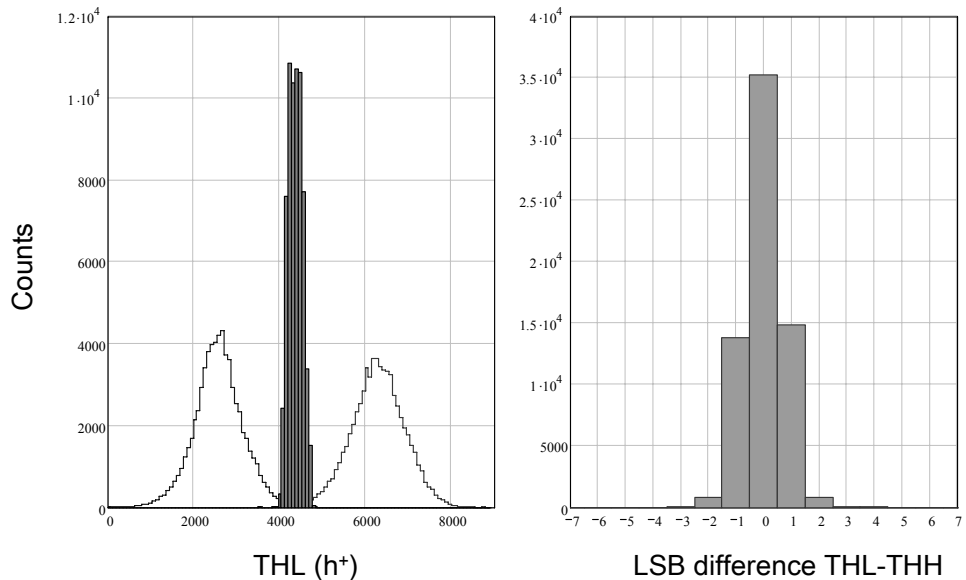


Figure 4.28. On the left: high threshold equalization distributions before (step traces) and after (solid bar trace) equalization. On the right the THL and THH equalization mask comparison.

##### 4.5.1 *Mpix2MXR20* overflow control

One of the new features of the new chip is the overflow control (section 4.2.3.1). Figure 4.29 shows an image taken with a  $\beta$ -source with 60 s exposure

time. As it is shown the pixel counter is stopped if the counter value exceeds 11810 counts.

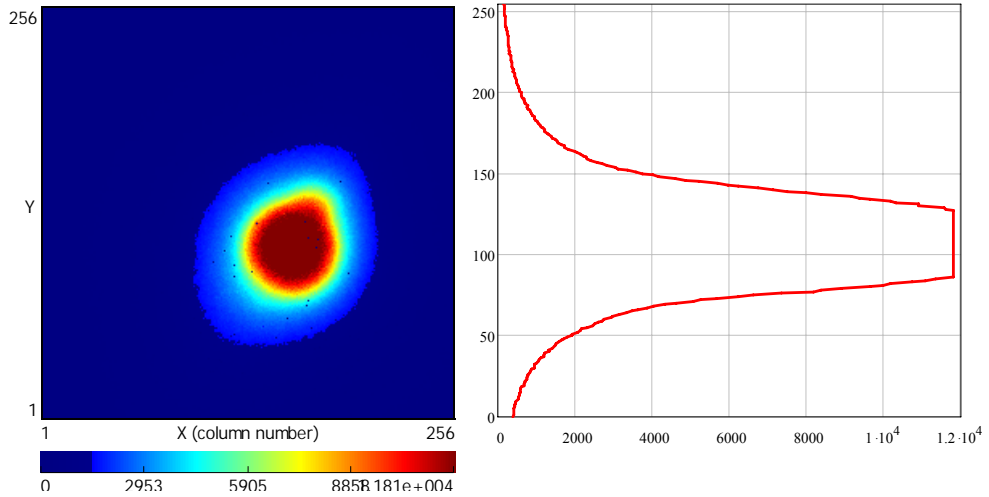


Figure 4.29. Image taken with a *Mpix2MXR20* bonded to a 300  $\mu\text{m}$  Si sensor of a  $^{90}\text{Sr}$   $\beta$ -source with 60 s exposure time. On the left the 2D image on the right the profile image. The pixel counter overflow control is stopped at 11810 counts.

#### 4.5.2 Absolute calibration

An absolute energy calibration of a single *Mpix2MXR20* bonded to a high resistivity 300  $\mu\text{m}$  Si sensor has been realized by scanning the threshold DAC over known X-ray sources and recording the effective threshold for each source. The K $\alpha$  and K $\beta$  fluorescence lines of several materials are excited by a X-ray tube at 50 kV. The materials used with its fluorescence lines are: Cd (23.1 / 26.1 keV), Pd (21.2 / 23.8 keV), In (24.2 / 27.3 keV), and Cu (8.05 / 8.9 keV). Figure 4.30 shows on the left the individual scans for each material and on the right the energy calibration plot obtained with the effective threshold of each fluorescence line. The measured gain slope is  $\sim$ 145 eV or  $\sim$ 40 e $^-$  per THL DAC<sup>14</sup> which is in agreement with the value reported in section 4.4.1 of  $\sim$ 38.6 e $^-$  per THL DAC step. As measured in 4.4.2.3 the linearity is better than 99.9 % in the studied energy range. The minimum detectable charge is  $\sim$ 3.8 keV or  $\sim$ 1050 e $^-$  for this setup.

---

<sup>14</sup> In Si the average energy per electron-hole pair at 300° K is 3.61.

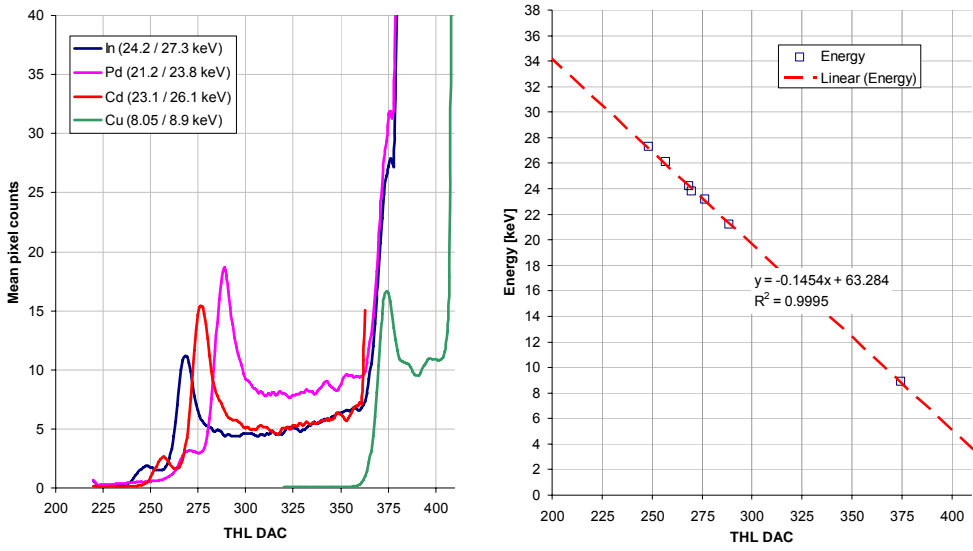


Figure 4.30. Energy calibration of a *Mpix2MXR20* bonded to a 300  $\mu\text{m}$  thick Si sensor. Several materials have been put in front of a X-ray tube in order to use the fluorescence lines  $\text{K}\alpha$  and  $\text{K}\beta$  as calibration references: Cd (23.1 / 26.1 keV) Pd (21.2 / 23.8 keV) In (24.2 / 27.3 keV) Cu (8.05 / 8.9 keV). The measured gain slope is  $\sim 145 \text{ eV per THL DAC step}$  and a minimum detectable energy of  $\sim 3.8 \text{ keV}$ .

#### 4.6 SUMMARY

The *Mpix2MXR20* is a successful redesign of the *Medipix2* with improved robustness and stability operation. The most important innovations on the new chip include: improved threshold dispersion, radiation tolerance enhancement, pixel overflow control logic, smaller threshold DAC LSB with improved linearity, unitary gain analog buffers, and 24-bit unique chip identification. Table 4.4 outlines the measured performance of the *Medipix2* and *Mpix2MXR20*.

	<i>Medipix2</i>	<i>Mpix2MXR20</i>
Measured pixel gain	$8.7 \text{ mV}/\text{k e}^-$	$10.7 \text{ mV}/\text{k e}^-$
Measured ENC	$\sim 167 \text{ e}^- \text{ rms}$	$\sim 110 \text{ e}^- \text{ rms}$
Radiation Hardness	$\sim 10 \text{ krad}$	$\sim 200 \text{ krad}$
Threshold dispersion before equalization	$\sim 450 \text{ e}^-$	$\sim 400 \text{ e}^- \text{ rms}$
Threshold dispersion after equalization	$\sim 120 \text{ e}^-$	$\sim 95 \text{ e}^- \text{ rms}$
Minimum detectable charge	$\sim 1100 \text{ e}^-$	$\sim 900 \text{ e}^-$
On-chip threshold DAC step	$\sim 1.9 \text{ mV or } \sim 218 \text{ e}^-$	$\sim 413 \mu\text{V or } \sim 40 \text{ e}^-$
On-chip threshold DAC INL over the full range	$< 9 \text{ LSB (1962 e}^-)$	$< 2 \text{ LSB (80 e}^-)$
Voltage DACs Temperature dependence	$1 \text{ mV/}^\circ\text{C}$	$60 \mu\text{V/}^\circ\text{C}$
Pixel counter depth-Overflow control	8001-No	11810-Yes
Maximum serial readout clock	$\sim 85 \text{ MHz}$	$\sim 180 \text{ MHz}$
Pixel static power consumption	$\sim 8 \mu\text{W}$	$\sim 8 \mu\text{W}$

Table 4.4. Comparison performance between the *Medipix2* and the *Mpix2MXR20*

## 5 TIMEPIX

Following the successful results using the *Medipix2* and *Mpix2MXR20* for the readout of electrons inside gas volumes (section 5.1), a new collaboration was formed to modify the *Mpix2MXR20* to provide arrival time information in each pixel with a time resolution of 10 ns. The new chip is called *Timepix*. Sections 5.2 and 5.3 describes the architecture and functional behaviour of the chip. Electrical characterisation results are explained in section 5.4 while first images using gas detectors are shown in section 5.5. Recently the first Timepix bump-bonded to a 300  $\mu\text{m}$  thick high resistivity Si have become available. An absolute calibration using X-ray sources is described in section 5.6.

### 5.1 GASEOUS DETECTORS: PIXEL AS A DIRECT ANODE

The *Medipix2* and *Mpix2MXR20* chips have shown great potential in different applications requiring single photon counting approach. Successful tests using the chips for the readout of a TPC<sup>15</sup> prototype for the ILC<sup>16</sup> showed very promising results when coupled to Gas Electron Multipliers (GEM) or Micromegas gain grids (papers VIII and IX). Although these experiments demonstrated that single primary electrons could be detected, the chip did not provide information on the arrival time of the electron in the sensitive gas volume nor on the quantity of charge deposited.

The *Timepix* chip is an evolution from the *Mpix2MXR20* chip which allows for measurement of arrival time, “time-over-threshold” (TOT) and/or event counting independently in each pixel. An external reference clock (*Ref\_Clk*) is used to generate the clock in each pixel that increments the counter depending in the selected operation mode with a maximum frequency of 100 MHz. The chip has the same dimensions readout architecture and floor plan as the *Mpix2MXR20* chip allowing almost full backward compatibility with all the existing *Medipix2* readout systems (see section 3.1).

### 5.2 TIMEPIX PIXEL CELL

Figure 5.1 shows the schematic of the *Timepix* pixel cell. Although the cell clearly resembles the *Mpix2MXR20* pixel (see Figure 4.1) it has three main differences:

- There is a single threshold with one 4-bit threshold adjustment DAC.
- Each pixel can be configured independently in three different operation modes (arrival time, TOT and event counting) through the configuration bits P0 and P1.

---

<sup>15</sup> TPC stands for Time Projection Chamber

<sup>16</sup> International Linear Collider. More information in <http://www.linearcollider.org>

- In acquisition mode (*Shutter* low) there is a counting clock (*Ref\_Clk*) distributed to the entire pixel matrix which is synchronised with the discriminator output (*HIT*) in the *Timepix Synchronization Logic* (TSL).

The pixel is divided into two large blocks: the analog side formed by the CSA, the discriminator (with polarity control pin) and 4 bit threshold adjustment, and the digital side formed by the *Timepix Synchronization Logic* (TSL), the 14-bit shift register, the overflow control logic, the *Ref\_Clk* pixel buffer and an 8-bit Pixel Configuration Register (PCR). The PCR contains 4 bits for the pixel threshold equalization, 1 bit for Masking (*MaskBit*), 1 bit for enabling the test pulse input (*TestBit*) and 2 bits for selecting the pixel operation mode (P0 and P1). The pixel cell area is  $55 \times 55 \mu\text{m}^2$  and contains  $\sim 550$  transistors. The static power consumption is  $\sim 6.5 \mu\text{W}$  in the analog side and  $\sim 7 \mu\text{W}$  in the digital side (in acquisition state and *Ref\_Clk*=80 MHz) at VDDA and VDD equals to 2.2 V.

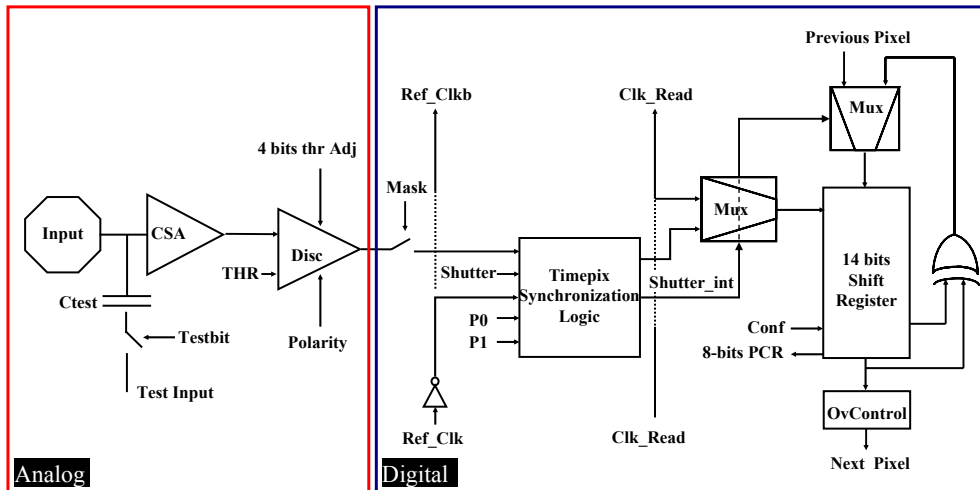


Figure 5.1. The *Timepix* pixel cell.

### 5.2.1 Modifications to the analog side of the pixel

Large electric fields are used to drift and amplify primary electrons converted in gas volumes towards the pixel readout anode. Typical fields, between the readout chip and the first layer of amplification, can range from 200 to 7000 V/mm depending on the gas mixture and type of gain grid (see paper VIII). The discharge probability towards the readout chip increases with the electrical field. The total charge collected in each pixel input pad is proportional to the electrical field. Therefore, a strong requirement for the *Timepix* front-end has been the reduction of chip minimum detectable charge limit. In order to achieve a lower minimum threshold the CSA and the discriminator have been slightly modified with respect to *Mpix2MXR20*.

### 5.2.1.1 Changes in the CSA

The pixel CSA includes a cascode in the transconductance amplifier which helps to reduce the total CSA input capacitance due to better isolation of the NMOS input transistors. The biasing of the cascode is controlled by a global 8-bit voltage DAC ( $V_{cas}$ ). The addition of the cascode pair has several implications in the behaviour of the CSA:

- The CSA output gain is improved as shown in Figure 5.2. The simulated gain for the same bias settings as the *Mpix2MXR20* is  $\sim 30\%$ . At the default bias conditions (i.e.  $I_{kruum}=10 \text{ nA}$  and  $I_{preamp}=1 \mu\text{A}$ ) the simulated gain is  $14.5 \text{ mV/ke}^-$ .
- The linear output voltage dynamic range is reduced compared to *MpixMXR20* and *Medipix2* chips, due to the gain increase. The simulated dynamic range shown in Figure 5.3 is  $\sim 55 \text{ ke}^-$ .
- The Signal to Noise Ratio (SNR) is improved due to the increment of the differential pair output resistance and the reduction of the input capacitance. The ENC has been calculated using an analog simulator as explained in section 2.3.1.1. The simulation uses the extracted parasitic capacitances of the full analog front-end. The simulated ENC is shown in Figure 5.4 for different bias conditions. At default settings the predicted ENC is  $\sim 70 \text{ e}^- \text{ rms}$ .
- Faster peaking time of the CSA output due to the reduction of the input capacitance as shown already in equation 2.2. Figure 5.5 shows the simulated peaking time at the CSA output compared with the *Medipix2* CSA. Faster rise times are important in *Timepix* in order to minimize the time-walk<sup>17</sup> in arrival time mode.

---

<sup>17</sup> The time-walk is defined as the time difference between an input charge which is  $1 \text{ ke}^-$  over threshold to an infinite input charge.

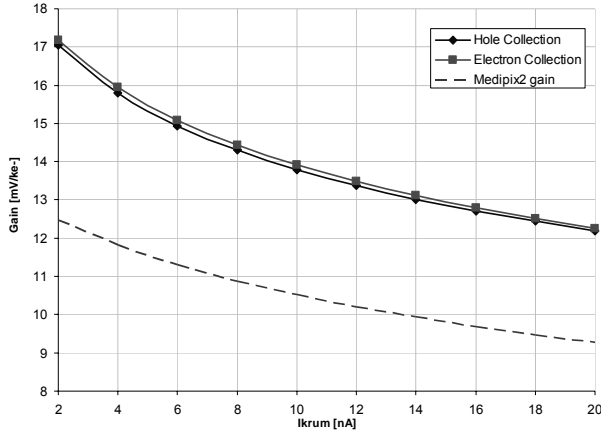


Figure 5.2. *Timepix* simulated CSA output gain versus Ikrum. The addition of the cascode in the differential pair of the preamplifier improves the gain by ~30% in both polarities. The dotted curve corresponds to the *Medipix2* gain shown in Figure 2.8.

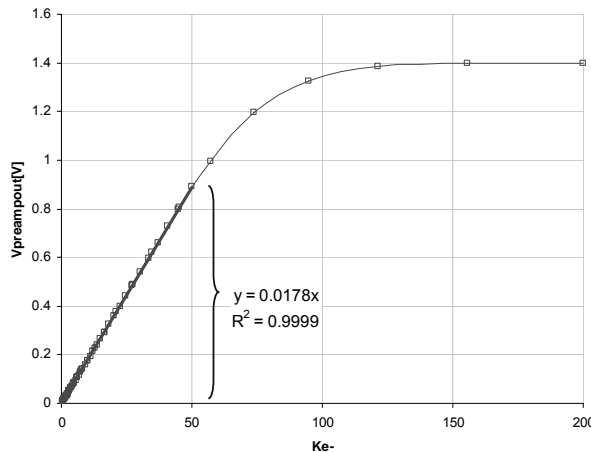


Figure 5.3. Preamplifier voltage output linearity and dynamic range versus input charge.

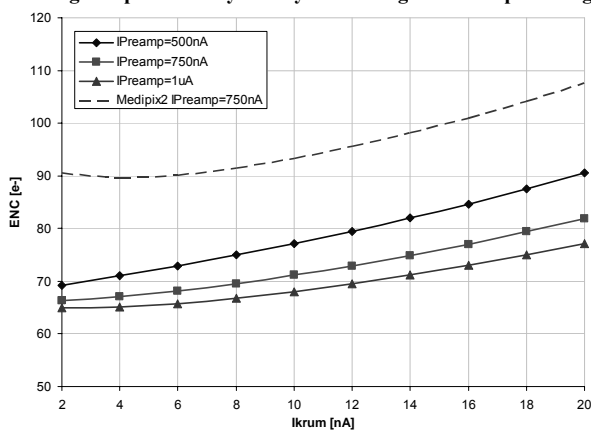
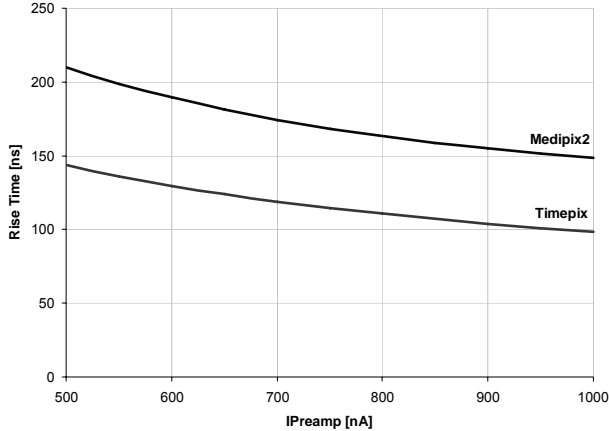


Figure 5.4. *Timepix* simulated CSA output ENC versus Ikrum and Ipreamp. The dotted curve corresponds to the *Medipix2* ENC for Ipreamp=750nA shown in Figure 2.12.



**Figure 5.5.** Simulated peaking time of the CSA output pulse. The cascode in the preamplifier reduces the CSA input capacitance and reducing the rise time for the same bias conditions as for *Medipix2* and *Mpix2MXR20*.

Table 5.1 summarizes the main characteristics of the CSA. The CSA output mismatch is lower than in the *Mpix2MXR20* for the same bias conditions and transistor dimensions due to the CSA gain increase.

<i>Preamplifier Gain</i>	$\sim 14.5 \text{ mV/ke-} [\text{h+}/\text{e-}]$ (see Figure 5.2)
<i>Peaking time</i>	$\sim 100 \text{ ns}$
<i>Dynamic Range</i>	$\pm 55 \text{ ke-}$
<i>Linearity</i>	$>99.9\%$ (Figure 5.3)
<i>Dead Time</i>	$<1 \mu\text{s}$ if $Q_{in} < 10 \text{ ke-}$
<i>Leakage current compensation</i>	Electron collection: -10 to 0 nA/pixel (-330 to 0 $\mu\text{A/cm}^2$ ) Holes collection: 0 to $\sim 20$ nA/pixel (0 to $\sim 660 \mu\text{A/mm}^2$ )
<i>Output Noise</i>	$\sim 70 \text{ e- rms}$
<i>Output mismatch</i>	$\sim 150 \text{ e- rms}$ (see equation 4.2)

**Table 5.1.** *Timepix* CSA summary table. All values given are simulations and they should be used as a trend

### 5.2.1.2 Changes in the discriminator

Figure 5.6 shows a schematic view of the *Timepix* discriminator. The main building blocks are: a multiplexer stage controlled by the Polarity pin, a OTA amplifier, one 4-bit current DAC for threshold adjustment, a zero crossing circuitry ( $Z_x$ ), and a hysteresis compensation circuitry. The OTA and the zero crossing circuitry are very similar to the ones implemented in *Mpix2MXR20* and will not be described again.

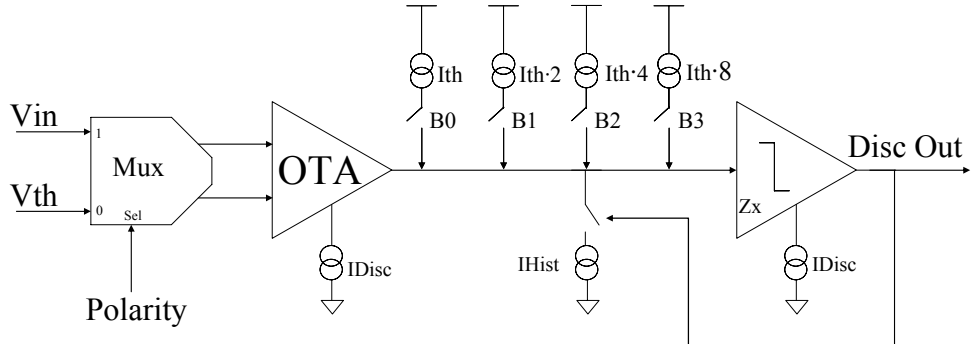


**Figure 5.6. Discriminator block diagram**

The hysteresis circuitry is used to eliminate high frequency pulses at the discriminator output that might upset the following logic. The multiplexer ensures that the Zx works always in the same polarity allowing the hysteresis circuitry to work independently of the sign of the input charge. This is achieved by changing the differential inputs of the OTA appropriately. At the rising edge of the Zx output a switch opens a diode transistor which is controlled by a global 8-bit current DAC ( $I_{Hist}$ ). When this switch turns on a negative current is added at the Zx input current generating a hysteresis effect. The discriminator hysteresis can be easily turned off by reducing the  $I_{Hist}$  current to zero by setting the  $I_{Hist}$  DAC to 00h.

With only one discriminator per pixel it has been possible to add a forth equalization bit due to the extra area and power available. The discriminator layout area is  $55 \mu\text{m} \times 9 \mu\text{m}$ . The power consumption is  $\sim 3.3 \mu\text{A}$  at  $V_{DDA}=2.2 \text{ V}$ .

### 5.2.2 Modifications of the digital side of the pixel

The extra area gained by having only one discriminator is used to fit much more complex pixel logic than in the previous chips. The *Mpix2MXR20* SR/C block diagram shown in Figure 4.6 is almost the same for *Timepix*. The same 14-bit counter with a dynamic range of 11810 counts and the overflow control logic are employed. The global *Shutter* is synchronized with the counting clock (*Ref\_Clk*) by the *Timepix Synchronization Logic* (*TSL*) resulting in a glitch-free internal shutter for each pixel.

During acquisition (*Shutter* low) the *Timepix Synchronization Logic* (*TSL*) controls the output of the discriminator (Hit), the operating mode selected (through P0 and P1), the opening and closing of the *Shutter*, and the counting clock (*Ref\_Clk*) used to increment the 14-bit counter. The pixel operating mode is controlled by bits P0 and P1:

- *Event counting mode* (P0=0 and P1=0): Each event above threshold increments the counter by 1. In this mode the counting pulse, which pulse width is half of the *Ref\_Clk* period, is generated at the beginning of Hit signal. With such design the dead time is only limited by the pulse

shape of the CSA improving the pixel maximum count rate compared to the previous designs (section 2.3.2.1).

- *TOT mode* ( $P0=1$  and  $P1=0$ ): The counter is incremented continuously as long as the output of the CSA is above threshold. The CSA resistive feedback loop produces a CSA output pulse width which is linear with the input charge, as already shown on the left of Figure 2.9, if the input charge is above  $\sim 3 \text{ ke}^-$ . In this mode the time-over-threshold is counted revealing the charge information of the input charge.
- *Arrival Time mode* ( $P0=1$  and  $P1=1$ ): The counter is incremented from the moment the discriminator is first activated until the global *Shutter* signal goes high. The dynamic range of the 14-bit counter limits the time interval that can be measured without saturation. With a 50 MHz clock the maximum time interval each pixel can measure is up to  $23.62 \mu\text{s}$ .

### 5.2.2.1 Timepix synchronization logic (TSL)

Figure 5.7 shows the schematic of the TSL. The output from the discriminator (HIT) is buffered and gated with the pixel *Maskbit*. The TSL control logic generates two positive output pulses if *Shutter* is opened: P-Shutter from the first HIT until the closing of the *Shutter*, and P-HIT for every HIT signal. The P-Shutter signal is used in arrival time mode while the P-HIT signal is used in TOT and event counting modes. These two signals are multiplexed at the input of the TSL core by  $P1$ . The TSL core includes two concatenated state machines: the first stage generates the TOT and arrival time output, and the second stage generates the event counting output from the output of the first stage. The TSL core is designed with an asynchronous network with S-R Flip-flops with race-free state assignment. The design requirements for this logic are:

- No glitches to avoid counter upsets.
- Logic only active when a *Hit* is present in order to reduce the digital power consumption.
- Controlled initialization through common line *Conf*.
- Minimum area.

The TSL core generates three outputs: one internal shutter which is synchronized with *Ref\_Clk* (*SyncShutter*), and one output for each state machine (*TOT/Time* and *Medipix*) which are multiplexed by  $P0$  to generate the counting clock (*ClkCounter*). Figure 5.8 shows an analog simulation of the Timepix front-end with the TSL for a pixel programmed in TOT (on the right) and in arrival time mode (on the left).

The buffering and distribution of *Ref\_Clk* is done by means of a minimum-sized transistor placed in the TSL logic (see section 5.2.4). The TSL is realized with 128 minimum-sized transistors. The layout area is  $18 \mu\text{m} \times 31 \mu\text{m}$ .

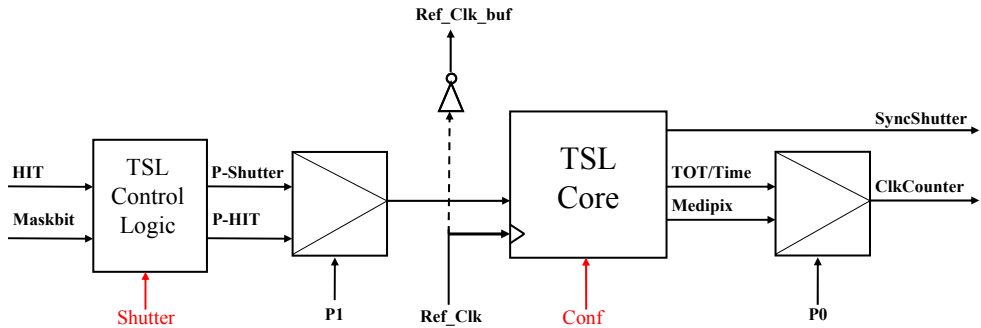


Figure 5.7. The TSL schematic. In red are displayed the global signals applied to all pixels simultaneously and in black the internal lines in each pixel.

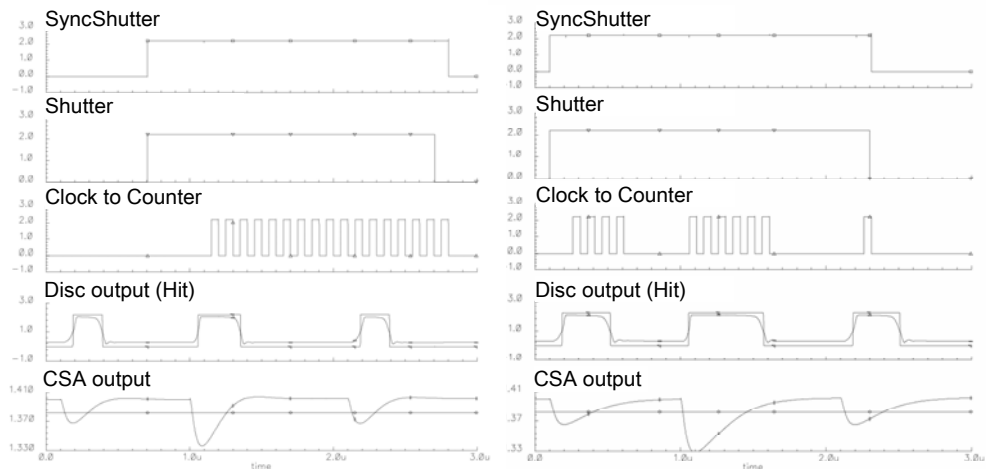


Figure 5.8. Simulated output of a pixel configured in arrival time mode (left) and in TOT mode (right).

### 5.2.2.2 Timepix Pixel Configuration Register (PCR)

The SR/C blocks of *Mpix2MXR20* and *Timepix* are almost identical. The 8 bits for the PCR are tapped from a different flip-flop outputs in the 14-bit shift register as shown in Figure 5.9.

b0	b1	b2	b3	b4	b5	b6	b7	b8	b9	b10	b11	b12	b13	Test Bit
X	X	X	X	X	X	P1	Mask	Thr Bit 0	P0	Thr Bit 2	Thr Bit 3	Thr Bit 1		

Figure 5.9. *Timepix* PCR is formed by latching 8 bits of the 14-bit shift register.

### 5.2.3 Pixel Layout

The *Timepix* pixel floor plan is very similar to the two previous pixels cells. The *Timepix* analog side occupies  $\sim 7\%$  less area due to the suppression of on discriminator branch compared to *Mpix2MXR20*. The saved area is used to fit the TSL in the digital side. The pixel layout is shown in Figure 5.10.

The analog power distribution has been recalculated. As seen in 2.3.3.1, the power distribution strategy is focused in splitting the power in the most efficient way in order to minimize gain and threshold mismatch between channels. The increased functionality of the pixel demands a different power distribution strategy. In TOT mode the return to zero (Ikrum DAC) pixel to pixel variation needs better matching to achieve uniform charge measurements across the pixel matrix. In arrival time mode the peaking time matching is important in order to have uniform time-walk (i.e. CSA output rise time) in all pixels. Table 5.2 summarizes the analog power distribution where special layout effort has been added in order to enlarge *Vdda\_Ikrum* and *Vssa\_Preampl* while keeping the rest of the power lines original widths. The larger power drops are located in the differential pair loads of the transconductance amplifiers where the  $V_{GS}$  variations do not limit the pixel to pixel performance.

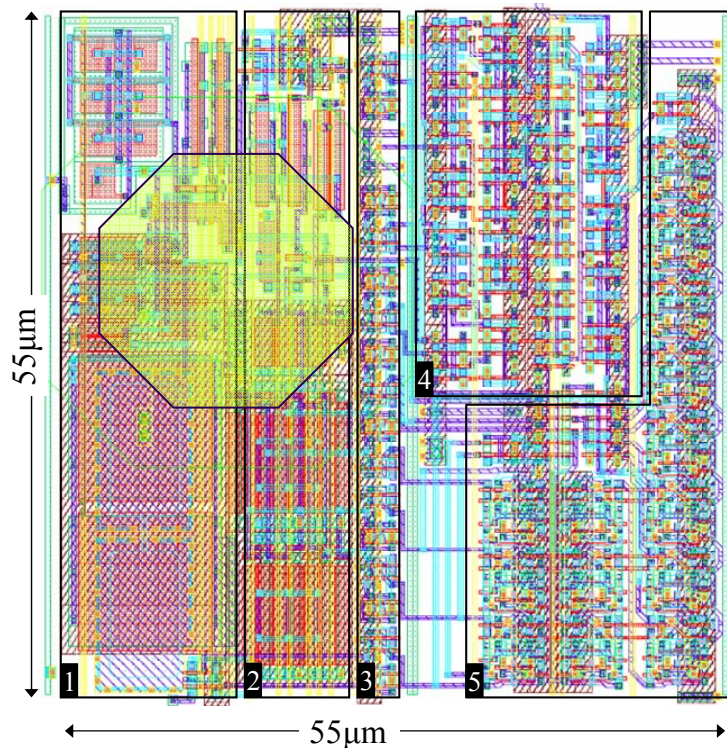


Figure 5.10. *Timepix* pixel cell layout: 1) CSA, 2) Discriminator with 4-bit threshold equalization, 3) 8-bit PCR, 4) *Ref\_Clk* buffer and TSL and 5) 14-bit shift register and overflow control.

<b>Power line</b>	<b>Nominal Current</b>	<b>Voltage drop [mV]</b>	<b>Metal width [<math>\mu\text{m}</math>]</b>
<i>Vdda_Preamp</i>	$1 \mu\text{A}$	50	2.8 (M4)
<i>Vssa_Preamp</i>	$1 \mu\text{A}$	9	14.7 (M5+LM)
<i>Vdda_Ikrum</i>	$15 \text{nA}$	3.5	0.6 (M4)
<i>Vssa_Ikrum</i>	$15 \text{nA}$	1	2 (M4)
<i>Vdda_Disc</i>	$1.5 \mu\text{A}$	62	3.4 (M4)
<i>Vssa_Disc</i>	$1.5 \mu\text{A}$	13.3	16 (M5+LM)
<i>Vdda_THS</i>	$300 \text{nA}$	4.6	9.22 (M4)
<i>Vssa_Hyst</i>	$200 \text{nA}$	14	2 (M5)

Table 5.2. *Timepix* metal widths for the different static analog power supplies.

### 5.2.4 The reference counting clock (*Ref\_Clk*)

An externally generated tunable clock reference (*Ref\_Clk*) is used as counting clock. *Ref\_Clk* is distributed throughout the pixel matrix in acquisition mode. As shown in Figure 5.7 each pixel includes a minimum-sized inverter to buffer the *Ref\_Clk* to the next pixel up in the column. With such a strategy the digital power supply shows a static behaviour since the *Ref\_Clk* phase changes every two pixels and the switching time is retarded by the propagation delay of the inverter (~195 ps). Furthermore, to minimize the digital coupling and to uniformly distribute the digital power, the *Ref\_Clk* phase is alternated between columns. As shown in Figure 5.11 after the *Ref\_Clk* is propagated to all the pixels, in ~50 ns, the power supply has a static behavior.

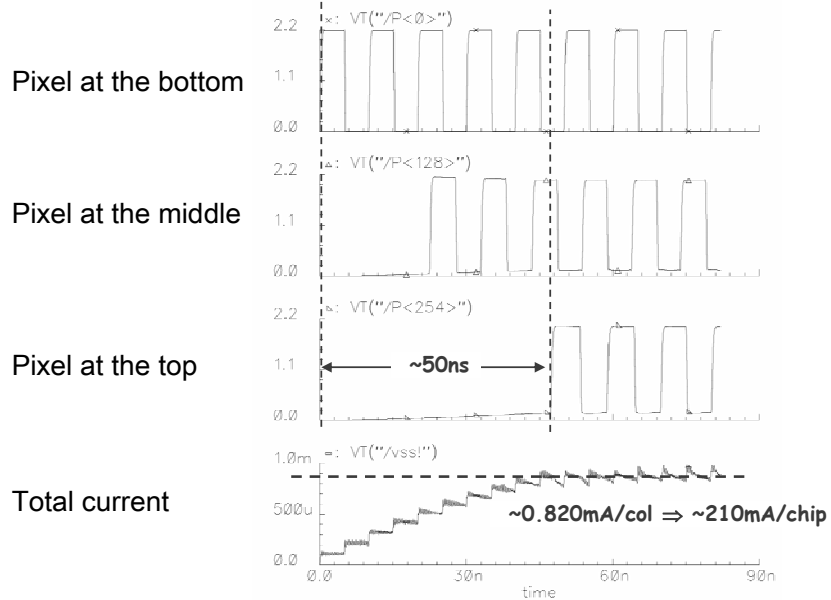


Figure 5.11. Digital power distribution simulation on a column of pixels during *Ref\_Clk* startup taking into account the parasitic capacitances and stray resistance at *Ref\_Clk*=100 MHz. Once the *Ref\_Clk* is fully propagated to all the column (~ 50 ns) the digital power consumption is quasi-static. This effect reduces the coupling to neighboring analog lines.

The disadvantage of this approach is the increase of digital power consumption in acquisition mode compared with the previous chips. It can be found out that power consumption is proportional to the *Ref\_Clk* frequency:

$$I \cong 2 \cdot f_{\text{Ref\_Clk}} \text{ [mA]} \quad (5.1)$$

Where  $f_{\text{Ref\_Clk}}$  is the *Ref\_Clk* frequency in MHz. With the maximum required *Ref\_Clk* frequency of 100 MHz the expected digital static power consumption in acquisition mode is  $\sim 440$  mW with VDD=2.2 V.

### 5.3 PERIPHERY DESIGN

The *Timepix* periphery floor plan resembles to the one shown for *Mpix2MXR20* in Figure 4.8. The main two differences between both chips are:

- DACs: The *Timepix* has eight 8-bit linear current DACs, four 8-bit linear voltage DACs, and one 14-bit linear voltage DAC used for precise setting of the threshold. Table 5.3 lists the *Timepix* DACs range, type and control code.
- Add *Ref\_Clk*: In the previous chips all the LVDS input and output ports were switched off during acquisition (*Shutter* low) in order to minimize any external noise source. In *Timepix* the LVDS *Fclock\_In* and *Fclock\_Out* ports are used to impose externally a counting clock (*Ref\_Clk*) in single chip and in daisy-chained multi-chip structures. This architecture choice allows a high compatibility of *Timepix* with the already existing *Medipix2* readout systems.

	<i>DAC NAME</i>	<i>Type</i>	<i>Bits</i>	<i>DAC CODE</i>	<i>Range</i>
<i>CSA</i>	<i>I Preamp</i>	<i>I</i>	8	0111	0-2 $\mu A$
	<i>I Ikrum</i>	<i>I</i>	8	1111	0-140 nA
	<i>V FBK</i>	<i>V</i>	8	1010	0-2.2 V
	<i>V Cas</i>	<i>V</i>	8	1100	0-2.2V
	<i>V GND</i>	<i>V</i>	8	1101	0-2.2 V
<i>Discriminator</i>	<i>I Disc</i>	<i>I</i>	8	1011	0-1.67 $\mu A$
	<i>I THS</i>	<i>I</i>	8	0001	0-40 nA
	<i>I Hyst</i>	<i>I</i>	8	1001	0-200 nA
	<i>V THL</i>	<i>V</i>	14	0110	0-2.2 V
<i>Analog Driver</i>	<i>I BuffA</i>	<i>I</i>	8	0011	0-10.2 $\mu A$
	<i>I BuffB</i>	<i>I</i>	8	0100	0-391 $\mu A$
<i>LVDS Driver</i>	<i>I LVDS tx</i>	<i>I</i>	8	0010	0-392 $\mu A$
	<i>V RefLVDS tx</i>	<i>V</i>	8	1110	0-817 mV

Table 5.3. *Timepix* DACs.

## 5.4 ELECTRICAL CHARACTERIZATION

The Muros2.1 readout board and Pixelman software has been updated to operate the chip with the existing readout systems. The main hardware modification is to provide a clock in acquisition mode (*Ref\_Clk*). The software control panel has been adapted to allow each pixel to be programmed in an independent operation mode.

The first *Timepix* wafers show similar yield as in *Mpix2MXR20* with ~65% of good chips (categories A, B, and C). The die analog test classification process is divided into two: one with all the pixels configured in event counting (as in the previous chips), and a second, with all pixels configured in TOT mode. In TOT mode the measured counts gives an indication of the total charge which is very helpful to quickly analyse any major pixel to pixel gain variation as shown in Figure 5.12.

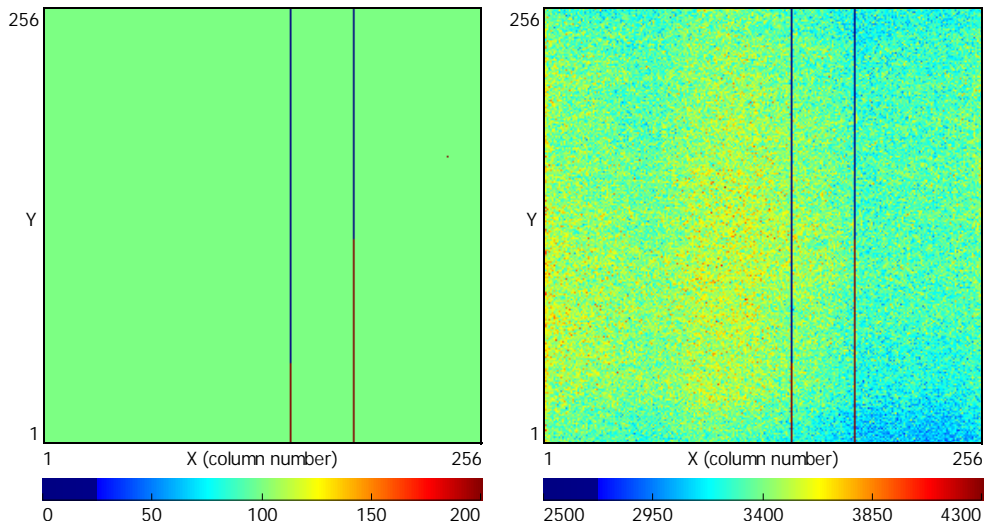


Figure 5.12. Analog wafer test for chip D10-W15 (class C chip). 100 pulses are sent in each acquisition. On the left all the pixels are in event counting mode: there is only information of number of dead columns. On the right all the pixels are in TOT mode: It can be seen the two dead columns and the pixel to pixel gain variations.

### 5.4.1 Optimization of the operating point of the pixel

The operating point optimization has been carried out with a naked chip mounted on a CERN *Medipix2* single chipboard connected to a MUROSV2.1 board with the Pixelman software. As with the previous chips the global threshold DAC (THL) is scanned across a fixed injection test pulse generating, in event counting mode, an s-curve. From the measured s-curves the electrical noise and gain is extracted for different biasing settings of Ipreamp and Ikrum DACs.

#### 5.4.1.1 Ipreamp DAC scan

The preamplifier bias current DAC scan is shown in Figure 5.13. The response is not monotonic due to latching errors of some binary codes on certain DAC registers. This problem has been traced to poor power distribution of the DACs registers. These registers are the same as in *Mpix2MXR20* where this problem affected other less important DACs. In any case this non-monotonic behaviour doesn't limit the chip performance since only few binary codes are affected. The pixel SNR is maximized at the maximum setting of Ipreamp with a gain of  $\sim 16.5$  mV/ke $^-$  and ENC of  $\sim 100$  e $^-$ .

The same trend is observed in order to optimize the time-walk of the front-end. The time-walk is defined as the response time difference of the discriminator between an input charge which is 1 ke $^-$  over threshold and an infinite input charge. In arrival time mode the counter is incremented from the activation of the discriminator until the closing of the global *Shutter*. As seen in Figure 5.14 (and in Figure 5.13) the gain is maximized for high Ipreamp biasing currents while the time-walk is minimized due to faster CSA output peaking time. The default Preamp DAC setting is set to the binary code FFH (i.e. Ipreamp=2  $\mu$ A) in those applications where the power dissipation is not an issue. The chip analog power consumption increase compared to the default settings is  $\sim 145$ mW.

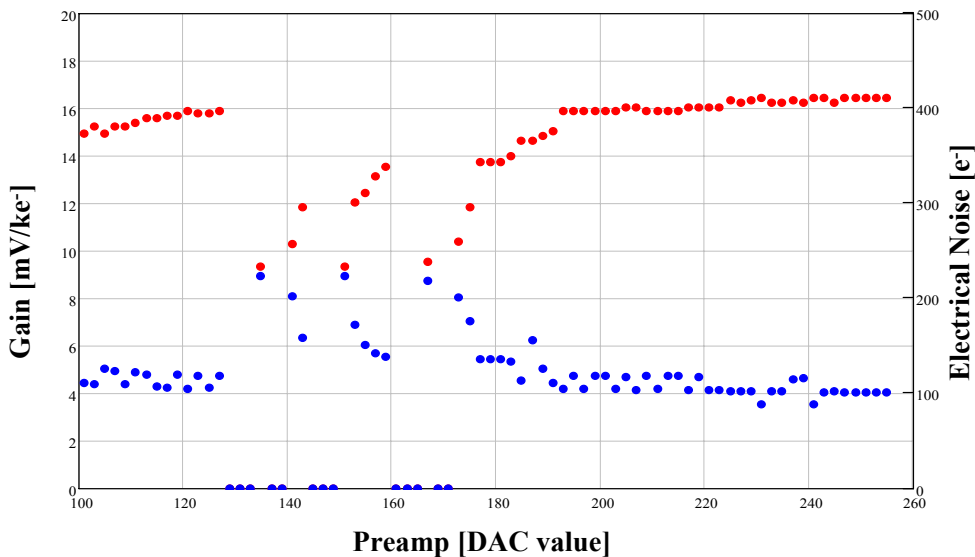
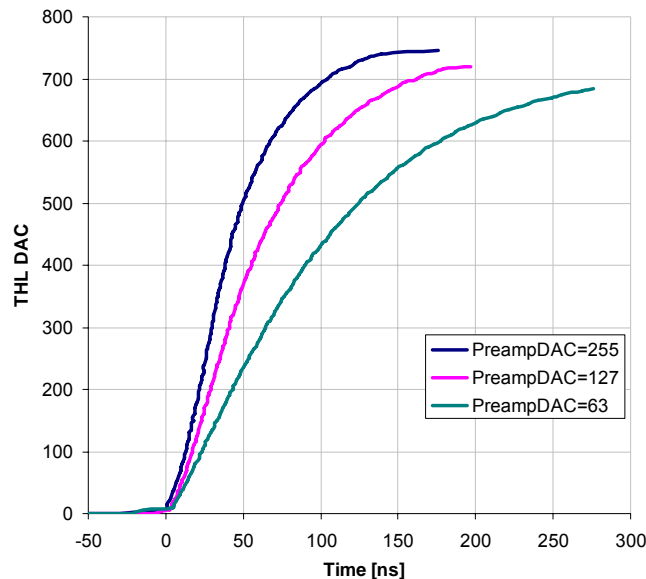


Figure 5.13. Gain (in red) and ENC (in blue) versus Preamp DAC measured in event counting mode. The non-monotonic behavior is due to a digital problem in the DACs registers which affect only certain binary codes in some DACs.



**Figure 5.14.** Measured peaking time variation for three Preamp DAC settings. The measurement is done by setting the matrix in arrival time mode and sending one test pulse of  $18.75 \text{ keV}$  while scanning the global threshold. As expected the time-walk and gain maximizes for high preamp currents.

#### 5.4.1.2 Ikrum DAC scan

As shown in section 4.4.2.2 the Ikrum biasing current controls the return to zero of the CSA output. The default Ikrum DAC setting for optimal SNR is set to 5 which corresponds to a biasing current of  $\sim 3 \text{ nA}$ .

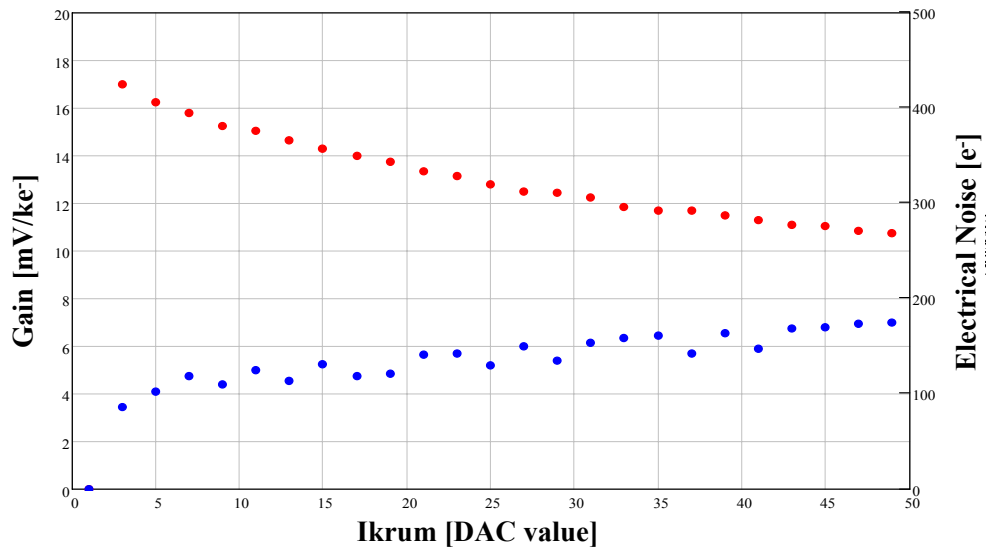


**Figure 5.15.** Gain (in red) and electrical noise (in blue) versus Ikrum biasing current measured in event counting mode.

### 5.4.2 Electrical characterization of the pixel

The electrical characterisation is reported in paper X. The linearity, electrical noise and gain are extracted using the event counting mode. The TOT linearity and resolution ( $\Delta\text{TOT}/\text{TOT}$ ) are measured with the chip configured in TOT mode. And the time-walk has been calculated with the chip set in arrival time mode. Threshold equalization for both polarities is also presented. In the same paper is shown the fixed pattern noise in TOT mode produced by pixel to pixel Ikrum mismatch which can be compensated using an appropriate mask. Table 5.4 summarizes the measurements reported in paper X. These measurements are later confirmed in section 5.6 with an absolute calibration using a *Timepix* bump bonded to a 300  $\mu\text{m}$  Si sensor and X-ray sources.

	<i>Holes [h<sup>+</sup>]</i>	<i>Electrons [e<sup>-</sup>]</i>
<i>Electronic noise</i>	$99.4 \pm 3.8 \text{ e}^- \text{ rms}$	$104.8 \pm 6 \text{ e}^- \text{ rms}$
<i>Gain</i>	$\sim 16.7 \text{ mV/ke}^-$	$\sim 16.3 \text{ mV/ke}^-$
<i>Threshold DAC step gain</i>	$24.7 \pm 0.7 \text{ e}^-$	$25.4 \pm 1.2 \text{ e}^-$
<i>CSA linearity [0-20 ke<sup>-</sup>]</i>		$> 99.9\%$
<i>TOT dynamic range</i>		$> 200 \text{ ke}^-$ (measured up to $\sim 40 \text{ ke}^-$ )
$\Delta\text{TOT}/\text{TOT}$ ( $Q_{in} > \text{Thr} + 1 \text{ ke}^-$ )		$< 5\%$
<i>Time-walk</i>		$< 50 \text{ ns}$
<i>Threshold variation before adjustment</i>		$\sim 240 \text{ e}^- \text{ rms}$
<i>Threshold variation after adjustment</i>		$\sim 35 \text{ e}^- \text{ rms}$
<i>Minimum detectable charge</i>		$\sim 650 \text{ e}^-$
<i>TOT energy resolution after correction</i>		$1300 \text{ e}^- \text{ FWHM}$
<i>Static pixel analog consumption</i>		$\sim 6.5 \mu\text{W}$
<i>Static pixel digital consumption</i>		$\sim 7 \mu\text{W}$ @ Ref_Clk = 80 MHz

Table 5.4. Summary of the electrical characterization reported in paper X.

### 5.5 FIRST MEASUREMENTS WITH GAS DETECTORS

Recently the *Timepix* has been successfully used as readout anode for two gas gain grids (triple-GEM and Micromegas). First images for both readout systems are shown in Figure 5.16 in TOT and arrival time modes. Figure 5.17 shows an example of a mixed mode measurement using a triple GEM configuration. The matrix is arranged as a chess pattern, whereby half the pixels are configured in TOT mode and the other half in arrival time mode. After data reconstruction two 2D images are created revealing the charge and arrival time information respectively. With such configuration the time-walk in each pixel can be off-line compensated using the TOT information.

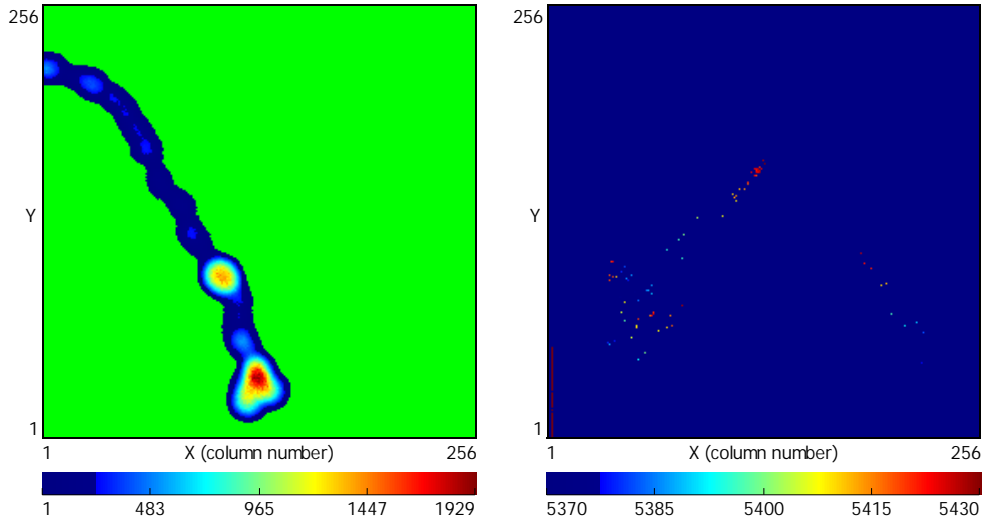


**Figure 5.16** On the left: TOT mode measurement of a single cosmic background particle interacting on a gas volume of a triple GEM detector. The maximum number pixel value of 1929 counts corresponds after calibration to  $\sim 120$  ke $^{\circ}$ . On the right: Arrival time measurement of a cosmic background particle obtained with a Micromegas gas gain grid coupled to the *Timepix* chip with a time resolution of  $\sim 20$  ns. Both 2D images are made with raw data. The green background on the left image displays pixels with no counts.

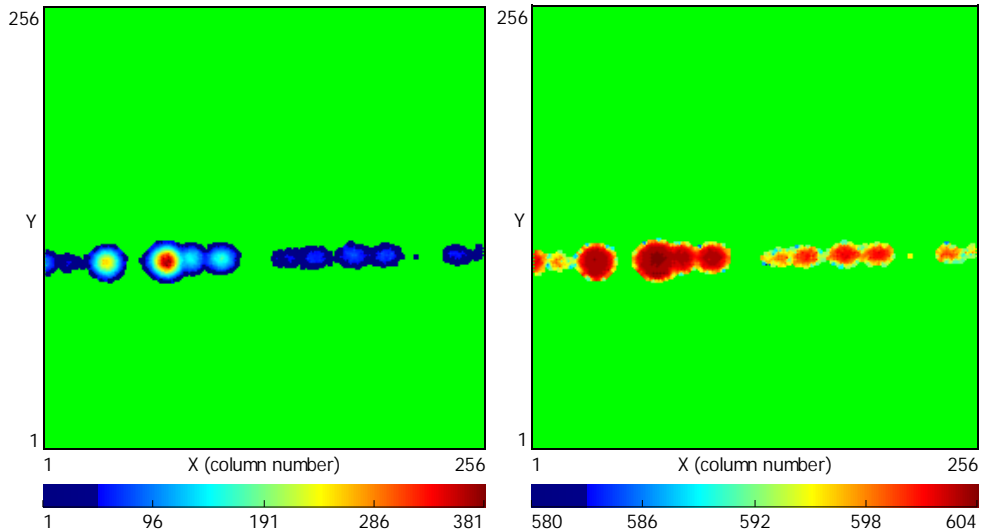


**Figure 5.17.** The full pixel matrix is in mixed-mode: every two pixels one is configured in TOT mode and the other in arrival time mode. After readout two images are generated from the same event using interpolation: On the left a TOT measurement, and on the right the arrival time measurement. Data taken during a test beam in DESY (Hamburg, November 2006). Green background shows pixels with no counts.

## 5.6 ABSOLUTE CALIBRATION

Recently the first *Timepix* chips bump bonded to a 300  $\mu\text{m}$  high resistivity Si sensor became available. An absolute energy calibration of a *Timepix* chip using a  $^{109}\text{Cd}$  and a  $^{55}\text{Fe}$  X-ray sources was realized. The effective energy threshold is calculated by scanning the THL DAC over the main emission lines of both X-ray sources (i.e. 22.1 and 24.9 keV for  $^{109}\text{Cd}$  and 5.9 keV for  $^{55}\text{Fe}$ ). The pixel matrix is configured in event counting mode in order to exploit the linear response of the measured effective threshold. As shown in Figure 5.18 the measured slope is linear with a gain of  $\sim 87.1$  eV or, in electrons,  $\sim 24.2$   $e^-$  per THL DAC step. The measured gain slope matches with the electrical characterization, realized in paper X and summarized in Table 5.4. The minimum detectable charge for the full chip is  $\sim 2.7$  keV or  $\sim 750$   $e^-$  for this setup which is higher than the value given in Table 5.4 ( $\sim 650$   $e^-$ ). This can be explained by the increase in the series noise of the CSA due to higher input pixel capacitance after detector bump-bonding as predicted in equation 2.7. Figure 5.19 shows two s-curves belonging to two different pixels, one from a bump-bonded chip and the other from a *naked* chip. The measured ENC degradation is  $\sim 16\%$ . The ENC is  $\sim 113$   $e^-$  rms for the chip bump bonded to the sensor. This raises the theoretical minimum detectable charge (see equation 4.5) to  $\sim 710$   $e^-$ .

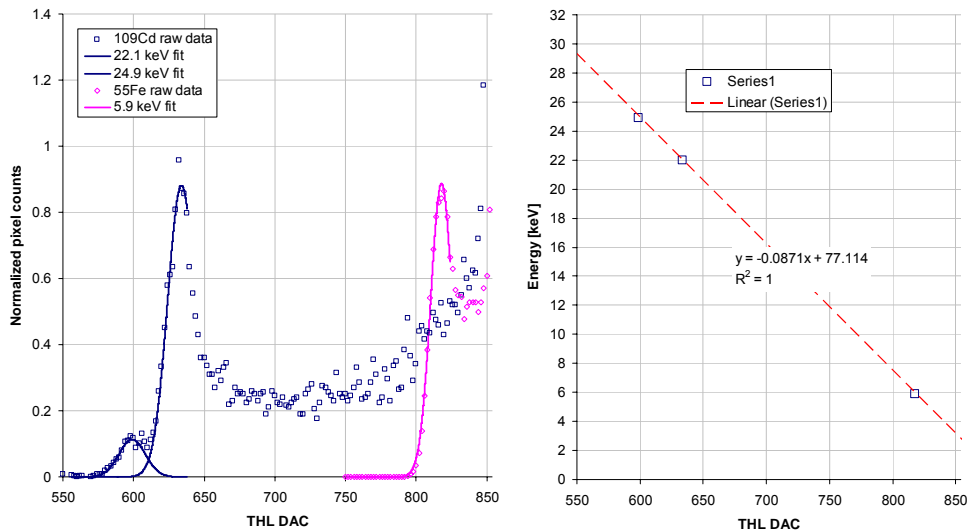


**Figure 5.18.** Energy calibration of a *Timepix* bonded to a 300  $\mu\text{m}$  high resistivity Si sensor.  $^{109}\text{Cd}$  (with 22.1 and 24.9 keV emission lines) and  $^{55}\text{Fe}$  (with a main 5.9 keV emission line) X-ray sources are used as energy references. The measured gain slope, on the right figure, is  $\sim 87$  eV per THL DAC step with a full chip minimum detectable charge of  $\sim 2.7$  keV.

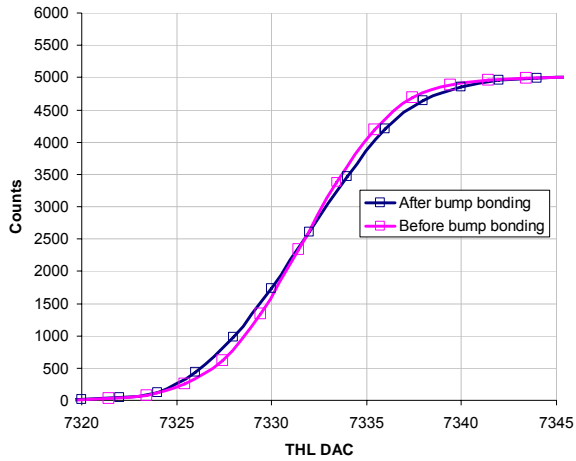


**Figure 5.19.** S-curve response of a pixel in the center of the matrix before and after bump-bonding for two different chips but under the same bias conditions. The injected test pulse is 4.7 ke<sup>-</sup>. The ENC is extracted from s-curve slope. After detector bump-bonding the measured ENC is ~16% higher than with a *naked* chip.

The TOT functionality has been explored with the calibrated chip using a <sup>241</sup>Am radioactive source. The <sup>241</sup>Am source emits  $\alpha$  radiation with an energy around 5.5 MeV together with  $\gamma$  radiation (i.e. photons) with main energy lines at 13.9 and 59.5 keV. Figure 5.20 shows on the left a full 2D image using a *Shutter* time of a 100 ms at a threshold of ~3.1 keV (THL=850). Large pixel clusters, with typically ~25 pixels, are the result of the charge deposition by single  $\alpha$  particles due to its high energy. The small pixel clusters (1-4 pixels) are the result of the detection of gamma radiation. The 3D image on the bottom right of Figure 5.20 shows the charge information measured with the TOT method. The central pixel in the large clusters has typically ~4000 counts which correspond to a pulse width of ~85  $\mu$ s at *Ref\_Clk* = 47.3 MHz and *Ikrum<sub>DAC</sub>*=5. As each large cluster corresponds to depositions of single  $\alpha$  radiation of ~5.5 MeV, the measured charge in the central pixels is then ~2.3 MeV or ~635 ke<sup>-</sup>.

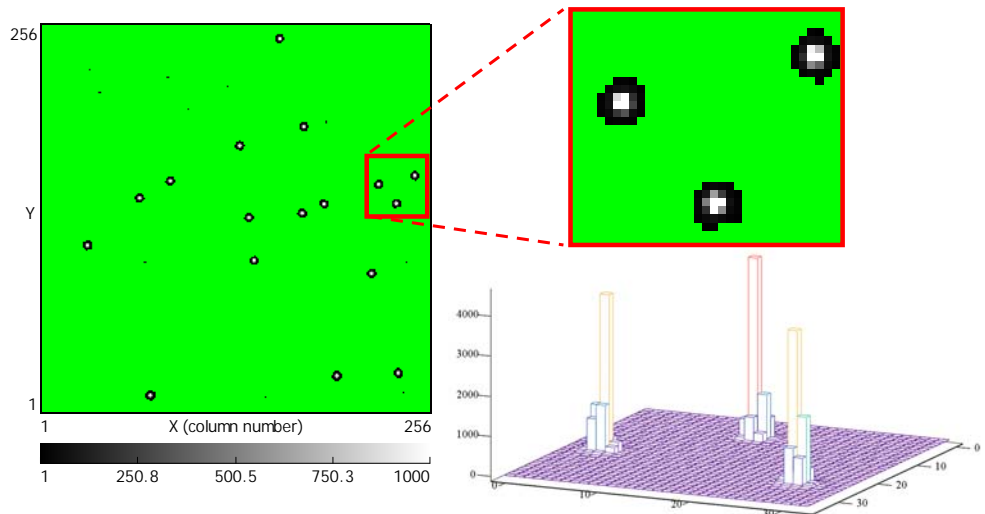


Figure 5.20. On the left is shown TOT raw data for the full chip exposed to a  $^{241}\text{Am}$  radioactive source with 100 ms *Shutter* time. The large pixel clusters are the result of the charge deposition by single  $\alpha$  particles (above 5 MeV). Three  $\alpha$  clusters are shown in the 3D plot revealing the energy information. The single hits are due to the  $^{241}\text{Am}$   $\gamma$  radiation (mainly 13.9 and 59.5 keV). The threshold is set  $\sim$ 3.1 keV, and *Ref\_Clk* = 47.3 MHz. The 2D images on the right and on the top left the green color indicates pixels with no counts.

## 5.7 SUMMARY

The *Timepix* is a successful modification of the *Mpix2MXR20* to provide arrival time information of primary electrons, with a precision up to 10 ns, in Micro-Patterned Gas Detectors (MPGD). Each *Timepix* pixel can be configured independently in arrival time, TOT or event counting mode. Special emphasis was placed on reducing the minimum detectable charge in order to minimize the discharge probability associated with the high electric fields used in MPGDs. The chip uses an external clock in acquisition mode, which is distributed to the pixel matrix, as a time reference.

First measurements with the chip coupled to gas gain grids show a very good performance of the three available operation modes. Recently an absolute calibration has been realized with a *Timepix* bump bonded to a 300  $\mu\text{m}$  Si sensor using X-ray sources. The gain, noise and linearity published in paper X are confirmed. After detector bump-bonding, the ENC is slightly degraded to  $\sim$ 113 e $^-$  rms and the full chip minimum detectable charge in event counting mode is measured to be  $\sim$ 2.7 keV or  $\sim$ 750 e $^-$ .



## 6 FUTURE DEVELOPMENTS IN PIXEL DETECTORS

This chapter describes the limitations of high granularity pixel detectors due to charge sharing. The charge sharing effects on the measured energy spectrum are briefly explained in section 6.1. The *Medipix3* collaboration has been set to fund a new prototype chip designed at CERN and manufactured in a commercial  $0.13\text{ }\mu\text{m}$  CMOS technology. The chip design and first results are reported in paper XI and only briefly described in section 6.1.1. New ideas for future developments are described in 6.2 and 6.4.

### 6.1 LIMITATION OF THE ACTUAL CHIP (CHARGE SHARING)

Charge diffusion in segmented semiconductors detectors generates a distortion in the energy spectrum seen by an individual pixel. As the ratio between detector thickness to pixel size increases the effect on the energy spectrum increases ([MIK00], [TLU05], paper V and paper XI). As an example, Figure 6.1 shows the charge collection of a 59.5 keV from a  $^{241}\text{Am}$  radioactive source in a 4 pixel cluster. The charge is split between the 4 channels generating a spectrum distortion when using the photon counting approach.

Even in monochromatic X-ray beams where the threshold is set well below the energy peak the pixel to pixel threshold variation creates a fix pattern noise in an image (Fig.9 in paper V). This fixed pattern noise varies depending on the spectrum of the incoming charge addressed.

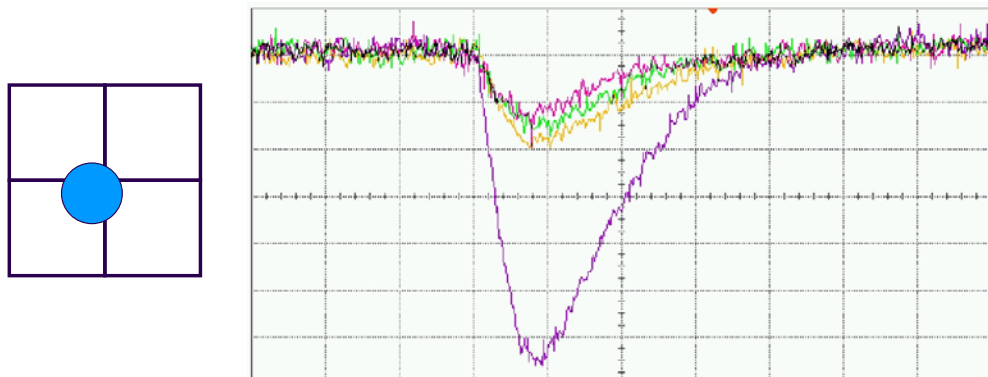


Figure 6.1. CSA output pulse of a 4 pixel cluster after detecting a 59.5 keV photon from a  $^{241}\text{Am}$  radioactive source. The event is split amongst the 4 pixels generating a distortion in the measured spectrum. Data taken using the *Medipix2* 3x3 analog output with 4 channels connected to a 1Gs/s digital oscilloscope. X= 200 ns/div and Y= 10 mV/div.

#### 6.1.1 The *Medipix3* Prototype chip

The *Medipix3* collaboration has been formed to develop a new chip with the same pixel size as the *Medipix2* series chips to correct the charge sharing by charge summing between neighbouring pixels as already reported at the end of paper I and paper V.

A commercial  $0.13\text{ }\mu\text{m}$  CMOS technology with 8-metal layers is used to deal with the high level of pixel interconnectivity and complexity while keeping a small pixel size. To gain experience with this new technology while testing all the new pixel functionality it was decided to design, as a first step, a *Medipix3* prototype chip with an  $8 \times 8$  matrix of square pixels of  $55\text{ }\mu\text{m}^2$ . The *Medipix3* measures  $2\text{ mm} \times 1\text{ mm}$  and it is shown in Figure 6.2.

Due to the small die size and the short clearance space between the pixel matrix and the bond pads the chip can not be bonded to a detector. In any case, the chip includes seven buffered injection test pulses to fully test electronically the new pixel architecture. The pixel also includes the two large metal plane use for bump bonding to better characterize the input capacitance of the front-end.

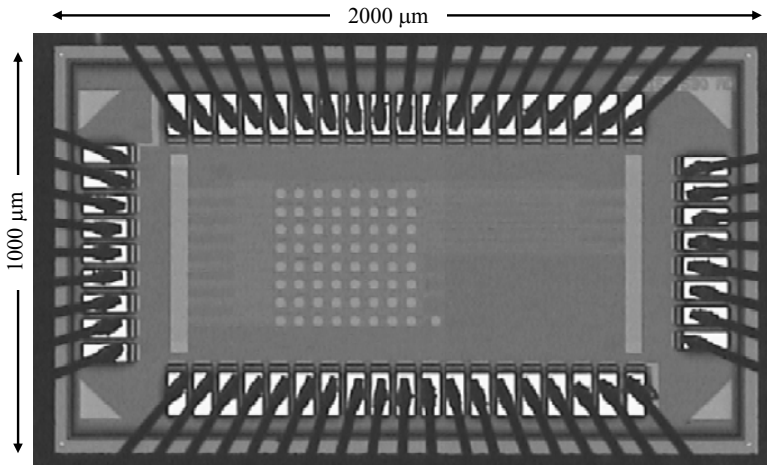


Figure 6.2. The *Medipix3* prototype. The  $8 \times 8$  pixel matrix is at the centre of the chip. The top and bottom bond pads are used for analog power, transistor biasing, and seven injection test pads. The lateral pads are used for digital power and digital communication.

### 6.1.1.1 *Medipix3* pixel cell

The *Medipix3* pixel schematic is shown in Figure 6.3. The analog pixel side includes: one CSA with the same architecture as the *Medipix2* series of chips, an AC coupled semi-gaussian shaper with 8 replica currents proportional to the detected charge, and two cross-over discriminators with 5 bits of threshold adjustment. The replica currents from the shaper are sent to nodes common to a cluster of four pixels before the discriminators. The pixel digital side contains: arbitration logic used to decide the pixel with the biggest charge in a time-over-threshold method, two 15-bit shift registers which are also used as linear feedback shift register counters with a single XOR tap and a dynamic range of 32768 counts, and a 19-bit pixel configuration register.

The pixel can be configured in four different collection modes depending on the pixel pitch and the charge summing strategy as shown in Table 6.1. The readout is configurable to be in Sequential Read-Write (SRW, as in the *Medipix2* chips) or in Continuous Read-Write (CRW). In CRW mode one counter is read out while the other is in acquisition mode and vice versa providing a dead-time free readout.

	<i>Pixel size</i>	<i>Area of charge collection</i>	<i>Number of thresholds</i>
<i>Fine pitch</i>			2 (in SRW)
<i>Single Pixel Mode</i>	$55 \mu\text{m} \times 55 \mu\text{m}$	$55 \mu\text{m} \times 55 \mu\text{m}$	1 (in CRW)
<i>Fine pitch</i>			2 (in SRW)
<i>Charge Summing Mode</i>	$55 \mu\text{m} \times 55 \mu\text{m}$	$55 \mu\text{m} \times 55 \mu\text{m}$	1 (in CRW)
<i>Spectroscopic</i>			8 (in SRW)
<i>Single Pixel Mode</i>	$110 \mu\text{m} \times 110 \mu\text{m}$	$110 \mu\text{m} \times 110 \mu\text{m}$	4 (in CRW)
<i>Spectroscopic</i>			
<i>Charge Summing Mode</i>	$110 \mu\text{m} \times 110 \mu\text{m}$	$220 \mu\text{m} \times 220 \mu\text{m}$	5

Table 6.1. *Medipix3* pixel collection modes.

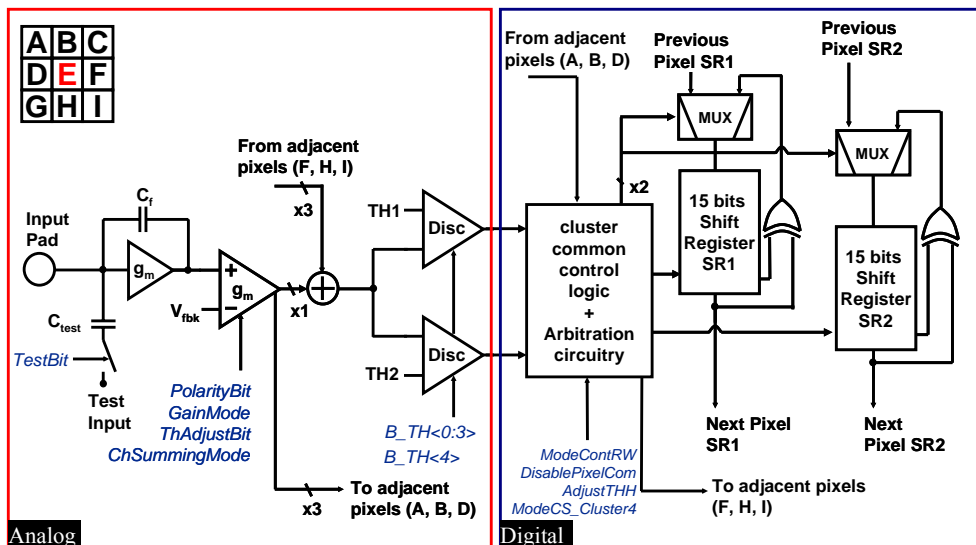


Figure 6.3. The *Medipix3* pixel cell schematic.

### 6.1.1.2 Electrical characterization

Table 6.2 summarizes the electrical measurements of the *Medipix3* prototype reported in paper XI. The pixel cell performs as expected from simulations. Two undesired effects appeared during testing: first an undesired digital to analog coupling, and second double counting between neighboring channels was measured when the input charge was close to threshold. Both problems have been identified and will be corrected in the new version of the *Medipix3* chip which will contain 64K pixels.

	<i>Single pixel mode</i>	<i>Charge summing mode</i>
<i>Pixel gain</i>		$11.4 \text{ mV}/\text{ke}^-$
<i>CSA-Shaper Gain</i>		$65 \text{ nA}/\text{ke}^-$ ( <i>High GainMode</i> ) $30 \text{ nA}/\text{ke}^-$ ( <i>Low GainMode</i> )
<i>Linearity</i>		$>95\%$ up to $9 \text{ ke}^-$ ( <i>High GainMode</i> ) $>98\%$ up to $22 \text{ ke}^-$ ( <i>Low GainMode</i> )
<i>Peaking time</i>		$\sim 100 \text{ ns}$
<i>Return to baseline</i>		$<1 \mu\text{s}$ for $4 \text{ ke}^-$
<i>Electronic noise (High GainMode)</i>	$72 e^- \text{ rms}$	$144 e^- \text{ rms}$
<i>Electronic noise (Low GainMode)</i>	$105 e^- \text{ rms}$	$210 e^- \text{ rms}$
<i>Threshold dispersion (adjusted)</i>	$55 e^- \text{ rms}$	$110 e^- \text{ rms}$
<i>Analog power dissipation</i>	$16.2 \mu\text{W}$ ( $V_{dd} = 1.5 \text{ V}$ )	

Table 6.2. Electrical characterization results extracted from paper XI.

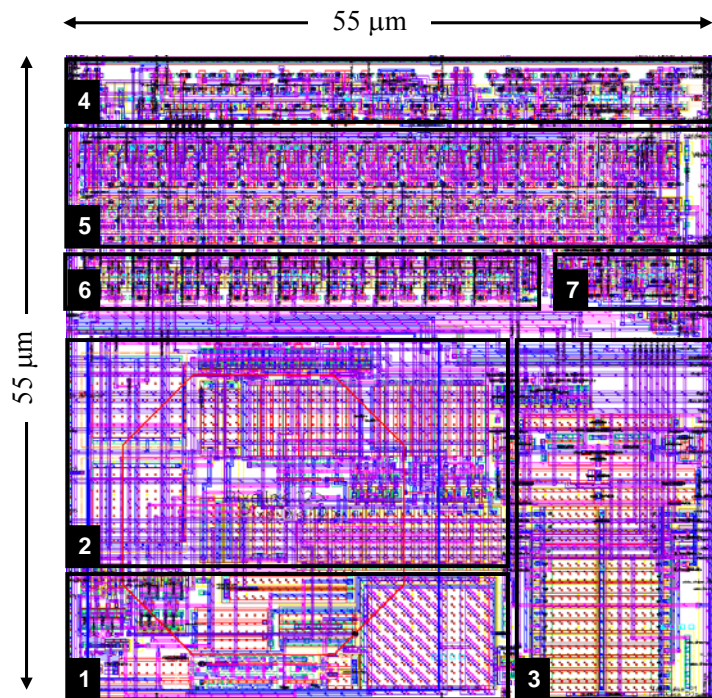


Figure 6.4. The *Medipix3* prototype pixel layout: 1) CSA, 2) Shaper and replica currents, 3) Discriminators with 5-bit threshold adjustment, 4) Control logic, 5) Two 15-bit shift register/counters, 6) 19-bit PCR and 7) Arbitration circuit.

## 6.2 FUTURE DEVELOPMENTS FOR TIMEPIX

A high spatial resolution spectroscopic pixel detector with no-dead time and tolerant to radiation might be the ultimate photon counting chip. The *Medipix3* is clearly a step forward towards this direction since the energy distortion due to charge sharing in the sensor will be corrected, as explained in section 6.1, and the dead-time due to readout will be eliminated by using a continuous read-write

architecture. On the other hand, the spectroscopic properties, even though better than *Medipix2* and *Mpix2MXR20*, will be limited to a discrete number of thresholds (5 to 8). The *Timepix* TOT approach seems more adequate for spectroscopic measurements since the linear dynamic range can be extended to energies above the saturation of the CSA output (i.e. above 200 ke<sup>-</sup>). The present pixel architecture of the *Timepix* has one main limitation: in case of 2 or more events falling on the same pixel during the same acquisition time the energy information is lost due to pile-up. This could be improved in two ways:

- *By adding a second counter* in each pixel which would register the total number of events (i.e. photon counting approach). The value obtained after each acquisition would then be the detected mean energy per pixel. The added complexity could be easily obtained by adopting the 0.13 μm CMOS process. In the other hand, a TOT counter with larger dynamic range should be included to avoid saturation.
- *By implementing a self-triggering sparse readout architecture* where each detected event is read out or stored locally. This approach is more challenging since a complete new read out architecture has to be developed but with the benefit of a true spectroscopic measure.

### 6.3 THE SQUARE TILE

One of the main remaining issues for hybrid pixel detectors is the tiling of large areas without loss of sensitive area. Many chips (i.e.,[PIL06], [PAN07], Medipix2 family chips, and others) allocate all the peripheral circuitry (i.e. IO logic, DACs, buffers...) and I/O wire bonding pads in one side of the readout chip. The other three sides of the chip can be as close as 60 μm to the chip edge, as shown in Figure 2.38, allowing tiling by the edges and/or by the top. With such an architecture several 2xN modules have been built [PIL06] and paper VII. In fact all these modules are limited:

- *By the sensor size* which typically have a ~500 μm guard-ring to avoid non-uniform fields around the sensor edges. Large Si sensors have been built minimizing the non-sensitive area ratio but dimensions are limited to the sensor wafer size (i.e. 6 inches). Moreover, large modules have an impact in the final yield as many readout chips are needed to complete the assembly.
- *By the wire bonds*. Wire bonding takes a lot of space. When bonding the clearance between the sensor edge and the tool head should be ~1 mm. Moreover, to achieve a reliable and robust connection, the ratio between the PCB bonding pad to the chip edge and the chip thickness should be a factor 2-3 [MCG06] (i.e. if the chip thickness is 700 μm the PCB bonding pad should be placed between 1.4 and 2.1 mm from the chip edge).

The optimum geometry would be a single square tile without non-sensitive area and with IO connections through the backside of the readout chip. The first step towards active edge silicon sensors have been already done [KEN01] with dead areas between the last active pixel and the sensor edge of  $\sim 20 \mu\text{m}$ . On the readout chip side wafer thinning ( $< 50 \mu\text{m}$ ) and through-wafer vias with a diameter below  $2 \mu\text{m}$  have been already demonstrated [HEI05]. Besides the IO wire bonds a chip periphery contains circuitry which is needed to operate the chips. Two solutions might be possible:

- To add an *interposer layer* as a fan-out structure between the readout chip and the sensor material. This technology is being used by the RELAXD project [REL] to cover large areas. The main building block is shown in Figure 6.5. Each tile is equipped with four Mpix2MXR20 chips bonded to a  $3 \text{ cm} \times 3 \text{ cm}$  edgeless Si sensor. The quad is connected via Ball-Grid-Array technology to a small PCB which incorporates an FPGA allowing 3Gbit/s serial data transmission.

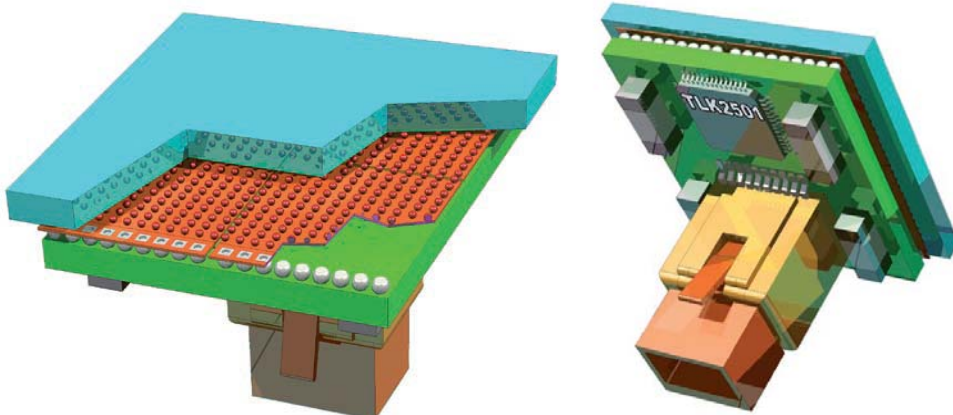


**Figure 6.5.** Drawing of the proposed RELAXD tile. The sensor (blue) is connected to 4 Mpix2MXR20 chips by (red) flip-chip solder balls. The Mpix2MXR20 chips (red) are connected to the printed circuit board (green) by etching holes through the chips, while on their backside contact is made via Ball-Grid-Array technology (white balls). [Vis06]

- Using multiple-chip *3D stacking* technology. A 3D chip is generally referred to as a chip comprised of two or more layers of active semiconductor devices that have been thinned, bonded, and interconnected to form a *monolithic* device. Industry is moving towards 3D to improve circuit performance and this technology has been already applied in high-end processors. Pixel detectors can benefit a lot from this technology as more functionality is possible per given area while the peripheral logic can be greatly reduced. Moreover, the processing in each layer can be optimized independently. Figure 6.6 shows a schematic of a possible building block composed of three layers: an edgeless sensor, a pixel matrix and a IO chip.

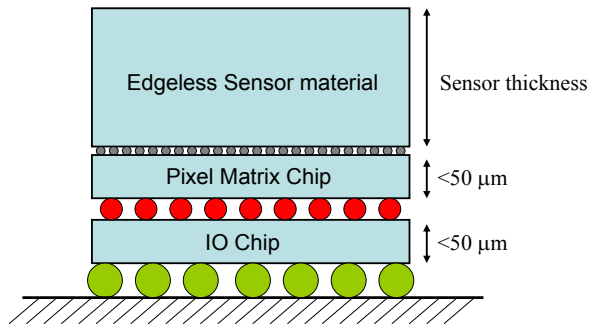


**Figure 6.6. The square tile.** Wafer thinning and thorough-wafer vias are built in order to interconnect the sensor material, the pixel matrix chip and the IO chip.

#### 6.4 SUMMARY

The spectrum distortion due to charge sharing in planar semiconductor detectors have been briefly described. This effect increases as the ratio between the sensor thickness and the pixel pitch increases. The Medipix3 collaboration has recently been formed to design and build a chip with the ability of correcting the charge sharing distortions. A first 8 x 8 pixel matrix prototype has been built with a pixel size of 55  $\mu\text{m} \times 55 \mu\text{m}$ . The charge between neighbour channels is summed and allocated to the pixel in the cluster with largest charge on an event by event basis. The prototype chip has demonstrated the feasibility of this approach. These encouraging results have lead to the design of a full scale 256 x 256 pixel matrix which is currently undergoing. Some new ideas about future developments have also been described.



## **7 SUMMARY OF PUBLICATIONS**

Paper I is a summary of the design of the *Medipix2* largely covered in Chapter 2. The electrical characterization and equalization of *Medipix2* is presented in paper II covering a large fraction of section 3.3. Paper III shows the first published X-ray image with a *Medipix2* Si assembly and a comparison with *Medipix1*. Three papers (IV, V and VI) relate to section 3.5 and concerns X-ray imaging with *Medipix2* with different sensor materials. The *Medipix2* Quad is used for electron imaging in paper VII. Papers VIII, IX and X relates to the *Timepix* motivation, design and characterization described in chapter 5. Paper XI covers the *Medipix3* prototype design and characterisation described in chapter 6.

### **7.1 PAPER I**

This paper presents the *Medipix2* photon counting chip where the author is the main designer. In this publication are briefly summarized the pixel and chip architecture together with some preliminary electrical tests. In the section of the publication it is explained for the first time the idea of inter-pixel communication to cope with charge spread on neighbouring pixels. The author wrote the article which has been cited by other scientific publications more than 91 times.

### **7.2 PAPER II**

Publication II reports in detail the first electrical measurements prior bump bonding to a semiconductor detector done in the full matrix. Figures of noise, gain, linearity and threshold variation (before and after threshold equalization) are reported. The author wrote the article which has been cited by other scientific publications more than 34 times.

### **7.3 PAPER III**

This paper describes the advantages and requirements of an X-ray medical imaging system using single photon counting method. As proposed pixel readout chips the *Medipix1* and *Medipix2* are compared. The first published X-ray image taken with a *Medipix2* chip bonded to a 300 µm Si sensor is shown. The author made that picture using Medisoft software and the Muros2 readout board.

### **7.4 PAPER IV**

This paper presents the first experimental tests of a *Medipix2* chip bonded to a CdTe 1mm thick sensor. Different artefacts from the sensor detector material and low bonding yield don't limit the expected energy range sensitivity. Preliminary measurements and calibration were done by the author.

## **7.5 PAPER V**

This paper studies the effects of charge sharing between neighbouring pixels and its consequences in an imaging system as *Medipix2*. The charge sharing slope depends on the energy of the detected photon. Many of the measurements shown are taken at the European Synchrotron Radiation Facility (ESRF, Grenoble) during a test beam where the author participated.

## **7.6 PAPER VI**

The energy window available in *Medipix2* is explored in this paper. Images were taken proving the potential for such spectroscopic imaging system. The minimum energy window ~1.4 keV was obtained with a new equalization algorithm developed by the author to overcome the test pulse non-uniformities.

## **7.7 PAPER VII**

This paper presents the measurements obtained by the *Medipix2* quad for electron imaging. The *Medipix2* quad is installed inside an electron microscope to detect electrons at energies between 120 and 300 keV. The author developed the equalization algorithm for multi-chip structures and participated in the installation and commissioning of the full set up.

## **7.8 PAPER VIII AND PAPER IX**

These two publications summarize the successful results of a TPC (Time Projection Chamber) prototype for the International Linear Collider (ILC) using the *Medipix2* chip as a direct readout anode when coupled to GEM (Gas Electron Multiplier) or Micromegas gain grids. These two publications demonstrate that *Medipix2* was able to read the drifted charge from gas converted primary ionizations. These results encourage the redesign of the *Mpix2MXR20* in order to provide arrival time information. The author has been responsible for the chip characterization and the debugging of the readout setups.

## **7.9 PAPER X**

Publication XI is the description of the *Timepix* chip where the author is the main designer. In this publication are described the pixel and chip architecture comparing to the *Medipix2* chip. Chip electrical characterization is reported with gain, linearity and noise measurements and matrix threshold equalization. The new operation modes (arrival time and time-over-threshold) are also described and measured. The author took place in a test beam in DESY (Hamburg, Germany) where some images are shown in the article. This article was presented in the *11<sup>th</sup> Vienna Conference on Instrumentation* where author received the *NIM-A Young Scientific Award* for “the development of pixel readout chips for a wide range of instrumentation applications”. The author wrote the article.

## **7.10 PAPER XI**

Publication X describes the design and characterization of first *Medipix3* prototype which corrects the spectrum distortion due to charge sharing effect in the sensor material. The author was one of the main supervisors and designed the chip periphery.



## 8 THESIS SUMMARY

Hybrid pixel detectors using the photon counting approach are excellent candidates for the detection of X-rays in applications requiring low noise and/or low count rate. In this thesis three different chips have been described. The small pixel size of 55 µm x 55 µm is the main feature shared by the three designs. This is comparable to the spatial resolution of medical X-ray film. Besides the spatial resolution, small pixels have two main advantages: first, reduced pixel occupancy which improves the maximum count rate per unit area, and second, tiny input pixel capacitances which reduces the power consumption per pixel keeping under control the power per unit area. On the other hand, smaller pixels suffer from larger charge sharing between neighbour channels, small bump-bonding pitch, mixed-mode design concerns due to the close proximity of analog and digital circuitry, and increased matrix readout complexity.

The actions taken for the design of small pixels with low power mixed-mode circuitry have been described in this thesis. The achieved analog power consumption is  $\sim 8 \mu\text{W}$  per pixel in *Medipix2* and *Mpix2MXR20*, and  $\sim 6.5 \mu\text{W}$  per pixel in *Timepix*. Analog and digital circuitry use independent power supplies while guard-ring structures are implemented to isolate the analog blocks. The on-chip DACs, used in all the chips, give a high degree of configurability and reproducibility. Moreover, *Mpix2MXR20* and *Timepix* include a band-gap reference circuitry which increases the power supply and temperature stability compared to *Medipix2*. In fact, these two chips can be fully operated by means of only 10 digital lines (i.e. 6 LVDS lines and 4 CMOS lines).

The ability to tile large areas has been a design priority. On the three designs pixels are placed very close, less than 60 µm, to the chip edge. The chips can be daisy chained using the LVDS serial link. With this approach, large sensitive areas of 2 x N chips can be covered. These multi-chips structures can be fully operated using the same readout systems as for the single chip with the penalty of read out time.

Several readout systems have been developed since the *Medipix2* chip became available in 2002. Using 100 MHz clock these systems can operate with the chip either through the LVDS serial link, reading out a single chip in less than 10 ms, or through the 32-bit CMOS parallel, reading out a single chip in less than 300 µs.

Many applications have used the chip, since it became available, with different detector types and front-end collection modes (Table 3.3). This demonstrates that the hybrid pixel detector technology is suited for a wide range of applications by choosing the appropriate sensor material while using the same readout chip. One of these applications, the Micro-Patterned Gas Detectors, has been the driving motivation for the design of the *Timepix* chip.

When coupled to different gas gain grids *Timepix* can measure the arrival time of single primary electrons detected in a gas volume. *Timepix* uses an external reference clock, which is distributed simultaneously to all the matrix, as a time

reference to measure the event time of arrival. Special care has been taken during the design of *Timepix* to avoid coupling between analog and digital blocks due to the presence of an external clock during acquisition. Measurements have shown no coupling even at very low thresholds validating the proposed architecture. Moreover, as the discriminator output pulse width is linear with respect to the input charge, a time-over-threshold (TOT) mode has been implemented. This mode reveals spectroscopic information in each pixel. In very low rate applications the spectral distortion produced by the charge sharing can be corrected using the TOT mode off-line. As shown in Figure 5.20, the TOT mode can be used to correct the arrival time, due to time-walk, of events with large charge spreading by configuring the pixel matrix appropriately.

As a final summary Table 8.1 shows a complete performance comparison of the three pixel chips described in this work.

	<i>Medipix2</i>	<i>Mpix2MXR20</i>	<i>Timepix</i>
<i>CMOS Technology</i>		$0.25 \mu\text{m}$ 6-metal	
<i>Square pixel size</i>		$55 \mu\text{m}$	
<i>Transistors per pixel</i>	$\sim 500$	$\sim 530$	$\sim 550$
<i>Pixel matrix</i>		$256 \times 256$	
<i>Pixel analog power</i>	$8 \mu\text{W} @ 2.2\text{V}$	$6.5 \mu\text{W} @ 2.2\text{V}$	
<i>Measured pixel gain</i>	$8.7 \text{ mV}/\text{ke}^-$	$10.7 \text{ mV}/\text{ke}^-$	$16.5 \text{ mV}/\text{ke}^-$
<i>Collection polarity</i>		$e^-$ and $h^+$	
<i>Peaking time</i>	$\sim 170 \text{ ns}$	$\sim 150 \text{ ns}$	$\sim 100 \text{ ns}$
<i>Return to baseline</i>		$< 1 \mu\text{s}$ for $Q_{in} \leq 10 \text{ ke}^-$	
<i>Dynamic range</i>		up to $\pm 85 \text{ ke}^-$	up to $\pm 55 \text{ ke}^-$
<i>Linearity</i>		$> 99.9 \%$	
<i>ENC</i>	$160 \text{ e}^- \text{ rms}$	$110 \text{ e}^- \text{ rms}$	$100 \text{ e}^- \text{ rms}$
<i>Number of Thresholds</i>		2	1
<i>Equalization bits</i>		$3 (\text{THL}) + 3 (\text{THH})$	4
<i>Threshold dispersion (non-adjusted)</i>	$450 \text{ e}^- \text{ rms}$	$400 \text{ e}^- \text{ rms}$	$250 \text{ e}^- \text{ rms}$
<i>Threshold dispersion (adjusted)</i>	$120 \text{ e}^- \text{ rms}$	$95 \text{ e}^- \text{ rms}$	$35 \text{ e}^- \text{ rms}$
<i>Minimum detectable charge</i>	$\sim 1100 \text{ e}^-$	$\sim 900 \text{ e}^-$	$\sim 650 \text{ e}^-$
<i>Window discrimination</i>		Yes	No
<i>Counter depth</i>	8001		11810
<i>Overflow control</i>	No		Yes
<i>Pixel operating modes</i>		PC	AT, TOT or PC
<i>On-chip band-gap</i>	No		Yes
<i>On-chip DACs</i>	7 8-bit [I] 8 8-bit [V]	8 8-bit [I] 3 8-bit [V] 2 14-bit [V]	8 8-bit [I] 4 8-bit [V] 1 14-bit [V]
<i>Readout board</i>		<i>Muros2.x</i> and <i>MedipixUSB</i>	<i>Muros2.1</i>
<i>Readout Program</i>		<i>Medisoft</i> and <i>Pixelman</i>	<i>Pixelman</i>
<i>Readout Time</i>		Serially (LVDS) $< 10 \text{ ms}$ at $100 \text{ MHz}$ Parallel (32-bit CMOS) $< 300 \mu\text{s}$ at $100 \text{ MHz}$	

Table 8.1. Comparison performance of the 3 pixel chips discussed in the thesis. PC (Photon Counting), AT (Arrival Time) and TOT (Time-Over-Threshold).





## 9 REFERENCES

- [AME99] S. R. Amendolia, et al., “MEDIPIX: a VLSI chip for a GaAs pixel detector for digital radiology”, *Nucl. Instr. Meth. A*, vol. 422, pp : 201-205, 1999.
- [ANE00] G. Anelli, “Conception et caractérisation de circuits intégrés résistants aux radiations pour les détecteurs de particules du LHC en technologies CMOS submicroniques profondes”, PhD Thesis, Institut National Polytechnique de Grenoble, pp.114-118, 2000.
- [ANE01] G. Anelli, et al., “Noise characterization of a 0.25  $\mu\text{m}$  CMOS technology for the LHC experiments “, *Nucl. Instr. Meth. A*, vol.457, pp: 361-368, 2001.
- [ANG92] F. Anghinolfi et al., “A 1006 Element Hybrid Silicon Pixel Detector with Strobed Binary Output”, *IEEE Trans. Nucl. Sci.*, vol. 39, pp: 654–661, 1992.
- [AUT05] M. Autiero, et al., “Experimental study on in vivo optical and radionuclide imaging in small animals”, *IEEE Trans. Nucl. Sci.*, vol. 52, pp: 205-209, 2005.
- [BAL07] R. Ballabriga, “Design of Digital to Analog Converters in IBM CMOS 0.25 $\mu\text{m}$  for the *Medipix2* chip”, Memoria per l’obtencio del Diploma d’estudis avançats, Universitat Ramon Llull, 2007.
- [BAR00] G. Bardelloni, et al., “A new Read-out System for an Imaging Pixel Detector”, *IEEE Trans. Nucl. Sci. (Conference Record)*, vol.2, pp:12/57-12/60, 2000.
- [BET07] S. Bettarini, et al., “Development of deep N-well monolithic active pixel sensors in a 0.13  $\mu\text{m}$  CMOS technology”, *Nucl. Instr. Meth. A*, vol. 572, pp: 277-280, 2007.
- [BRO06] C. Brönnimann, et al., “The Pilatus 1M Detector”, *J. Synchrotron Rad.*, vol. 13, pp: 120-130, 2006.
- [CAM94] M. Campbell, et al., “Development of a Pixel Read-Out Chip Compatible with Large Area Coverage”, *Nucl. Instr. Meth. A*, vol. 342, pp: 52-58, 1994
- [CAM98] M. Campbell, E. H. M. Heijne, G. Meddeler, E. Pernigotti, and W. Snoeys, “Readout for a 64 x 64 Pixel Matrix with 15-bit Single Photon Counting”, *IEEE Trans. Nucl. Sci.*, vol. 45, pp: 751–753, 1998.
- [CHA91] Z.Y. Chang and W.M.C. Sansen, “Low-noise wide-band amplifiers in bipolar and CMOS technologies”, Kluwer Academic Publishers, 1991.
- [CHM06] M. Chmeissani, et al., “Dear-Mama: A photon counting X-ray imaging project for medical applications”, *Nucl. Instr. Meth. A*, vol. 569, pp: 136-139, 2006.
- [COL97] C. Colledani, et al., “Castor 1.0, a VLSI Analog-Digital Circuit for Pixel Imaging Applications”, *Nucl. Instr. Meth. A*, vol. 395, pp: 435–442, 1997
- [DEP02] G. Deptuch, et al., “Design and testing of monolithic active pixel sensors for charged particle tracking”, *IEEE Trans. Nucl. Sci.*, vol. 49, pp: 601-610, 2002.
- [DIB97] D. Di Bari, et al., “Performance of  $0.5 \times 10^6$  sensitive elements pixel telescope in the WA97 heavy ion experiment at CERN”, *Nucl. Instr. Meth. A*, vol. 395, pp. 391-397, 1997.
- [DIE93] B. Dierickx, et al., “Integration of CMOS-electronics and particle detector diodes in high-resistivity silicon-on-insulator wafers”, *IEEE Trans. Nucl. Sci.*, vol. 40, pp: 753-758, 1993.
- [EUD] Detector R&D for the International Linear Collider. <http://www.eudet.org>
- [EVA02] D.S. Evans, A. Workman, and M. Payne, “A comparison of the imaging properties of CCD-based devices used for small field digital mammography”, *Phys. Med. Biol.*, vol. 47, pp: 117-135, 2002.
- [FAR05] A.R. Faruqi, R. Henderson and L. Tlustos, ”Noiseless direct detection of electrons in *Medipix2* for electron microscopy “, *Nucl. Instr. Meth. A*, vol.

- 546, pp: 160-163, 2005.
- [FIS99] P. Fischer, et al., “A Counting Pixel Chip and Sensor System for X-ray Imaging”, *IEEE Trans. Nucl. Sci.*, vol.46, pp: 1070–1074, 1999.
- [FOR03] A. Fornaini, et al., “A multi-chip board for X-ray imaging in build-up technology”, *Nucl. Instr. Meth. A*, vol. 509, pp: 206-212, 2003
- [FOS97] E. R. Fossum, “CMOS Image Sensors: Electronic Camera-On-A-Chip”, *IEEE Trans. On Electron Devices*, vol. 44, no.10, pp: 1689-1698, 1997.
- [FUJ92] H. Fujita, et al., “A simple method for determining the modulation transfer function in digital radiography”, *IEEE Trans. Med. Imag.*, vol. 11, pp: 34–39, 1992.
- [GAT84] E. Gatti and P.Rahal, “Semiconductor drift chamber — An application of a novel charge transport scheme”, *Nucl. Instr. Methods Phys. Res.*, vol. 225, pp: 608–614, 1984.
- [GAT86] E. Gatti and P.F. Manfredi, “Processing the signal from Solid-State Detectors in Elementary-particle Physics”, *Riv. Nuovo Cimento*, vol. 9, no. 3, 1986.
- [GEO01] M. George and P. Alfke, “Linear Feedback Shift Registers in Virtex Devices“, Application Note: Virtex Series and Virtex-II Series.  
<http://www.xilinx.com/bvdocs/appnotes/xapp210.pdf>, 2001.
- [GIR00] A. Giraldo, et al., “Aspect ratio calculation in n-channel MOSFETs with a gate-enclosed layout”, *Solid-State Electronics*, vol.44, pp: 981-989, 2000.
- [GRU02] S. Gruner, M. Tate, and E. Eikenberry, “Charge-coupled device area x-ray detectors”, *Rev. Sci. Instrum.*, vol. 73, pp: 2815-2842, 2002.
- [HEI05] E. H. M. Heijne, “Future semiconductor detectors using advanced micro-electronics with post-processing, hybridization and packaging technology”, *Nucl. Instr. Meth. A*, vol. 541, pp: 274–285, 2005.
- [HEI89] E. H. M. Heijne and P. Jarron, “Development of Silicon Pixel Detectors: an Introduction”, *Nucl. Instr. Meth. A*, vol. 275, pp: 467–471, 1989.
- [HEI90] E. H. M. Heijne, et al., “Development of Hybrid and Monolithic Silicon Micro-Pattern Detectors”, *CERN DRDC 90-81, R&D Proposal*, 1990.
- [HOL00] P. Holl, et al., “Active pixel matrix for X-ray satellite missions”, *IEEE Trans. Nucl. Sci.*, vol. 47, pp: 1421–1425, 2000.
- [HOL06] T. Holy, et al., “Data acquisition and processing software package for *Medipix2*”, *Nucl. Instr. Meth. A*, vol. 563, pp: 254-258, 2006.
- [HOR80] P. Horowitz and W. Hill, “The Art of Electronics”, Cambridge University Press, pp: 438, 1980.
- [HUN04] D. C. Hunt, O. Tousignant, and J.A. Rowlands, “Evaluation of the imaging properties of an amorphous selenium-based flat panel detector for digital fluoroscopy”, *Med. Phys.*, vol 31, pp: 1166-1175, 2004.
- [IEA] Institute of experimental and applied physics – Czech Technical University in Prague. <http://www.utef.cvut.cz>
- [IFA] Institut de Física d'Altes Energies. <http://www.ifae.es>
- [INF] L'Istituto Nazionale di Fisica Nucleare di Napoli. <http://www.na.infn.it>
- [JAK04] J. Jakubek, et al., “Properties of neutron pixel detector based on Medipix-2 device”, *IEEE Trans. Nucl. Sci.*, vol. 2, pp: 945-949, 2004.
- [JAK05] J. Jakubek, et al., “Neutron radiography with isotropic illumination by diffuse source”, *IEEE Trans. Nucl. Sci.*, vol. 5, pp: 2859–2862, 2005.
- [KAR05] J. Karg, D. Niederlöhner, J. Giersch and G. Anton, “Using the *Medipix2* detector for energy weighting “, *Nucl. Instr. Meth. A*, vol. 546, pp: 306-311, 2005.

- [KEM87] Kemmer and Lutz, “New structures for position sensitive semiconductor detectors”, *Nucl. Instrum. Methods Phys. Res. A*, vol. 273, pp. 608–614, 1987.
- [KEN01] Christopher J. Kenney, Sherwood Parker, and Edith Walckiers, “Results From 3-D Silicon Sensors With Wall Electrodes: Near-Cell-Edge Sensitivity. Measurements as a Preview of Active-Edge Sensors”, *IEEE Trans. Nucl. Sci.*, vol. 48, pp: 2405-2410, 2001.
- [KNO79] G.F. Knoll, “Radiation detection and measurement”, John Wiley & Sons, 1979.
- [KOH03] R. Kohrs, et al., “A DEPFET Pixel Vertex Detector for TESLA”, DESY Report PRC R&D 03/01, 2003.
- [KRU91] F. Krummenacher, “Pixel detectors with local intelligence: an IC designer point of view”, *Nucl. Instr. Meth. A*, vol. 305, pp: 527-532, 1991.
- [KUC04] W. Kucewicz, et al., “Fully depleted monolithic active pixel sensor in SOI technology”, *IEEE Nucl. Sci. Symposium Conf. Record*, vol. 2, pp: 1227-1230, 2004.
- [KUI73] K.E.Kuijk, “A precision reference voltage source”, IEEE Journal of Solid-State Circuits, vol. Sc-8, pp: 222-226, 1973.
- [LAK94] R. Laker and W. M. C. Sansen, “Design of Analog Integrated Circuits and Systems”, McGraw-Hill international editions, 1994.
- [LEP05] D. Lepori, et al., “Performance comparison of an active matrix flat panel imager, computed radiography system, and a screen-film system at four standard radiation qualities”. *Med. Phys.*, vol. 32, pp: 343\_350, 2005.
- [LUT99] G. Lutz, “Semiconductor radiation detectors”, Springer, 1999.
- [MAI03] M. Maiorino, et al., “Preliminary test of Medisoft 4: control software for the *Medipix2* readout chip”, *IEEE Trans. Nucl. Sci.*, vol. 50, pp: 869-877, 2003
- [MAN04] E. Manach and O. Gal ,”Experimental and simulation results of gamma imaging with hybrid pixel detectors” *Nucl. Instr. Meth. A*, vol. 531, pp: 38-51, 2004.
- [MAR07] R. Marzeddu, et al., “Optical link based readout system for *Medipix2* quad X-ray detector”, *Nucl. Instr. Meth. A*, In Press, Uncorrected Proof, Available online 6 February 2007.
- [MCG06] Personal communication with Ian McGill. DSF-Bond Lab at CERN.
- [MET04] G. Mettivier, et al., “A digital autoradiography system based on the *Medipix2* chip: images of 3H and 14C microscales”, *Nucl. Instr. Meth. A*, vol. 518, pp: 404-405, 2004.
- [MIK00] B. Mikulec, “Single Photon Detection with Semiconductor Pixel Arrays for Medical Imaging Applications”, PhD Thesis, University of Vienna, pp.127-140, 2000.
- [MIK03] B. Mikulec, “Development of segmented semiconductor arrays for quantum imaging”, *Nucl. Instr. Meth. A*, vol. 510, pp: 1-23, 2003.
- [MIK06] B. Mikulec, et al., “A noiseless kilohertz frame rate imaging detector based on microchannel plates read out with the *Medipix2* CMOS pixel chip”, *Nucl. Instr. Meth. A*, vol. 567, pp :110-113, 2006
- [MIT05] M. Mitschke, et al., “‘In-situ’ observation of dynamical diffraction by means of *Medipix2* sensor crystal fulfilling Bragg condition”, *Nucl. Instr. Meth. A*, vol. 546, pp: 135-139, 2005.
- [MOO65] G. E. Moore, “Cramming More Components onto Integrated Circuits”, Electronics, vol. 38, pp: 114-117, 1965 114–117.
- [NAT98] National Semiconductors, “LVDS Signal Quality: Cable Drive Measurements using Eye Patterns Test Report #3”, Application Note 1088, July 1998

- [NIK] The National Institute for Nuclear Physics and High Energy Physics in The Netherlands. <http://www.nikhef.nl>
- [PAN] PANalytical B.V., Lelyweg 1, 7602 EA ALMELO (The Netherlands)  
<http://www.panalytical.com/>
- [PAN07] P. Pangaud, et al., "XPAD3: A new photon counting chip for X-ray CT-scanner", *Nucl. Instr. Meth. A*, vol. 571, pp: 321-324, 2007
- [PAR02] M. Partridge, "A performance comparison of direct- and indirect-detection flat-panel imagers". *Nucl. Instr. Meth. A*, vol. 484, pp: 351-363, 2002.
- [PEL89] M. J. M. Pelgrom, A. C. J. Duinmaijer and A. P. G. Welbers, "Matching Properties of MOS Transistors", *IEEE Journal of Solid-State Circuits*, vol. 24, pp: 1433-1440, 1989
- [PEN96] F.X. Pengg, "Monolithic silicon pixel detectors in SOI technology", Ph.D. Dissertation, Linz University, Linz 1996.
- [PIL06] <http://pilatus.web.psi.ch/pilatus.htm>
- [PON07] C. Ponchut, et al., "Photon-counting X-ray imaging at kilohertz frame rates", *Nucl. Instr. Meth. A*, In Press, Uncorrected Proof, Available online 4 February 2007
- [REL] RELAXD : high-REsolution Large-Area X-ray Detector  
<http://www.nikhef.nl/pub/experiments/medipix/relaxd.html>
- [RIZ07] G. Rizzo, "Recent development on CMOS monolithic active pixel sensors", *Nucl. Instr. Meth. A*, In Press, Uncorrected Proof, Available online 4 February 2007.
- [ROE96] C. Roennqvist, et al., "A 64-Channel Pixel Readout Chip for Dynamic X-Ray Imaging", Presented at the IEEE Nuclear Science Symposium and Medical Imaging Conference, 1996.
- [ROP00] I. Ropotar, "An Investigation of Silicon Pixel Tracking Detectors and their Application in a Prototype Vertex Telescope in the CERN NA50 Heavy-Ion Experiment", PhD Thesis, Bergischen Universität Gesamthochschule Wuppertal, Germany, WUB-DIS 99-20, 2000.
- [RTI] RTI International, Research Triangle Park, NC 27709-2194, US.
- [SAN03] D. San Segundo, et al., "An interface board for the control and data acquisition of the Medipix2 chip", *Nucl. Instr. Meth. A*, vol. 509, pp:164-170, 2003
- [SCH01] C. Schwarz, et al., "Measurements with Si and GaAs pixel detectors bonded to photon counting readout chips", *Nucl. Instr. Meth. A*, vol. 466, pp. 87-94, 2001.
- [SEL01] P. J. Sellin, et al., "Performance of semi-insulating gallium arsenide X-ray pixel detectors with current-integrating readout", *Nucl. Instr. Meth. A*, vol. 460, pp:207-212, 2001.
- [TLU05] L.Tlustos, "Performance and limitations of high granularity single photon processing X-ray imaging detectors", PhD Thesis, University of Vienna, pp.39-46, 2005.
- [TRA92] H. Traff, 'Novel approach to high speed CMOS current conveyor', Electronics Letters, vol. 28, pp : 310-312, 1992
- [TUI98] H. P. Tuinhout, "Matching of MOS Transistors", Lecture at the Course "DEEP SUBMICRON : Modeling & Simulation", Ecole Polytechnique Fédérale de Lausanne, Lausanne, Switzerland, 12-15 October 1998.
- [TUR01] R. Turchetta, "A monolithic active pixel sensor for charged particle tracking and imaging using standard VLSI CMOS technology," *Nucl. Instrum. Methods Phys. Res. A*, vol. 458, pp. 677–689, 2001.

- [ULR05] J. Ulrici, et al., "Imaging performance of a DEPFET pixel Bioscope system in Tritium autoradiography", *Nucl. Instr. Meth. A*, vol.547, pp: 424-436, 2005.
- [UTE07a] <http://www.utef.cvut.cz/medipix/USB/usb.html>
- [UTE07b] <http://www.utef.cvut.cz/medipix/Pixelman/pixelman.html>
- [VAL05] J. Vallerga, et al., "Optically sensitive *Medipix2* detector for adaptive optics waveform sensing", *Nucl. Instr. Meth. A*, vol. 546, pp : 263-269, 2005.
- [VAV05] D. Vavrik, et al., "X-ray micro radiography using beam hardening correction", *IEEE Trans. Nucl. Sci.*, vol. 5, pp :2989-2992, 2005.
- [VIS06] J. Visschers and K. Bethke, "Medipix and RELAXD: a succesful collaboration between Science and Industry", Nikhef Annual Report 2006. [http://www.nikhef.nl/jv06/NIKHEF\\_Annual\\_Report\\_2006.pdf](http://www.nikhef.nl/jv06/NIKHEF_Annual_Report_2006.pdf)
- [VRI07] R.I. de Vries, et al. , "Medipix 2 in X-ray diffraction", *Nucl. Instr. Meth. A*, in Press, Corrected Proof, Available online 15 February 2007.
- [VTT] VTT Electronics, P.O.Box 1101, FIN-02044 VTT, Finland.
- [VYK06] Zdenek Vykydal, Jan Jakubek and Stanislav Pospisil, "USB interface for *Medipix2* pixel device enabling energy and position-sensitive detection of heavy charged particles", *Nucl. Instr. Meth. A*, vol. 563, pp: 112-115, 2006.
- [XU01] C. Xu, et al., "A low voltage hybrid bulk/SOI CMOS active pixel image sensor", *IEEE Electron Device Letters*, vol. 22, pp: 248-250, 2001
- [ZHA05] W. Zhao, et al., "Amorphous selenium flat panel detectors for medical applications", *Nucl. Instr. Meth. A*, vol. 549, pp: 205-209, 2005.
- [ZHE03] X. Zheng, et al., "New process and pixel structure of an SOI-CMOS imager", *IEEE SOI Conference*, pp: 101-102, 2003.



**PAPER I**

***Medipix2, a 64k pixel readout chip with 55µm square elements working in  
single photon counting mode***



**P a p e r I**



# Medipix2: a 64-k Pixel Readout Chip With 55- $\mu\text{m}$ Square Elements Working in Single Photon Counting Mode

X. Llopert, M. Campbell, R. Dinapoli, D. San Segundo, and E. Pernigotti

**Abstract**—The Medipix2 chip is a pixel-detector readout chip consisting of  $256 \times 256$  identical elements, each working in single photon counting mode for positive or negative input charge signals. Each pixel cell contains around 500 transistors and occupies a total surface area of  $55 \mu\text{m} \times 55 \mu\text{m}$ . A  $20\text{-}\mu\text{m}$  wide octagonal opening connects the detector and the preamplifier input via bump bonding. The preamplifier feedback provides compensation for detector leakage current on a pixel by pixel basis. Two identical pulse height discriminators are used to create a pulse if the preamplifier output falls within a defined energy window. These digital pulses are then counted with a 13-b pseudorandom counter. The counter logic, based in a shift register, also behaves as the input–output register for the pixel. Each cell also has an 8-b configuration register which allows masking, test-enabling and 3-b individual threshold adjust for each discriminator. The chip can be configured in serial mode and readout either serially or in parallel. The chip is designed and manufactured in a 6-metal  $0.25\text{-}\mu\text{m}$  CMOS technology. First measurements show an electronic pixel noise of  $140 \text{ e}^-$  root mean square (rms) and an unadjusted threshold variation around  $360 \text{ e}^-$  rms.

**Index Terms**—CMOS, Medipix, photon counting, pixel, X-rays.

## I. INTRODUCTION

ADVANCES in CMOS technology open up new possibilities in particle detection and imaging. In recent years particle physics experiments have been transformed by the introduction of application specified integrated circuit (ASIC) circuits particularly for tracking detectors. Pixel detectors have become key components in tracking systems especially in high multiplicity environments where excellent spatial resolution is combined with extremely high signal to noise ratios allowing physicists to find traces of rare particle tracks in very complicated events [1]. At the same time investigations have been continuing into the adaptation of this technology to X-ray imaging applications. In particular, this technology enables the counting of particles which are deposited in each pixel. A first large proto-

type chip, the photon counting chip (PCC or Medipix1) [2], has been successfully developed and measured. This chip demonstrated that the photon counting approach provides images with excellent dynamic range which are practically free of nonphotonic noise [3], [4]. The performance of the system was limited mainly by the size of the pixel ( $170 \mu\text{m} \times 170 \mu\text{m}$ ) which was determined by the component density of the  $1\text{-}\mu\text{m}$  CMOS process used.

Encouraged by these results we decided to make a new version of the chip in a  $0.25\text{-}\mu\text{m}$  CMOS technology. Each pixel measures only  $55 \mu\text{m} \times 55 \mu\text{m}$  and contains around 500 transistors. This reduction in pixel dimension is possible because of the tiny dimensions of the individual transistors as well as the high number of metal interconnect layers. The new system provides a spatial resolution comparable to that achieved by much simpler integrating readout systems while keeping excellent signal-to-noise and dynamic range, inherent properties of the photon counting method. Moreover, some new features could be included in the pixel cell: leakage current compensation on a pixel by pixel basis, sensitivity to carriers of both types and an energy windowed discriminator.

The architecture and functional behavior of Medipix2 chip are described in this paper. First, preliminary measurements are presented. Some new ideas for future pixel detectors are explained at the end of this paper.

## II. CHIP DESCRIPTION

The Medipix2 chip has been designed to minimize the dead area between chips covering large areas when butting several chips together. This is achieved placing the *periphery* at the bottom of the chip, and minimizing the *nonsensitive area* in the other three edges to less than  $50 \mu\text{m}$ . Fig. 1 shows the *Medipix2* floor plan organization. The *sensitive area* (top box) is arranged as a matrix of  $256 \times 256$  pixels of  $55 \times 55 \mu\text{m}^2$  resulting in a detection area of  $1.98 \text{ cm}^2$  which represents 87% of the entire chip area. The periphery (bottom box) contains 13 8-b DACs and the input–output (I/O) control logic. There are five lateral I/O wire-bonding pads which can be used to make a daisy chain of chips. In a multichip detector there would be no dead area between neighboring chips except two  $200\text{-}\mu\text{m}$  wide pixel rows and columns.

Both the analog and digital circuitry have been designed to operate with independent 2.2-V power supplies with a total analog power consumption of about 500 mW. The chip contains around 33 million transistors.

Manuscript received November 26, 2002; revised June 5, 2002. This project has been undertaken in the framework of the Medipix2 Collaboration, <http://www.cern.ch/MEDIPIX>.

X. Llopert, M. Campbell, and R. Dinapoli are with the European Organization for Nuclear Research (CERN), Geneva 23, Switzerland (e-mail: llopert@cern.ch).

D. San Segundo is with The National Institute for Nuclear Physics and High Energy Physics (NIKHEF), 1098 SJ Amsterdam, The Netherlands.

E. Pernigotti was with the European Organization for Nuclear Research (CERN), Geneva 23, Switzerland, the University of Pisa and the National Institute of Nuclear Fusion (INFN), 56010 Pisa, Italy. He is now with ST Microelectronics, 20127 Milano, Italy.

Digital Object Identifier 10.1109/TNS.2002.803788

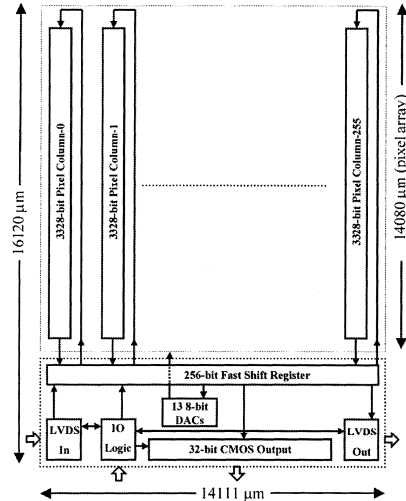


Fig. 1. Schematic floorplan of the Medipix2 chip.

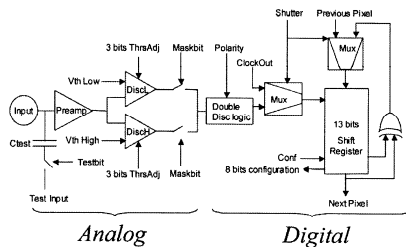


Fig. 2. Medipix2 pixel cell schematic.

#### A. Pixel Cell

When a charged particle interacts in the detector material it deposits a charge which drifts toward the collection electrode. This charge is then amplified and compared with two different thresholds that form an energy window. If the detected charge falls inside this energy window the digital counter is incremented.

The pixel has two working modes depending on the CMOS input *shutter* state. When the *shutter* signal is low the pixel is in acquisition mode. In this case, the output of the double discrimination logic (see Section II-A.2) is used as the clock of the counter [5]. When the *shutter* is high an external clock is used to shift the data from pixel to pixel (see Section II-A.3). Each pixel has eight independent configuration bits. Six of them are used for the fine threshold adjustment (3 b for each discriminator), one for masking noisy pixels, and one to enable the input charge test through the 8 ff-on-pixel capacitance. Fig. 2 shows

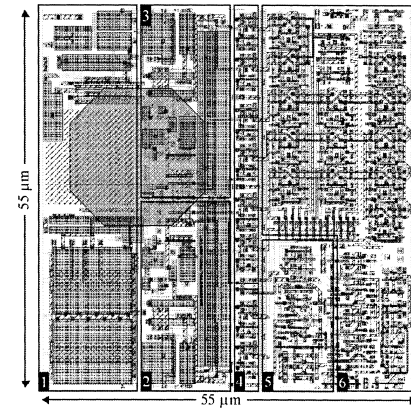


Fig. 3. Medipix2 pixel cell layout. 1: Preamplifier. 2: High threshold discriminator. 3: Low level discriminator. 4: 8-b configuration register. 5: Double discriminator logic. 6: Shift register and control logic.

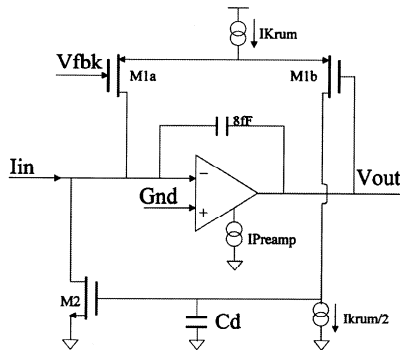


Fig. 4. Preamplifier scheme.

the schematic of the Medipix2 pixel cell. The analog side contains a charge preamplifier with dc leakage current compensation, a test capacitance, and two branches of identical discriminators. The digital side contains the double discriminator logic (DDL) and the 13-b shift register. The dimensions of the cell are  $55 \times 55 \mu\text{m}^2$ . Each pixel has 504 transistors and a static power consumption of  $\sim 8 \mu\text{W}$ . The octagonal bump bond opening, placed on top of the analog side, has a diameter of  $20 \mu\text{m}$ . In Fig. 3 the layout of the pixel cell is shown where the most important blocks are confined in a box.

*1) The Charge Preamplifier:* The preamplifier follows the scheme proposed by Krummenacher [6] based on a differential CMOS amplifier as shown in Fig. 4. A differential input amplifier was chosen for better rejection of substrate and power supply noises.

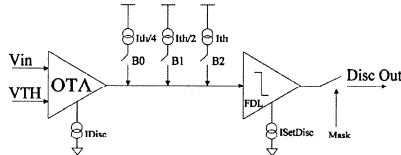


Fig. 5. Discriminator scheme.

This configuration provides a constant current fast return to zero through the transistors M1a and M1b controlled by the *IKrum* current digital-to-analog converter (DAC). The M2 transistor compensates the detector dc leakage current. Positive leakage currents (hole collection) smaller than *IKrum* and negative (electron collection) smaller than *IKrum/2* can be compensated in each pixel. Another voltage DAC controls the *Vfbk* node. This node sets the dc output voltage optimizing the dynamic range depending whether holes or electrons are being collected. The polarity of collection is selected using the *Polarity* input pad at the DAC level. The change of this voltage affects the overall gain of the preamplifier due to the change in the biasing point, resulting in slightly different gains for the two collection modes.

2) *The Discriminator*: The output of the preamplifier feeds two identical discriminators which have a linear behavior up to  $80 \text{ ke}^-$ . These two branches are independent and the discrimination energy can be set differently depending on the application. The difference between the two energy levels ( $W_{\text{th}} = V_{\text{thHigh}} - V_{\text{thLow}}$ ), defines the energy window ( $W_{\text{th}}$ ) into which the incoming particle energy has to fall in order to increment the counter. This window discrimination is performed by the DDL.

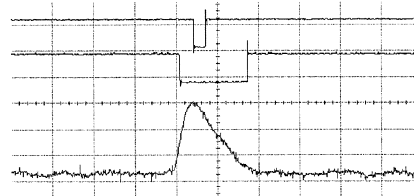
If the  $V_{\text{thHigh}}$  is set to be smaller than  $V_{\text{thLow}}$ , the DDL works in single discrimination mode, and the counter is incremented when the incoming particle energy exceeds the  $V_{\text{thLow}}$  threshold.

In Fig. 5, only one discriminator branch is shown. Each branch includes a differential amplifier configured to work as an *operational transimpedance amplifier* (OTA), three independent selectable current sources to minimize the spread of the threshold distribution from pixel to pixel, and a current discriminator. The output can be masked in case of malfunction or excessive noise.

3) *The Shift Register*: The shift register has two modes depending on the state of the *shutter* signal. When the *shutter* is low the shift register works as a pseudorandom counter of 13 b with a dynamic range of 8001 counts. Every pulse coming from the discriminator logic increments by one the counter value. When the *shutter* is high an external clock can be used to shift the data from pixel to pixel. This mode is used both for setting the 8 configuration bits and for reading the 13-b counter information.

4) *The Periphery*: The periphery contains:

- 13 8-b DACs [7] which set the different bias voltages in the chip;
- A 256-b *fast shift register* (FSR) used to write in or readout the sensitive area;
- 127 I/O pads;

Fig. 6. Preamplifier analog output response to an injected charge of  $17200\text{e}^-$  (bottom), and discriminator digital output with threshold setting at  $16400\text{e}^-$  (top) and  $6300\text{e}^-$  (middle).  $X = 500 \text{ ns}$ ,  $Y_{\text{analog}} = 50 \text{ mV}$ ,  $Y_{\text{digital}} = 2 \text{ V}$ .

- LVDS drivers and receivers;
- I/O logic that controls the chip.

When the matrix is accessed to perform any I/O operation the data is organized in 256 columns of  $256 \times 13$  b. Therefore, each chip has 851 968 b to be read or written for any matrix I/O operation. The *Medipix2* uses a high-speed *low voltage differential signaling (LVDS)*, [8] logic for configuration and readout of the chip in serial mode. Also, a parallel 32-b single-ended CMOS bus is present for applications requiring even higher frame rates. The readout can be performed serially by using the LVDS output drivers or in parallel by means of the 32-b CMOS bus. The setting of the configuration register in the entire matrix and of the 13 8-b DACs is always done serially through the LVDS receivers. Using a clock of 100 MHz the entire matrix is readout in less than 9 ms through the serial port, while using the parallel option the readout is done in  $266 \mu\text{s}$ .

### III. MEASUREMENTS

Preliminary measurements were performed using an Integrated Measurement System's abstract test suite digital IC tester. All of the logic at the chip periphery (see Fig. 1) performed without error at 100 MHz, which is the highest clocking frequency available on the IC tester. The setting of the DACs, the FSR, the peripheral control logic, the 32-b CMOS bus, and the LVDS drivers and receivers performed without errors.

A first characterization of the pixel front-end has been achieved by applying a test pulse to the on-pixel injection capacitance of several pixels. Output pads from a  $3 \times 3$  pixel cluster of the active matrix have been provided to allow direct testing. Each of the preamplifier outputs of these test pixels and one digital output resulting from OR-gating the nine-discriminator outputs are accessible via output pads in the chip. An example of these test outputs is seen in Fig. 6. Using these test pads and reading the pixel counter information the pixel cell can be characterized.

Table I summarizes these measurements. All the sub-blocks of the pixel cell perform as in simulation.

Depending on the collection type different bias conditions of the amplifier are used achieving different results in gain and linearity. For deposited charges smaller than  $50 \text{ ke}^-$  a maximum count rate of 1 MHz per pixel is obtained without pile-up following the specifications.

The electronic noise is measured using the s-curve method [9] because of the poor precision in the measurement of the pream-

TABLE I  
PREAMPLIFIER MEASURED CHARACTERISTICS

	Electron Collection	Holes Collection
Gain	12.5 mV/ke <sup>e</sup>	13.25 mV/ke <sup>e</sup>
Non linearity	<3% to 100 ke <sup>e</sup>	<3% to 80 ke <sup>e</sup>
Peaking time	<150ns	
Return to baseline	<1μs for Qin < 50 ke <sup>e</sup>	
Electronic Noise	$\sigma_{nL} \sim 141 e^-$ $\sigma_{nH} \sim 200 e^-$	
Threshold dispersion in 1 row	$\sigma_{nTHL} \sim 360 e^-$ $\sigma_{nTHH} \sim 800 e^-$	
Analog power dissipation	~8 μW/channel for 2.2V supply	

plifier noise at its output. This method gives information of the noise in all the front-end chain. Having a fixed threshold an input charge is swept from no counter counts (under threshold) to 100% hits, creating an s-shaped curve. The effective threshold is at 50% of this s-curve. The charge difference between the 97.75% and 2.25% of the s-curve is four times the RMS noise of the front-end assuming Gaussian distributed noise. Having a double discriminator system, an electronic noise for each branch can be given. One is generated when the injected charge crosses the *Vth low* threshold ( $\sigma_{nL}$ ), and the second when crossing the *Vth high* threshold ( $\sigma_{nH}$ ). The threshold dispersion in one row is also shown for both threshold crossings ( $\sigma_{nTHL}, \sigma_{nTHH}$ ). The threshold dispersion between pixels can be later corrected adjusting the 3-b threshold fine-tuning present in each discriminator branch.

A radiation hardness measurement of *Medipix2* has been made using a dedicated machine (*Seifert RP149*). The target material used in the tube was tungsten and the X-ray energy peaked at 10 keV. Doses of 3.9 krad/min up to 150 krad and 8.04 krad/min from 150 to 500 krad were applied to the chip. An increase of the analog power supply current was observed from 200 to 260 mA, while a knee at around 200 krad was observed in the digital power supply, which feeds more than the 90% of the chip transistors. The chip worked properly up to 300 krad but with an overall increase of the power supply currents. After an irradiation of 500 krad the chip was annealed (one week at 100 °C) and it recovered to preirradiated values.

#### IV. FUTURE DEVELOPMENTS

When using the *photon counting* method with very small pixel cells (less than about 100-μm side), the phenomenon of *charge sharing* has to be addressed [10]. The photon interaction with the detecting medium convoluted with diffusion gives rise to an extended cloud of charge, whose lateral dimension might reach a size comparable to the pixel pitch. The study of energy deposition in segmented sensors and the signal formation in pixel detectors with different geometries will be the subject of numerous future studies.

At this point a short description of some aspects can be given already. We describe two different approaches to reduce or cancel the effects of charge sharing, one at the detector level and the other one at the electronics level.

##### A. Proposed detector solution

In a  $3 \times 3$  square pixel matrix the distance between the central pixel and the orthogonal pixels is shorter than to the diag-

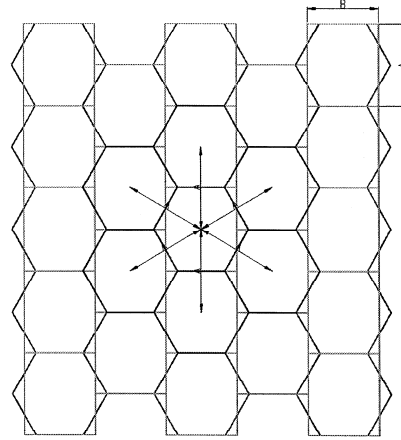


Fig. 7. Proposed detector layout  $B = 3A/2\sqrt{3}$ .

onal pixels. Using hexagonal pixels, as shown in Fig. 7, one can create an homogeneous environment for each pixel, with six equivalent neighbors. By doing this, the distance between neighboring pixels is constant in all directions achieving a much better spatial uniformity than square pixels.

This homogeneity in the sensor can only be achieved at the cost of more complexity in the readout. In order to physically match the hexagonal detector with the electronics, the pixel cells at the electronics level must be rectangular, as shown in Fig. 7. Moreover from column to column they have to be shifted up or down half a cell.

##### B. Proposed Electronic Solution

*Charge sharing* is related to the comparator threshold at the electronics level: as soon as the charge collected on one pixel falls below the threshold the hit will be ignored. Thus, in practice, the threshold would have to be set low enough to still increment the pixel's counter with the bigger fraction of collected charge without counting the event more than once. Consequently one would lose one advantage of a very precise threshold setting close to the incident photon energy. The other possibility of simply accepting the lower detection efficiency would imply an increased dose to patients and is, therefore, undesirable for medical applications. Assuming that the *charge sharing* effect only happens between adjacent pixels, a charge sharing control system can be built using the information coming from the six surrounding pixels and comparing it with the central pixel creating a seven-pixel cluster cell, as shown in Fig. 7.

In the proposed scheme of Fig. 8 the pixels in the cluster share the information of their discriminator output pulse (*DiscOut*). A voltage level discriminator generates this pulse with a threshold level set to a fixed value in the entire pixel matrix, slightly higher than the amplifier electronic noise (typically three times

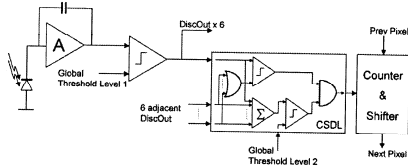


Fig. 8. Scheme of the proposed solution to take into account charge sharing effects.

higher). The discriminator output pulse length is proportional to the charge of the detected particle in this case. Two items of useful information can be obtained from the local pulse and the six neighboring pixels pulses. First, if the local pulse length is longer than any of the other six neighboring pixel pulses, then the local pixel collected the biggest *share* of charge generated by the incoming detected particle. This gives information of the position where the particle converted with an error smaller than  $2A/\sqrt{3}$  with respect to the pixel centroid (where  $A$  is the apothem of the hexagonal pixel). Second, adding up all the discriminator pulses, one can get the total deposited charge in this seven-pixel cluster, which is compared with a global threshold level (*global threshold level2*) in order to count only the photons with energies higher than the fixed threshold. These two last conditions must then be asserted at the same time to increment the counter.

This proposed system has to face two major constraints. First, the design and layout of a multipixel structure with connections between them, which must be contained in a very small pixel size (between 40–60  $\mu$ m side), is very difficult to achieve with our actual design technology (0.25- $\mu$ m minimum gate length and 6-metal layers). This can be overcome by moving to newer commercial CMOS deep submicron technologies with smaller gate length and more interconnection metal layers. The second constraint is the design of very low noise amplifier and discriminator cells, in order to minimize the threshold spread distribution and mismatch between adjacent channels.

## V. CONCLUSION

The *Medipix2* chip has been designed using a commercial deep-submicron technology building a pixel cell of 55  $\mu$ m  $\times$  55  $\mu$ m.

First measurements show an electronic pixel noise of 140 e<sup>-</sup> rms and an unadjusted threshold variation around 360 e<sup>-</sup> rms. A final design of a dedicated *Medipix2* readout system is in its last production stages. Once this readout system is finished, more precise and complete measurements about threshold calibration and variation will be done in order to provide a full calibration of the chip.

## ACKNOWLEDGMENT

The authors would like to thank all members of the *Medipix Collaboration* for their support and encouragement.

## REFERENCES

- [1] D. Di Bari *et al.*, "Performance of  $0.5 \times 10^6$  sensitive elements pixel telescope in the WA97 heavy ion experiment at CERN," *Nucl. Instrum. Methods in Phys. Res. A, Accel. Spectrom. Detect. Assoc. Equip.*, vol. A395, pp. 391–397, 1997.
- [2] M. Campbell *et al.*, "Readout for a  $64 \times 64$  pixel matrix with 15-b pixel photon counting," *IEEE Trans. Nucl. Sci.*, vol. 45, pp. 751–753, June 1998.
- [3] C. Schwarz *et al.*, "Measurements with Si and GaAs pixel detectors bonded to photon counting readout chips," *Nucl. Instrum. Methods Phys. Res. A, Accel. Spectrom. Detect. Assoc. Equip.*, vol. A466, pp. 87–94, 2001.
- [4] B. Mikulec, "Single photon detection with semiconductor pixel arrays for medical imaging applications," Ph.D. dissertation, Univ. Vienna, Vienna, Austria, June 2000.
- [5] P. Horowitz and W. Hill, *The Art of Electronics*. Cambridge, U.K.: Cambridge Univ. Press, 1980, p. 438.
- [6] F. Krummenacher, "Pixel detectors with local intelligence: An IC designer point of view," *Nucl. Instrum. Methods Phys. Res. A, Accel. Spectrom. Detect. Assoc. Equip.*, vol. A305, pp. 527–532, 1991.
- [7] F. Corsi *et al.*, "Design and characterization of a DAC for the slow control of the pixel chip," in *Proc. 6th Workshop Electronics for LHC Experiments*, Cracow, Poland, Sep. 11–15, 2000, pp. 560–564.
- [8] [Online]. Available: <http://www.national.com/appinfo/lvds/>.
- [9] F. Anghinolfi *et al.*, "A 1006 element hybrid silicon pixel detector with strobed binary output," *IEEE Trans. Nucl. Sci.*, vol. NS-39, pp. 654–661, Aug., 1992.
- [10] M. Chmeissani and B. Mikulec, "Performance limits of a single photon counting pixel system," *Nucl. Instrum. Methods Phys. Res. A, Accel. Spectrom. Detect. Assoc. Equip.*, vol. A460, pp. 81–90, 2001.



**PAPER II**

**First test measurements of a 64k pixel readout chip working in single photon  
counting mode**

**P a p e r II**





ELSEVIER

Available online at [www.sciencedirect.com](http://www.sciencedirect.com)



Nuclear Instruments and Methods in Physics Research A 509 (2003) 157–163

NUCLEAR  
INSTRUMENTS  
& METHODS  
IN PHYSICS  
RESEARCH

Section A

[www.elsevier.com/locate/nima](http://www.elsevier.com/locate/nima)

## First test measurements of a 64k pixel readout chip working in single photon counting mode

X. Llopard\*, M. Campbell

CERN, 23 1211 Geneva, Switzerland

### Abstract

The Medipix2 chip is a pixel detector readout chip consisting of  $256 \times 256$  identical elements, each working in single photon counting mode for positive or negative input charge signals. The chip is designed and manufactured in a six-metal  $0.25\text{ }\mu\text{m}$  CMOS technology. This paper describes several electrical measurements which have been carried out on the chip prior to detector bump bonding using a dedicated readout system. Threshold linearity and variation has been measured for both electron and hole collection. The noise is  $\sim 100\text{e}^-$  RMS and the threshold can be adjusted to  $\sim 120\text{e}^-$  RMS for both polarities. The minimum operating threshold is  $\sim 1000\text{e}^-$ .  
© 2003 Elsevier B.V. All rights reserved.

PACS: 07.50.Qx; 07.85.Fv; 85.60.Gz; 87.85.Mj; 87.59.–e

Keywords: Photon counting; Pixel; CMOS; X-rays; Medipix

### 1. Introduction

There is growing interest in the application of hybrid pixel detector technology to fields outside of elementary particle physics. In response to this interest a number of developments are taking place which are well summarized in Ref. [1]. One of the most ambitious of these developments is the Medipix2 chip [2] which has been supported by a large multi-national collaboration [3]. In this paper we report on first detailed measurements of the electrical behaviour of the chip. In particular, measurements of the noise, threshold variation and minimum threshold are presented.

### 2. Brief review of the chip architecture

The Medipix2 chip is composed mainly of an *active area* of  $256 \times 256$  pixels. Each pixel measures  $55 \times 55\text{ }\mu\text{m}^2$  resulting in a total sensitive detection area of  $1.98\text{ cm}^2$  representing 87% of the entire chip area. The *periphery* includes the IO control logic, 13 8-bit DACs and 127 IO wire-bonding pads. The *periphery* is placed at one side of the chip allowing for three-side buttability. Most of the wire-bonding pads are arranged in a single row but there are also five lateral IO wire-bonding pads which can be used to make a daisy chain between neighbouring chips. In a multi-chip configuration, an example of which is shown in Fig. 1, there would be no dead area between neighbouring chips but there is a slight loss in spatial resolution as two  $165\text{-}\mu\text{m}$ -wide pixel rows

\*Corresponding author.

E-mail address: [xavier.llopard@cern.ch](mailto:xavier.llopard@cern.ch) (X. Llopard).

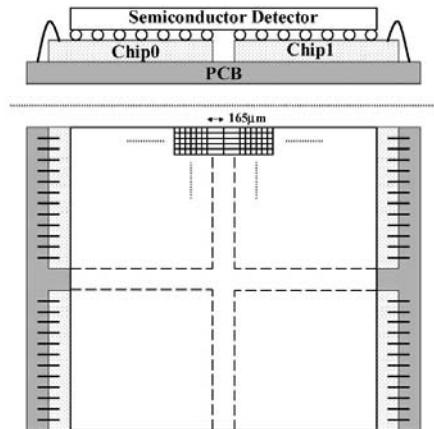


Fig. 1. Lateral and top view of a 4-chip structure. Between chips there will be special pixels which are three times longer than normal.

and columns are used to cover the unavoidable gaps between the chips.

Both the analog and digital circuits have been designed to operate with independent 2.2 V power supplies with a total analog power consumption of  $\sim 500$  mW. The digital power consumption varies as a function of the readout frequency and peaks during the readout phase. Using an 80 MHz clock the peak digital consumption is  $\sim 100$  mW. The chip contains around 33 million transistors.

### 2.1. Pixel cell

The pixel cell works in photon counting mode. When a charged particle interacts in the detector material it deposits a charge which drifts towards the collection electrode. This charge is then amplified and compared with two different thresholds that form an energy window. If the detected charge falls inside this energy window a 13-bit digital counter is incremented. If the high threshold is set below the level of the low threshold all hits above the low threshold are counted. Fig. 2 shows the schematic of the Medipix2 pixel cell.

The pixel has two working modes depending on the state of the CMOS input signal *Shutter*. When

the *Shutter* signal is low the pixel is in acquisition mode. In this case, the output of the double discrimination logic is used as the clock of the counter as described above. When the *Shutter* is high an external clock is used to shift the data from pixel to pixel.

Each pixel has eight independent configuration bits. Six of them are used for the fine threshold adjustment (three bits for each discriminator), one for pixel masking and one to enable the input charge test through the 8 fF on-pixel capacitance. Each pixel has 504 transistors and a static power consumption of  $\sim 8$   $\mu$ W. Particular care has been taken in the design in order to minimize any systematic deviations in the behaviour of the cells as a consequence of effects such as top-down power supply voltage drops.

### 2.2. The periphery

When the matrix is accessed to perform any IO operation the data are organized in 256 columns of  $256 \times 13$  bits. Therefore, each chip has 851968 bits to be read or written for any matrix IO operation. The Medipix2 uses a high-speed *low-voltage differential signaling (LVDS [4])* logic for configuration and serial readout. Readout may also be carried out using a parallel 32-bit single-ended CMOS bus for applications requiring even higher frame rates. The setting of the configuration register in the matrix and of the 13 8-bit DACs is always done serially through the LVDS receivers. Using a clock of 100 MHz the matrix is readout in less than 9 ms through the serial port, while using the parallel option the readout is done in 266  $\mu$ s.

### 3. Electrical measurements on the matrix

In order to characterize the electrical behaviour of the chip prior to detector bump bonding, precise and complete measurements for both electron and hole collection have been carried out.

To perform these different measurements a dedicated readout system was used. The readout chain consists of a PC/PCI standard acquisition card sitting in a PC connected through a 68-pin

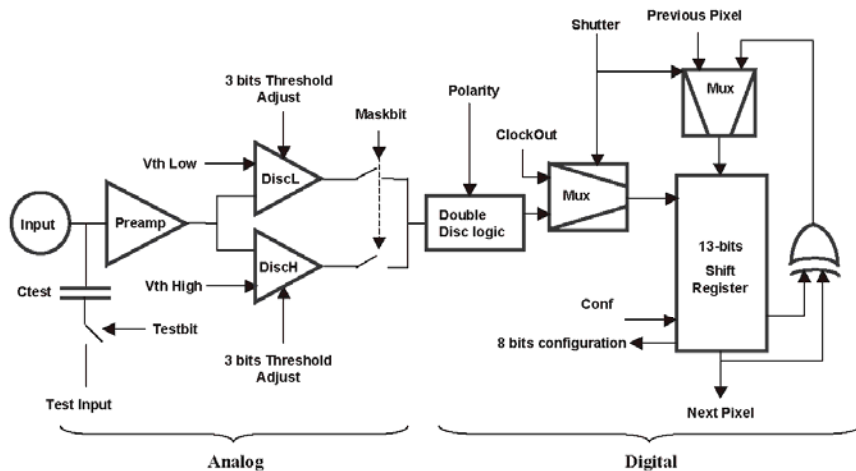
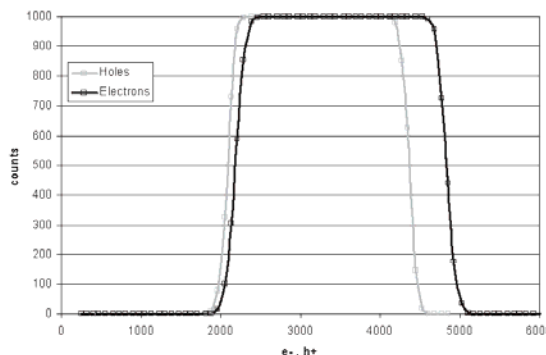


Fig. 2. Schematic of the Medipix2 pixel cell.

Fig. 3. Hat-curve for electron and hole collection. From the rising and falling edge of each curve and electronic noise of  $\sim 100e^-$  RMS can be extracted for both thresholds.

cable to an interface card called Muros2 [5]. This card generates the various digital signals and analog voltages needed to operate the chip and acts as an interface between the chip and the PC. The Medipix2 chip is glued to a custom-designed chipboard and is in turn connected through a 64-

pin VHDCI<sup>1</sup> cable to the Muros2 card. The full readout chain is controlled with specially designed software running under LabWindows [6] called Medisoft4 [7,8].

<sup>1</sup>VHDCI stands for Very High Digital Cable Interconnect.

An Agilent 81110A GPIB<sup>2</sup> controlled pulser generator was used to provide the precise electrical input pulse necessary to measure the performance of the pixels.

In order to estimate the injected charge in each pixel two parameters have been extracted from simulations. Firstly, the injection capacitance could not be calibrated, but only estimated from the data on layer-to-layer capacitance provided by the chip manufacturer. And secondly, the analog buffers used to transmit the external test pulse to each column have a certain attenuation that could not be measured but only estimated from HSPICE simulations. All numbers given in electrons ( $e^-$ ) are based on these both estimates, which may cause some systematic deviations.

To extract the effective low and high thresholds as well as the electronic noise from each pixel the *hat-curve* method was used. Setting the low and high thresholds to a fixed value (usually through two internal 8-bit DACs) 1000 pulses were applied to each pixel and the counter value read out. The test input charge is gradually increased from no counter counts (under threshold) to 100% hits (inside energy window) and, for bigger input charges, to no counter counts (over threshold), see Fig. 3. The effective low threshold is at 50% of the rising edge of this *hat-curve* while the effective high threshold is at 50% of the falling edge. The charge difference between 97.7% and the 2.3% in both slopes is four times the RMS noise of the front-end seen for each discrimination branch assuming Gaussian distributed noise. The electronic noise found for both thresholds and collection modes is  $\sim 100e^-$  RMS at the default preamplifier current. Tuning this current the electronic noise can be lowered to  $\sim 90e^-$  RMS.

It is possible to tune the threshold using the 3-bits available for each threshold in each pixel. However, since there are 65536 pixels in the matrix, two assumptions have been made to speed up the threshold adjustment calculation procedure. Firstly, having one analog buffer to restore the calibration pulse for each column allows us to pulse all the columns and several rows at once. It

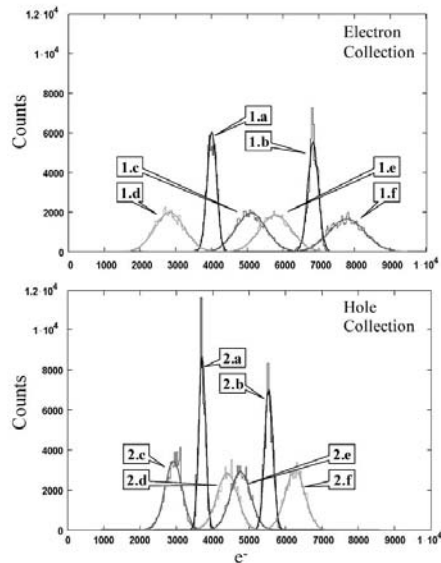


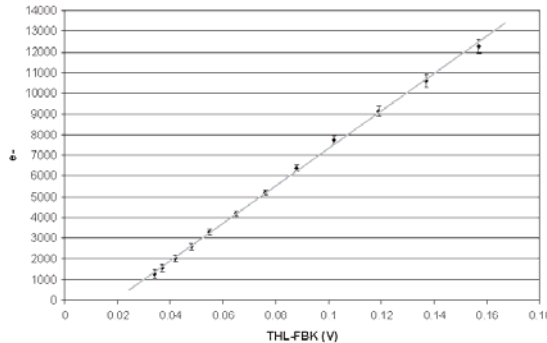
Fig. 4. Electron collection (top): (1.a) adjusted low threshold; (1.b) adjusted high threshold; (1.c) unadjusted low threshold *LowCode*; (1.d) unadjusted low threshold *HighCode*; (1.e) unadjusted high threshold *HighCode*; (1.f) unadjusted high threshold *LowCode*. Hole collection (bottom): (2.a) adjusted low threshold; (2.b) adjusted high threshold; (2.c) unadjusted low threshold *LowCode*; (2.d) unadjusted low threshold *HighCode*; (2.e) unadjusted high threshold *LowCode*; (2.f) unadjusted high threshold *HighCode*.

has been found experimentally that by pulsing 16 or less rows simultaneously the calculated threshold was unchanged. And secondly, as the average DNL<sup>3</sup> is less than 2% for all the 3-bit threshold adjustment current DACs present in the chip, a linear interpolation between the code 0h (*LowCode*) and the code 7h (*HighCode*) has been made to calculate the intermediate adjustment distributions.

In Fig. 4 two plots are shown. The top plot shows the threshold adjustment distributions for negative charge collection; while the bottom one

<sup>2</sup>GPIB stands for General Purpose Interface Bus. This bus is also known as IEEE-488.

<sup>3</sup>Differential non-linearity.

Fig. 5. Threshold linearity in electrons collection mode up to 12ke<sup>-</sup>.

shows the same for positive charge collection. In each plot there are two histograms corresponding to the *LowCode* and the *HighCode* for the low unadjusted threshold and two histograms corresponding to the *LowCode* and the *HighCode* for the high unadjusted threshold. The mid-point between the *LowCode* and *HighCode* distributions is the centre of the new adjusted distribution for each threshold. All the histograms are successfully fitted with a Gaussian distribution. From each fit the threshold mean and sigma can be extracted. The sigma of the unadjusted threshold dispersion is around 450e<sup>-</sup> RMS for negative charges whilst for positive charge collection it is around 250e<sup>-</sup> RMS. Some systematic behaviour has been detected for electron collection. This is thought to be due to an unforeseen sensitivity of the discriminator to top-down power supply voltage drops for this polarity only. Nevertheless, by tuning each pixel threshold with the 3-bit adjustment, the systematic and random mismatches are corrected achieving a sigma around 120e<sup>-</sup> RMS for both thresholds and for each collection mode.

The threshold linearity is shown in Fig. 5. Although the threshold setting should be linear up to 80ke<sup>-</sup>, the threshold linearity scan was limited to injected charges up to 12ke<sup>-</sup> in order to work in the linear range

of the external pulser. Each data point of the plot in Fig. 5 shows the mean threshold and  $\pm 1\sigma$  of the threshold variation for different global low thresholds from 0 to 12ke<sup>-</sup> set using the internal THL 8-bit DAC. Note that the threshold variations indicated on this curve are subsequent to threshold tuning. For these measurements the chip was working in single discrimination mode. The measured non-linearity is less than 3% over the studied range.

An important measurement for applications that need to detect low-energy particles is the effective minimum threshold. Applying the calculated equalization map, the global threshold can be lowered to a mean minimum of  $\sim 1000e^-$  with a sigma of  $\sim 180e^-$  RMS for both collection modes. It may be possible to further reduce this variation with a more sophisticated threshold tuning procedure. Fig. 6 shows the threshold distribution for electrons which has been tuned at around 4000e<sup>-</sup> and then reduced to 1100e<sup>-</sup>. Fig. 7 shows an image taken with the Medisoft 4.0 [7,8] with the previous settings and injecting 1000 pulses of 2ke<sup>-</sup> simultaneously to the pixels selected by the Medipix2 and CERN logos, while keeping all the rest of the pixels in the matrix unmasked. Some missing columns and one defective column are evident but the unpulsed pixels are otherwise quiet.

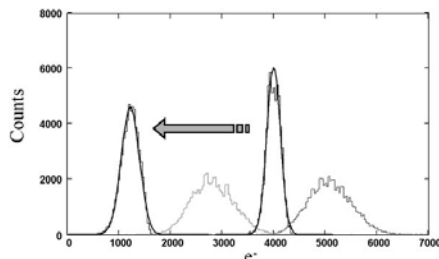


Fig. 6. Example of minimum threshold distribution in electron collection mode.

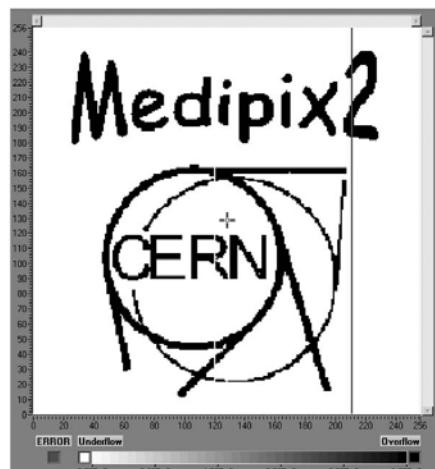


Fig. 7. Image taken using the calculated threshold adjustment map and applying the logo mask to the Testbit. The rest of the matrix is unmasked, the equivalent low threshold is set at  $1.1\text{ke}^-$  and 1000 pulses of  $2\text{ke}^-$  were injected to each pixel simultaneously.

#### 4. Conclusions and future work

The Medipix2 has been successfully measured and calibrated prior to bump bonding. The measurements done in the chip are in almost perfect agreement with simulations. The chip has a threshold variation of  $\sim 450\text{e}^-$  RMS for electron

collection and  $\sim 250\text{e}^-$  RMS for hole collection before adjustment. After tuning the threshold variation is  $\sim 120\text{e}^-$  RMS for both collection polarities. The electronic noise is  $\sim 100\text{e}^-$  RMS depending on the amplifier biasing. The minimum threshold is  $\sim 1000\text{e}^-$  for both polarities. The differential non-linearity of the threshold is less than 3% over  $12\text{ke}^-$ .

The first Medipix 2 chips bump-bonded to Silicon detectors will be available shortly. It will then be possible to explore the potential of the chip for different applications. Moreover the new assemblies will permit a precise calibration of the values described in this paper. Looking ahead, 4-chip detectors (*Quads*) have been fabricated and are ready to be assembled to readout chips resulting in a total sensitive area of greater than  $8\text{ cm}^2$  with more than 256k active pixels.

In the future larger areas should be covered. Using present day interconnect techniques one edge of the chip is always reserved for IO. It is becoming increasingly popular in the microelectronics industry to drill holes through the readout chip to bring in power supplies and other signals anywhere across the chip surface. Such techniques may be applied in future pixel readout chip designs to obtain the desired four-sided buttability.

#### Acknowledgements

Erik Heijne is a constant source of guidance and inspiration for the authors. We would also like to thank the developers of the Muros2 readout system led by Jan Visschers: David San Segundo, Alessandro Fornaini and Hans Verkooijen from NIKHEF, Amsterdam. We also gratefully acknowledge the authors of Medisoft4 led by Paolo Russo: Marino Maiorino (now in IFAE, Barcelona), Cristina Montesi and Gianni Mettivier from the University Federico II and INFN, Naples.

#### References

- [1] B. Mikulec, Developments of segmented semiconductor arrays for quantum imaging, Samba II Conference, 27–29 May 2002, Trieste, Italy.

- [2] X. Llopart, et al., IEEE Trans. Nucl. Sci. NS-49 (2002) 2279.
- [3] <http://www.cern.ch/medipix>.
- [4] <http://www.national.com/appinfo/lvds/>.
- [5] D. San Segundo Bello, et al., An interface board for the control and data acquisition of the Medipix2 chip, IWORID2002 (Amsterdam) Proceedings, 2002.
- [6] <http://www.ni.com/cvi>.
- [7] Bertolucci, et al., Medisoft4: a software procedure for the Medipix2 Readout chip, Conference Record of the IEEE Nuclear Science Symposium and Medical Imaging Conference, San Diego, USA, November 4–10, 2001.
- [8] Bertolucci, et al., Preliminary test of Medisoft4: Control Software for the Medipix2 Read out chip, Conference Record of the IEEE Nuclear Science Symposium and Medical Imaging Conference, Norfolk, USA, November 10–16, 2002.



**PAPER III**

**X-ray imaging using single photon processing with semiconductor pixel  
detectors**



P a p e r III





ELSEVIER

Available online at [www.sciencedirect.com](http://www.sciencedirect.com)



Nuclear Instruments and Methods in Physics Research A 511 (2003) 282–286

NUCLEAR  
INSTRUMENTS  
& METHODS  
IN PHYSICS  
RESEARCH

Section A

[www.elsevier.com/locate/nima](http://www.elsevier.com/locate/nima)

## X-ray imaging using single photon processing with semiconductor pixel detectors

B. Mikulec<sup>a,\*1</sup>, M. Campbell<sup>a</sup>, E. Heijne<sup>a</sup>, X. Llopard<sup>a</sup>, L. Tlustos<sup>a</sup>

<sup>a</sup> Medipix Collaboration, CERN, Division ETT, 1211 Geneva 23, Switzerland

### Abstract

More than 10 years experience with semiconductor pixel detectors for vertex detection in high-energy physics experiments together with the steady progress in CMOS technology opened the way for the development of single photon processing pixel detectors for various applications including medical X-ray imaging. The state of the art of such pixel devices consists of pixel dimensions as small as  $55 \times 55 \mu\text{m}^2$ , electronic noise per pixel  $<100 \text{ e}^- \text{ rms}$ , signal-to-noise discrimination levels around  $1000 \text{ e}^-$  with a spread  $<50 \text{ e}^-$  and a dynamic range up to 32 bits/pixel. Moreover, the high granularity of hybrid pixel detectors makes it possible to probe inhomogeneities of the attached semiconductor sensor.

© 2003 Elsevier B.V. All rights reserved.

PACS: 29.40.Gx; 29.40.Wk; 87.59.-e

Keywords: Single photon detection; Quantum imaging; Semiconductor detector; X-ray imaging; Medipix

### 1. Introduction

Hybrid semiconductor detectors represent the basic tools to perform particle tracking in the vertex region in high-energy physics experiments. The introduction of silicon strip detectors into this field dates back to 1980 [1], whereas silicon pixel detectors appeared at the beginning of the 1990s [2]. Silicon sensors have considerably improved since then, but the continuing popularity of semiconductor detectors can be accredited mainly

to progress in microelectronics. With reduced feature size the density of electronic components per unit area increases exponentially with time allowing increased functionality per unit area and/or reduced pixel size. With deep sub-micron technology it is currently possible to squeeze about 200 000 transistors into an area of  $1 \text{ mm}^2$ .

Small pixel sizes and correspondingly tiny input capacitance together with high electronics component densities, optimized transistors and chip design opened the new field of quantum processing for imaging applications [3,4]. Quantum processing implies that a particle signal can be distinguished from background noise. This noise discrimination is implemented with the help of a noise reducing pre-amplifier shaper circuit and a discriminator in each readout channel where it

\*Corresponding author. Tel.: +41-22-767-3788; fax: +41-22-767-3394.

E-mail address: [bettina.mikulec@cern.ch](mailto:bettina.mikulec@cern.ch) (B. Mikulec).

<sup>1</sup>Now with the University of Geneva, 30 Quai Ernest-Ansermet, 1211 Geneva 4, Switzerland.

must be possible to set the discrimination level safely above the noise level. With steadily shrinking pixel sizes this concept gets more complicated as the signal charge from one particle might be shared between a number of pixels. As a consequence, a solution should be found to sum up the charge fractions belonging to the charge deposition of one particle and compare the summed charge to a threshold [5].

The simplest example of quantum processing is photon counting; as soon as the processed signal passes the threshold the counter value of the readout channel is incremented. However, there is a great potential to be explored with more elaborated ways of processing single photon signals. Some projects start to use already two thresholds to select an energy band out of a continuous spectrum or perform subtraction images with one X-ray illumination (see Ref. [3]). For the future one can imagine to include a multi-bit ADC in each readout cell to provide ‘colour’ X-ray images [3,6]. Then it would also become possible to weight each of the ADC channels with its ideal energy weighting factor to increase the image contrast [7]. Noise discrimination is absolutely necessary to do low-dose or low-rate imaging, but it seems evident by now that energy information is ultimately wanted as well.

## 2. Detector requirements in medical imaging applications

In many aspects, detector requirements for medical imaging applications are very similar to high-energy physics applications. These include the need for high true two-dimensional spatial resolution and high sensitivity, but medical imaging should deliver in addition the lowest possible dose to the patient.

In general, detector requirements depend strongly on the imaging task. Therefore, detectors (sensors and electronics) should be optimized for different imaging applications. Protein crystallography, angiography, mammography or  $\gamma$ -ray imaging may have differing and sometimes conflicting requirements. As mammography has some of the most stringent specifications within all

medical imaging fields it was chosen as an example to illustrate the requirements for a dedicated imaging detector:

- (1) High spatial resolution: The required spatial resolution is different for analog and digital systems. Analog systems must comply with a spatial resolution of 15–20 lp/mm<sup>2</sup>, whereas 5–13 lp/mm for digital systems seem to be equivalent (see next point). High spatial resolution is necessary to detect tiny micro-califications, early indicators of breast cancer. This point is addressed in hybrid semiconductor detector development on one hand through steadily evolving miniaturization and on the other hand through direct detection of the X-rays in the semiconductor sensor without conversion layer (as used with CCDs, film and most flat panel imagers) to avoid image blurring.
- (2) High contrast resolution <3%: Contrast resolution is the greatest advantage of digital imaging systems compared to analog ones. Especially in regions of low detector illumination film is limited by the so-called fog level in the toe region of its characteristic curve. Superior contrast resolution is expected to be most beneficial for cancer detection in radiodense breasts (e.g. for younger women). Quantum processing can improve contrast resolution considerably.
- (3) Uniform response: Related to the previous point; for hybrid detectors this point concerns in particular the sensors (see Section 4).
- (4) Patient dose <3 mGy: To achieve low patient dose without information loss it is necessary to have imaging systems with high DQE<sup>3</sup> over a wide spatial frequency range. This implies high absorption and charge collection efficiency of the sensor as well as good noise performance of the readout chain. Direct detection and quantum processing are beneficial as well [7–9]. It is evident that the system has to possess as well sufficient counting rate capability.

<sup>2</sup>lp/mm—line pairs/mm.

<sup>3</sup>DQE—detective quantum efficiency.

- (5) Image area  $18 \times 24$  ( $24 \times 30$ )  $\text{cm}^2$ : This is still an unsolved problem for hybrid pixel detectors. One solution adopted especially with strip detectors is a scanning slit system with a linear detector covering one dimension. Pixel chips can now be designed to be three-side buttable which enables to make continuous arrays of pixel detectors along three sides. The fourth side is still needed for I/O. To solve this problem it might be possible in the future to make use of a technique increasingly popular in microelectronics industry, which is to etch holes through the readout chip to route power supply and other signal lines.
- (6) Digital system,
- (7) Compactness, simple handling, stable operation, no cooling, etc.,
- (8) Cheap.

### 3. The Medipix single photon processing ASICs

The Medipix1 chip was the first full-size photon counting ASIC and was designed with mainly mammography and dental imaging in view [10]. It emerged from experience gained with the design and the application of pixel chips for high-energy physics experiments; parts of the front-end of the Medipix1 chip were even taken over from the Omega3/LHC1 pixel chip. The Medipix1 chip has been extensively studied over the years leading to the design of an improved version of the chip, Medipix2, within the framework of the Medipix2 collaboration [5,11]. Just recently, Medipix2 arrived back from the foundry as well as the first Medipix2/Si assemblies. First electrical measurement results show that the chip is working in agreement with the simulations [12]. Table 1 shows a comparison between Medipix1 and Medipix2.

In Fig. 1 (left) an image of a  $300 \mu\text{m}$ -thick copper mask was taken with a  $^{109}\text{Cd}$  source and one of the first bump-bonded Medipix2/Si assemblies to give an impression of the tiny pixel size. The chip used for this image came from the first production run which showed a yield problem resulting in some dead columns. Moreover, during bump-bonding the sensor was shifted by three rows with respect to the chip. This misalignment is

Table 1  
Comparison between the Medipix1 and the Medipix2 single photon processing pixel chips

Medipix1	Medipix2
Square pixels; $170 \mu\text{m}$ at the side	Square pixels; $55 \mu\text{m}$ at the side
$64 \times 64$ pixels (4096)	$256 \times 256$ pixels (65 536)
Sensitive to pos. input charge	Sensitive to pos. and neg. input charge; free choice of sensor material
Sensor leakage current compensation columnwise	Pixel-by-pixel sensor leakage current compensation
One discriminator	Two discriminators (energy window) designed to be linear over a wide range
15-bit counter per pixel	13-bit counter per pixel
Max. counting rate	Max. counting rate
$\approx 1 \text{ MHz/pixel}$	$\approx 1 \text{ MHz/pixel}$
$(3.5 \text{ GHz/cm}^2)$	$(33 \text{ GHz/cm}^2)$
	$3 \times 3$ Matrix of pixels with analog output to study charge sharing
	Three-side buttable
Parallel I/O	Serial or parallel I/O
$1 \mu\text{m}$ SACMOS technology	$0.25 \mu\text{m}$ technology
(1.6 M transistors/chip)	(33 M transistors/chip)

visible as three dead rows at the bottom of the image and means that the guarding of the sensor was not connected. Neglecting these problems, the resulting image is very promising.

As a comparison an image of the same object under similar measurement conditions was made with a Medipix1/Si assembly (see right Fig. 1).<sup>4</sup> Due to the larger pixel size the number of counts/pixel is higher, but the contour of the letters is much worse.

At present, Medipix2 is the single photon processing pixel chip with the smallest pixel size and the highest counting rate per unit area. It will offer the possibility to study optimal pixel sizes for different applications and the implication of charge sharing effects to DQE and contrast resolution.

<sup>4</sup>The top right corner of the assembly shows some bump-bonding problems.

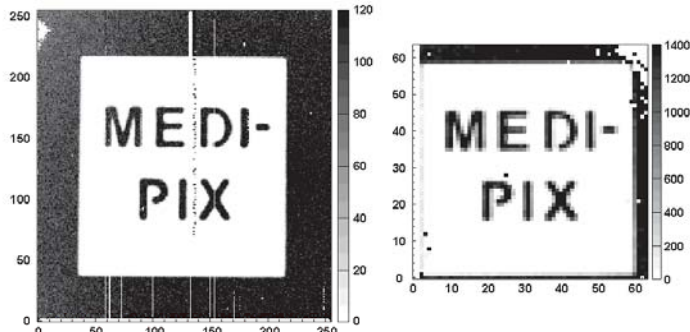


Fig. 1. Image of a copper mask taken with a  $^{109}\text{Cd}$  source; the left image comes from a Medipix2/Si assembly, the right one from a Medipix1/Si assembly.

#### 4. Low- and high-frequency noise in silicon detectors

For medical imaging applications it is imperative to reach a high DQE as mentioned before. The DQE describes how the SNR at the input of the imaging system ( $\text{SNR}_{\text{in}}$ ) is transferred to the output ( $\text{SNR}_{\text{out}}$ ) and can be written as  $\text{SNR}_{\text{out}}^2/\text{SNR}_{\text{in}}^2$ . Taking uniform illuminations of several Medipix1/Si assemblies (flood images) it was seen that the SNR defined in this case simply by the fraction (mean number of counts/sigma of the count distribution) quickly flattens out at values around 20 instead of following a square-root dependence predicted by Poisson statistics. Nevertheless, applying a flat-field correction resulted in a curve representing the theoretically predicted limit over the full dynamic range of the chip and reaching values of  $\text{SNR} > 160$  [3]. The flat-field correction is a correction method applied routinely in the imaging field. It consists of multiplying each imaging element with its calibration or ‘efficiency’ factor attributed beforehand with a certain number of flood fields. Investigations were, therefore, started to understand the reasons for the relatively large spread in counts under uniform illumination without flat-field correction.

Several observations were made and are summarized below [3,13,14]:

- (a) Low spatial frequency patterns: The silicon detectors show a ‘wave’ pattern of higher and lower counting regions, in particular visible while working in under-depletion. These ‘waves’ of period of the order of 1 mm move slightly increasing the detector bias voltage from a few volts until the depletion voltage ( $\approx 20$  V in our case). Increasing the bias voltage further, the location of the waves is stable and the amplitude decreases. Nevertheless, even at voltages above 100 V the wave structure is still visible with count variations around  $\pm 2\%$ . This low-frequency noise has been ascribed to bulk inhomogeneities due to doping fluctuations during crystal growth (see Ref. [15]). As it is stable in time it can be corrected for with a flat-field correction made at the corresponding detectors bias voltage.
- (b) High spatial frequency pattern: Besides the macroscopic fluctuations mentioned in (a), a fixed pattern noise locally varying from pixel to pixel has been observed. This high-frequency noise is independent of its location from the applied bias. A flat-field map made even in under-depletion can smoothen the pixel-to-pixel variations of an image taken in over-depletion. The reason for this observed high-frequency noise is still under investigation. Possible explanations might be variations in the pixel geometry and/or electric field

components parallel to the pixel surface due to doping inhomogeneities, which lead to differences in charge collection, or threshold variations.

(c) Energy dependence of the flat-field correction: It has been observed that the flat-field correction was ineffective in the case of an image taken with a mammographic phantom (objects embedded in 4 cm-thick PMMA) and a Mo X-ray tube (spectral X-ray source) where the flat field was calculated in the absence of any PMMA. Due to the higher absorption probability of low-energy X-rays in the PMMA (or the patient) compared to X-rays from the upper end of the spectrum, the X-ray spectrum incident on the detector is hardened. This results in a different mean conversion depth of the X-rays in the sensor leading to a different count distribution on the pixel matrix. Under real medical imaging conditions, this represents a problem as it might result in image artifacts and false diagnosis. Fortunately it was shown that an interpolated flat field map could effectively correct the data [14]. Thus, provided the thickness and density of the imaged object is known, an appropriate flat field correction can be used.

To conclude, it has been shown that single photon pixel detectors with small pixel size can be used as well to probe the connected semiconductor sensor. Even silicon sensors show pronounced low and high spatial frequency patterns in the count distribution of a uniform illumination. Due to the energy dependence of some correction methods used for imaging applications it would be desirable to improve the sensor uniformity.

## 5. Conclusions

Single photon processing is becoming more and more popular for various kinds of imaging applications due to its advantages compared to charge integrating systems. It has a huge and still unexploited potential as use of the energy information may lead to ‘colour’ X-ray imaging.

## References

- [1] E.H.M. Heijne, L. Hubbeling, B.D. Hyams, P. Jarron, P. Lazeyras, F. Piuz, J.C. Vermeulen, A. Wylie, Nucl. Instr. and Meth. 178 (1980) 331, CERN/ECP 91–26.
- [2] F. Anghinolfi, et al., IEEE Trans. Nucl. Sci. NS-39 (1992) 654.
- [3] B. Mikulec, Development of segmented semiconductor arrays for quantum imaging, Presented at the Samba2 Conference, Trieste, Italy, May 27–29 2002, Nucl. Instr. and Meth. A (2003), in press.
- [4] M. Campbell, Electronics for pixel detectors, Proceedings of the Seventh Workshop on Electronics for LHC Experiments, Stockholm, Sweden, 10–14 September 2001.
- [5] X. Llopert, M. Campbell, R. Dinapoli, D. San Segundo, E. Perdigotti, IEEE Trans. Nucl. Sci. NS-49, (2002) 2279.
- [6] S. Cadeddu, C. Caligiore, M. Caria, A. Lai, D. LoPresti, S. Panebianco, C. Pettà, P. Porcu, N. Randazzo, S. Reito, G.V. Russo, Nucl. Instr. and Meth. A 419 (1998) 270.
- [7] R.N. Cahn, B. Cederström, M. Danielsson, A. Hall, M. Lundqvist, D. Nygren, Med. Phys. 26 (12) (1999) 2680.
- [8] J. Watt, D.W. Davidson, C. Johnston, C. Smith, L. Thustos, B. Mikulec, K.M. Smith, M. Rahman, Dose reductions in dental X-ray imaging using Medipix, Presented at the Sixth International Conference on Position Sensitive Detectors, Leicester, England, 9–13 September 2002, Nucl. Instr. and Meth. A, (2003) accepted for publication.
- [9] D.W. Davidson, J. Watt, L. Thustos, B. Mikulec, M. Campbell, K. Mathieson, V. O’Shea, K.M. Smith, M. Rahman, Detective quantum efficiency of the Medipix pixel detector, Presented at the IEEE NSS/MIC Conference, Norfolk, Virginia, 10–16 November 2002, to appear in the Conference Records.
- [10] M. Campbell, E.H.M. Heijne, G. Meddeler, E. Perdigotti, W. Snoeys, IEEE Trans. Nucl. Sci. NS-45(3) (1998) 751, CERN-ECP/97-010.
- [11] The Medipix2 Collaboration consists of 16 European institutes; see <http://medipix.web.cern.ch/MEDIPIX/>.
- [12] X. Llopert, M. Campbell, First test measurements of a 64k pixel readout chip working in single photon counting mode, Presented at the IWORID Conference 2002, Amsterdam, The Netherlands, 2002, Nucl. Instr. and Meth. A, (2003) in press.
- [13] L. Thustos, D. Davidson, M. Campbell, E. Heijne, B. Mikulec, Fixed pattern deviations in Si pixel detectors measured using the Medipix1 readout chip, Presented at the IWORID Conference 2002, Amsterdam, The Netherlands, 2002, Nucl. Instr. and Meth. A, (2003) in press.
- [14] D.W. Davidson, C. Frödjh, V.O’Shea, H.-E. Nilsson, M. Rahman, Limitations to flat-field correction methods when using an X-ray spectrum, Presented at the IWORID conference 2002, Amsterdam, The Netherlands, 2002, Nucl. Instr. and Meth. A, (2003) in press.
- [15] W. von Ammon, H. Herzer, Nucl. Instr. and Meth. 226 (1984) 94–102.



**PAPER IV**

**First Experimental Tests with a CdTe Photon Counting Pixel Detector  
Hybridized with a *Medipix2* Readout Chip**



**P a p e r I V**



# First Experimental Tests With a CdTe Photon Counting Pixel Detector Hybridized With a Medipix2 Readout Chip

M. Chmeissani, C. Frojdh, O. Gal, X. Llopert, J. Ludwig, M. Maiorino, E. Manach, G. Mettivier, M. C. Montesi, C. Ponchut, P. Russo, *Member, IEEE*, L. Tlustos, and A. Zwerger

**Abstract**—We present preliminary tests of hybrid pixel detectors consisting of the Medipix2 readout chip bump-bonded to a 1-mm-thick CdTe pixel detector. This room temperature imaging system for single photon counting has been developed within the Medipix2 European Collaboration for various imaging applications with X-rays and gamma rays, including dental radiography, mammography, synchrotron radiation, nuclear medicine, and radiation monitoring in nuclear facilities. The Medipix2 + CdTe hybrid detector features  $256 \times 256$  square pixels, a pitch of  $55 \mu\text{m}$ , a sensitive area of  $14 \times 14 \text{ mm}^2$ . We analyzed the quality of the detector and bump-bonding and the response to nuclear radiation of the first CdTe hybrids. The CdTe pixel detectors, with Pt ohmic contacts, showed an ohmic response when negatively biased up to less than 60 V (electrons collection mode). Tests were also performed in holes collection mode, where a nonresistive behavior was observed above +15 V. We performed a series of imaging tests at low voltage bias with gamma radioactive sources and with an X-ray tube. Under uniform irradiation, we observed for all detectors the presence of numerous, stable structures in the form of small circles of about  $200 \mu\text{m}$  diameter, with the central pixels showing a reduced counting efficiency with respect to the periphery (in electrons counting regime). Also long filament structures have been observed. Further investigations will reveal whether they are due to an intrinsic detector response (e.g., due to Te inclusions) or to the bump-bonding process.

**Index Terms**—CdTe, hybrid detectors, Medipix2.

## I. INTRODUCTION

RECENTLY, the Medipix2 European Collaboration<sup>1</sup> has produced the first version of the Medipix2 application-specific integrated circuit (ASIC), a CMOS chip (designed

at CERN, Geneva, Switzerland) for the readout of pixel semiconductor detectors to be used in a variety of imaging applications with X-rays, gamma-rays and beta-rays, in the acquisition modality of single photon counting [1], [15]. Using the flip-chip technology, the readout chip is connected pixel by pixel via bump-bonding to a matching pixel detector to form a so-called hybrid detector. [2] This configuration has the advantage of optimizing separately the microelectronics technology (reduced pixel pitch, increased density of transistors per cell) implemented in the low resistivity silicon substrate of the ASIC, and the room temperature semiconductor pixel detector, implemented using material substrates like high-resistivity silicon, bulk or epitaxial GaAs, CdTe, and CdZnTe. Different semiconductors (elemental or compound), as well as different substrate thicknesses, can then be selected in order to cope with different application needs.

This Medipix2-based hybrid detector (the successor of the Medipix1 photon counting chip [3]) features high intrinsic spatial resolution ( $55 \mu\text{m}$  pixel pitch) and double-polarity charge sensitivity, i.e., either electrons or holes collection of the radiation induced ionization charge. This last feature is important for room temperature compound semiconductors like Cd(Zn)Te, where transport and collection of electrons is preferred over holes transport.

We are interested in producing a hybrid pixel detector with the Medipix2 technology, in diverse imaging fields that span from digital mammography (low-energy X-rays, about 20 keV) (at IFAE, Spain), dental radiography (low- to medium-energy X-rays) (at Mid-Sweden University, Sweden), imaging with synchrotron radiation (low-energy intense X-ray beams) (at ESRF, France), nuclear medicine (single photon gamma-ray imaging at medium and high energy, up to about 150 keV) (at University and INFN Napoli, Italy), and radiation monitoring in nuclear facilities (very high-energy gamma-ray imaging, up to 1.5 MeV) (at CEA/Saclay, France). For all these applications, high efficiency in photon detection is required in the detector. This calls for the use of dense and high Z materials like Cd(Zn)Te or GaAs, but up to now, the Medipix2 ASIC has been hybridized only with a  $300 \mu\text{m}$  thick silicon detector, whose intrinsic detection efficiency is less than 1% at energies above 60 keV. With this Medipix2 silicon hybrid detector, some electronic and imaging tests have been presented [4]–[6].

After the successful tests with this silicon detector, we are now interested in producing a hybrid Medipix2 detector with an efficient CdTe pixel detector. The fabrication of thick CdTe de-

Manuscript received November 11, 2003; revised February 18, 2004.  
M. Chmeissani and M. Maiorino are with IFAE, Institut de Física d'Altes Energies, Barcelona, Spain (e-mail: chmeissani@ifae.es).

C. Frojdh is with Mittlångskolan, Mid-Sweden University, Sundsvall, Sweden (e-mail: christr.frojdh@mh.se).

O. Gal and E. Manach are with Commissariat à l'Energie Atomique (CEA), Laboratory of Integration of Systems and Technologies (LIST), Saclay, France (e-mail: gal@cea.fr).

X. Llopert and L. Tlustos are with CERN, Geneva, Switzerland (e-mail: xavier.llopert@cern.ch).

J. Ludwig and A. Zwerger are with Albert-Ludwigs-Universität Freiburg, Physikalisches Institut, Arbeitsgruppe Halbleiterdetektoren, Freiburg, Germany (e-mail: jens.ludwig@physik.uni-freiburg.de).

C. Ponchut is with European Synchrotron Radiation Facility, Grenoble, France (e-mail: ponchut@esrf.fr).

G. Mettivier, M. C. Montesi, and P. Russo are with Dipartimento di Scienze Fisiche, Università di Napoli Federico II, and with INFN Sezione di Napoli, I-80126 Napoli, Italy (e-mail: paolo.russo@na.infn.it).

Digital Object Identifier 10.1109/TNS.2004.832324

<sup>1</sup>Medipix2 Collaboration, www.cern.ch/MEDIPIX.

tectors with as many as 65 000 pixels and a pixel pitch as small as  $55 \mu\text{m}$  over a  $2 \text{ cm}^2$  sensitive area is a challenging technological task, when aiming at detectors with high uniformity of response and high charge collection efficiency. Moreover, in these photon counting detectors, the problem of charge sharing between adjacent pixels with high-energy photons is an investigation area to be explored.

Here, we show preliminary results obtained with a number of detectors, each obtained by bump-bonding a Medipix2 chip to a 1-mm-thick CdTe detector: they are the first run of a larger number of hybrids, to be produced also on the basis of the knowledge gained in the present experimental study. We also plan in the future to use 2-mm- and 4-mm-thick CdTe detectors of this type.

## II. THE MEDIPIX2 CHIP AND ITS READOUT INTERFACE

The Medipix2 single photon counting  $0.25 \mu\text{m}$  CMOS integrated circuit contains a matrix of  $256 \times 256$  cells, each featuring a double-polarity charge preamplifier, a double-threshold (window) discriminator, and a 13-bit counter, all included in a  $55 \mu\text{m}$  square cell. Its main characteristics and performance have been described elsewhere [1], [4], [15]. In particular, the charge preamplifier peaking time is less than 200 ns. Each of the two (low, high) detection thresholds in the Medipix2 cell can be finely adjusted via a 3-bit setting. The hardware readout of Medipix2 occurs via a dedicated serial interface board (MUROS2) [7]. The software readout is accomplished by a dedicated software system (Medisoft 4) [8].

Electrical measurements on first-available chips have been presented recently [4]. The data show an electronic noise  $\sigma_n \sim 105$  electrons, an unadjusted threshold dispersion  $\sigma_n \sim 500$  electrons which reduces to  $\sigma_n \sim 110$  electrons after 3-bit fine adjustment of the pixel thresholds. These electrical tests refer to the readout chip only, and have been assessed using the test input option of each cell which has a nominal capacitance of  $8 \text{ fF}$ .

## III. CdTe PIXEL DETECTORS AND BUMP-BONDING

The CdTe detectors have on one side  $256 \times 256$  square pixels (Pt contact pads, electroless deposition) of  $45 \mu\text{m}$  side, separated by a gap of  $10 \mu\text{m}$ , matching the  $55 \mu\text{m}$  pitch of Medipix2, for a total sensitive area of  $14 \times 14 \text{ mm}^2$ . The other side (onto which the nuclear radiation impinges) is covered with a continuous Pt electrode. The single crystal CdTe:Cl detectors were fabricated on our specifications by ACRORAD (Japan) with the Traveling Heater method [9]. A first run of four detectors out of 11 bump-bonded detectors was tested in this preliminary evaluation study (indicated as D8, C8, I2, K3), in addition to some dummy detectors. The indium bump-bonding has been made by Advanced Interconnect Technology (AIT, Hong Kong).

## IV. RESULTS

### A. Quality of Contact Deposition and Bump-Bonding

A detailed study of two CdTe detectors for detector processing faults reveals very good quality of surface manufacturing: about six bad contacts pads per detector out of

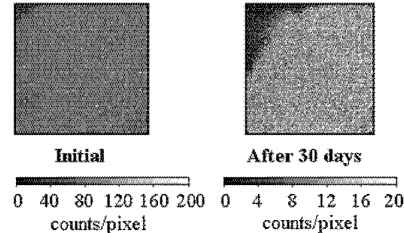


Fig. 1. Side-by-side comparison of two blank images taken with the same hybrid D8 after a period of one month shows how severely the no responsive area (black level) in the upper left corner increased in size, with aging.

65 536, and only few defects in a very uniform passivation processing. Dummy hybrids were analyzed for bump-bonding quality by separating the readout chip from the detector and by scratching. The strength of indium bonding, and the dimension and shape of the bumps after separation revealed a satisfactory bump-bonding processing, at this first level of testing. Notwithstanding these data indicating uniform applied pressure during bonding, the adhesion of the detector and readout chip may change with time: the claim for a defective bump-bonding was the tentative explanation of the degradation of detector D8 (kept without applied bias voltage), whose initial dead area at one corner increased a noteworthy amount, after one month (Fig. 1). For the bonding problem at corners, flip-chip handling might be responsible, and for bonding weakening with time from a corner, uniformity of detector thickness (wedge effect) should also be investigated as a cause.

### B. Electrical Characterization

The  $I-V$  curve [Fig. 2(a)] shows an ohmic behavior—as expected by the contacting method—with a resistivity greater than  $10^9 \Omega\text{cm}$ , with a negative bias (electrons collection). This voltage biasing was the intended one for optimal charge collection efficiency. On the other hand, some detectors show an ohmic behavior in negative bias but a deviation from linearity of response under positive bias greater than +15 V (holes collection on the pixel side) [Fig. 2(b)].

As for a possible “polarization effect” with our CdTe detectors (an effect here studied only as a settling time dependence of leakage current), Fig. 3 gives indications that this detector stabilization problem could have an effect also on these detectors, with possible influence on exposure repeatability. Finally, a spatial mapping of resistivity (with a grid of  $1 \text{ mm}^2$ ) over a detector reveals good uniformity in the range  $3-6 \times 10^9 \Omega\text{cm}$  (Fig. 4).

### C. Imaging Tests: Beta Source

By collecting electrons at the pixel side, we irradiated the detectors from the cathode with a  $^{90}\text{Sr}$  beta source. Hybrid I2 shows a large zone of no response (upper left corner) and no responsive upper and lower right corners (Fig. 5). However, the striking feature observed relates to the presence of numerous small circle structures with central reduced counting efficiency with respect to the circumferential pixels, and to the appearance

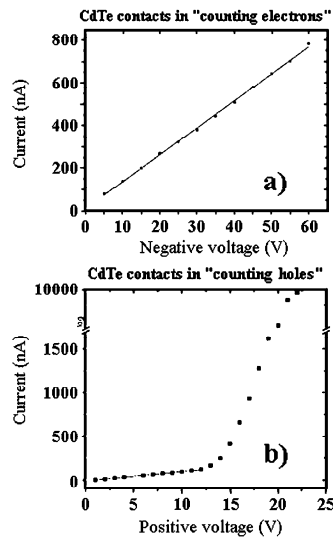


Fig. 2.  $I$ - $V$  curve of detector C8 with all pixels on one side grounded and the continuous electrode on the other side biased (a) negatively (counting electrons) or (b) positively (counting holes). The ohmic response in (a) indicates a resistivity greater than  $10^9 \Omega\text{cm}$ . A soft breakdown is observed at voltages higher than  $\pm 15$  V when in holes collection, whereas the response of this detector is ohmic under electrons collection, and up to  $\pm 15$  V.

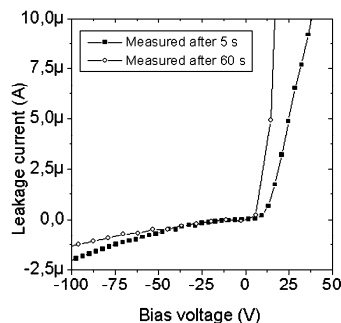


Fig. 3.  $I$ - $V$  curve of detector C8 in both polarities, after allowing for a short time period (5 s) or a longer time (60 s) for measuring the leakage current, after setting the bias voltage. Under negative bias, there is little difference in leakage current up to about  $-50$  V, but a time dependency is present under higher negative bias or positive bias.

of "filament" structures. Some other small circular structures in this image seem to be disposed on large circles. All these features are stable and reproducible, hence indicating a peculiar small-scale and large-scale behavior of this detector. The circles have been identified by software with digital image processing,

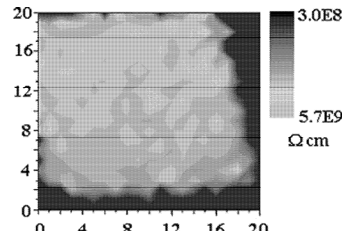


Fig. 4. Resistivity map of a detector: in the large area the resistivity varies in the range  $2\text{--}5.7 \times 10^9 \Omega\text{cm}$ . The scanned area is  $20 \times 20 \text{ mm}^2$ .

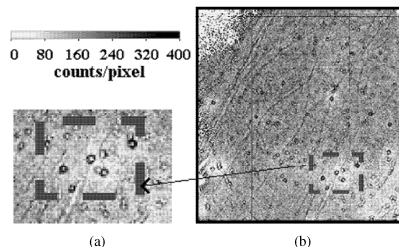


Fig. 5. (b) A 10 s uniform exposure (bias,  $-70$  V) to an intense  $^{90}\text{Sr}$  beta source of hybrid I2 ( $14 \times 14 \text{ mm}^2$  sensitive area) reveals large defective zones on the corners and, worth noting, small circular structures [like, e.g., the ones present in the dashed rectangular zone, zoomed 2X in (a)] which identify a distinctive behavior of the detector + chip hybrid. The circles have a diameter of about four pixels (corresponding to  $200 \mu\text{m}$ ). Other peculiar thin, long filament structures are also visible.

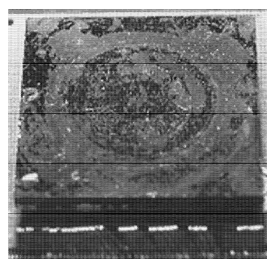


Fig. 6. View of the top surface of a detector hybrid (I2), showing anomalous round features.

counted, and their shape analyzed. Their average diameter is  $200 \pm 4 \mu\text{m}$ . As for the global uniformity of response, in Fig. 5 the average count rate is  $160 \pm 50 \text{ cps}/\text{pixel}$  (mean  $\pm$  standard deviation), with a signal-to-noise ratio (SNR = mean / standard deviation) of about three. We note that under visual inspection, the surface of the top continuous electrode of this and the other detectors shows anomalous rings (Fig. 6). One could tentatively ascribe them to mechanical handling during hybrid manufacturing. However, they could have been produced in the crystal

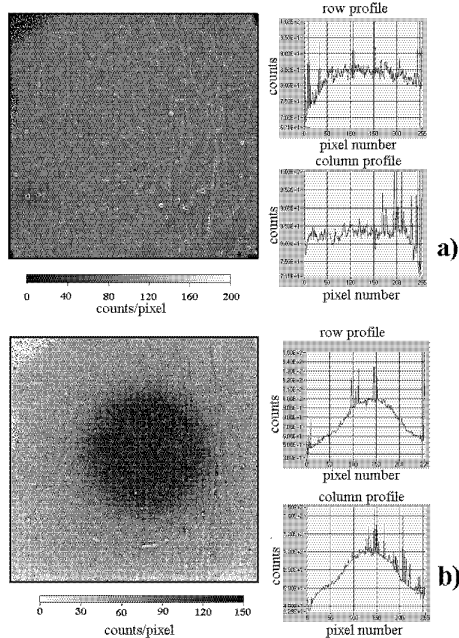


Fig. 7.  $^{57}\text{Co}$  gamma irradiation of detector D8. (a) Flat field exposure. (b) The point-like source is imaged with a 1 mm collimator, after flat field correction with the image in (a). Bias =  $-70\text{ V}$ . The threshold calibration procedure (pixel equalization) has been applied. On the right side of each image are shown the integrated row and column profiles over the whole image array.

growth process itself, since a circular distribution of small circle defects is present also in the images with penetrating radiation sources (Fig. 5). In the same experimental conditions, hybrids D8 and C8 show similar image structures: the latter detector features a distinctive large central area, and the former one long “filaments,” both with no counts inside.

#### D. Imaging Tests: Gamma Sources

Under negative bias (electrons collection), irradiation tests were performed with radioactive gamma sources of low and high energy ( $^{241}\text{Am}$ , 60 keV;  $^{57}\text{Co}$ , 122 keV;  $^{137}\text{Cs}$ , 662 keV;  $^{60}\text{Co}$ , 1.25 MeV), in flood (i.e., uniform and high intensity) irradiation and using collimators for imaging tests. We were also interested in assessing the recovery of uniformity of response over the whole detector area, by applying a flat field correction algorithm, as well as by equalizing the response of the detection threshold of the array of Medipix2 cells via its 3-bit adjustment feature. This last operation (threshold mask procedure) was actually substituted by a noise equalization procedure, in which the lower threshold above electronic noise was evaluated, for each pixel, and finely adjusted. Fig. 7 shows that, after equalizing the response of the pixel, the small scale circle structures are present also in gamma irradiation (at 122 keV),

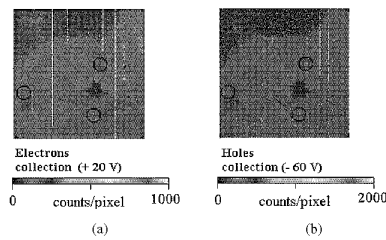


Fig. 8.  $^{57}\text{Co}$  irradiation of detector C8 in either modality: (a) electrons counting or (b) holes counting. Three indicative circle structures have been outlined in both images, to show that the same small scale structures are visible in identical positions on the detector, in both modes. Note the large star-shaped no-response area close to the center of this detector. In both images, vertical blank lines are due to column defects in the readout chip.

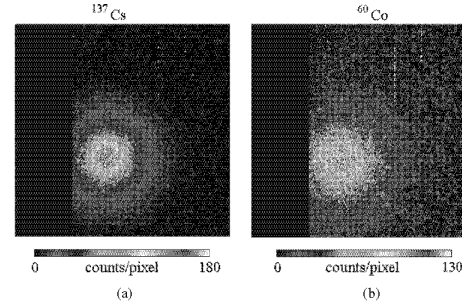


Fig. 9. Point-like gamma source of (a)  $^{137}\text{Cs}$  and (b)  $^{60}\text{Co}$  are imaged through a  $50^\circ$  double-cone opening tungsten collimator and a Pyrex screen in front of the detector I2 (electrons collection). Detection threshold, 30 keV. A large rectangular area in the images has been masked.

thus confirming they represent a peculiar feature of these detectors. Moreover, Fig. 8 gives indications that the circle structure is present also in holes collection, and that the low-counts inner pixels in electrons collection correspond to central high counts, inside the circles. However, the flat field correction and threshold equalization procedures are able to produce an acceptable image quality, apart from no responsive pixel areas. Gamma-ray imaging at 662 keV and 1.25 MeV confirm this finding (Fig. 9).

As for the dependence of the counting efficiency on the (negative) bias voltage, Fig. 10 shows that for high energy detection ( $^{137}\text{Cs}$ , 662 keV), with a 20 keV detection threshold, increasing the bias above  $40-50\text{ V}$  has little effect on the pixel counting efficiency. On the contrary, for  $^{241}\text{Am}$  (60 keV photons, 15 keV detection threshold), up to  $90-100\text{ V}$  are necessary for maximum counting efficiency, as a result of increased charge collection efficiency with increasing bias. Moreover, Fig. 10 shows that at 60 keV and a given voltage bias, by increasing the detection threshold from 15 to 22 keV, a sizeable decrease of counting efficiency is observed, to be related to the influence of the CdTe photoelectric effect, close to the Cd and Te absorption K-edges. How this phenomenon is also influenced by charge sharing effects between adjacent pixels when fluorescence X-ray photons

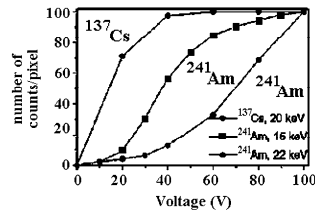


Fig. 10. The normalized (at 100 V) mean number of counts per pixel under irradiation with  $^{137}\text{Cs}$  or  $^{241}\text{Am}$  gamma-rays has been determined as a function of the negative voltage bias. For 60 keV gamma-rays, a marked decrease in counting efficiency is observed when changing the detection threshold from 15 to 22 keV (estimated values), namely, across the absorption edges of CdTe, which is not observed at 662 keV ( $^{137}\text{Cs}$ ).

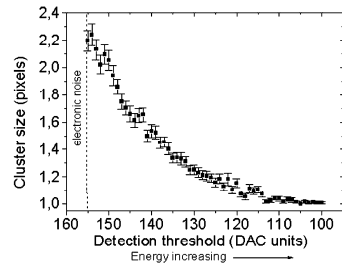


Fig. 11. Mean cluster size of pixels hit by single 122 keV ( $^{57}\text{Co}$ ) photons, as a function of the (uncalibrated) detection threshold (energy values increase to the right). Detector C8, holes collection, bias voltage = +40 V.

escape from the pixel of initial interaction is a matter of further investigation. By irradiation at 122 keV, we looked at the distribution of the size of cluster of adjacent pixels that have been hit by each single photon. A preliminary evaluation of the size of the cluster of hit pixels (Fig. 11) shows that the cluster size (number of pixels) depends on the detection threshold (as expected) and that close to the electronic noise it does correspond to just over 2 pixels.

#### E. Imaging Tests: X-Ray Tube

Irradiation tests have been performed with detector C8 and with an X-ray tube (tungsten anode), at 70 kV (10 keV spectral cutoff) and with a fixed short exposure of 0.16 s, with a tube current low enough to ensure that the dynamic range (13 bit) of the pixel counter was not exceeded. For these tests, we used a low bias voltage up to  $-10\text{ V}$  or  $+15\text{ V}$ . We first investigated the X-ray imaging performance, in both polarities, when applying the flat field procedure, after equalizing the pixel threshold over the matrix array. Fig. 12(a) and (b) (positive bias, holes collection) shows that by applying the flat field correction the image is more uniform and the image histogram shrinks: the SNR increases from one to five.

When changing the bias to negative ( $-10\text{ V}$ , electrons collection) [Fig. 12(c)] the corrected image appears less uniform than in holes collection, but the counting efficiency is significantly higher than at  $+15\text{ V}$  and may reach a +40% increase. As a

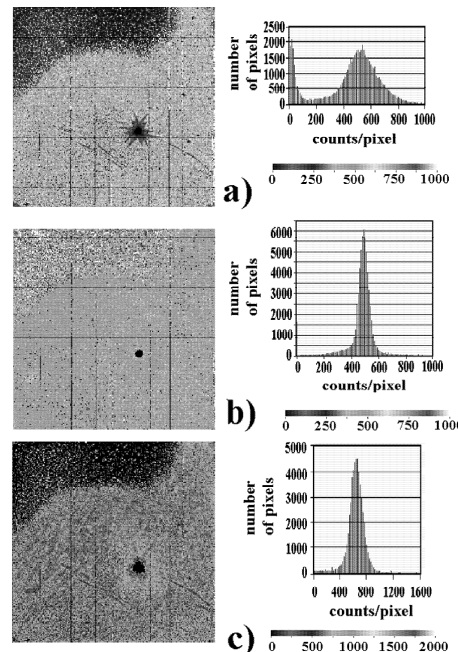


Fig. 12. X-ray tube uniform irradiation (70 kV, 0.16 s exposure) of detector C8. (a) Bias voltage =  $+15\text{ V}$  (counting holes), without flat field correction, SNR = 1. (b) Bias =  $+15\text{ V}$ , with flat field correction, SNR = 5. (c) Bias =  $-10\text{ V}$ , with flat field correction, SNR = 4. On the right of each image is the pixel counts histogram. The “hole” visible close to the center of the detector is a no-response area, as well as the large zone of zero counts visible on the upper left corner.

final image quality test at low voltage bias, a plastic encapsulated integrated circuit has been imaged under 70 kV X-ray tube irradiation, with a  $-10\text{ V}$  and then a  $+15\text{ V}$  voltage bias to the 1 mm CdTe detector (Fig. 13). Allowing for a reduced counting efficiency, here the image quality in holes collection mode may be considered acceptable and providing more uniformity and details than in electrons collection. In Fig. 13, the circuit tracks to the external connections are easily identified (estimated track width: 0.5 mm). Some contrast features, though unresolved, are barely seen in the  $2 \times 2\text{ mm}^2$  area (estimated) central chip core. However, the full counting efficiency allowed by high voltage negative bias (electrons collection) to the 1-mm CdTe detectors is expected to improve the imaging performance in future tests. Actually, our preliminary imaging tests have been performed just at very low voltage, also in order to keep the leakage current (and noise) as low as possible and to limit any possible polarization effect due to high voltage bias. On the other hand, under negative bias and 60 kV X-ray irradiation, the counting efficiency increases significantly, up to as much as  $-350\text{ V}$  (Fig. 14) which was the maximum voltage bias tested. However, high-voltage extrapolation and sigmoidal fitting of data in this

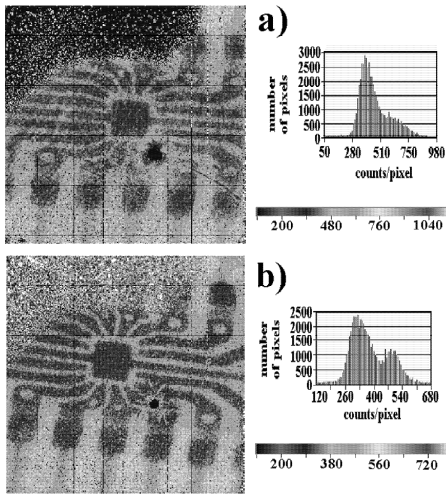


Fig. 13. X-ray tube irradiation (70 kV, 0.16 s exposure) of detector C8 in an imaging test of an encapsulated integrated circuit. (a) Detector bias = -10 V. (b) Bias = +15 V.

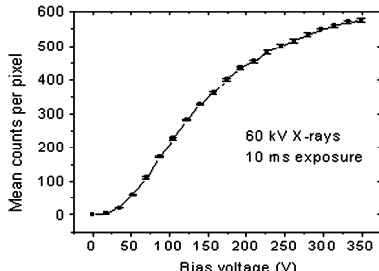


Fig. 14. X-ray tube flood irradiations (60 kV, 0.01 s exposure) of detector C8 under negative bias voltages do increase significantly the mean number of counts per pixel. Minimum detection threshold set just above system noise (DAC value = 156).

figure indicate that saturation in counting efficiency would have not been attained even at -500 V.

#### V. DISCUSSION AND CONCLUSION

A hybrid pixel detector consisting of the Medipix2 readout chip bump-bonded to a 1-mm-thick CdTe pixel detector has been assembled and tested. This system has potential for high resolution imaging (55  $\mu\text{m}$  pixel pitch) and larger area than the present  $1.4 \times 1.4 \text{ cm}^2$ , by making a mosaic of a number of chips in a multichip module (e.g. a mosaic of four readout chips of  $256 \times 256$  pixels each, arranged in a  $2 \times 2$  matrix bump-bonded to a single  $512 \times 512$  pixel semiconductor detector). In this experimental study, the main result is that we have successfully

achieved single photon counting with gamma rays with a thick CdTe pixel detector, at 55  $\mu\text{m}$  pitch. Also, a number of issues have been encountered and investigated, related to the optimal quality and operation of this detector.

Few published results are available on CdTe or CdZnTe hybrid pixel detectors at this low level of pixel pitch ( $\approx 50 \mu\text{m}$ ). Yin *et al.* have reported results of a (not single photon counting) digital mammography system based on Si, CdTe, and CdZnTe pixel detectors indium bump-bonded to an application-specific integrated circuit CCD readout chip, with a pixel pitch of 50  $\mu\text{m}$  and a sensitive area up to  $9.6 \times 19.2 \text{ mm}^2$  [10], [11].

In the case of the CdTe detectors [11], their thickness was 0.15 or 0.2 mm. In their detectors, with a mobility-lifetime product in the order of  $10^{-4} \text{ cm}^2/\text{V}$ , under 39-keV X-ray exposure, a bias voltage of a few volts (with their hole-carrying readout chip) was sufficient to reach full charge collection by holes, since in that case the hole propagation length (0.2 mm) was higher than the crystal thickness (0.15 mm). This is not the case for our 1-mm-thick CdTe detectors, working in positive bias at few tens of volts.

As for photon counting CdTe pixel detectors, inefficiency in hole collection has been reported by others for 0.5-mm-thick detectors of analogous fabrication with ohmic contacts, as well as recovery of image SNR after application of a flat field correction [12]; they also report a good homogeneity of their pixel detectors under holes collection.

In this study, the polarization effect (whereby the amount of radiation induced charge in the detector may alter the internal electric field conditions and deteriorate the collection efficiency or count rate) has been faced in a very particular way by only analyzing the dependence of the  $I$ - $V$  curve on the measurement time. In this regard, we limited our imaging studies to very low voltages, but we note that the counting efficiency curve seems not to saturate at high voltages (Fig. 14). Moreover, in Fig. 13 the average detector counts are about  $3 \times 10^5 \text{ mm}^{-2}$  (count rate of about  $2 \times 10^6 \text{ cps/mm}^2$ ) and X-ray flux induced polarization could occur [13], but a detailed study of the polarization effect for our detectors deserves future work.

This preliminary evaluation indicates that the quality of bump-bonding permits some elementary imaging tests, but it must be improved for full-area chip imaging. "Aging" problems of bump-bonding are to be investigated, also in the direction of the detector geometrical uniformity. The detector response is characterized by the presence, in the acquired images with ionizing radiation, of numerous circle structures at a scale of 200  $\mu\text{m}$ , whose origin remains to be determined. These structures modulate, at the scale of 3–4 pixels, the counting efficiency of the detector. An interesting finding is the presence of these structures both in positive and in negative detector voltage bias, with the profile of the pixel counts across a circle diameter (about 4 pixels) being reversed in either polarity (i.e., the same inner pixels behave as high counters or low counters by reversing the polarity). This would call for specific charge transport or trapping effects inside the detectors. Different explanations could account for this type of detector inhomogeneity, including the hypothesis that they originate from spherical (or filament) Te precipitations in the CdTe crystal growth. Tellurium inclusions in single CdTe detectors

have been reported under infrared transmission imaging, with a "relatively uniform distribution" [14]. However, the hypothesis that the small scale structures visible in our images are related to some bump-bonding effect is not completely ruled out. As well, large-scale defective detector areas could correspond to regions of weak or null indium bump-bonding of the detector to the readout chip. Also, the origin of the nonresistive behavior of the  $I$ - $V$  curve of our detectors equipped with ohmic contacts, when in the "holes-counting regime," is to be understood. Nevertheless, we consider extremely informative the mass of data we gathered from this test on four first-available CdTe hybrids, since they indicate the path to detailed investigations on detector quality. In particular, a microirradiation at the level of, e.g.,  $10 \times 10$  pixels, could give answers on the circle structure and on charge sharing between adjacent pixels. Starting from these first results, we now will investigate on the best charge collection tradeoffs between bias voltage, counting efficiency, carrier polarity, and noise level.

#### ACKNOWLEDGMENT

In the framework of the Medipix2 Collaboration—a CERN-based consortium of European universities and research centers—the Medipix2 chip has been designed by CERN (Geneva, Switzerland); the MUROS2 interface has been designed by NIKHEF (Amsterdam, The Netherlands) by the group directed by J. Visschers; the Medisoft 4 software has been written by University and INFN Napoli (Italy); and the CdTe detectors have been designed by IFAE (Barcelona, Spain). Thanks are given to all members of this Collaboration and in particular to M. Campbell (CERN, Medipix2 Collaboration spokesperson).

#### REFERENCES

- [1] X. Llopart, M. Campbell, R. Dinapoli, D. San Segundo, and E. Pernigotti, "Medipix2, a 64 k pixel readout with  $55 \mu\text{m}$  square elements working in single photon counting mode," in *Conf. Rec. IEEE Nuclear Science Symp. Medical Imaging Conf.*, San Diego, CA, Nov. 4–10, 2001.
- [2] P. Russo, "Hybrid semiconductor pixel detectors for low- and medium-energy X- and gamma-ray single photon imaging using the medipix read-out chip," in *Encyclopedia of Imaging Science and Technology*, J. P. Hornak, Ed. New York: Wiley Interscience, 2002.
- [3] M. Campbell, E. H. M. Heijne, G. Meddeler, E. Pennigotti, and W. Snoeys, "A readout chip for a  $64 \times 64$  pixel matrix with 15 bit single photon counting," *IEEE Trans. Nucl. Sci.*, vol. 45, pp. 751–753, 1998.
- [4] X. Llopart and M. Campbell, "First test measurements of a 64 k pixel readout chip working in single photon counting mode," *Nucl. Instrum. Meth.*, vol. A 509, pp. 157–163, 2002.
- [5] G. Mettivier, M. C. Montesi, and P. Russo, "First images of a digital autoradiography system based on a Medipix2 hybrid silicon pixel detector," *Phys. Med. Biol.*, vol. 48, pp. N173–N181, 2003.
- [6] ———, "Tritium digital autoradiography with a Medipix2 hybrid silicon pixel detector," *Nucl. Instrum. Meth.*, vol. A 516, pp. 554–563, 2004.
- [7] D. San Segundo Bello, M. van Beuzekom, P. Jansweijer, H. Verkoojen, and J. Visschers, "An interface board for the control and data acquisition of the Medipix2 chip," *Nucl. Instrum. Meth.*, vol. A 509, pp. 164–170, 2002.
- [8] M. Conti, M. Maiorino, G. Mettivier, M. C. Montesi, and P. Russo, "Preliminary test of Medisoft 4: control software for the Medipix2 readout chip," *IEEE Trans. Nucl. Sci.*, vol. 50, pp. 869–877, 2003.
- [9] M. Funaki, T. Ozaki, K. Satoh, and R. Ohno, "Growth and characterization of CdTe single crystals for radiation detectors," *Nucl. Instrum. Meth. A*, vol. 436, pp. 120–126, 1999.
- [10] S. Yin, T. O. Turner, D. Maeding, J. Mainprize, G. Mawdsley, M. J. Yaffe, and W. J. Hamilton, "Hybrid direct conversion detectors for digital mammography," *IEEE Trans. Nucl. Sci.*, vol. 46, pp. 2093–2097, 1999.
- [11] S. Yin, T. O. Turner, D. Maeding, J. Mainprize, G. Mawdsley, M. J. Yaffe, E. E. Gordon, and W. J. Hamilton, "Direct conversion CdZnTe and CdTe detectors for digital mammography," *IEEE Trans. Nucl. Sci.*, vol. 49, pp. 176–181, 2002.
- [12] P. Fisher, M. Konda, H. Kruger, A. Lindner, G. Sato, T. Takahashi, S. Watanabe, and N. Wermes, "A counting CdTe pixel detector for hard X-ray and  $\gamma$ -ray imaging," *IEEE Trans. Nucl. Sci.*, vol. 48, pp. 2401–2404, 2001.
- [13] T. Tuemer, S. Yin, V. Cajipe, H. Flores, J. Mainprize, G. Mawdsley, J. A. Rowlands, M. J. Yaffe, E. E. Gordon, W. J. Hamilton, D. Rhiger, S. O. Kasap, P. Sellin, and K. S. Shah, "High-resolution pixel detectors for second generation mammography," *Nucl. Instrum. Meth. A*, vol. 497, pp. 21–29, 2003.
- [14] C. M. Stahle, B. H. Parker, A. M. Parsons, L. M. Barbier, S. D. Barthelmy, N. A. Gehrels, and D. M. Palmer, "CdZnTe and CdTe detector arrays for hard X-ray and gamma-ray astronomy," *Nucl. Instrum. Meth. A*, vol. 436, pp. 138–145, 1999.
- [15] X. Llopart, M. Campbell, R. Dinapoli, D. San Segundo, and E. Pernigotti, *IEEE Trans. Nucl. Sci.*, vol. 49, pp. 2279–2283, 2002.



**PAPER V**

**Signal variations in high-granularity Si pixel detectors**

**P a p e r V**



# Signal Variations in High-Granularity Si Pixel Detectors

Lukas Tlustos, Michael Campbell, Erik Heijne, and Xavier Llopert

**Abstract**—Fixed-pattern noise is one of the limiting factors of image quality and degrades the achievable spatial resolution. In the case of silicon sensors, the effects of nonuniformities due to doping inhomogeneities can be limited by operating the sensor in strong overdepletion. For high-granularity photon-counting pixel detectors, an additional high-frequency interpixel signal variation is an important factor for the achievable signal-to-noise ratio (SNR). It is a common practice to apply flatfield corrections to increase the SNR of a detector system. For the case of direct conversion detectors, it can be shown theoretically that the Poisson limit can be reached for floodfield irradiation. However, when used for imaging with spectral X-ray sources, flatfield corrections are less effective. This is partly a consequence of charge sharing between adjacent pixels, which gives rise to an effective energy spectrum seen by the readout, which is different from the spectral content of the incident beam. In this paper, we present simulations and measurements of the limited applicability of flatfield corrections for spectral source imaging and investigate the origins of the high-frequency interpixel noise component. The model, calculations, and measurements performed suggest that flatfield correction maps for photon-counting detectors with a direct conversion Si sensor can be obtained from electrical characterization of the readout chip alone.

## I. INTRODUCTION

**L**OW-NOISE, high-resolution, and high-dose efficiency are the common requirements for most imaging applications. These three properties are closely linked together and can be described in a combined parameter, the detective quantum efficiency (DQE) [1]. The DQE describes in terms of spatial frequency the ratio between the signal-to-noise ratio (SNR) at the output of the detector system and the SNR of the signal presented to the detector system, thus giving a measure for the achievable resolution for a given acquisition dose. Especially in medical applications, the dose efficiency is a key characteristic for detector systems. In general, noise contributions from photonic noise, photon conversion, electronic noise, and fixed-pattern noise limit the achievable DQE [2].

The conversion of the incident photons into electron-hole pairs can be achieved either directly or indirectly. In indirect detection, the X-ray is converted into visible light in a scintillator layer and then converted into electron-hole pairs in a photodiode. In case of direct conversion, the X-ray is converted into electron-hole pairs without the intermediate step, with the advantage of eliminating the additional noise introduced by the primary conversion [3]. From theoretical considerations, it can be shown that photon-counting systems in combination with

direct photon detection can provide excellent performance with respect to the requirements mentioned above [4]. The impact of front-end noise on the image can be almost excluded by setting the discriminating threshold well below the energy of the incident photons. The DQE for such a counting system is limited only by the quantum efficiency (QE) of the sensor part and the magnitude of fixed-pattern noise [4]. Fixed-pattern noise may stem from beam inhomogeneity and general gain variations of the detector response due to inhomogeneities in the photon conversion yield, losses in charge transport, charge trapping, etc., or variations in the performance of the readout. This fixed-pattern noise cannot be suppressed by increasing acquisition dose. Furthermore, the applied dose cannot be increased at will for medical applications and for some other commercial applications measurement time is the critical factor which limits the number of photons per acquisition. Therefore various efforts are undertaken to increase the QE efficiency and to reduce fixed-pattern noise.

Due to its homogeneity and its well-known characteristics, high-resistivity silicon at present is the standard material for particle detection. Unfortunately, for X-ray detection, the conversion efficiency of silicon rapidly decreases with photon energy, thereby reducing the maximum achievable DQE. To meet the given requirements, different approaches are currently under way. On the one hand, progress in material homogeneity and processing technology recently opened the possibility to fabricate devices with new detector materials, e.g., GaAs, CdTe with high-Z components and, therefore, higher QE. On the other hand, efforts are undertaken to increase the performance of Silicon based devices. Important in both approaches is that with smaller pixel size the contribution of sensor inhomogeneities plays an increasing role. In previous work [5], we have shown that even the very small inhomogeneities in the doping of standard high-resistivity silicon wafers can lead to signal distortion, which can introduce variations in the signal height of up to 1%–2% in a fully depleted detector. These variations gradually disappear when putting the sensor in strong overdepletion.

In this article, we present measurements and simulations related to residual high-frequency interpixel variations in strong overdepletion as seen with the Medipix1 and Medipix2 detector systems [6], [7].

## II. EXPERIMENTAL DATA

All measurements were performed using a Medipix2 chip, a  $0.25\text{-}\mu\text{m}$  CMOS readout chip operating in single photon-counting mode, bump bonded to a  $300\text{-}\mu\text{m} p^+ n$  silicon sensor. The active matrix consists of  $256 \times 256$  cells, each  $55\text{-}\mu\text{m}$  pixel size, which include a double-threshold window

Manuscript received November 14, 2003; revised April 20, 2004.  
The authors are with the CERN, 1211 Geneva 23, Switzerland (e-mail: Lukas.Tlustos@cern.ch; Michael.Campbell@cern.ch; Erik.Heijne@cern.ch; Xavier.Llopert@cern.ch).  
Digital Object Identifier 10.1109/TNS.2004.839095

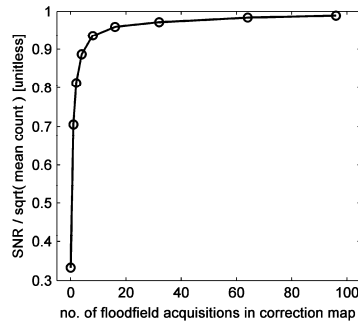


Fig. 1. SNR of a uniform exposure corrected with a flatfield correction map calculated from an increasing number of floodfields as indicated on the abscissa. The values are normalized to Poisson noise, the square root of the mean count rate. The SNR approaches the Poisson limit when increasing the statistical base of the flatfield correction.

discriminator and a 13-bit counter [7]. The discriminator thresholds are set globally for the whole matrix and are fine tuned using a 3-bit adjustment register in each pixel, resulting in residual threshold dispersion lower than 100 electrons rms. The chip is designed to provide a linear threshold, adjustable from  $\sim 3$  up to  $\sim 100$  keV. Measurements so far have been performed up to 60 keV showing linearity of 99.96% [8].

#### A. Flatfield Correction

As already described, flatfield corrections are used to remove accumulated fixed-pattern detection inhomogeneities. To correct for these imperfections, a large number of acquisitions with uniform irradiation is used to calculate an efficiency map of the detector. The Medipix2 as a direct conversion photon-counting detector can reach the Poisson limit given a sufficiently high number of photons contributing to the correction map. Fig. 1 shows the SNR of a single uniform signal acquisition corrected with a flatfield correction map calculated from an increasing number of floodfield acquisitions. We used a Seifert FK 61-04  $\times$  12 W-target X-ray source with 35-kV, 2.5-mm Al equivalent Perspex filtering for this measurement. It can be seen that by increasing the statistical base of the correction map, the obtained SNR of a single floodfield approaches the maximal achievable value of the square root of the number of photons.

The procedure of calculating a flatfield correction assumes that the acquisition conditions are identical to those used when measuring the efficiency map. For absorption imaging, contrast is achieved by attenuating photons out of the incident beam. Since low-energy photons have a much higher probability to be absorbed in matter, the transmitted beam is subject to beam hardening when spectral X-ray sources are used.

Fig. 2 shows such a correction map applying a dose of 296 mGy air kerma and its corresponding histogram of correction factors. The distribution follows as expected a Gaussian form, with an rms of  $\sim 4\%$ .

Fig. 3 illustrates the effects of beam hardening on the achievable SNR. Again a W-tube with 35-kV, 2.5-mm Al equivalent filtering was used with additional layers of 1, 2, and 4 cm of

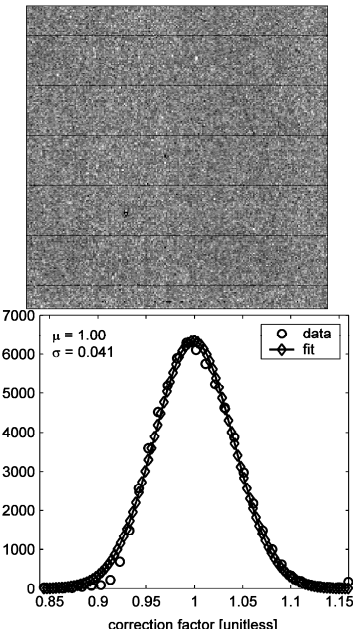


Fig. 2. (a) Flatfield correction map, obtained with a W-target X-ray source with 35-kV and 2.5-mm Al equivalent filtering. (b) Histogram of factors in the flatfield correction map, together with a fitted Gaussian distribution of 4.1% rms.

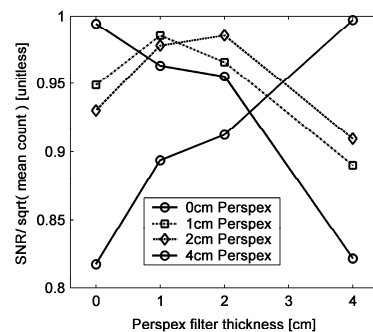


Fig. 3. SNR normalized to Poisson limit when combining different acquisition conditions for image and correction map. The individual curves represent the normalized SNR of a single acquisition with 0-, 1-, 2-, and 4-cm prefiltering, which is then corrected with correction maps obtained with Perspex prefiltering denoted on the abscissa. The Poisson limit, which is given by the square root of the mean count rate, can only be approached when using identical photon spectra for acquisition and flatfield correction.

Perspex. One hundred floodfields were taken for each thickness of Perspex and used to calculate the corresponding correction maps for each configuration. Then the resulting four correction maps were applied to a single floodfield acquisition of the same

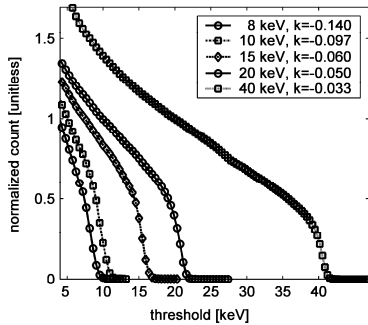


Fig. 4. Average normalized count rate of 1-mm<sup>2</sup> active area irradiated with monochromatic X-rays versus discriminator threshold. The curves are normalized to the count rate obtained with the threshold set to half the energy of the incident photons. The charge-sharing slope ( $k$ ) was determined at the point of normalization and strongly depends on the incident photon energy.

thickness of Perspex, as well as “wrongly” applied to a flood-field obtained with a different thickness. With increasing deviation of the object thickness from the one used to measure the correction map, the SNR degrades from the maximum value, which as mentioned before (Fig. 1) is close to the Poisson limit. The loss of SNR goes up to 20%, much less than seen with similar measurements with the Medipix1 [9].

#### B. Charge Sharing

In order to investigate the effects of charge sharing, a series of measurements were performed at the beamline BM5 of the ESRF, Grenoble. Within these measurements, the spectral signal of the mono-energetic photons of 8, 10, 15, 20, and 40 keV of a field size of 1 mm<sup>2</sup> was measured using the wide threshold range of the Medipix2. The sensor used was a 300-μm-thick Si segmented  $p^+n$  diode reverse biased with 100 V. We decreased the discriminator threshold in steps of about 0.42 keV until reaching the noise floor of the readout electronics at about 4 keV. Photons in the energy range up to 40 kV convert into charge clouds with rms smaller than ~1.5 μm and are then transported by the applied electrical field to the collection electrodes to be further processed by the readout electronics of the Medipix2. While drifting toward the collection electrode, the charge cloud is subject to diffusion and coulomb repulsion, leading to an increase of its initial diameter. Depending on the depth of the conversion in the sensor, the drift time varies, therefore inducing different pulse shapes on the electrodes. In the case of conversion close to or at the border between pixels, the signal will be shared by neighboring pixels.

Fig. 4 shows the obtained data averaged over the active area and normalized to the count registered with the threshold set to half the photon energy. At this threshold setting, charge sharing does not influence to the recorded count rate and therefore represents the number of correctly counted photons. Deadtime and pileup effects are negligible since the maximum count rate was about 5 kHz with shaping times of < 2 μs and a discriminator delay of 1 μs. The plot shows a strong decrease of counts with threshold depending on the photon energy. In the ideal case

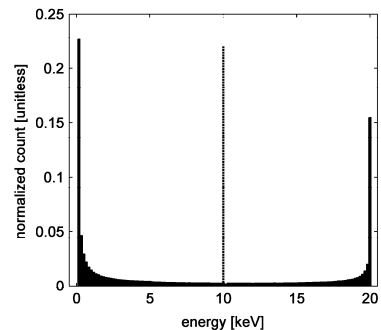


Fig. 5. Simulated signal spectrum on the collection electrode for a monochromatized 20-keV photon beam. Charge sharing between neighboring pixels results in a continuous pulse height spectrum on the collection electrodes.

without charge sharing the curves would follow the form of an s-curve with a plateau of 1 until the threshold surpasses the photon energy and then drop to 0 with the width given by the noise of the discrimination process [8]. In fact, this shape can be produced when limiting the incoming radiation to an area of about 10 μm<sup>2</sup> in the center of a pixel. The descending slope in Fig. 4 is introduced by charge sharing between adjacent pixels leading to a significant change of the actual signal registered by the front-end electronics.

### III. SIMULATION

In order to better understand contributions to the data shown in Fig. 4, we simulated the distribution of the signal height on the individual pixel electrode. In the simulation, we included the diameter of an average initial charge cloud, conversion probability, the drift time, and Coulomb repulsion. The rms of the initial charge cloud after conversion was simulated using PENELOPE [10], the drift time was calculated using the expression

$$t_{\text{drift}} = -\frac{\varepsilon}{n_{\text{eff}} \cdot e \cdot \mu} \cdot \log \left( 1 - \frac{n_{\text{eff}} \cdot e \cdot z \cdot d}{\varepsilon \left( \frac{n_{\text{eff}} \cdot e \cdot d^2}{2 \cdot \varepsilon} + V_{\text{bias}} \right)} \right) \quad (1)$$

where

- $e$  elemental electron charge;
- $\varepsilon$  dielectric permittivity of Silicon;
- $n_{\text{eff}}$  effective bulk doping density;
- $\mu$  hole mobility;
- $d$  sensor thickness;
- $z$  conversion depth;
- $V_{\text{bias}}$  sensor bias voltage.

The Coulomb repulsion was obtained by solving numerically the continuity equation

$$\frac{dn}{dt} = \nabla(\mu \cdot n \cdot E) + D \cdot \Delta n \quad (2)$$

where

- $n$  carrier density;
- $E$  electric field;
- $D$  diffusion constant;
- $T$  time.

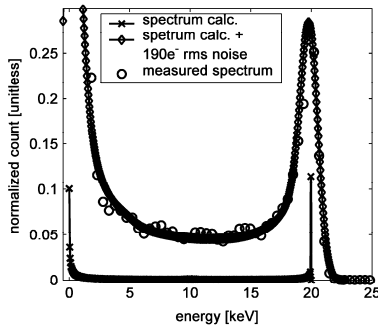


Fig. 6. Effects of charge sharing and additional front-end noise on the measured spectrum. The measured spectrum obtained with a monochromatic 20-keV photon beam of  $1 \text{ mm}^2$  is plotted together with the simulated spectrum as seen on the collection electrodes and the simulated spectrum with an additional 190 electrons rms front-end noise.

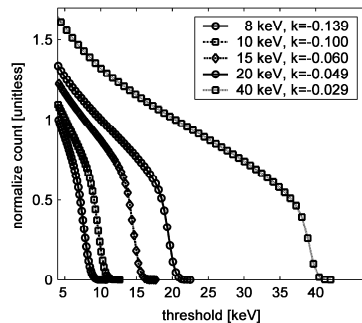


Fig. 7. Simulation of the measurements presented in Fig. 4. Again, the curves are normalized to the count rate obtained with the threshold set to half the energy of the incident photons. The charge-sharing slope ( $k$ ) was determined at the point of normalization.

The rms of the charge cloud arriving at the collection electrode was calculated for  $2 \cdot 10^5$  different conversion positions within the center cell of a neighborhood of nine pixels, each 55- $\mu\text{m}$  square. The total charge on each of the nine electrodes was registered for each individual event.

#### IV. RESULTS

##### A. Pulse Height Distribution

Fig. 5 shows the simulated apparent spectrum of a 20-keV photon beam as seen on the collection electrode of a single pixel. The initially mono-energetic signal is transferred into a continuous spectrum with a significant component of very small signal heights. This is due to the fact that only photons converted in the center of a pixel or very close to the collection electrode will yield the full pulse height. All other events are shared to a different extent with neighboring pixels. All signals contributing

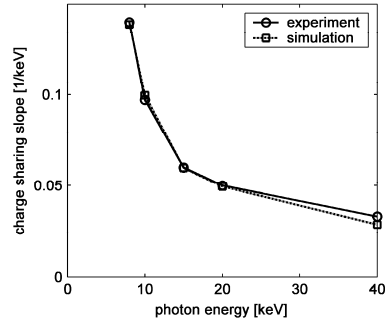


Fig. 8. Measured and simulated charge-sharing slope in the threshold scans for irradiation with monochromatic photons, taken from Figs. 4 and 7.

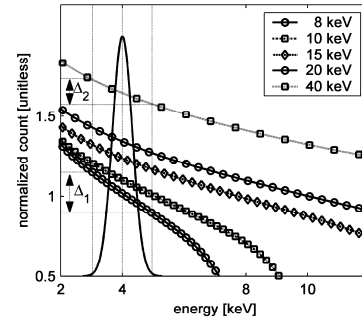


Fig. 9. Range of flatfield correction factors depends on the actual spread of pixel threshold and the incoming photon spectrum. The curves for 8–40-keV photons are a zoom into Fig. 7. Superimposed is a Gaussian distribution of pixel thresholds with 90 electrons rms dispersion. Note the difference in the resulting spread of correction factors— $\Delta_2$  for 40 keV and  $\Delta_1$  for 8 keV.

from half the photon energy to the full pulse height stem from photons converted within the pixel itself. The signals with lower energy originate from charge-shared events in the direct vicinity of the pixel.

In Fig. 6, the effect of the additional noise introduced by the amplification and discrimination process is illustrated, again calculated for 20-keV photons. It also shows the measured spectrum obtained by the derivative of the 20-keV data shown in Fig. 4. The simulated apparent spectrum convolved with a Gaussian noise of 190 electrons rms reproduces very accurately the experimental data.

The simulated threshold scan curves in Fig. 7 are in very good agreement with the experimental data in Fig. 4. Fig. 8 presents slope ( $k$ ) of the tail of the signal  $s$  curves calculated at the point of half the incident energy for the simulated and the measured data. Again, the simulations reproduce the measurements very well, the slightly lower simulated value for the 40-keV slope will be subject of further investigation.

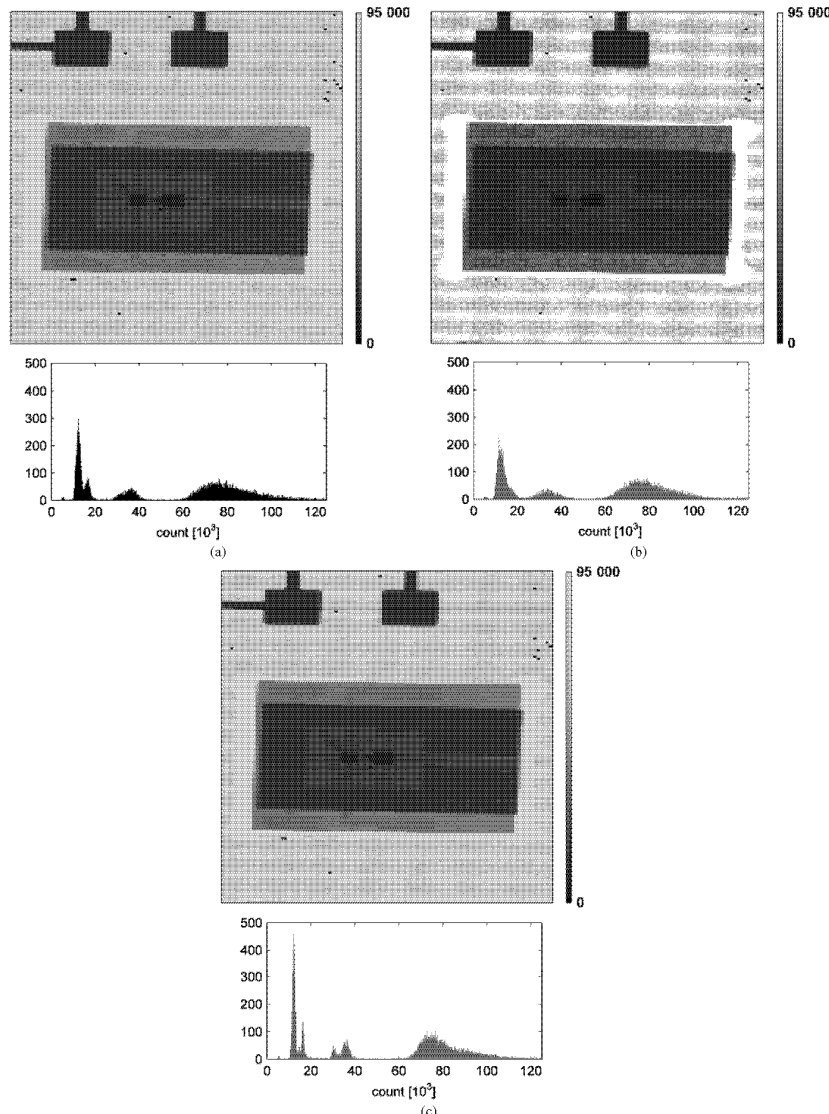


Fig. 10. (a) Image of an encapsulated laser diode taken with W-tube, 20-kV, 0.125-mm Al filter, no flatfield correction applied. Below, the corresponding histogram is shown. Count rates higher than  $50 \cdot 10^3$  represent the area of the printed circuit board. (b) Acquisition settings as in (a), but with a standard flatfield correction applied. The image noise is amplified with respect to the uncorrected image and the separation of components with high absorption is lost in the histogram. (c) Acquisition settings as in (a), but the correction map was derived from data obtained with additional 5-mm Perspex filtering. The improvement of image quality is clearly visible and the separation of the components in the histogram is improved.

Fig. 9 illustrates the effects of the threshold dispersion on the flatfield correction map. The plot is a zoom into Fig. 7 at low en-

ergies. The Gaussian distribution represents a typical threshold dispersion of the Medipix2 with 90 electrons rms and centered

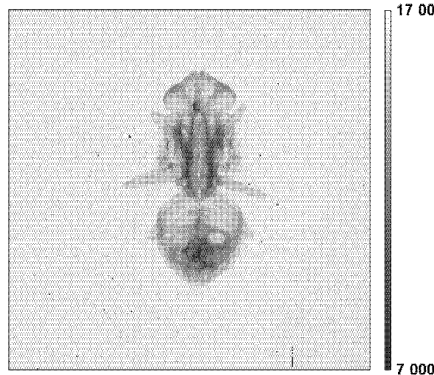


Fig. 11. Example of a low-absorption object; the spectrum of the incident photons is changed very little. Acquisition settings: W-tube, 14-kV, 0.125-mm Al, and 5-mm Perspex prefiltering.

around 4 keV, again a typical value for the lowest achievable threshold with the full matrix active. Since the slope of the count rate follows the trend given in Fig. 8, higher energy photons produce a narrower distribution of the factors in the flatfield correction map. The resulting spread in correction factors  $\Delta_1$  for 8 keV and  $\Delta_2$  for 40-keV photons, respectively, is indicated in Fig. 9.

The most pronounced change in charge-sharing slope (Fig. 8) occurs for photons below  $\sim 15$  keV. This means that imaging with a spectral content lower than  $\sim 15$  kV needs special considerations when significant beam hardening occurs. This is illustrated in Fig. 10. The object shown is an encapsulated laser-diode mounted on a printed circuit board. In order to see the different details, a W-tube was used with 0.125-mm Al filter and 20 kV tube voltage. In Fig. 10(a), the uncorrected image and its histogram are shown. In Fig. 10(b), the effects of beam hardening are clearly visible. The application of a conventional flatfield correction leads to a strong increase of image noise, masking even details visible in the uncorrected image, and the separation of components with high absorption in the histogram is lost. Fig. 10(c) shows the same data corrected with a flatfield correction obtained with a prefiltering of 5-mm Perspex in order to include the effects of beam hardening also in the correction map. The resulting image shows a clear improvement with respect to both the uncorrected data and the one with the standard correction map applied, and the improvement of the contrast between the different components of the laser diode is also evident in the histograms.

However, the standard correction map still is sufficient when the incident photon spectrum is hardly changed or the spectrum is confined to an energy range where the charge-sharing slopes depend less strongly on the photon energy. Fig. 11 illustrates the situation for a very low-attenuation object, a fly. In order to obtain contrast the W-tube voltage was set to 14 kV and the prefiltering was 0.125-mm Al and 5-mm Perspex. The image shown was obtained using conventional flatfield correction and

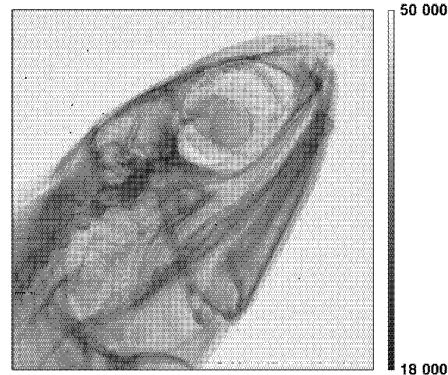


Fig. 12. Anchovy, acquisition settings: W-tube, 35-kV, 2.5-mm Al equivalent prefiltering. In this case, almost the entire spectrum is above 15 keV. The charge-sharing slope is almost constant in this energy range (Fig. 8) and, therefore, the flatfield correction is insensitive to beam hardening.

the anatomical features of the fly are clearly visible. In Fig. 12, the W-tube settings were 35 kV and 2.5-mm Al, resulting in an X-ray spectrum almost entirely above 15 keV. The correction factors are almost identical for the photon energies present, since the charge-sharing slopes in this range change very little with energy (Fig. 8). The image obtained with standard flatfield correction again gives very high contrast and resolution.

## V. DISCUSSION AND CONCLUSION

Charge sharing between neighboring cells in photon-counting pixel detectors is dependent on the photon energy, while the factors in the flatfield correction map depend predominantly on the dispersion of the actual threshold level of the individual pixels. Compressing the threshold dispersion by fine tuning, the pixel thresholds reduces the spread of correction factors but cannot completely remove the dispersion. Flatfield-correcting acquisitions, therefore, are less effective when beam hardening occurs. In case of a significant change of the energy spectrum of the incident beam the correction may even introduce strong image distortion.

One way to deal with this is to use monochromatic or narrow-spectrum beams for photon energies where charge sharing is strong, in order to reduce the effects of threshold dispersion on the correction map. Since this is not always possible, the effects of beam hardening can be decreased by deriving the flatfield correction from data obtained with a photon spectrum as close as possible to the one arriving at the detector. The good agreement of model calculations and experimental data suggests that, knowing the correction map for a given photon energy, it is possible to calculate the corresponding map for different photon energies. Furthermore, provided a sufficiently accurate on-chip calibration using an analog test input via a capacitor per pixel (as for the Medipix2), the individual threshold of each pixel can be determined. The calibration map then can be calculated for any given spectrum directly from an electrical characterization

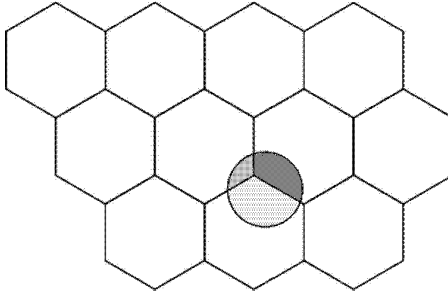


Fig. 13. Proposed geometry for summing charge-shared signals from neighboring pixels. Octagonal pixel geometry is better suited for this task as standard quadratic geometry. The total charge collected is compared against the threshold and valid counts are assigned to the pixel with the highest signal in a winner takes all logic.

of the chip, without floodfield measurements. This technique to obtain correction maps requires a very homogeneous sensor response, since sensor inhomogeneities are not taken into account. With high-resistivity silicon sensors, signal homogeneities of well below a percent can be reached [5], opening the possibility to correct selectively for features stemming from structures with different absorption in a spectral source X-ray acquisition using calculated correction maps. Another way to reduce the effects of charge sharing is to use new detector geometries such as three-dimensional detectors currently under development [11]. These detectors should confine the charge much better to the pixel, avoiding charge-sharing effects in signal formation.

A different approach is to deal with charge-shared events in the readout electronics. Effects of charge sharing can be removed entirely by increasing the functionality of the readout chip, notably to take into account the signal heights of neighboring pixels during the process of signal discrimination. The proposed improvement is to sum up the pixel signal with the charge-shared signals of its neighbors. If the total charge collected in the direct vicinity exceeds the given threshold, the count is assigned to the pixel with the highest signal in a winner takes all logic [7]. Fig. 13 illustrates the situation in hexagonal

pixel geometry. In a further extended version one could also calculate the center of mass for each event, in this way increasing the actual resolution beyond limits given by the pixel size.

#### ACKNOWLEDGMENT

The authors would like to thank K. Bethke (Panalytical), A. Fornaini (NIKHEF), H. Graafsma (ESRF), M. Mitschke (Univ. Erlangen), C. Ponchut (ESRF), P. Russo (Univ. Napoli), J. Visschers (NIKHEF), and R. de Vries (Panalytical) for the enduring efforts during the common measurements at ESRF, Grenoble.

#### REFERENCES

- [1] "Medical imaging—The assessment of image quality (ICRU Rep. 54)," Int. Commission Radiation, 1996.
- [2] P. Ottomello, G. A. Rottigni, C. Sartori, G. Zanella, and R. Zannoni, "MTF and DQE measurements in imaging detector by their single event response," *Nucl. Instrum. Methods A*, vol. 419, pp. 731–735, Dec. 1998.
- [3] D. S. Evans, A. Workman, and M. Payne, "A comparison of the imaging properties of CCD-based devices used for small field digital mammography," *Phys. Med. Biol.*, vol. 47, pp. 117–135, Jan. 2002.
- [4] G. Zanella and R. Zannoni, "DQE of imaging detectors in terms of spatial frequency," *Nucl. Instrum. Methods A*, vol. 437, pp. 163–167, Nov. 1999.
- [5] L. Ilustros, D. Davidson, M. Campbell, E. Heijne, and B. Mikulec, "Fixed pattern deviations in Si pixel detectors measured using the Medipix1 readout chip," *Nucl. Instrum. Methods A*, vol. 509, pp. 102–108, Aug. 2003.
- [6] M. Campbell, E. H. M. Heijne, G. Meddeler, E. Pernigotti, and W. Snoeyns, "Readout for a  $64 \times 64$  pixel matrix with 15-bit single photon counting," *IEEE Trans. Nucl. Sci.*, vol. 45, pp. 751–753, June 1998.
- [7] X. Llopart, M. Campbell, R. Dinapoli, D. San Segundo, and E. Pernigotti, "Medipix2, a 64k pixel readout with  $55 \mu\text{m}$  square elements working in single photon counting mode," *IEEE Trans. Nucl. Sci.*, vol. 49, pp. 2279–2283, Oct. 2002.
- [8] X. Llopart, K. Bethke, M. Campbell, A. Fornaini, H. Graafsma, E. Heijne, M. Mitschke, C. Ponchut, P. Russo, L. Ilustros, J. L. Visschers, and R. d. Vries, "Performance of the 65536 pixel Medipix2 assembly operating in single photon counting mode," in *Proc. 5th Int. Workshop Radiation Imaging Detectors*, Riga, Latvia, 2003.
- [9] D. W. Davidson, C. Frojdh, V. O'Shea, H.-E. Nilsson, and M. Rahman, "Limitations to flat-field correction methods when using an X-ray spectrum," *Nucl. Instrum. Methods A*, vol. 509, pp. 146–150, Aug. 2003.
- [10] J. Baró, J. Sempau, J. M. Fernández-Varea, and F. Salvat, "PENELOPE: An algorithm for Monte Carlo simulation of the penetration and energy loss of electrons and positrons in matter," *Nucl. Instrum. Methods B*, vol. 100, pp. 35–46, May 1995.
- [11] C. Da Via, G. Anelli, J. Hasi, P. Jarron, C. Kenney, A. Kok, S. Parker, E. Perozziello, and S. J. Watts, "Advances in silicon detectors for particle tracking in extreme radiation environments," *Nucl. Instrum. Methods A*, vol. 509, pp. 86–91, Aug. 2003.



**PAPER VI**

**Imaging properties of the *Medipix2* system exploiting single and dual energy thresholds**

**P a p e r VI**



# Imaging Properties of the Medipix2 System exploiting Single and Dual Energy Thresholds

L. Tlustos, R. Ballabriga, M. Campbell, E. Heijne, K. Kincade, X. Llopert, and P. Stejskal

**Abstract**—Low noise, high resolution, and high dose efficiency are the common requirements for most X-ray imaging applications. The dose efficiency is especially important for medical imaging systems. We present the imaging performance of the Medipix2 readout chip bump bonded to a  $300\ \mu\text{m}$  thick Si detector as a function of the detection threshold, a free parameter not available in conventional charge integrating imaging systems. Spatial resolution has been measured using the modulation transfer function (MTF) and it varies between 8.2 line-pairs/mm and 11.0 line pairs/mm at an MTF value of 70%. An associated measurement of noise power spectrum (NPS) permits us to derive the detective quantum efficiency (DQE) which can be as high as 25.5% for a broadband incoming spectrum. The influence of charge diffusion in the sensor together with threshold variation in the readout chip is discussed. Although the Medipix2 system is used in photon counting mode with a single threshold in energy, the system is also capable of counting within a given energy window as narrow as  $\sim 1.4\text{ keV}$ . First measurements and images using this feature reveal capabilities that allow identifying fluorescence and other sources of disturbance.

**Index Terms**—Radiation detectors, X-ray image sensors, X-ray spectroscopy detectors.

## I. INTRODUCTION

LOW NOISE, high spatial resolution, and high dose efficiency are key requirements in most X-ray imaging applications, with high dose efficiency a necessity in medical applications. In this paper, we present the imaging performance of the Medipix2 pixel detector readout chip [1] bump-bonded to a  $300\ \mu\text{m}$  thick  $p^+$  on n silicon sensor. The Medipix2 chip is designed and fabricated in a  $0.25\ \mu\text{m}$  CMOS technology and operates in single photon counting mode. It is usually operated with a single energy threshold on all pixels, but can also operate using an energy window. The modulation transfer function (MTF) describing the spatial resolution properties, the noise power spectrum (NPS) describing the image noise, and the detective quantum efficiency (DQE) giving a measure for image quality with respect to the incoming photonic signal have been measured as a function of the single energy threshold. The measurements obtained are in good agreement with a simple analytical model which describes charge deposition, drift, and diffusion in the sensor.

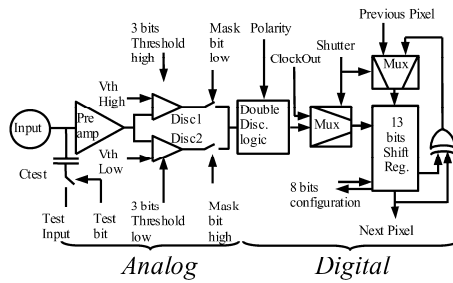


Fig. 1. Medipix2 pixel cell schematic [1].

ical model which describes charge deposition, drift, and diffusion in the sensor.

Almost all measurements carried out to date use only the low energy threshold [2]–[5]. In this paper, we present first results obtained using an energy window.

We start by briefly revisiting the functionality of the Medipix2 chip. Following that we describe measurements of MTF, NPS, and DQE for different values of the low energy threshold. The technique used to tune the low and the high energy thresholds is then described, and finally some images which were taken using the energy window are presented and discussed.

## II. MEDIPIX2 SYSTEM

The Medipix2 system comprises a  $256 \times 256$  channel CMOS readout chip which is bump bonded using solder bumps to an identically segmented sensor. The most commonly used sensor type is  $300\ \mu\text{m}$  thick high resistivity  $p^+$  on n Si sensor because it is relatively cheap and uniform. Incoming photons enter the unsegmented rear side of the sensor chip with the readout below. Each readout cell, Fig. 1, comprises a charge sensitive preamplifier-shaper, two discriminators, double discrimination logic and a 13-bit counter. Each pixel cell measures  $55\ \mu\text{m} \times 55\ \mu\text{m}$  and contains  $\sim 500$  transistors.

The preamplifier can be programmed for electron or hole collection. The low and the high thresholds of the window comparator are defined globally on the entire pixel matrix by individual 8-bit threshold DACs at the periphery of the chip. In order to minimize residual threshold variations, an independent 3-bit fine tuning for both thresholds is available in every pixel. An externally applied shutter determines whether the chip is in counting or readout mode. For randomly arriving particles, each pixel counts linearly up to an average rate of  $\sim 100\ \text{kHz}$ .

Manuscript received October 20, 2004; revised November 15, 2005. This work was supported in part by the Medical Physics Programme at the University of Canterbury, Christchurch, New Zealand, and in part by the New Zealand Foundation for Research, Science, and Technology under Contract UOAX0210.

L. Tlustos, R. Ballabriga, M. Campbell, E. Heijne, and X. Llopert are with the PH Division, CERN, 1211 Geneva 23, Switzerland (e-mail: Lukas.Tlustos@cern.ch).

K. Kincade is with the University of Canterbury, Christchurch 8020, New Zealand.

P. Stejskal is with the Institute of Experimental and Applied Physics, Technical University of Prague, Prague CZ-12800, Czech Republic.  
Digital Object Identifier 10.1109/TNS.2006.869844

Readout of the entire matrix takes  $\sim 10$  ms using the serial port or  $\sim 300 \mu\text{s}$  using the 32-bit parallel bus. The total power consumption is  $\sim 500$  mW, which means that the chip can be operated without cooling.

#### A. Threshold Fine Tuning

In order to obtain a uniform detector response, the narrowest possible distribution of pixel threshold levels across the matrix has to be found. This is achieved using a separate dedicated 8-bit threshold adjustment DAC (THS) at the periphery set uniformly across the matrix which determines the maximal offset to the unadjusted threshold position. In the individual pixel, this offset is scaled by the 3-bit fine tuning DAC.

To fine-tune the thresholds, the optimal value for THS and the optimal setting for adjustment bits have to be found. First the amplitude of the actual threshold level for the 8 possible adjustment values has to be determined in each pixel. For the low threshold this is done by using a constant input signal to the pixel preamplifier, while scanning the low threshold DAC (THL) value across the input signal level for each 3-bit threshold adjust code.

To generate the constant input signal, a known external voltage step pulse is injected through the injection capacitor present on each pixel. Each pixel is pulsed a fixed number of times during the shutter opening interval and the ratio of recorded hits divided by the number of input pulses is registered and plotted against the value of THL. The result of this scan is a series of s-shaped curves. The threshold is defined as the DAC value at which 50% of the applied signals are recorded. The same procedure can be applied using a monochromatic line of a radioactive source, e.g.,  $^{109}\text{Cd}$  (K lines at  $\sim 22$  keV and  $\sim 25$  keV) as constant input signal.

Both methods have limitations. Threshold tuning using a radioactive source is extremely time consuming due to the limited activity of the available sources. The test pulse method yields distorted results, since it is impossible to guarantee a perfectly uniform value of injection capacitance and moreover in the present chip there is a systematic nonuniformity of the pulse amplitude across the chip.

An alternative method for tuning the low threshold uses the so-called noise floor (at around  $1000 \text{ e}^-$ ) of the readout chip. As the threshold in any given pixel is lowered toward the noise floor it starts to count. The threshold DAC value at which a pixel starts to count is considered to be proportional to its inherent threshold.

Whichever way the actual pixel threshold levels are measured, a histogram of the measured values is then constructed for each of the 8 adjustment codes. The resulting histograms of the 8 threshold scans are Gaussian distributions of threshold voltages. The threshold-tuning DAC THS now is used to adjust the relative position of the Gaussian distributions. To obtain an optimal compression of the threshold spread the threshold tuning value is chosen such that the Gaussian distributions obtained with the adjustment value set to 0 and 7 overlap by 1/8 of the width of the unadjusted distribution. Then for each pixel, the adjustment value giving the threshold closest to the crossing point of the uncompressed distributions is chosen to obtain the compressed threshold distribution. Fig. 2 shows the respective

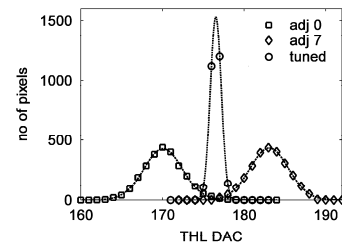


Fig. 2. Medipix2 threshold adjustment: The untuned threshold distributions with the adjustment bits in all pixels set to 000 and 111, respectively, are plotted, together with the compressed threshold distribution after adjustment. The Gaussian fits to the distributions are also plotted.

threshold distributions for the adjustment value set to 0 and 7 in all pixels together with the final compressed distribution. It has been shown [2] that differences in adjustment maps obtained using noise floor and radioactive sources lie within the accuracy of the 8-bit DAC.

The high threshold can be tuned analogous to the low one using either test pulses or radioactive sources. Because of the above mentioned limitations we decided neither to rely on the test pulse amplitude nor on the very slow source measurement technique for the high threshold tuning. Instead, we made use of a particular feature of the double discrimination logic. The energy window logic in the pixel is designed such that if the high threshold DAC is set to a value lower than the low threshold DAC then only the low threshold is used [1]. This is how the mode of the chip can be changed from energy window operation to single threshold operation. Therefore, we inject very high input charge pulses, fixing the high threshold well below this input charge level, and then decrease the high threshold DAC value until it crosses the already fine tuned low threshold.

With the high threshold set above the low threshold, the input signal is outside the valid energy window and no counts are recorded. By crossing low threshold level with the higher threshold, the pixel is switched from energy window mode to single threshold mode and starts counting the test pulses. In this way, response s-curves can be constructed per pixel, and a high threshold mask can be generated using a procedure which is similar to that used for generating the low threshold mask. Interestingly, we observe little correlation between the low and the high threshold masks, which indicates that the threshold variation is not dominated by the common preamplifier but rather by variations in the discriminator switching points. Testing later with a  $^{109}\text{Cd}$  radioactive source showed that the narrowest usable window corresponds to a difference of 2 DAC values between the low and the high thresholds of this chip, corresponding to an energy difference of  $\sim 1.4$  keV.

### III. OPERATION AND PERFORMANCE WITH A SINGLE THRESHOLD

A number of studies are already published on the behavior of the system as an imaging device [3]–[5]. In particular, we reported in [3] that the combination of charge diffusion in the

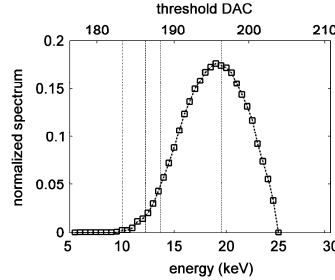


Fig. 3. Simulation of the absorbed photon spectrum in a  $300\text{ }\mu\text{m}$  Si sensor for a W-target expected from the X-ray tube with 2.5 mm Al filter operated at 25 keV. Also indicated are the DAC values and corresponding thresholds in energy used for the measurements.

sensor and residual pixel-to-pixel threshold variations in the readout chip even after threshold adjustment lead to virtual changes in the effective size of a pixel. Photons which deposit their energy near the pixel boundaries are more or less detected as a consequence. This obliges us to apply a flat-field correction to data which corrects for residual count variations in the order of up to  $\pm 4\%$ .

Having explored and understood the flat field corrections, we were interested in also studying the effect of varying the global threshold on the imaging properties of the system as such a possibility does not exist in conventional charge integrating systems. For the measurements which follow in this section, we used a Seifert FK-61-04x12 X-ray tube with a W-target, a 2.5 mm thick Al filter and a tube voltage of 25 kV.

Fig. 3 illustrates the positions of the threshold used in the measurements with respect to the calculated spectrum of photons converted in  $300\text{ }\mu\text{m}$  of Si. The incident photon spectrum produced by the X-ray tube was calculated following [6]. The thresholds in energy corresponded to 9.1 keV, 11.3 keV, 12.8 keV, and 18.8 keV. The energy calibration of the threshold DAC used in Fig. 3 was obtained by performing threshold scans for several tube voltages in the range from 20 to 55 keV and using endpoints of the so obtained photon spectra as reference values. In order to quantify the imaging performance at the 4 threshold levels given above, the MTF and the NPS have been measured at each threshold setting.

The spatial resolution properties of an imaging system as a function of the spatial frequency of the input signal are described by the modulation transfer function (MTF) by giving a measure of the frequency response of the system to a sinusoidal input of a given spatial frequency.

To exclude the effects of under-sampling in the process of measuring the MTF, it is common practice to determine the presampling MTF<sub>pre</sub> which is the MTF of the system prior to digitization. It was measured using an angulated slit technique [7] with a lead edge mask placed at an angle of  $\sim 2^\circ$  to a column or row. In this way an increasing fraction of the pixel area is covered along the column or row. The perpendicular distance from each pixel to the edge then was calculated, in this way

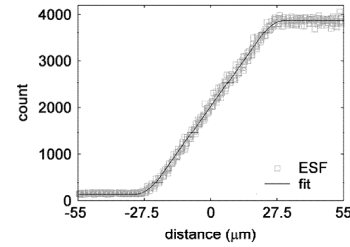


Fig. 4. Over-sampled edge spread function (ESF) measured with the low energy threshold set to 11.3 keV.

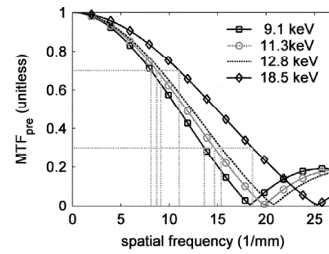


Fig. 5. Calculated presampling modulation transfer function (MTF<sub>pre</sub>) based on an edge measurement for the system at different threshold levels.

providing an over-sampled edge spread function (ESF). A modified erf function was fitted to the data and the derivative of the fitted function underwent a Fourier transform, thereby yielding the presampling MTF. The over-sampled edge spread function measured with the lower energy threshold set to 11.3 keV is plotted in Fig. 4.

The results for the presampling MTF are plotted in Fig. 5. The effect of increasing the threshold is to improve the MTF. Increasing the threshold diminishes the equivalent active size of the pixel. With increasing threshold an increasing fraction of photons whose charge is shared between pixels will be omitted from the image, leading to a nonresponding area around the pixel borders. The resulting decrease in active pixel size enables an improvement in MTF beyond the value predicted by Nyquist Sampling Theory for the given pixel pitch.

However, the tradeoff in terms image noise can be inferred from the noise power spectrum (NPS), Fig. 6. All images contain some noise, which, in a digital system, may be measured as the variance of the pixel to pixel fluctuations present in a flood image. The NPS provides a spectral decomposition of the variance to estimate the spatial frequency dependence of the noise.

The variance of the pixel to pixel values analyzed in terms of its spatial frequency content is given by the NPS. It is defined as the Fourier transform of the noise auto-covariance function. To calculate the NPS for each low threshold value 100 flood-field images were recorded. 80 of these images were used to calculate the flat-field correction maps and the remaining 20 frames were used to derive the NPS. First, the flat-field correction was

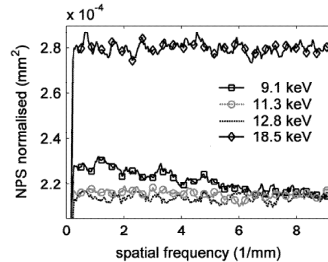


Fig. 6. Calculated NPS at different thresholds.

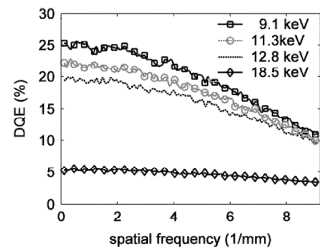


Fig. 7. Detective quantum efficiency (DQE) at different thresholds.

applied to each frame, then linear trends in the frame were removed and finally the 2-dimensional Fourier transform of each of the resulting frames was calculated. The normalized NPS was calculated by

$$NPS_{norm} = \left| \text{Fourier} \left( \frac{X_{ij} - \mu}{\mu} \right) \right|^2$$

with  $X_{ij}$  denoting the measured counts over the entire matrix after flat-field correction and detrending and  $\mu$  the mean count on the entire matrix.

Different doses given in Table I were used at the different thresholds in order to calculate the NPS from data with the same mean count. This explains why the NPS at a threshold of 9.1 keV looks to be greater than those at 11.3 and 12.8 keV.

The DQE describes the image quality with respect to the incoming signal, thus characterizing the system performance. It gives the fraction of incident quanta contributing to image quality, in other words the degradation of information in the signal in the detector system

$$DQE(f) = \frac{SNR_{out}^2}{SNR_{in}^2} = \frac{MTF^2(f)}{\Phi \cdot NPS_{norm}(f)} \leq 1$$

with  $\Phi$  denoting the number of incident photons.

Fig. 7 shows the computed DQEs for the different threshold settings. A characteristic value of the DQE is its value at zero spatial frequency, which is a measure of the effective quantum efficiency (QE) of the system. The lowest threshold gives the highest QE of ~25–26%. This approaches very closely the maximum theoretical value of 27%, given by the total attenuation of

TABLE I  
SUMMARY OF IMAGING RESULTS FOR A SINGLE THRESHOLD

Threshold Energy [keV]	MTF @ 70 % [line pairs/mm]	Dose used for DQE Measurement [mGy]	DQE @ 0 line pairs/mm [%]
9.1	8.2	1.05	25.5
11.3	8.8	1.26	22.0
12.8	9.2	1.43	19.5
18.8	11.0	3.99	5.5

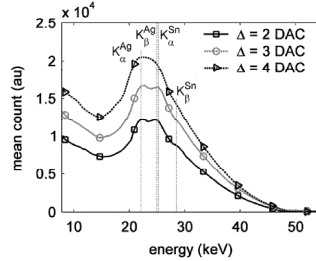


Fig. 8. Photon spectrum of W target X-ray tube with 2.5 mm Al filter, measured using the window threshold mode of the Medipix2. The upper curve shows the total number of counts for an energy window of 4 DAC values (~2.8 keV) between the low and the high threshold, the middle curve for 3 DAC values (~2.1 keV), and the lower curve for 2 DAC values (~1.4 keV). Note the lines indicating the nominal energies of the  $K\alpha$  and  $K\beta$  lines of Sn and Ag.

a 25 kV W-tube spectrum in a 300  $\mu$ m Si sensor. The penalty for the increased spatial resolution obtained at higher energy thresholds is the reduction of the  $DQE(0)$ . The most pronounced decrease was observed for the threshold set to 18.6 keV with a DQE of ~5% at zero spatial frequency. Table I summarizes the results.

We can conclude from this study that increasing the threshold in the pixels is one means of improving the spatial resolution of the system but only at the expense of a decreased DQE. More complex functionality may eventually be implemented in the pixel electronics to overcome this degradation.

#### IV. ENERGY WINDOW MEASUREMENTS

The measurements in the previous section were made using the single low threshold. In what follows, we examine the behavior of the system using an energy window in all pixels.

The threshold tuning was performed for both the low and the high threshold as described in Section II-A. The tuned device was placed under the X-ray tube mentioned earlier using the usual W target with 2.5 mm Al filter, but this time setting a tube voltage of 50 kV. The photon spectrum was measured by scanning the low threshold over an energy range from 7 to 55 keV, at the same time adjusting also the high threshold with a fixed offset in DAC steps from the low threshold DAC. In this way, a constant energy window between the low and the high threshold was achieved.

In Fig. 8, the mean count is plotted as a function of the center of the energy window. Three threshold windows widths were used: 2, 3, and 4 DAC steps, corresponding to 1.4, 2.1, and

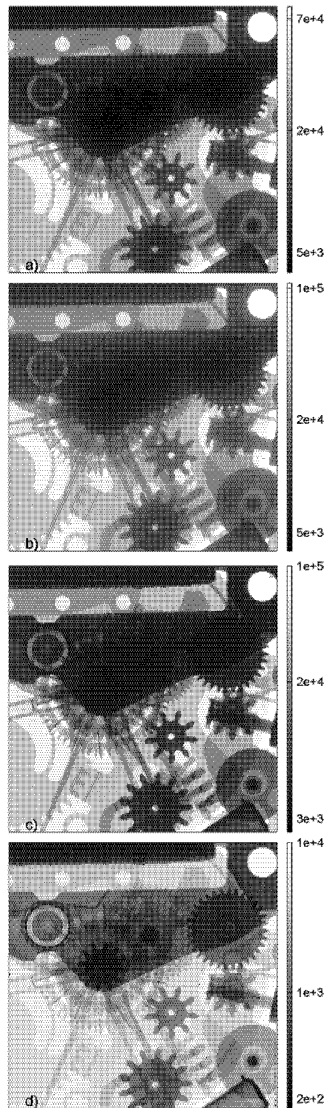


Fig. 9. Images of a plastic Swatch obtained with an energy window of  $\sim 3.5$  keV, selecting an energy range of (a) 16–19.5 keV, (b) 22–25.5 keV, (c) 27–30.5 keV, and (d) 40–43.5 keV.

2.8 keV, respectively. The overall shape of the so measured spectrum shows a tail at lower energies as a consequence of charge diffusion in the sensor. Furthermore, we observed peaks

which were associated with the Sn of the eutectic Sn/Pb bump bonds (K-alpha 25.2 keV, K-beta 28.5 keV) as well as peaks coming from the Ag (K-alpha 22.1 keV and K-beta 24.9 keV) which is contained in the glue used to mount the detector/sensor assembly on the PCB. Fluorescence from the silicon itself and from Al lines is very weak and occurs at much lower energies ( $< 2$  keV) and other metals such as Ti are present in much smaller quantities. As the observed fluorescence photons come from behind the sensor, they should also distort any image.

A plastic Swatch watch was placed near to the entry of the sensor and images taken at different energies with an energy window of  $\sim 3.5$  keV. Some of these images are shown in Fig. 9. In Fig. 9(a) the image is rather clear although, as expected, the higher density components of the watch are rather opaque as the lower energy photons are easily absorbed. In Fig. 9(b), the effect of the fluorescence photons is quite evident. Even though we are selecting harder photons than in Fig. 9(a), there is a blurring of the image probably due to the fluorescence photons coming from underneath the sensor or chip. In Fig. 9(c), the image becomes much clearer as the energy window is now above the emission lines of Sn and Ag. Finally, in Fig. 9(d), one observes that these harder X-rays reveal more objects hidden behind the denser components of the watch. Although a more systematic and quantitative study is needed, these results may be the first images taken using such a spectroscopic imager revealing the potential of such devices where only broadband X-ray sources are readily available.

#### V. CONCLUSION

In this paper, we have examined the influence of a low threshold on the performance of a photon counting X-ray imaging system. By increasing the low threshold used, it is possible to have improved spatial resolution but at the expense of DQE.

The high threshold of the Medipix2 system has been tuned, and a minimum window width of  $\sim 1.4$  keV was obtained. Images were taken proving the potential for such a spectroscopic imaging system where only broadband X-rays are available. Fluorescence as a source of image degradation could be identified by the study of spectra taken with different windows. These results are important as they provide first hints of the potential for such spectroscopic imaging devices.

There is ample room for improvements in a future system. Using a deeper submicron CMOS process, it should be possible to overcome the combined effects of charge diffusion and threshold variation on the performance of such a system in terms of energy resolution by summing the charge between neighboring pixels [1]. It is also possible to envisage the integration of several threshold windows with multiple counting registers on every pixel. This opens up the possibility of true color X-ray imaging. In particular one could think to filter out unwanted fluorescent energies. A 4-side buttable assembly should be developed enabling the construction of a large area imager.

#### ACKNOWLEDGMENT

The authors would like to thank their colleagues in the Medipix2 Collaboration (see <http://www.cern.ch/MEDIPIX>).

In particular, H. Verkooijen and J. Visschers provided much support with the readout system, and the software used here was based on the Medisoft4.0 which was provided by their colleagues in the University and INFN Section, Naples, Italy.

#### REFERENCES

- [1] X. Llopert, M. Campbell, R. Dinapoli, D. S. Segundo, and E. Pernigotti, "Medipix2, a 64 k pixel readout with 55  $\mu\text{m}$  square pixels working in single photon counting mode," *IEEE Trans. Nucl. Sci.*, vol. 49, no. 5, pp. 2279–2283, Oct. 2002.
- [2] X. Llopert, K. Bethke, M. Campbell, A. Fornaini, H. Graafsma, E. Heijne, M. Mitschke, C. Ponchut, P. Russo, L. Tlustos, J. L. Visschers, and R. de Vries, "Performance of the 65 536 pixel Medipix2 assembly operating in single photon counting mode," presented at the *5th Int. Workshop on Radiation Imaging Detectors (IWORD)*, Riga, Latvia, 2003.
- [3] L. Tlustos, M. Campbell, E. Heijne, and X. Llopert, "Signal variations in high-granularity Si pixel detectors," *IEEE Trans. Nucl. Sci.*, vol. 51, pp. 3006–3012, Dec. 2004.
- [4] B. Mikulec, M. Campbell, E. Heijne, X. Llopert, and L. Tlustos, "X-ray imaging using single photon processing with semiconductor pixel detectors," *Nucl. Instrum. Methods A*, vol. 511, pp. 282–286, 2003.
- [5] M. G. Bisogni, P. Delogu, M. E. Fantacci, G. Mettivier, M. C. Montesi, M. Novelli, M. Quattrochi, V. Rosso, P. Russo, and A. Stefanini, "A medipix2-based imaging system for digital mammography with silicon pixel detectors," *IEEE Trans. Nucl. Sci.*, vol. 51, no. 6, pp. 3081–3085, Dec. 2004.
- [6] J. M. Boone and J. A. Seibert, "An accurate method for computer generating tungsten anode X-ray spectra from 30 to 140 kV," *Medical Phys.*, vol. 24, no. 11, pp. 1661–1670, Nov. 1997.
- [7] H. Fujita *et al.*, "A simple method for determining the modulation transfer function in digital radiography," *IEEE Trans. Med. Imag.*, vol. 11, no. 3, pp. 34–39, Mar. 1992.

**PAPER VII**

**Electron imaging with *Medipix2* hybrid pixel detector**

**P a p e r VII**





Available online at [www.sciencedirect.com](http://www.sciencedirect.com)



*Ultramicroscopy* 107 (2007) 401–413

---

**ultramicroscopy**

---

[www.elsevier.com/locate/ultramic](http://www.elsevier.com/locate/ultramic)

## Electron imaging with Medipix2 hybrid pixel detector

G. McMullan<sup>a</sup>, D.M. Cattermole<sup>a</sup>, S. Chen<sup>a</sup>, R. Henderson<sup>a</sup>, X. Llopis<sup>b</sup>,  
C. Summerfield<sup>a</sup>, L. Tlustos<sup>b</sup>, A.R. Faruqi<sup>a,\*</sup>

<sup>a</sup>MRC Laboratory of Molecular Biology, Hills Road, Cambridge CB2 2QH, UK

<sup>b</sup>PH Division, CERN, 1211 Geneva 23, Switzerland

Received 24 June 2006; received in revised form 4 October 2006; accepted 17 October 2006

---

### Abstract

The electron imaging performance of Medipix2 is described. Medipix2 is a hybrid pixel detector composed of two layers. It has a sensor layer and a layer of readout electronics, in which each  $55\text{ }\mu\text{m} \times 55\text{ }\mu\text{m}$  pixel has upper and lower energy discrimination and MHz rate counting. The sensor layer consists of a  $300\text{ }\mu\text{m}$  slab of pixellated monolithic silicon and this is bonded to the readout chip. Experimental measurement of the detective quantum efficiency, DQE(0) at 120 keV shows that it can reach ~85% independent of electron exposure, since the detector has zero noise, and the DQE(Nyquist) can reach ~35% of that expected for a perfect detector ( $4/\pi^2$ ). Experimental measurement of the modulation transfer function (MTF) at Nyquist resolution for 120 keV electrons using a 60 keV lower energy threshold, yields a value that is 50% of that expected for a perfect detector ( $2/\pi$ ). Finally, Monte Carlo simulations of electron tracks and energy deposited in adjacent pixels have been performed and used to calculate expected values for the MTF and DQE as a function of the threshold energy. The good agreement between theory and experiment allows suggestions for further improvements to be made with confidence. The present detector is already very useful for experiments that require a high DQE at very low doses.

© 2006 Elsevier B.V. All rights reserved.

PACS: 85.60.G; 07.78.+s; 87.64.Ee

Keywords: Hybrid pixel detectors; Imaging detectors; Electron microscopy

---

### 1. Introduction

Electron cryomicroscopy (cryoEM) has become a widely used technique over the past few years in biological structure determination, with potential for substantial improvement [1]. Several different approaches are used depending on the size of the biological structure, the resolution required and the nature of the problem to be tackled. Recent improvements in microscope technology allow higher-resolution images to be acquired more conveniently. For example, field emission guns provide a more spatially and temporally coherent source of illumination, which enables images to be recorded with greater defocus and therefore improved contrast at low resolution, yet retain excellent high-resolution contrast. However, the

full potential of the new microscopes can only be realised if the image recording medium also undergoes significant improvement. The most important detector qualities required are a high detective quantum efficiency (DQE), excellent resolution as measured by modulation transfer function (MTF), insensitivity to long-term radiation damage and other useful features such as convenience, rapid readout, simplicity of archiving and reasonable cost. A high DQE implies high detection efficiency and a narrow gain variance coupled with low added noise, while a high MTF requires minimal signal or charge spreading to adjacent pixels. If readout noise can be completely eliminated, as with the Medipix2 detector described here, then a high DQE can be retained down to arbitrarily low-dose exposures.

The general advantages of electronic detectors over the more traditional film methods have been reviewed [2] and only the key conclusions will be summarised here. The

---

\*Corresponding author.

E-mail address: [arf@mrc-lmb.cam.ac.uk](mailto:arf@mrc-lmb.cam.ac.uk) (A.R. Faruqi).

outstanding advantage of film is the excellent spatial resolution, with pixel sizes of 5–10 µm (film scanners are able to scan with a resolution of 1 µm [3]). The sensitive area of the film is over 10,000 pixels square (100 Mpixels). However, there are also some major disadvantages with film. The inherent fog level produces a high background at the level of several primary electrons per pixel, resulting in poor signal-to-noise ratio (SNR) for weaker exposures [4]. The processing and scanning steps are also laborious introducing an inconvenient delay between image acquisition and assessment of the results. Detectors which allow the user to carry out on-line assessment of the data are desirable.

The first widely used electronic detectors for cryoEM were based on cooled, low-noise CCDs, developed originally for optical astronomy [5,6]. However, CCDs have not been used for direct detection of electrons because radiation damage causes rapid deterioration in performance [2]. A common technique, which avoids radiation damage and is used in most CCD cameras, is to use a phosphor-coated fibre optics assembly, optically coupled to the CCD. The primary electrons incident on the phosphor produce visible light photons, which are imaged onto the CCD through the fibre optics. The transfer of light involves a number of optical interfaces, where multiple scattering results in loss of resolution [7]. Binning adjacent pixels can help but reduces the number of independent pixels to far less than are available with film. Although CCDs have much lower noise than film, significant levels of readout noise and dark current noise remain. The former is minimised by employing double correlated sampling at the output and the latter by cooling. In many applications, the intrinsic CCD noise is much less than the shot noise in the image in which case the intrinsic noise is acceptable. The main applications of CCDs have been in those situations where the somewhat lower resolution (compared to film) is acceptable, e.g. in recording electron diffraction data [6], in focusing and alignment of the beam [5], or where the advantage in having immediate access to the stack of aligned images outweighs any disadvantage, such as with electron tomography [8].

Hybrid pixel detectors like Medipix2, are direct electron detectors, that count individual events, rather than giving an output proportional to the charge created by multiple events. Before we describe our evaluation of Medipix2, it is worth mentioning two other detectors we have recently investigated.

Monolithic active pixel sensors (MAPS [9]) give a proportional output in a similar way to phosphor-coated, fibre-optics-coupled CCD detectors. They operate by collecting charge from the cloud of electron hole pairs generated in a semiconductor epilayer by the passage of a high-energy electron. The charge collection, readout and reset electronics for a pixel is contained within the pixel and fabricated in CMOS on the epilayer. One MAPS device tested previously for electron detection [9,10] contained 525 × 525 pixels with a 25 µm pitch, and a ~4 µm epilayer.

The MAPS device, which was not radiation hardened, was evaluated at 120 keV for resolution, sensitivity and susceptibility to radiation damage [10]. More recent unpublished tests have extended these measurements up to 300 keV. The main conclusions are that the resolution and sensitivity are very good but the devices need to be radiation hardened before being suitable for practical use.

We also tested another CMOS sensor, the STAR250 (512 × 512 pixels with a 25 µm pitch), designed by FillFactory using radiation hard technology [11]. The tests on the STAR250 complemented our work on MAPS [10] and focused on the radiation hardness, by measuring the degradation in imaging performance at 300 keV following irradiation. The results showed that residual contrast was >80%, after correction for increased dark current, following irradiation with  $5 \times 10^7$  electron/pixel (80,000 electron/µm<sup>2</sup>), which corresponds to 1 Mrad. With this tolerance to radiation damage, the STAR250 would have a useful lifetime of ~1 year in cryoEM applications clearly demonstrating the feasibility of radiation hard direct electron detectors.

## **2. Technical description of the Quad-Medipix2 hybrid pixel detector**

The Medipix2 chip (designed within the Medipix collaboration [12]) was derived from a series of similar detectors, which have been developed in particle physics at CERN [13] for precise particle tracking under hostile conditions. The main changes to the design have resulted in a square pixel of smaller size along with different readout electronics needed for imaging rather than particle tracking applications. Medipix2 is a hybrid pixel detector, consisting of a pixelated monolithic sensor layer (a thin layer of silicon, with metal electrodes arranged in a square lattice) with individual pixels bump bonded to a readout electronics chip [14,15] with the same pitch and number of pixels. A review, containing a much more detailed description of direct detectors will be published shortly [16]. An incident photon or electron interacting with the silicon sensing material creates electron hole pairs in the sensor layer, which has a bias voltage applied across it. Under the influence of the drift field, the charge (electrons or holes depending on the polarity of the bias voltage) drifts to a collecting electrode and is transferred across the bump bond to the input amplifier on the readout chip for further processing. The amount of charge collected is proportional to the number of electron hole pairs produced, which in turn is proportional to the energy deposited in the sensor layer. For this reason, the terms “collected charge” and “deposited energy” will often be used interchangeably. Each pixel on the readout chip consists of an amplifier, a discriminator with a lower and upper threshold and a 13-bit counter allowing each pixel to act as an independent detector. Each pixel is capable of counting at 1 MHz, though this may be slightly lower if a large amount of energy is deposited in each event. An image is acquired by

allowing all pixels to count (in parallel) for a selected time, which can be set from a fraction of a second to many minutes; they are read out, at present serially, at the end of the ‘exposure’.

The development of the first photon counting chip within the Medipix collaboration [12] was the Medipix1 chip [17], consisting of an array of  $64 \times 64$  pixels, each pixel being  $170 \times 170 \mu\text{m}^2$  in area. An early evaluation of the Medipix1 chip (with a  $300 \mu\text{m}$  thick sensor) was made for recording electrons at  $120 \text{ keV}$ . The results showed a number of useful properties (excellent linearity and high counting rates per pixel) but also highlighted some of the shortcomings in the design (non-linearity in threshold settings at higher energies and the small total area) [18]. These and many other measurements made within the Medipix collaboration have influenced the design of the more recent Medipix2 chip (14,15), which this paper investigates.

Medipix2 has  $256 \times 256$  pixels, each of  $55 \times 55 \mu\text{m}^2$  area and bonded to an Application Specific Integrated Circuit (ASIC) chip with the readout electronics and containing the same number of pixels. The Medipix2 ASIC was designed in  $0.25 \mu\text{m}$  CMOS technology (as opposed to the  $1 \mu\text{m}$  SACMOS technology used for Medipix1), which allowed far more functionality to be incorporated in the electronics despite the smaller pixel size. Although the pixel is now only  $55 \mu\text{m}^2$ , each pixel has 504 transistors and a single chip contains  $\sim 33$  million transistors.

The operation of the Medipix2 is arranged as follows. Charge collected from the silicon detector layer by an incoming electron is amplified by the first element of the pixel electronics. The dual discriminator has both lower and upper thresholds, but only the lower threshold has been used for all measurements described here. The design of the new ASIC [14] ensures excellent linearity up to  $\sim 80,000$  electron hole pairs, which makes it possible to set the lower threshold over the range of energies of interest for EM applications (it takes  $3.6 \text{ eV}$  to produce an electron hole pair in silicon and so a single  $120 \text{ keV}$  primary electron can produce  $\sim 30,000$  electron hole pairs). Events which satisfy the threshold criterion increment the counter, which is read out sequentially at the end of the exposure. Since the energy deposited by electrons is large (typically up to  $100 \text{ keV}$ ) compared to the noise levels it is possible to obtain excellent signal-to-noise ratio for their detection. It has been shown already [4] that noise levels in single chip recording of  $120 \text{ keV}$  electrons are vanishingly small. This makes Medipix2 unique amongst electron detectors in providing noiseless operation, which is potentially very attractive for some applications; e.g. recording of an image in a number of successive frames (dose-fractionated image acquisition), which can be analysed later to observe the changes during the series of images. If this is attempted for detectors with some readout noise, such as CCD detectors, noise is simply accumulated with a reduction in  $S/N$  ratio.

Most of the results in this paper were obtained with a tiled multichip detector [14], consisting of four readout chips bonded to a single  $300 \mu\text{m}$  silicon detector. We refer to this as the Medipix\_Quad. The Quad detector contains  $516 \times 516$  pixels with the same pixel size as for the single chip, viz.  $55 \mu\text{m}$ . The readout ASIC was originally designed to be 3-side buttable, which allows linear tiling of two rows of four chips without dead spaces, but with one proviso. Due to some space constraints, the edge pixel between chips is three times larger than the other pixels – this factor needs to be corrected in the analysis software. The pixel in the centre of the detector, at the centre of the ‘cross’, is thus nine times bigger than the other pixels. A special multilayer board was designed and constructed [19] for tiling up to eight chips on the board in a  $4 \times 2$  configuration. However, only four chips, in a  $2 \times 2$  configuration were mounted in the assembly used in these measurements. Data readout for the Quad is carried out serially by connecting the four chips in a daisy chain; the readout time is increased by a factor of 4 compared to a single chip, but this constraint could easily be removed.

The complete cycle of exposure, readout and data storage in Medipix2 is controlled by Medisoft4 software [21]. When initially powering up the chip there is an initialising phase when the software carries out a series of checks; for the presence of the National Instruments Digital Input/Output (DIO) card in the control computer; the operation of the MUROS2 interface [20]; the operation of the Medipix2 chip; the counting of the number of chips in a multichip module; a check on the quality of bump-bonding; and a check for the functionality of the communications registers on the chip. There is a global setting for the lower threshold value but additionally, a 3-bit DAC is used for correcting the small differences in the thresholds in different pixels to obtain a better uniformity of response. A mask file, containing the optimised DAC values and location of malfunctioning pixels is loaded prior to data acquisition. The noise levels in the threshold distribution can be reduced from  $\sim 550 \text{ e}^-$  to  $110 \text{ e}^-$  by adopting this procedure [14].

### 3. Experimental details

#### 3.1. Quad mounting in the F30 electron microscope

The multilayer board carrying the Quad detector is mounted on a specially constructed steel plate as shown in Fig. 1. The plate forms the base of a cylindrical vessel, which becomes part of the microscope vacuum chamber. The readout electronics, located at the edges of the detector, are protected by a metal shield against direct electrons to reduce the effects of radiation damage. As mentioned earlier the detector is mounted on a board designed for eight chips but with only four positions populated by the Quad, which is located below the metal shield centred under the square hole. The output signals and the detector bias voltage are connected via a multi-pin

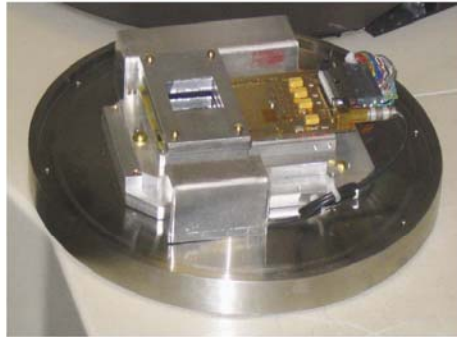


**Fig. 1.** Photograph of Medipix2\_Quad mounted on the steel base plate prior to installation in the FEI Tecnai F30 electron microscope. The Quad detector is located under the metal shield, which protects peripheral electronics, with a central square hole. The four Medipix2 readout chips are bump-bonded to the detector layer and the whole assembly is mounted on a multilayer board with decoupling capacitors visible on the right side. The signals are carried out via a SCSI connector. Vacuum feedthrough connectors are located under the metal shield in the top of the photograph.

plug and a coaxial cable (on the right side in the photograph shown in Fig. 1) to the vacuum feed-through connectors and on to the readout electronics, which is located outside the vacuum. Great care was exercised in the mechanical design of the base plate to avoid any radiation leakage.

### 3.2. Energy calibration of the threshold voltage

In order to set the threshold voltages accurately for different electron energies, it is essential to calibrate the threshold voltage as a function of the incident electron energy. Fig. 2 shows the measured response of the Medipix2, in terms of counts/s/pixel, at 20, 40, 80 and 120 keV, to a uniform beam as a function of the threshold voltage,  $V_{th}$ . At each energy the beam intensity was adjusted to ensure approximately 4000 counts/pixel in each frame at high  $V_{th}$ , where only a small amount of energy needs to be deposited in a pixel in order to record an event; the actual number of primary electrons was substantially less than 4000. The extrapolated intercepts at zero counts in Fig. 2 are assumed to be the threshold voltages corresponding to 20, 40, 80 and 120 keV. This assumes that a fraction of the electrons enter and deposit all their energy near the centre of a pixel and that the collected charge for these events corresponds to that generated by the total energy. The inset in Fig. 2 plots the extrapolated threshold setting versus the incident energy along with the least-squares fit to a straight line through the data. The least-squares fit gives a conversion factor from  $V_{th}$  to incident electron energy of  $-0.40 \text{ keV/mV}$ . As the negative slope implies, higher values of the threshold control voltage

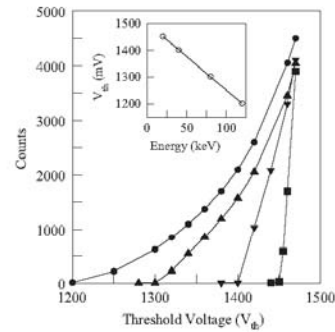


**Fig. 2.** Plot of experimental results on Medipix2 showing the variation in counts recorded per pixel as a function of threshold voltage,  $V_{th}$  in mV applied to each pixel of the chip, for 20 (square), 40 (down triangle), 80 (uptriangle) and 120 (circle) keV electrons. The detector was uniformly illuminated with electrons and results obtained from the average of large number of pixels. Inset shows the extrapolated zero count intercept values (open circles) plotted versus incident electron energy,  $E$ . The straight line shows the least-squares fit given by  $V_{th} = 1500.4 - 2.4879E$  in which  $V_{th}$  and  $E$  are in units of mV and keV.

applied to each pixel in the chip and expressed in mV, correspond to a smaller amount of energy, expressed as keV, deposited in the pixel and required to trigger a count.

### 3.3. Response of the Quad to electrons at energies between 120 and 300 keV

To assess the overall imaging performance of the Quad over a wide range of energies, the shadow image formed by introducing a standard EM grid into the position normally occupied by the pointer (a 300-mesh grid produced a pattern with  $\sim 650 \mu\text{m}$  spacing at the detector) was recorded at a number of energies between 120 and 300 keV. A montage of six such images is shown in Fig. 3(a). The most striking feature of the images, easily visible, is the gradual deterioration of the resolution as the electron energy is increased above  $\sim 180$  keV; at the two extreme energies, the difference is striking: the image at 120 keV is very sharp whereas the one at 300 keV is very blurred. The resolution problem is also illustrated by an alternative technique illustrated in the two images of single electron events recorded at 120 and 300 keV in Fig. 3(b) and (c). Single electron images are obtained by reducing the illumination of the electron beam to extremely low levels in these cases to  $\sim 1$  electron/100 pixels/frame. It can be observed that the number of multi-pixel events per electron is higher at 300 keV than at 120 keV due to greater charge spreading to adjacent pixels. This extra charge sharing accounts for the poor resolution in Fig. 3(a) at high electron energy. Monte Carlo simulations of electron tracks in silicon were performed to explain these results and these are discussed in greater detail in Section 4.

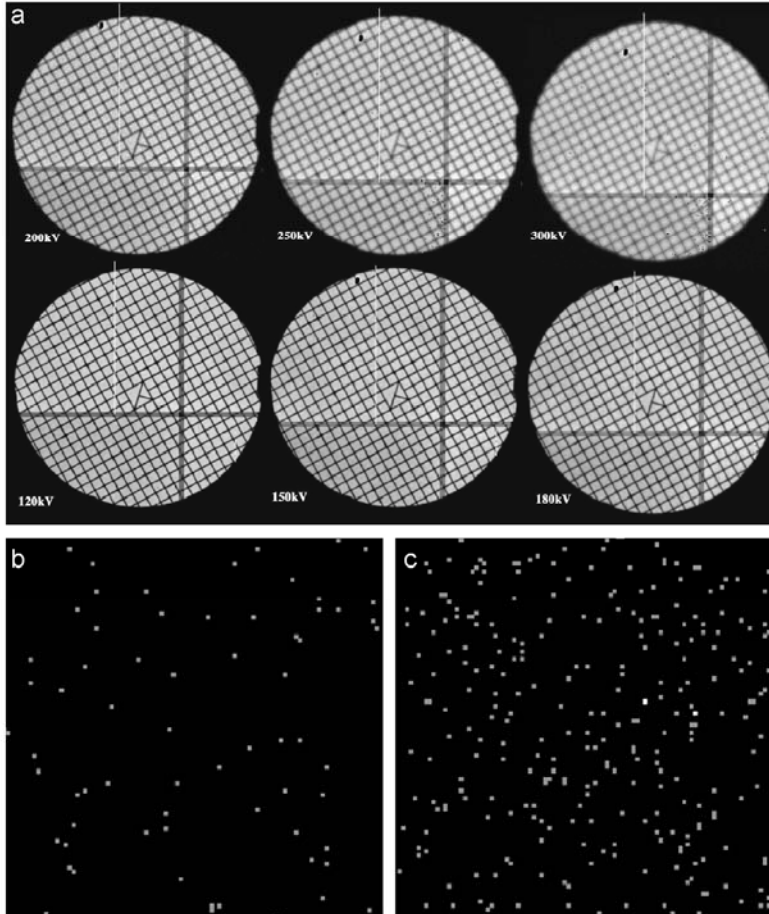


Fig. 3. (a) Montage of shadow images of an EM grid recorded on the Medipix\_Quad at 120, 150, 180, 200, 250 and 300 keV. As discussed in the text a 300-mesh grid was used for these images, which produced a regular pattern with a spacing of  $\sim 650 \mu\text{m}$  at the detector. The image of the grid bars is very sharp at 120 keV but gets progressively blurred as the electron energy is increased. As shown in Fig. 4, this blurring is due to the angular straggling of the primary electrons in the thick sensor layer, and is not seen with thin detectors such as film. (b) Observed single electron events at 120 keV recorded on the Medipix\_Quad with the threshold set to 45 keV. The majority of events are recorded in a single pixel with very few in two adjacent pixels. (c) Observed single electron events recorded at 300 keV on Medipix\_Quad with the threshold set to 80 keV. Due to increased charge sharing there is a greater fraction of events with 2 counts/electron compared to the image recorded at 120 keV.

We have already discussed the complete lack of radiation damage to the single Medipix2 chip at 120 keV [4]. The experiments for radiation damage measurements have been repeated at 120, 150, 180, 200 and 300 keV. As for our previous experimental set-up, the edges of the Quad were protected by a metal shield so that the readout electronics

were protected from direct radiation. The only radiation affecting the readout electronics chip would need to have travelled through the silicon detector layer. The tests for radiation damage were made by illuminating a very small circular area of the detector at high intensity. The irradiation period was kept short to minimise beam

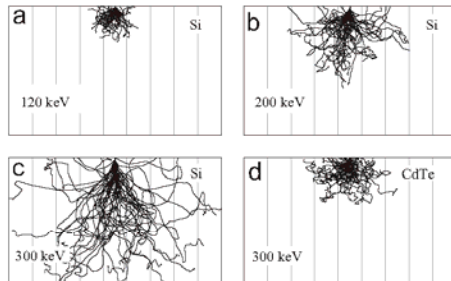


Fig. 4. Examples of calculated Monte Carlo electron trajectories obtained using the CSDA as described in the text, for electrons of different energy normally incident on a 300  $\mu\text{m}$  detector layer. The 55  $\mu\text{m}$  pixel spacing of the Medipix2 is indicated by the vertical bars and the electrons are incident at the centre of the middle pixel. The corresponding detector materials and incident electron energies are: (a) Si and 120 keV; (b) Si and 200 keV; (c) Si and 300 keV and (d) CdTe and 300 keV. The calculations for CdTe were carried out using an averaged mean ionisation potential (516 eV), atomic weight(120.0) and atomic number (50.0).

drift small drifts were corrected manually during the experiment. The intensity of the beam at the detector was set at 115,000 electron/pixel/s, which produces a total of  $4 \times 10^8$  electron/pixel over a period of 1 h. This corresponds to  $\sim 1.5$ – $3.0$  Mrad [11] of radiation depending on the incident electron energy. There was no discernible damage, as seen in grid images examined at the completion of the exposure, up to 200 keV. However, there was rapid deterioration of the image when the energy was set to 300 keV. In fact, at a dose level estimated to be between 100 and 150 krad, the irradiated area was non-functioning, and effectively dead. The experiment has not been repeated to establish the threshold for radiation damage as it was decided to operate Medipix2 only at those lower energies at which there was no radiation damage. The results on radiation damage at 300 keV (and no damage at lower energies) can be explained on the basis of the Monte Carlo simulations shown in Fig. 4(c) in Section 4. The range of 300 keV electrons in silicon is such that a fraction of the incident electrons is transmitted through the detector layer and is presumed to cause the damage. Since these radiation damage measurements were made, a newer version of the Medipix2 chip that is more radiation tolerant has become available but this has not yet been tested.

#### 4. Monte Carlo simulations

Monte Carlo simulations are a valuable tool for understanding the interactions of high-energy electrons and matter. Computer programs, such as EGSnrc [22], GEANT4 [23] and Penelope [24] are readily available for performing detailed simulations. A number of models for Medipix2 were tried but the simple one described here gives a surprisingly good description of the observed behaviour.

We assume that monochromatic high-energy electrons, at normal incidence, instantaneously pass through, back-scatter from, or come to rest in the sensor layer. The energy lost along the trajectory of an incident electron is assumed to be deposited locally and results in the production of electron hole pairs, with the number produced being proportional to the energy deposited. Under the influence of the applied bias, electrons and holes migrate to opposite sides of the detector. Because of the high bias voltage and purity of the detector layer it is assumed that lifetime effects can be ignored. The charge distribution arriving at the pixellated electrode will, however, be broadened by the lateral diffusion of the charge carriers as they migrate across the detector layer. The displacement of charge carriers inside the detector layer will also produce transient voltages at the pixel electrode but their contribution to the total integrated signal is small. The final analogue signal passed to the threshold electronics is directly proportional to the integral of the charge distribution. In the present model, this depends only on the initial distribution of energy and lateral diffusion of charge carriers. Even if the charge collection efficiency was not exactly 100%, this would not significantly affect the final conclusions.

To model the energy deposition in the detector layer a Monte Carlo program was written that explicitly keeps track of the energy loss and its position along the incident electron trajectory. The program follows the approach outlined in the book by Joy [25], in which elastic scattering is described by a screened Rutherford cross-section and energy loss by the continuous slowing down approximation, CSDA. Trajectories were terminated when the energy fell below 1 keV. Relativistic corrections were found to be important: for example, ignoring relativistic corrections leads to an upturn in the predicted back scattering coefficient above 50 keV which is not seen experimentally [26]. Full Monte Carlo calculations in which inelastic collisions were treated explicitly using inelastic cross-sections provided by Bichsel [27] were also carried out. While this did produce a few rare events in which electrons had far greater range, the calculated properties of Medipix2 were almost identical to those from CSDA calculations. With hindsight this is not surprising since, except for very low thresholds, the response of an individual pixel always involves a large fraction of the total energy of an incident electron. Note that this will not be the case for detectors such as the MAPS detector described earlier, where only a small part of the trajectory of an incident electron is recorded. In such detectors, there will be an intrinsic variability in the amount of energy deposited and a consequent reduction in the DQE.

The lateral diffusion of charge carriers between the point of generation and point of collection was taken into account by convoluting the deposited energy with a Gaussian distribution whose width,  $\sigma$ , depends on the deposition depth. In simulations by Tlustos [28] of the charge carrier diffusion in Medipix2 resulting from  $\gamma$ -ray absorption, the width of the distribution was found to be a

function of deposition depth, but since 120 keV electrons do not penetrate very deeply, a single fixed width of 10  $\mu\text{m}$  was used here. Tlustos [28] found a value of 7.5  $\mu\text{m}$  for shallow deposition depths such as found for 120 keV electrons, but a value of 10.0  $\mu\text{m}$  gave a better agreement with the shape of the curves in Fig. 2. Note that, for an incident 120 keV electron, the contribution from lateral diffusion to the overall charge distribution width seen at the pixel electrode is much smaller than that resulting from the chaotic trajectory of the primary electron, so the exact width is relatively unimportant.

The Medipix2 simulation program accumulates all the contributions from along the trajectory of each electron arriving within a given pixel boundary and records a signal in the pixel, if the sum exceeds a specified threshold. Various refinements of this procedure were also included. In particular, the calculations were also done with the detector layer divided into multiple layers of possibly different materials. Non-uniform collection efficiency over a pixel was also simulated by dividing a pixel into sub-pixels and calculating an effective pixel response from the weighted sum of the sub-pixels.

Examples of calculated electron trajectories for 120, 200 and 300 keV electrons in 300  $\mu\text{m}$  silicon are shown in Fig. 4(a)–(c), respectively. The rapid increase in electron range with energy can be seen. This, coupled with the increase in rate of energy deposition per unit length as electrons slow down, explains the increased blurring with incident energy evident in Fig. 3(a). At 200 keV none of the incident electrons in a CSDA calculation is able to penetrate through the 300  $\mu\text{m}$  silicon layer. However, in our full Monte Carlo calculations, in which both inelastic and elastic collisions are treated stochastically, 1 in  $2 \times 10^6$  electrons do get through. At 300 keV, approximately 7% are transmitted in both the CSDA and non-CSDA calculations. Assuming the ASIC is damaged by transmitted electrons the simulations confirm our findings on radiation damage, which was not detected at 200 keV but becomes very severe at 300 keV. To operate at higher voltages, a thicker sensor layer could be used but, due to the increased lateral spread of incident electrons, any such detector would also require a greater pixel size. Alternatively, a denser material such as CdTe could be used in the sensor. Fig. 4(d) shows calculated trajectories of 300 keV electrons in a 300  $\mu\text{m}$  CdTe layer. No electrons pass through the layer and the lateral spread is not that much greater than that of 120 keV electrons in silicon. Provided fabrication difficulties can be overcome, a detector with a 300  $\mu\text{m}$  CdTe sensor layer and 55  $\mu\text{m}$  pixels should therefore be usable with 300 keV electrons.

The simulated electron tracks at different energies shown in Fig. 4(a)–(d) do not contain any detailed information about the amount of energy deposited along each path in the detector layer. It is possible to calculate the volume over which the total energy is deposited but this information is not enough to predict the sensitivity of adjacent pixels to incident electrons. For example, it can be seen

from Fig. 4(a) that a 120 keV electron entering the centre of a 55  $\mu\text{m}$  pixel would generally deposit most of its energy in that central pixel and not share much charge with any adjacent pixels. However, if the electron were to enter near one edge, then two pixels might share the energy. An electron hitting near a corner might share its energy between 3 or 4 pixels and have a good chance of triggering 3 or 4 pixels, depending on the energy threshold selected and the precise path of that individual electron. The number of triggered pixels at 200 or 300 keV is considerably higher than at 120 keV. A critical parameter in calculating the number of triggered pixels is the lower threshold preset for each pixel. We have seen in Section 3.3 that it is possible to reduce the number of counts per electron by operating at a higher threshold.

#### 4.1. Variation of counts with threshold: simulations and experimental measurements

Monte Carlo simulations were used to predict the response of Medipix2 to 120 keV electrons in terms of the variation of the measured total counts as a function of the applied threshold. It can be seen intuitively that for threshold values greater than 60 keV it is only possible for a 120 keV electron to deposit sufficient energy for a pixel to record a count in a single pixel. As the threshold is lowered below 60 keV, it is possible to deposit sufficient energy in two adjacent pixels above the threshold value resulting in two counts from a single incident electron. With progressively decreasing threshold it is possible to record an event in 3 or 4 and very rarely 5 pixels from a single incident electron.

In Fig. 5, the measured counts versus threshold voltage using the same data shown in Fig. 2 for 120 keV have been re-plotted against threshold energy using the conversion derived in Section 3.2. Also plotted are simulation results for the expected total number of counts and its decomposition, as explained in the figure caption, in terms of events involving 1–5 pixels. The simulation results were obtained by calculating the response as a function of threshold to electrons randomly distributed over a pixel. The experimental number of incident electrons per pixel was not known accurately, and so the simulation results were scaled to fit the observed number of counts at low threshold energy. This required 2100 incident electrons per pixel in agreement with rough estimates based on the illuminated area and total beam current. With this assumption, the predicted total number of counts versus threshold energy can be seen to fit the measured results very well.

The dotted region in Fig. 5 represents the contribution to the total counts from events where an incident electron is recorded in only one pixel. This is quite small at low thresholds as the nature of the trajectory of a 120 keV electron and lateral charge diffusion within the sensor layer conspire to make it unlikely for charge to be collected in only one pixel. As the threshold is increased the overall number of counts falls, but the fraction recorded as single count events increases.

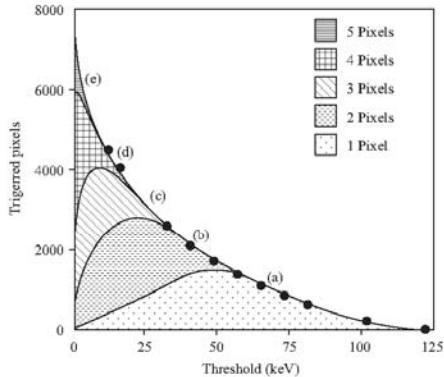


Fig. 5. Monte Carlo simulations for the predicted number of triggered pixels versus threshold in Medipix2 subject to 2100 incident 120 keV electrons. The contributions from events with 1, 2, 3, 4 and 5 pixels are indicated by different patterns in the figure. The lowest distribution in the figure, shown as dots and labelled (a), show the variation of single counts per incident electron as a function of threshold. The dashes show the number of double counts (labelled (b)). The left sloping dotted vertical lines show three counts (labelled (c)) and the square grid lines show four counts per electron (labelled (d)). A small number of events with 5 triggered pixels per electron is shown with horizontal lines (labelled (e)). The envelope of the five distributions is the smooth curve, which gives the total expected number of triggered pixels per 2100 incident electrons over the range of thresholds. Experimental measurements showing the total number of triggered pixels recorded as a function of threshold are shown as black filled circles and are in excellent agreement with the predictions.

Beyond 60 keV only single pixel events are recorded. At a threshold of 60 keV,  $\sim 1330$  counts are recorded and, as explained in Section 6, since these are single pixel events the corresponding DQE(0) is simply  $1330/2100 = 0.63$ .

#### 4.2. Simulation of single electron events at 120 keV

The simulations described in Section 4.1 predict the number of counts per electron expected in Medipix2 but do not address the question of the spatial distribution of the counting pixels. To investigate this, Monte Carlo simulations were carried out in which 120 keV electrons were randomly distributed over a seed pixel and the various patterns of response in the seed and neighbouring pixels recorded as a function of threshold energy. A montage of the most likely patterns of response to an electron incident on the centre pixel of the  $5 \times 5$  grid is shown in Fig. 6. Only representatives of symmetry related patterns and events in which at least 10 keV is deposited in each pixel are shown. As the threshold is varied the possible events and their relative probability change. The patterns in Fig. 6(a)–(n) represent all possible events that occur with a total probability of greater than 0.5%, when the threshold is set to 10 keV. Of these only Fig. 6(a)–(j) occur with the

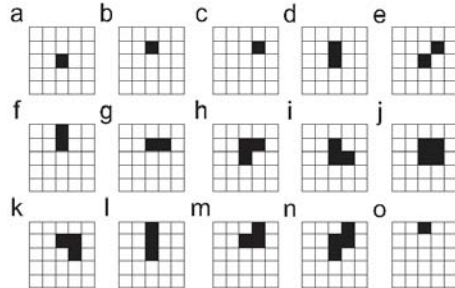


Fig. 6. Simulation results for the different classes of Medipix2 response to 120 keV electrons incident randomly on the centre pixel in a  $5 \times 5$  pixel array. Examples in (a)–(n) show the class of events expected with greater than 0.5% probability in which more than 10 keV is deposited in a pixel. The example in (o) shows an event that can occur, but at very low probability, with the threshold set around 50 keV. In this event the electron is incident on the centre pixel but is scattered through the neighbouring pixel, without being registered in it, and finally deposits most of its energy in the next-nearest neighbour pixel. If the energy deposition criterion is set to 20 keV, examples (a)–(j) would be recorded, at 40 keV (a)–(g) would be recorded and at 80 keV (a)–(c) would be recorded.

threshold set to 20 keV, Fig. 6(a)–(g) at 40 keV and Fig. 6(a)–(c) at 80 keV. With the threshold set above one half the incident energy, an incident electron is only ever recorded in a single pixel, but this need not be the pixel on which the electron was incident. Fig. 6(o) shows an event which occurs with greater than 0.1% probability at thresholds around 50 keV, in which the incident electron is scattered through the neighbouring pixel to be recorded in the next-nearest neighbour pixel.

#### 5. MTF

The MTF describes the spatial frequency variation or the response of a detector to a sinusoidal input signal. It is measured by comparing the measured output amplitude spectrum to that of an input signal with a known amplitude spectrum. In electron microscopy, the shadow of a straight edge [29,30] is usually used but other sources such as holographic fringes [31] may also be used.

The MTF of the Medipix2 was measured at 40, 80 and 120 keV using a variation on the edge-spread method. We used shadow images of a 0.5 mm gold wire held at the pointer position of the microscope, the edges of the wire being oriented at a slight angle to the detector pixel grid. As the observed number of counts in a pixel decreases with increasing threshold, the beam intensity was adjusted at each electron energy to ensure as many counts as possible without overflowing the pixel counter. In practice, this meant 4000 counts in each pixel during a 1 s frame. In order to improve statistical precision, 20 frames were added together at each threshold. The Medipix2 detector

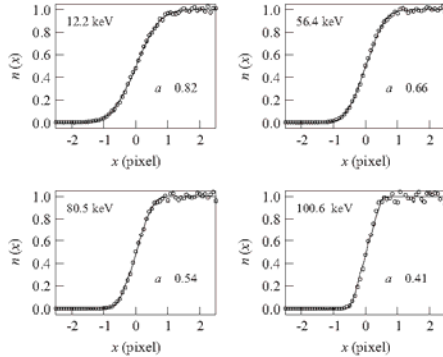


Fig. 7. Normalised edge spread curves as defined in Eq. (1), recorded with threshold settings of 12.2, 56.4, 80.5 and 100.6 keV, and an incident beam energy of 120 keV. As discussed in the main text the data, shown as circles, can be fitted by a model in which the line spread function consists of a single Gaussian. The fitted edge spread functions are indicated by the continuous curves with corresponding values of the parameter  $a$  in Eq. (2) shown.

used here contained a number of defective pixels and, to avoid using these, a mask from a bright field image was used to eliminate them from subsequent analysis.

In the analysis, the position and orientation of an edge was first determined and then the distance of each pixel from the edge determined. One edge of the wire was found to be slightly curved and this edge was fitted by a quadratic and the perpendicular distances of the pixels from the edge determined. Results from the edges analysed together, separately and by breaking the edges into small sections, gave similar results. Having found the edge position, bright,  $b$ , and dark,  $d$ , field values were determined from averages of the pixel values on opposite sides, and well away from the edge. The bright and dark values were then used to define a normalised edge spread curve,  $n(x)$ :

$$n(x) = (e(x) - d)/(b - d) \quad (1)$$

in which  $e(x)$  consists of the average pixel values at distance,  $x$ , from the edge and with the convention that negative distance corresponds to being in the shadow of the gold wire. Edge spread curves obtained with 120 keV electrons at four different energy thresholds are given in Fig. 7. As the threshold is increased, viz. 12.2, 56.4, 80.5 and 100.6 keV, the slope of the edge can clearly be seen to increase.

Analysis of the edge spread function results was made easier by the observation that a model for the pixel response function consisting of single, threshold-dependent, Gaussian is sufficient to describe the observed results. Within this model both the line spread function and MTF are also Gaussians [32], while the normalised edge spread function can be expressed, in terms of the complementary

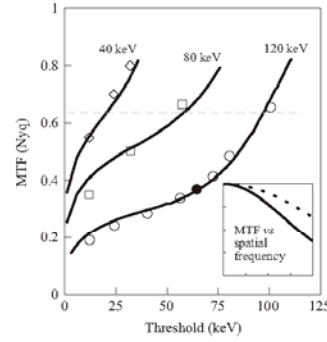


Fig. 8. Plots of MTF at Nyquist frequency as a function of threshold energy showing experimental data (points) and simulations results (lines) for incident electrons with energies of 40, 80 and 120 keV. As discussed in the main text, the results were obtained by analysing recorded, or simulated, images of an opaque edge at a slight angle to the detector axis. Note that at high thresholds the values of experimental and simulation MTF exceed the limiting value of  $2/\pi$  (indicated by dotted horizontal line) for a perfect detector with 100% filling factor due to the reduction in effective pixel size. The solid line in the inset shows the spatial frequency dependence (between zero and Nyquist) of the MTF for the highlighted point (120 keV incident electrons and a threshold of 64.4 keV). The dotted line indicates corresponding dependence for a perfect pixellated detector.

error function  $\text{erfc}$ , as

$$n(x) = (1/2) \text{erfc}(-x/a) \quad (2)$$

in which  $a$  is the half-width of the corresponding line-spread function at  $(1/e)$ .

The final model parameters (edge position and orientation, dark and bright field values, and line spread width) were obtained by a least-squares minimisation of the difference between the measured and predicted values for each pixel. The fitted edge spread curves are shown in Fig. 7 and, while more complicated models could have been used, the agreement with experiment made this unnecessary.

Monte Carlo simulations of an opaque edge were used to generate images analogous to those obtained experimentally. As with the experimental data, the resulting edge spread curves could also be fitted by a single Gaussian line spread model.

The MTF is given by the Fourier transform of the Gaussian line spread function [32] and, in the present case, this means that the MTF is also given by a single Gaussian. In particular, the Nyquist MTF is given by  $\exp(-\pi^2 a^2/4)$ . The Nyquist MTFs obtained for 40, 80 and 120 keV as a function of threshold, along with corresponding simulation results, are shown in Fig. 8. The agreement between the measured and simulated results is very good.

As the threshold is increased, the MTF rises above the value of  $2/\pi$  that would be expected for a perfect detector. This represents a reduction in the effective pixel size at high thresholds due to the fact that an electron effectively has to be incident on the centre of a pixel in order to be counted [33]. The increase in MTF with threshold is accompanied by a reduction in the number of electrons being counted, and a consequent drop in the DQE, and so using high values for the threshold to take advantage of the increased MTF would not normally be recommended.

#### 6. DQE: theoretical and experimental value

The DQE provides a figure of merit for a detector. It measures how much noise is added to the image by the detector and is defined as [32]

$$\text{DQE} = (S/N)_{\text{out}}^2 / (S/N)_{\text{in}}^2 \quad (3)$$

in which  $S$  and  $N$  refer to the signal and noise, respectively. Medipix has no intrinsic noise in so far as there are no counts when there are no incident electrons. However, there is stochastic noise which depends on the particular path taken by a particular electron and this causes the rms deviation (the noise) in the number of counts to exceed that expected from the incident electron statistics. The DQE of the Medipix2 is a function of the threshold and, as with all detectors, the  $S/N$  at the output is smaller than at the input and so the DQE is always less than 1. The Medipix2 is always used with the lower threshold set above the noise level. In this mode, it acts as a noiseless quantum detector whose DQE can be measured in the novel way described below.

The dispersed energy deposition along the chaotic trajectories of incident electrons, coupled with the drift of charge carriers in the detector layer, results in the signal from an electron incident on one pixel spilling into adjacent pixels. With the threshold set to greater than one half of the incident energy, an electron can only ever be recorded in one pixel, which may or may not be the one on which an electron was incident. As the threshold is lowered below half of the incident energy it becomes possible to record an incident electron in 2 pixels and on further lowering the threshold it is possible to record counts from single electrons in 3 or more pixels. The Medipix2 detector is therefore acting as a stochastic amplifier of the type studied by Zweig [34,35]. The output signal and noise from such an amplifier with average gain,  $\bar{g}$ , and gain variance,  $\sigma_g^2$ , are related to the input values by

$$S_{\text{out}} = \bar{g} S_{\text{in}} \quad (4)$$

and

$$N_{\text{out}}^2 = \bar{g}^2 N_{\text{in}}^2 + \sigma_g^2 S_{\text{in}}. \quad (5)$$

The arrival of incident electrons is a random process for which  $N_{\text{in}}^2 = S_{\text{in}}$ . Using this, and Eqs. (3)–(5), gives

$$\text{DQE} = \bar{g}^2 / (\bar{g}^2 + \sigma_g^2). \quad (6)$$

If the number of incident electrons is known, the probability of recording the arrival of an electron in 0, 1, 2, ... pixels can be estimated by counting the number of corresponding events. If  $p_i$  is the probability of recording an incident electron in  $i$  pixels then

$$\bar{g} = \sum_i i p_i \quad (7)$$

and

$$\sigma_g^2 = \sum_i i^2 p_i - \bar{g}^2 \quad (8)$$

Substituting these into Eq. (6) gives

$$\text{DQE} = \left( \sum_i i p_i \right)^2 / \left( \sum_i i^2 p_i \right) \quad (9)$$

Note that when the threshold is set above half the incident energy,  $p_i = 0$  for all  $i$  greater than 1 and the DQE becomes simply equal to  $p_1$ . That is, the DQE is simply equal to the probability of recording an incident electron in a pixel.

Measurements of the DQE of the Medipix2 as a function of threshold were made by illuminating it with a uniform electron beam containing on average 240 electron/s (all images were recorded for 1 s). Since there are ~65,000 pixels available in Medipix2 the probability of a pixel being hit by 2 or more electrons, as well as neighbouring pixels being hit, is very small. The individual electron events in each image were analysed and the number of events with 1, 2, 3 or 4 pixels recorded. The total number of incident electrons varies from image to image and in order to calculate the probabilities needed in Eq. (9) an estimate of the total number of incident electrons is needed. To obtain this, the number of “zero count” events was estimated based on the actual number of observed single, double and triple events and their predicted ratios to “zero count” events from Monte Carlo simulations. Fig. 9 shows the measured number of events involving 1, 2, 3 and 4 pixels, along with the estimated number of “zero count” events. Also shown are simulation predictions for the number of 0, 1, 2, 3 and 4 pixel events based on there being 240 incident electrons per image. Note that, since the detector has no intrinsic noise, the DQE should not change with the number of incident electrons counted per frame, up to the maximum count rate (~1 MHz/pixel), and the maximum number of counts able to be stored ( $2^{13}$ ).

The DQE as a function of threshold, calculated using the experimental results in Fig. 9, is plotted alongside the predicted behaviour from Monte Carlo simulations in

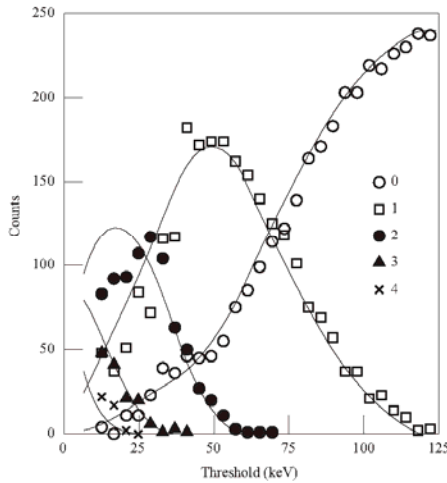


Fig. 9. Plot of the number of registered single electron events (Counts) as a function of the threshold energy with 120 keV incident electrons. The data plotted were obtained from a series of single frame exposures using about 240 electron/frame. The lines are derived from simulations.

Fig. 10(a). Also shown is the Nyquist frequency DQE obtained using the spatial frequency,  $\omega$ , generalisation of the expression for the DQE:

$$DQE(\omega) = DQE(0)MTF(\omega)^2/NTF(\omega)^2 \quad (10)$$

in which MTF( $\omega$ ) is the modulation transfer function described in the previous section and NTF( $\omega$ ) is the noise transfer function defined by Meyer and Kirkland [30].

When the threshold in a Medipix2-like detector is set above half the incident energy, the noise power spectrum is a constant (since an incident electron is either recorded in a single pixel or not recorded at all). In this case, NTF( $\omega$ ) = 1 and the spatial frequency dependence of the DQE is determined solely by that of the MTF( $\omega$ )<sup>2</sup>. At lower threshold settings, the NTF falls below 100% and experimental and theoretical values are also shown in Fig. 10(b).

The Nyquist MTF of a perfect homogenous detector with 100% pixel filling factor is limited to  $2/\pi = 0.636$ , which limits the Nyquist DQE of a Medipix2-like detector to at most  $(2/\pi)^2 \approx 0.405$ , even if DQE(0) = 1. Fig. 10(a) shows that the best that can be obtained for Medipix2 at 120 keV in practice is 0.14 using a rather low threshold setting.

For a good compromise between high DQE and high MTF, we recommend using a detector such as the Medipix2 with the threshold set to half of the incident

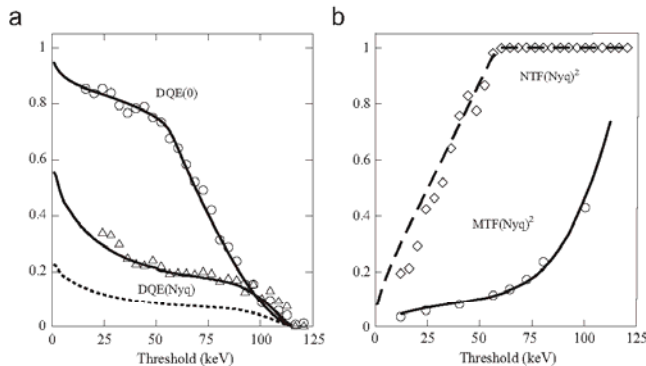


Fig. 10. (a) Experimental (points) and simulation (lines) results for DQE at zero and Nyquist spatial frequencies of Medipix2 as a function of threshold energy with 120 keV incident electrons. The experimental DQE(0) values (shown as circles) are based on the results given in Fig. 9 and Eq. (9). At high threshold energy, DQE(0) is small as very few of the incident electrons are detected. As the threshold is decreased, the DQE(0) increases in an almost linear progression up to ~60 keV. At about this threshold 2 pixels are occasionally counted resulting in a clear change in gradient which shows up as a shoulder in the experimental and predicted DQE(0) curves. At still lower thresholds, 3 or 4 pixels can occasionally count, limiting the increase in DQE(0). The maximum value of DQE(0), at a threshold of ~5 keV is 86%. DQE(Nyquist) is calculated from Eq. (10) using DQE(0) and the values of MTF<sup>2</sup> and NTF<sup>2</sup> shown in (b). Since the maximum value of DQE(Nyquist) is  $(2/\pi)^2 = 0.405$  for any pixelated detector, the experimental values of DQE(Nyquist) (shown as triangles) are plotted as a percentage of this maximum possible value for a perfect detector. The theoretical DQE(Nyquist) curve is also shown as a percentage of the maximum value for a perfect detector (full line) and as its absolute value (dashed line). (b) Experimental and Monte Carlo simulation results for the square of both the noise transfer function and MTF at Nyquist frequency (replotted from Fig. 8) as a function of threshold energy for 120 keV electrons.

energy. With this setting the measured DQE at zero spatial frequency and Nyquist are 0.65 and 0.08, respectively. It is worth mentioning that these values are obtained even at extremely low incident flux and the Medipix2 is therefore an excellent detector for low-dose imaging. These values represent 65% and 20% of DQE(0) and DQE (Nyquist), respectively, for a perfect detector. Both of these numbers would be expected to improve if a high-density, high-Z material was used for the sensor layer, such as gallium arsenide or cadmium telluride instead of silicon, because of the expected improvement in MTF.

## 7. Conclusions

The performance of Medipix2 in detection of 120 keV electrons is very good in terms of MTF and DQE at the Nyquist resolution limit. At the optimal setting of the discriminator threshold at just below half the incident electron energy, it also has no noise and therefore no decrease in DQE for low-dose exposures. At higher voltages, the 300 μm thick sensor allows the energy and charge to spread to adjacent pixels, which reduces the MTF and DQE at Nyquist. This, together with the onset of radiation damage between 200 and 300 keV limits the use of the detector to lower energies, though the range of useful energies could be extended by using a cadmium telluride detector layer. Nevertheless Medipix2 in its current form will be very useful for certain kinds of very low-dose microscopy experiments. For example, it is believed (Glaeser and Henderson [36] and Henderson [37]) that mechanical movement or specimen charging blurs the low-dose images of organic or biological specimens as a result of radiation damage: dose-fractionated or stroboscopic imaging using a very low noise detector accompanied by extensive image processing of the resulting movies, may provide a way to circumvent the problem. In principle, images of moving specimens can be recorded on a sequence of frames using any type of detector, but these images can only be added together without loss of signal-to-noise ratio if the detector has no intrinsic noise.

Data from Medipix2 are read out serially, taking ~30 ms for a single chip. The four chips in a Quad are read out sequentially with a correspondingly increased readout time (120 ms). Future readout systems, employing parallel readout from groups of eight columns simultaneously, could decrease the readout times of each chip by a factor ~32 to less than 1 ms. It would also be useful if the number of point defects, seen most clearly in the 300 keV panel of Fig. 3(a), could be decreased, and the number of pixels increased from 512 × 512 through a greater amount of tiling.

A program to extend the Quads into larger areas has already been initiated, in a project called High Resolution Large Area X-ray Detector (RELAXD) by Panalytical [38], an industrial company, which has been closely associated with the Medipix2 collaboration. The Medipix2 chip needs to be re-designed to make it 4-side buttable, to be tiled into a larger array. The first phase should lead to a

detector with a 3 × 3 array of Quads, i.e. with 1.5 k × 1.5 k in the detector. Depending on the experience with the first design, more challenging designs, with larger arrays, could be undertaken in future.

## Acknowledgements

We are grateful to the CERN Medipix group for help and advice regarding all aspects of the Medipix assembly and its operation, the NIKHEF group for the hardware interface MUROS2, the Napoli group for the control software Medisoft and members of the Medipix collaboration for general advice and useful discussions. We would also like to thank H. Bichsel for providing tables of inelastic cross-sections for silicon.

## References

- [1] R. Henderson, Quart. Rev. Biophys. 37 (2004) 3.
- [2] A.R. Faruqi, S. Subramaniam, Quart. Rev. Biophys. 33 (2000) 1.
- [3] R. Henderson, D. Cattermole, G. McMullan, S. Scotcher, M. Fordham, W.B. Amos, A.R. Faruqi, Ultramicroscopy, accepted, 2006.
- [4] A.R. Faruqi, R. Henderson, L. Tustos, Nucl. Instrum. Methods A 546 (2005) 160.
- [5] O.L. Krivanek, P.E. Mooney, Ultramicroscopy 49 (1993) 95.
- [6] A.R. Faruqi, R. Henderson, S. Subramaniam, Ultramicroscopy 75 (1999) 235.
- [7] A.R. Faruqi, H.N. Andrews, Nucl. Instrum. Methods A 392 (1997) 233.
- [8] W. Baumeister, R. Grimm, J. Walz, Trends Cell Biol. 9 (1999) 81.
- [9] M.L. Prydderch, N.J. Waltham, R. Turchetta, M.J. French, R. Holt, A. Marshall, D. Burt, R. Bell, P. Pool, C. Eyles, H. Mapson-Menard, Nucl. Instrum. Methods A 512 (2003) 358.
- [10] A.R. Faruqi, R. Henderson, M. Prydderch, R. Turchetta, P. Allport, A. Evans, Nucl. Instrum. Methods A 546 (2005) 170.
- [11] A.R. Faruqi, R. Henderson, J. Holmes, Nucl. Instrum. Methods A 565 (2006) 139.
- [12] <http://www.cern.ch/MEDIPIX>.
- [13] H. Krüger, Nucl. Instrum. Methods A 551 (2005) 1.
- [14] X. Llopert, M. Campbell, Nucl. Instrum. Methods A 509 (2003) 157.
- [15] X. Llopert, M. Campbell, R. Dimapoli, D. San Secundo, E. Pernigotti, IEEE Trans. Nucl. Sci. 49 (2002) 2279.
- [16] A.R. Faruqi, in: P. Hawkes (Ed.), *Advances in Imaging and Electron Physics*, 2007, accepted.
- [17] M. Campbell, E.H.M. Heijne, G. Meddeler, E. Pernigotti, W. Snoeys, IEEE Trans. Nucl. Sci. 45 (1998) 751.
- [18] A.R. Faruqi, D.M. Cattermole, R. Henderson, B. Mikulec, C. Raeburn, Ultramicroscopy 94 (2003) 263.
- [19] A. Fornaini, T. Boerkamp, R. de Oliveira, J. Visschers, Nucl. Instrum. Methods A 509 (2003) 206.
- [20] D. San Secundo Bello, M. van Beuzekom, P. Janweijer, H. Verkooijen, J. Visschers, Nucl. Instrum. Methods A 509 (2003) 164.
- [21] M. Conti, M. Maiorino, G. Mettivier, M.C. Montesi, P. Russo, IEEE Trans. Nucl. Sci. 50 (2003) 869.
- [22] I. Kawrakow, D.W.O. Rogers, The EGSnrc code system. Report PIRS-701. NRCC, Ottawa, 2003. Available at <http://www.irs.inms.nrc.ca/irns/EGSnrc>.
- [23] S. Agostinelli, et al., GEANT4—a simulation toolkit, Nucl. Instrum. Methods A 506 (2003) 250. Available at <http://geant4.web.cern.ch/>.
- [24] J. Sempau, E. Acosta, J. Baró, J.M. Fernández-Varea, F. Salvat, Nucl. Instrum. Methods B 132 (1997) 377.
- [25] D.C. Joy, Monte Carlo Modeling for Electron Microscopy and Microanalysis, Oxford University Press, Oxford, 1995.

- [26] J.W. Martin, J. Yuan, A. Hoedl, B.W. Filippone, D. Fong, T.M. Ito, E. Lin, B. Tipton, A.R. Young, Phys. Rev. C 68 (2003) 055503.
- [27] H. Bichsel, Rev. Mod. Phys. 60 (1988) 663.
- [28] L. Tlustos, Ph.D. thesis, University of Technology, Vienna, CERN-THESIS-2005-032, 2005.
- [29] H. Fujita, D.-Y. Tsai, T. Itoh, K. Doi, J. Morishita, K. Ueda, A. Ohtsuka, IEEE Trans. Med. Imaging 11 (1992) 34.
- [30] R.R. Meyer, A.J. Kirkland, Microsc. Res. Technol. 49 (2000) 269.
- [31] W.J. de Ruijter, J.K. Weiss, Rev. Sci. Instrum. 63 (1992) 4314.
- [32] J.C. Dainty, R. Shaw, Image Science, Academic Press, New York, 1974.
- [33] L. Tlustos, R. Ballabriga, M. Campbell, E. Heijne, K. Kincade, X. Llopis, P. Stejskal, IEEE Trans. Nucl. Sci. 53 (2006) 367.
- [34] H.J. Zweig, J. Opt. Soc. America 55 (1965) 525.
- [35] M. Rabbani, R. Shaw, R. Van Metter, J. Opt. Soc. Am. A 4 (1987) 895.
- [36] R. Henderson, R. Glaeser, Ultramicroscopy 16 (1985) 139.
- [37] R. Henderson, Ultramicroscopy 46 (1992) 1.
- [38] K. Bethke, R. deVries, V. Kogan, J. Vasterink, R. Verbruggen, P. Kidd, P. Fewster, J. Bethke, Nucl. Instrum. Methods 563 (2006) 209.



## PAPER VIII

**The readout of a GEM or Micromegas-equipped TPC by means of the  
*Medipix2 CMOS sensor as direct anode***

P a p e r VIII





ELSEVIER

Available online at [www.sciencedirect.com](http://www.sciencedirect.com)

SCIENCE @ DIRECT®

Nuclear Instruments and Methods in Physics Research A 535 (2004) 506–510

NUCLEAR  
INSTRUMENTS  
& METHODS  
IN PHYSICS  
RESEARCH  
Section A

[www.elsevier.com/locate/nima](http://www.elsevier.com/locate/nima)

## The readout of a GEM or Micromegas-equipped TPC by means of the Medipix2 CMOS sensor as direct anode

P. Colas<sup>a</sup>, A.P. Colijn<sup>b</sup>, A. Fornaini<sup>b</sup>, Y. Giomataris<sup>a</sup>, H. van der Graaf<sup>b,\*</sup>, E.H.M. Heijne<sup>c</sup>, X. Llopart<sup>c</sup>, J. Schmitz<sup>d</sup>, J. Timmermans<sup>b</sup>, J.L. Visschers<sup>b</sup>

<sup>a</sup>DAPNIA, CEA Saclay, 91191 Gif sur Yvette cedex, France

<sup>b</sup>Nationaal Instituut voor Kernfysica en Hoge-Energiefysica (NIKHEF), P.O. Box 41882, 1009DB Kruislaan 409, Amsterdam, The Netherlands

<sup>c</sup>CERN/Medipix Consortium, Geneva, Switzerland

<sup>d</sup>University of Twente/MESA+, The Netherlands

Available online 17 August 2004

### Abstract

We have applied the Medipix2 pixel CMOS chip as direct anode readout for a TPC. For the gas amplification two options have been investigated: (i) a three-stage GEM system and (ii) a Micromegas mesh. The structure of the cloud of primary electrons, left after interactions of  $^{55}\text{Fe}$  quanta with the gas is visible with unprecedented precision. This proof-of-principle is an essential step in our project to realize a monolithic pixel sensor with integrated Micromegas, to be developed specially for the readout of TPCs, and applicable for drift chambers in general.

© 2004 Elsevier B.V. All rights reserved.

PACS: 29.40.Cs; 29.40.Gx

Keywords: GEM; Micromegas; Medipix2; TPC; Pixel; Pixel-segmented anode

### 1. Introduction

Our goal is to develop a single-electron-sensitive monolithic device *TimePixGrid* consisting of a CMOS pixel matrix *TimePix* covered with a Micromegas [1]. Each pixel is equipped with a preamp, a discriminator, a threshold DAC and time stamp circuitry. Such a sensor would replace

the wires (or GEMs, or Micromegas), anode pads, feedthrough, readout electronics and cables of TPCs and could generally be applied in gaseous (drift) chambers. We intend to fabricate the Micromegas grid onto the TimePix chip by means of wafer post-processing technology.

The aim of the research presented in this paper is to prove the feasibility of a TPC readout system based on a CMOS pixel sensor in combination with either GEM foils or Micromegas.

\*Corresponding author.

E-mail address: [vdgraaf@nikhef.nl](mailto:vdgraaf@nikhef.nl) (H. van der Graaf).

0168-9002/\$ - see front matter © 2004 Elsevier B.V. All rights reserved.  
doi:10.1016/j.nima.2004.07.180

## 2. A pixel sensor + GEM system

We applied the Medipix2 chip [2–4] as experimental readout device. This monolithic CMOS chip contains a square matrix of  $256 \times 256$  pixels, each with dimensions  $55 \times 55 \mu\text{m}^2$ . Each pixel is equipped with a low-noise preamp, discriminator, threshold DACs, a 14-bit counter and communication logic. One edge of the chip has aluminum bonding pads. The outer dimensions of the chip are  $16.12 \times 14.11 \text{ mm}^2$ . The Medipix2 chip has been designed for X-ray imaging applications. For that particular application, an X-ray semiconductor converter (i.e. Si or CdZnTe), in the form of a

corresponding pixel matrix, is mounted onto the Medipix2 chip by means of bump-bonding. The assembly of a Medipix2 CMOS chip and an X-ray semiconductor converter forms a complete X-ray imaging device. For each pixel the number of absorbed X-ray quanta in a given acquisition time is counted, and the combined pixel content forms the X-ray image.

For a proof-of-principle, we combined a stack of three GEMs [5] with the Medipix2 chip (without the X-ray semiconductor converter), as depicted in Fig. 1. A small TPC was made with a drift volume of  $100 \times 100 \times 100 \text{ mm}^3$ . The electric field in the drift volume was created by electrodes in the form of square wire loops put at linearly decreasing potentials. Insulating pillars placed outside the drift volume supported the corners of the wire loops. The printed circuit board of the Medipix2 was mounted in an insert in the aluminum base plate of the chamber. The surface of the Medipix2 was flush with the top plane of the base plate in order to create an homogeneous drift field between the bottom GEM and the Medipix2.

All potentials were derived from a single resistor chain; the effective gas multiplication of the triple GEM could be varied by changing the potential of the top of the drifter. The dimensions and potentials of all the electrodes are listed in Table 1.

The readout of our system is organized in the following way. The Medipix2 chip is connected through a Muros2 interface [4] to a PC equipped with a commercial NI PCI board. No triggering

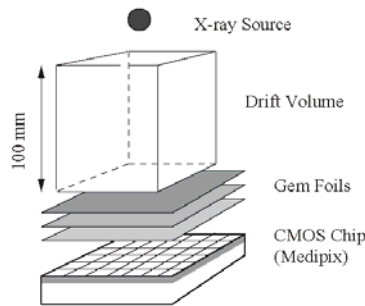


Fig. 1. The layout of the drift space, triple GEM and Medipix2 in the prototype test TPC.

**Table 1**  
Parameters of the triple GEM/Medipix2 setup

MEDIPIX2 + Triple GEM	April 1, 2003		February 9, 2004	
	Distance to Medipix2 (mm)	Potential (−V)	Distance to Medipix2 (mm)	Potential (−V)
Top Drifter	117.2	5580	118.0	5400
Bottom Drifter	17.2	3355	18.0	3560
GEM 1	9.8	Top Bottom	10.6 2770 2420	Top Bottom 3075 2785
GEM 2	8.2	Top Bottom	8.6 1830 1480	Top Bottom 2300 2010
GEM 3	6.6	Top Bottom	6.6 893 541	Top Bottom 1525 1230
Gas Gain		13k		18k
Gas mixture	Ar/methane	90/10	Ar/isobutane	95/5

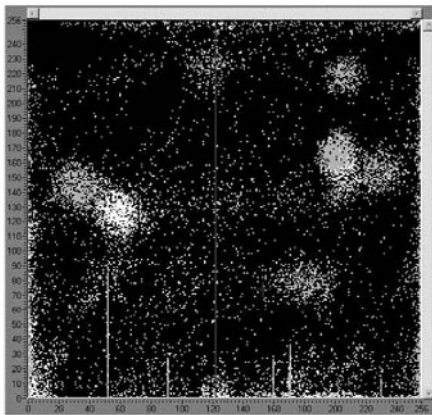


Fig. 2. Image recorded from the Medipix2 sensor placed below the triple GEM: all the ionization charge during an acquisition time of 1 s is recorded. An  $^{55}\text{Fe}$  source was placed close to the chamber. The gas employed is Ar/methane 90/10, the gas gain is 13k. The resulting charge distribution is wider than expected. Color scheme: black = 0 hits above threshold, gray = 1 hit, white = 2 hits during the acquisition time window.

system was implemented: our readout was collecting all the ionization charge during a fixed acquisition time.

We irradiated the chamber with X-rays from  $^{55}\text{Fe}$  and  $\beta$ 's from  $^{90}\text{Sr}$ , using an Ar/methane gas mixture. On April 1, 2003, we recorded the image of Fig. 2. The signal response of the  $^{55}\text{Fe}$  quanta was distributed over more pixels than expected, and a gain of 13k was required for the local pixels to cross their thresholds. We repeated these measurements in February 2004 with Ar/isobutane 95/5, allowing an even higher gas gain (18k), and an image is shown in Fig. 3. Here, too, the distribution of the charge cloud ending on the pixel segmented anode is quite wide. Most of the  $^{55}\text{Fe}$  quanta will be absorbed in the top section of the drift space, and the cloud of primary electrons will be widened due to diffusion during the drift over a large section of the 100 mm long drift length. This in combination with de-focusing effects in GEMs seen by other groups [6] may explain the images. Another explanation may be the too low extracting field below the GEMs.

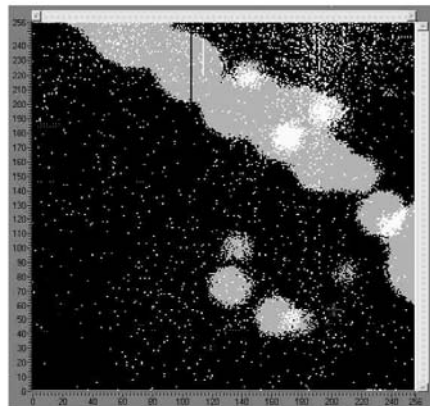


Fig. 3. As Fig. 2, but with Ar/isobutane 95/5, gain 18k, no radioactive source present and a 2 s acquisition time. A non-typical image of a cosmic-ray track is visible.

We note that Bellazzini et al. [7] have applied a single GEM in combination with a direct pixel-segmented anode, where strong de-focusing was not seen. In his setup, diffusion of primary and secondary electrons was limited to a minimum by a small distance between the GEM and the anode, and a small drift space.

### 3. A pixel sensor + Micromegas system

In a second step, we placed a Micromegas onto the Medipix2. The Micromegas itself is a copper foil, thickness 5  $\mu\text{m}$ , with holes of 30  $\mu\text{m}$  diameter in a square pattern with 60  $\mu\text{m}$  pitch. The Micromegas is fixed onto the Medipix2 by means of poly-imide pillars (height 50  $\mu\text{m}$ , diameter 200  $\mu\text{m}$ , pitch (square) 0.8 mm).

Originally, each pixel of the Medipix2 chip is covered with an insulating passivation layer; the conductive pad (octagonal pads 25  $\mu\text{m}$  wide) is large enough to accommodate a bump bond sphere. The electric field in the gap between the Medipix2 and the Micromegas is of the order of 7 kV/mm, and discharges may be expected when

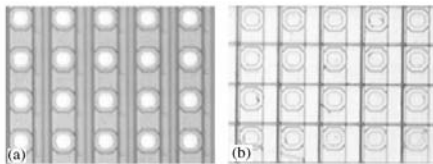


Fig. 4. The Medipix2 chip before (a) and after (b) the wafer post processing. The original pad ( $Al, 25 \times 25 \mu m^2$ ) is covered with an aluminum pad of  $45 \times 45 \mu m^2$ . Note that no Micromegas mesh has yet been mounted on the chips shown in this figure.

some 70 percent of the anode surface is covered with an insulating material.

For this reason, the Medipix2 chips were post-processed at wafer level in the MESA + clean room. The post-processing consisted in depositing a thin aluminum layer using lift-off lithography. This allows deposition of metal on the anode matrix without modification of the bond pads. The pixel pads were enlarged to reach a metal coverage of 80% in the anode plane (see Fig. 4). Electrical tests showed that the pre-amplifier functionality was unaffected by this post-processing.

A cathode plane 15 mm above the Micromegas creates a drift gap. On the drift cathode, a voltage of  $-600 V$  was applied and  $-(250\text{--}350 V)$  on the Micromegas. The Medipix2 pixel pads were at ground potential. We flushed the chamber with Ar/isobutane 95/5.

The signals from  $^{55}Fe$  became visible at a Micromegas potential of 290 V. We measured a gas multiplication factor of 300 for this voltage. Assuming an average number of 220 primary electrons released by most interacting  $^{55}Fe$  quanta, about 66 000 electrons will enter the anode plane. With a pixel discriminator threshold of about 3000 electrons, this signal can be detected even if the initial electron cloud is spread over an area of about 20 pixels.

When raising the HV of the Micromegas to 350 V, micro-discharges at or near the Micromegas pillars became apparent (see Fig. 5). The current due to these discharges was less than 0.5 nA and could not be measured. The discharges decreased rapidly in amplitude and frequency. During operation, we never experienced a measurable

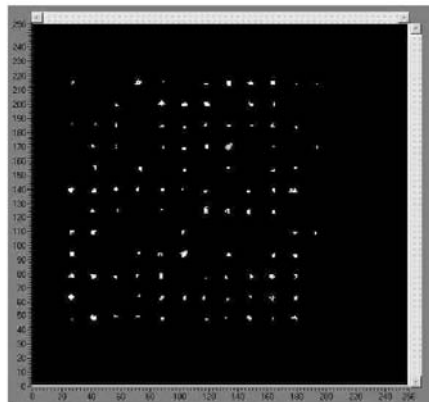


Fig. 5. Image acquired with the Medipix2/Micromegas prototype TPC. The measured gas multiplication factor is 1200. Discharges near the pillars are apparent.

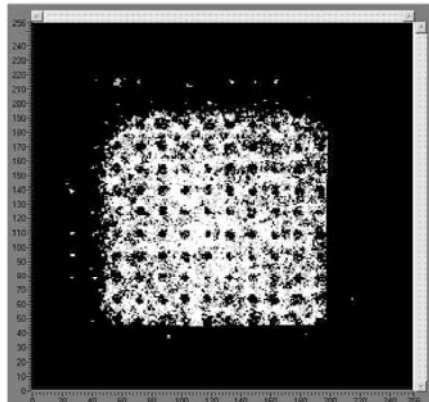
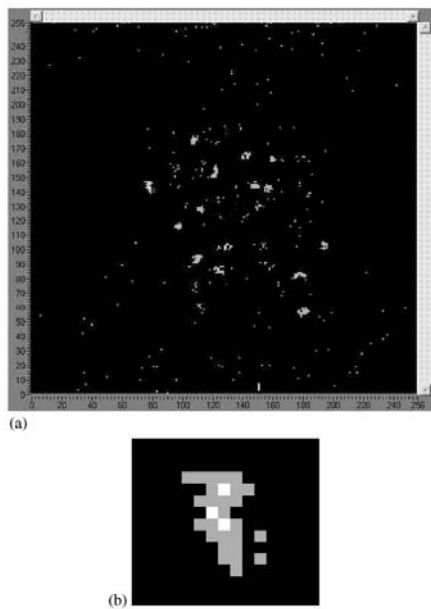


Fig. 6. Image acquired with the Medipix2/Micromegas prototype TPC. Strong irradiation with  $^{90}Sr$ . The shadows of the pillars are clearly visible.

excess current. Fig. 6 shows the image taken after strong irradiation with  $\beta^-$ 's from a  $^{90}Sr$  source. The dead regions caused by the pillars is clearly visible. Fig. 7 shows some  $^{55}Fe$  events with an enlarged



**Fig. 7.** (a) Image acquired with the Medipix2/Micromegas prototype TPC. (b) Enlarged view of an  $^{55}\text{Fe}$  event from (a): this structure results from detecting two clusters of charge, one originating from a fluorescence electron and the other from an Auger electron.

view of one of them. As is already visible from these few events, a readout system based on CMOS pixel sensor offers the unique possibility to directly view the processes involved in the absorption of X-ray quanta. In a more developed version of detectors based on this technology it is expected that for example Compton scattering, the photoelectric effect and the emission of Auger or  $\delta$  electrons can be fully disentangled on an event-by-event basis [8].

#### 4. Conclusions

We have successfully operated the Medipix CMOS pixel sensor as a direct anode. In a first

setup, the primary electrons originating from  $^{55}\text{Fe}$  quanta absorbed in the drift gas were multiplied by means of a set of three GEM foils. Probably due to the long drift path and the large distance between the last GEM and the Medipix2, and possibly due to de-focusing effects, diffuse images of X-ray conversions and charged particle tracks were recorded. In a second setup, we combined the Medipix2 with a Micromegas, and sharp images of  $^{55}\text{Fe}$  events were observed. Apparently, the CMOS pixel sensor can withstand a strong electric field at its surface. This opens the possibility for a new readout technology of gaseous (drift) chambers.

#### Acknowledgements

We thank the Medipix Collaboration for providing us with several wafers with Medipix2 chips, for the readout software and hardware, and for valuable advice. We would like to thank Arnaud Giganon, Wim Gotink and Joop Rövekamp for their creative and essential contributions to the realization of the test detectors. We thank Tom Aarnink, Ad Berkien, Edward Berbee, Frank de Zwart, Dimitri John, Jan Martis and Jan van Veen for their contributions.

#### References

- [1] Y. Giomataris, et al., Nucl. Instr. and Meth. A 376 (1996) 29.
- [2] X. Llopert, M. Campbell, R. Dinapoli, D. San Segundo, E. Pernigotti, IEEE Trans. Nucl. Sci. NS-49 (2002) 2279.
- [3] M. Conti, M. Maiorino, G. Mettivier, M.C. Montesi, P. Russo, IEEE Trans. Nucl. Sci. NS-50 (4) (2003) 869.
- [4] D. San Segundo Bello, M. van Beuzekom, P. Jansweijer, H. Verkooijen, J.L. Visschers, Nucl. Instr. and Meth. A 509 (2003) 164.
- [5] F. Sauli, et al., Nucl. Instr. and Meth. A 386 (1997) 531.
- [6] D. Karlen, et al., Investigation of GEM Space Point Resolution for a TPC Tracker, Proceedings of the Linear Collider Workshop 2000, FNAL, USA, [http://www-lc.fnal.gov/proceedings/d3\\_vertex/Dean\\_Karlen.pdf](http://www-lc.fnal.gov/proceedings/d3_vertex/Dean_Karlen.pdf).
- [7] R. Bellazzini, Nucl. Instr. and Meth. A (2004) these proceedings.
- [8] M. Hauschild, in: J.S. Kang, S.K. Oh (Eds.), Proceedings of the International Workshop on Linear Colliders, Jeju, Korea, 2002, pp. 464–469.



## PAPER IX

**Detection of single electrons by means of a Micromegas-covered *Medipix2*  
pixel CMOS readout circuit**

P a p e r I X





ELSEVIER

Available online at [www.sciencedirect.com](http://www.sciencedirect.com)

SCIENCE @ DIRECT®

Nuclear Instruments and Methods in Physics Research A 540 (2005) 295–304

NUCLEAR  
INSTRUMENTS  
& METHODS  
IN PHYSICS  
RESEARCH  
Section A

[www.elsevier.com/locate/nima](http://www.elsevier.com/locate/nima)

## Detection of single electrons by means of a Micromegas-covered MediPix2 pixel CMOS readout circuit

M. Campbell<sup>a</sup>, M. Chefdeville<sup>b</sup>, P. Colas<sup>b</sup>, A.P. Colijn<sup>c</sup>, A. Fornaini<sup>c,d</sup>, Y. Giomataris<sup>b</sup>, H. van der Graaf<sup>c</sup>, E.H.M. Heijne<sup>a</sup>, P. Kluit<sup>c</sup>, X. Llopert<sup>a</sup>, J. Schmitz<sup>d</sup>, J. Timmermans<sup>c,\*</sup>, J.L. Visschers<sup>c</sup>

<sup>a</sup>CERN/MediPix Consortium, Geneva, Switzerland

<sup>b</sup>DAPNIA, CEA Saclay, 91191 Gif sur Yvette Cedex, France

<sup>c</sup>NIKHEF, PO Box 41882, #1009 DB Amsterdam, The Netherlands

<sup>d</sup>University of Twente/MESA, The Netherlands

Received 2 September 2004; received in revised form 17 November 2004; accepted 19 November 2004

Available online 25 December 2004

---

### Abstract

A small drift chamber was read out by means of a MediPix2 readout chip as a direct anode. A Micromegas foil was placed 50 µm above the chip, and electron multiplication occurred in the gap. With a He/isobutane 80/20 mixture, gas multiplication factors up to tens of thousands were achieved, resulting in an efficiency for detecting single electrons of better than 90%. We recorded many frames containing 2D images with tracks from cosmic muons. Along these tracks, electron clusters were observed, as well as δ-rays.

© 2004 Elsevier B.V. All rights reserved.

**Keywords:** Micromegas; MediPix2; TPC; Single electron; Pixel; Pixel segmented anode

---

### 1. Introduction

Recently [1] we have demonstrated the possibility to read out a drift chamber by means of a direct, pixel segmented active anode. Images of the interaction of  $^{55}\text{Fe}$  quanta with the gas were obtained (see Fig. 1) with a rather low gas

amplification factor, since these quanta create some 220 primary electrons in a small volume of argon gas. The aim of the research presented in this paper is to prove the feasibility of the detection of single (drifting) electrons, based on the same pixel sensor/Micromegas combination.

Our goal is to develop a single-electron sensitive monolithic device *TimePixGrid* consisting of a CMOS pixel matrix *TimePix* covered with a Micromegas [2]. Each pixel will be equipped with a preamp, a discriminator, a threshold DAC

\*Corresponding author. Tel.: +31 20 5925112; fax: +31 20 5925155.  
E-mail address: timmermans@nikhef.nl (J. Timmermans).

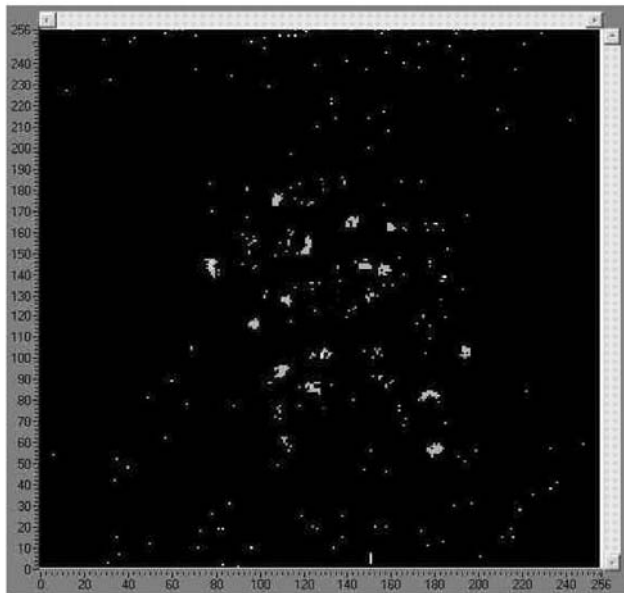


Fig. 1. Image acquired with the MediPix2/Micromegas prototype TPC [1].

and time stamp circuitry. Such a sensor would replace the wires (or GEMs, or Micromegas), anode pads, feedthroughs, readout electronics and cables of TPCs and could generally be applied in gaseous (drift) chambers. We intend to integrate the Micromegas grid onto the *TimePix* chip by means of wafer post-processing technology (*In-Grid*).

In Section 2 the test chamber including the MediPix2 readout chip and the Micromegas are described. In Section 3 details on single-electron detection and signal development are presented. Section 4 describes the data readout and the analysis of the cosmic ray tracks. It includes a discussion on the observation of so-called Moiré patterns in the detected hit pixel distribution. The paper ends with conclusions on the present work and an outlook to our future plans.

## 2. The chamber, MediPix2 and Micromegas

### 2.1. The chamber

The test chamber is depicted in Fig. 2. Above an aluminium base plate, a cathode foil is fixed, by means of spacers, forming a drift gap of 15 mm height. By means of a cut-out in the base plate, the MediPix2 chip (mounted on a brass pedestal) is placed flush with the base plate upper plane. On top of the chip, a Micromegas foil, fixed on a frame, is held in position by means of two silicon rubber strings (see Fig. 3).

### 2.2. The MediPix2 CMOS pixel sensor

A MediPix2 chip [3–5] was applied as an experimental readout device. This CMOS chip

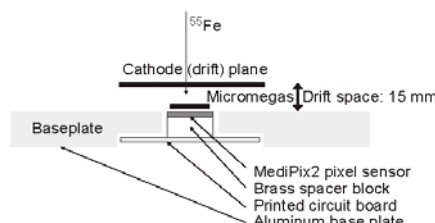


Fig. 2. Layout of the chamber with the MediPix2, the Micromegas and the drift gap.

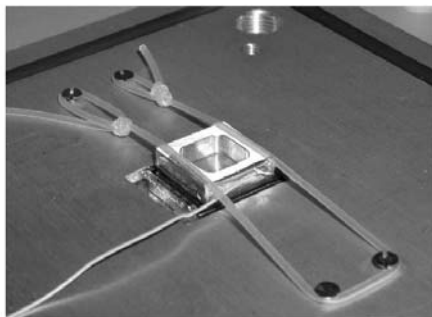


Fig. 3. Mounting of the Micromegas onto the MediPix2 sensor.

contains a square matrix of  $256 \times 256$  pixels, each with dimensions  $55 \times 55 \mu\text{m}^2$ . Each pixel is equipped with a low-noise preamp, discriminator, threshold DACs, a 14-bit counter and communication logic. One edge of the chip has aluminium bonding pads. The outer dimensions of the chip are  $16.12 \times 14.11 \text{ mm}^2$ . The MediPix2 chip has been designed for X-ray imaging applications. For that particular application, an X-ray semiconductor converter (i.e. Si or CdZnTe), in the form of a corresponding pixel matrix, is mounted onto the MediPix2 chip by means of bump bonding. The assembly of a MediPix2 chip and an X-ray converter forms a complete X-ray imaging device. For each pixel the number of absorbed X-ray quanta in a given acquisition time is counted, and

the combined pixel content forms the X-ray image. In our application we use the “naked” MediPix2 chip, without an X-ray convertor.

Originally, each pixel of the MediPix2 chip is covered for a large part with an insulating passivation layer; the conductive pad (octagonally shaped,  $25 \mu\text{m}$  wide) is large enough to accommodate a bump bond sphere. The electric field in the gap between the MediPix2 and the Micromegas is in the order of  $7 \text{ kV/mm}$ , and discharges were expected when some 70% of the anode surface is covered with an insulating material.

In order to prevent these discharges, the MediPix2 wafers were post-processed by MESA+ [6]. The post-processing consisted of a deposition of a thin aluminium layer using lift-off lithography. This allows deposition of metal on the anode matrix without modification of the bond pads. The pixel pads were thus enlarged to reach a metal coverage of 80% of the anode plane (see Fig. 4). Electrical tests showed that the preamplifier functionality was unaffected by this post-processing. We have applied both the modified and the non-modified versions of the MediPix2 chip.

### 2.3. The Micromegas

The Micromegas is a copper foil, thickness  $5 \mu\text{m}$ , with holes of  $35 \mu\text{m}$  diameter in a square pattern with  $60 \mu\text{m}$  pitch [7]. At the foil side facing the MediPix2 chip, poly-imide pillars (height  $50 \mu\text{m}$ , diameter  $80 \text{--} 140 \mu\text{m}$ , pitch (square)  $840 \mu\text{m}$ ) are attached. The Micromegas, in its frame, was held on the MediPix2 chip by means of two silicon rubber strings. When the voltage on the Micromegas was applied ( $200 \text{--} 500 \text{ V}$ ), the electrostatic force pulls the mesh towards the chip, and the insulating pillars define the proper gap size.

In order to prevent HV breakdowns, a square kapton foil, with a square hole of  $10.5 \times 10.5 \text{ mm}^2$ , was placed between the Micromegas and the MediPix2. The chamber was placed such that the drift direction was vertical. The fiducial drift volume of  $10.5 \times 10.5 \times 15 \text{ mm}^3$  is hit by a cosmic ray particle about once per minute [8].

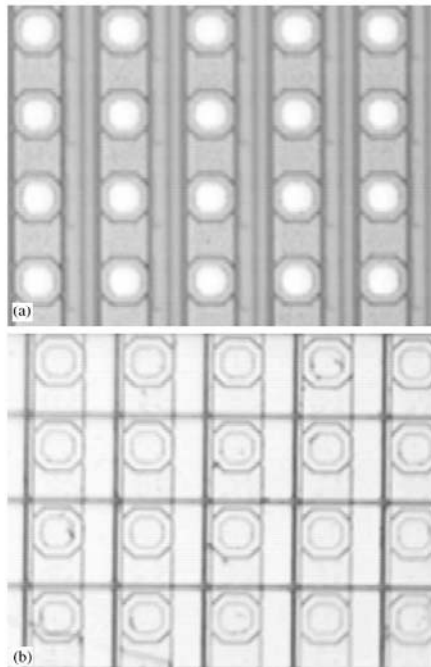


Fig. 4. The Medipix2 chip before (a) and after (b) the wafer post-processing. The original pad ( $25 \times 25 \mu\text{m}$ ) is covered with an aluminium pad of  $45 \times 45 \mu\text{m}$ . Note that no Micromegas mesh has yet been mounted on the chips shown in this figure.

### 3. Single-electron detection; signal development

A muon, originating from a cosmic shower, traversing the drift volume, will create clusters of electrons along its track. The cluster density, and the distribution of the number of electrons per cluster depends on the gas composition, gas density and the muon momentum. If argon is the main component of the gas (at atmospheric pressure), some 3 clusters per millimetre are created for a minimum ionising muon, and the average number of electrons per cluster is 2.5 [9].

Consequently, on average some 7 primary electrons are created per track length of 1 mm. The mean distance between two primary electrons, projected onto the anode plane, is much larger than the pixel pitch, and therefore typically single electrons will enter a Micromegas hole. For this reason the single-electron response is essential for the performance of the pixel-segmented anode readout. The counting of primary ionisation clusters would allow a precise measurement of the energy loss  $dE/dx$  [10].

After an electron has entered a hole, it will be multiplied, and the number of electrons grows exponentially towards the anode pads. The centre of gravity of the points of electron-ion separations is positioned at  $D \ln 2 / \ln M$  away from the anode, where  $D$  is the distance between the Micromegas and the anode and  $M$  is the gas multiplication factor. With  $D = 50 \mu\text{m}$  and  $M = 3000$  the charge centre of gravity is about  $4 \mu\text{m}$  away from the anode. The electrons will all arrive within 1 ns at the anode. Most of the ions, moving much slower, arrive within 30–50 ns at the Micromegas, depending on the gas composition and pressure. If a point charge crosses the avalanche gap, then the potentials of both the Micromegas and the anode change linearly with the distance of the point charge to the anode plane. The charge on the anode pad below the avalanche is the sum of the negative electron charge and the positive induced ion charge. The fast component has an amplitude of 10% of the total charge. The latter (slow) component decreases during the drift of the ions towards the Micromegas. On adjacent pads, however, the same ions will induce a positive charge, which will be at a maximum when the ions are halfway (after some 25 ns) between the anode and the Micromegas. This charge is only a fraction of the avalanche charge, and is back to zero after the arrival of the ions at the Micromegas. On these pads we may thus expect a bipolar current signal.

The peaking time constant of the MediPix2 preamp/shaper is 150 ns. This is large with respect to time constants of the signal development. The preamp/shaper output is therefore proportional to the avalanche charge, and the discriminator threshold can be expressed unambiguously in the number of electrons appearing at the input pad.

Although the design value of the input noise equivalent of the pixel preamps was 90 electrons, the thresholds were set at 3000 electrons in order to limit background hits due to (digital) feedback noise, possibly caused by the 4 mm long bonding wires.

The average of the number of electrons in an avalanche, initiated by a single electron is the gas multiplication factor  $M$  [9]. The fluctuations in the number of electrons in an avalanche follow an exponential function [11]:

$$p(n) = \frac{1}{M} e^{-n/M},$$

where  $p(n)$  equals the probability to have an avalanche with  $n$  electrons in total. The avalanche distribution is shown for several values of the gain  $M$  in Fig. 5. Since the preamp noise is small with respect to the threshold, and since there is no electron attachment, we apply the simple exponential distribution instead of approaches like the Polya distributions [12] which include several 2nd-order effects.

With a threshold set at  $T$  electrons, avalanches smaller than that are not detected. The efficiency  $\varepsilon$  to detect single electrons is then given by

$$\varepsilon = e^{-T/M}.$$

If, for instance, the threshold is set to a value that equals the gain, the efficiency equals  $1/e = 0.37$ . In Fig. 6 the efficiency curve is depicted as a function of the gain  $M$  for a threshold  $T = 3000$ .

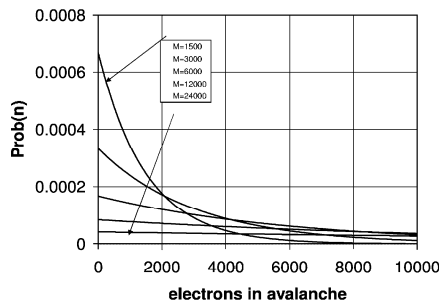


Fig. 5. Probability distribution for the number of electrons in an avalanche for several values of the gas gain  $M$ .

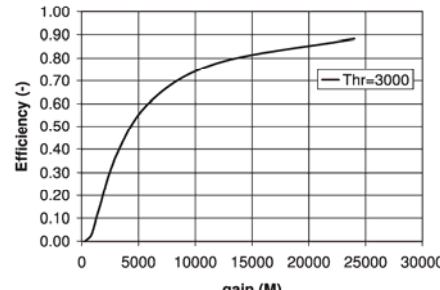


Fig. 6. Single-electron detection efficiency as a function of the gas gain for a threshold set at 3000 e<sup>-</sup>.

We would like to keep the gas gain as low as possible in order to (a) limit the risk of discharges and ageing and (b) limit the ion space charge. With the present MediPix2, with its lowest threshold of 3000 electrons, a gain of 10 k would correspond to a single-electron efficiency of 0.74. For this reason we used He mixtures which allow a high gain, with a small risk of discharges.

Due to discharges, four MediPix2 chips were destroyed within 24 h of operation. The MediPix2 chip has no protection circuitry at its pixel input pads other than the source and drain diffusions of the transistors responsible for leakage current compensation. We noticed some damage of the pixel pads, probably due to a high temperature in the discharge region. For *InGrid*, we intend to eliminate discharge damage by (a) covering the bottom of the Micromegas with a (high) resistive layer, limiting the participating charge, (b) covering the anode pads with a (high) resistive layer, in combination with (c) a protective network, for each pixel, connected to the anode pad.

#### 4. Results

##### 4.1. Cosmic ray tracks and data readout; calibration

The MediPix2 sensor can be externally enabled and stopped, followed by a readout sequence in

which the pixel counter data is transferred to a computer. We enabled the counters during an exposure time of 15 or 60 s, followed by recording the image frame in the form of 65 k counter contents. No trigger was applied.

The (positive) charge signals on the Micromegas were read out by means of a low-noise charge sensitive preamp, with a decay time constant of 1  $\mu$ s. Signals from a  $^{55}\text{Fe}$  source could be recorded, and the preamp was calibrated with charge signals from a block wave, injected by means of a 10 pF capacitor. Together with the known number of primary electrons per  $^{55}\text{Fe}$  quantum, the gas amplification can be measured.

With a He/isobutane 80/20 mixture, we observed signals from  $^{55}\text{Fe}$  events with  $-390\text{ V}$  on the Micromegas and  $-1000\text{ V}$  on the drift cathode plane. This is expected given the large density of primary electrons in the interaction point [1] and the gain at this voltage of about 1k. We then increased the voltage on the Micromegas to  $-470\text{ V}$ , corresponding to a gain of approximately 19k. With a threshold setting of  $3000\text{ e}^-$ , we expect a single-electron efficiency of 0.85, and cosmic rays were observed.

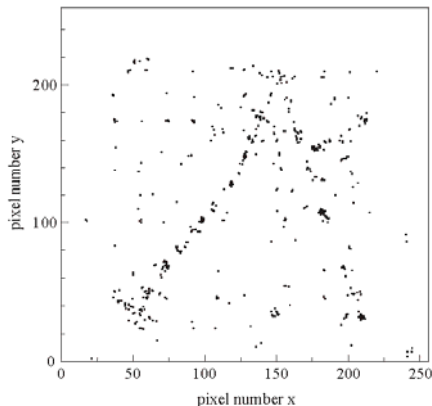


Fig. 7. Image recorded from the MediPix2/Micromegas prototype TPC showing cosmic charged particle tracks together with some background. All the hit pixels during an acquisition time of 15 s are shown.

Some typical events are shown in Figs. 7–9. Fig. 7 shows a cosmic event with environmental background. Fig. 8 shows a cosmic muon that knocks out a delta electron. Fig. 9 shows a selected

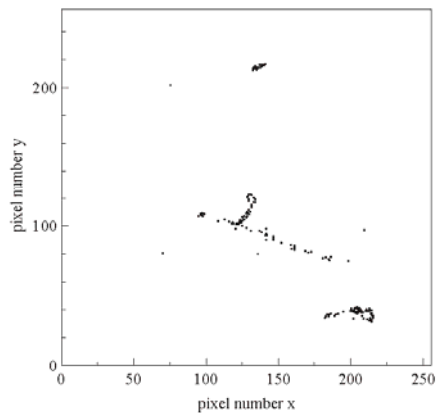


Fig. 8. Image recorded from the MediPix2/Micromegas prototype TPC showing a cosmic charged particle track together with a  $\delta$ -electron.

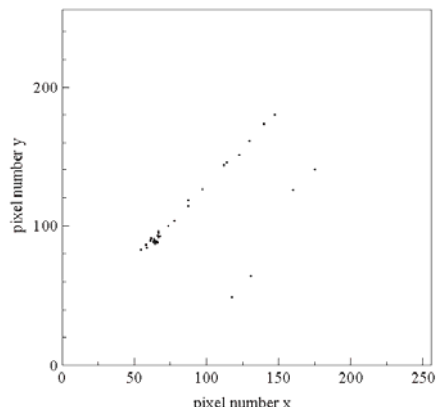


Fig. 9. Image recorded from the MediPix2/Micromegas prototype TPC showing selected cosmic charged particle tracks. The selections and noise filtering are described in the text.

cosmic muon. The selection cuts are described below. In this event the effect of diffusion can be observed in the spread of the hits along the track.

A selection to obtain a sample of clean cosmic events was made. For the data a map of the noisy pixels was made. The signal from the edges and the inefficient upper left corner of the detector were removed. First, a straight line was searched using a Hough transform. Pixels within a distance of 20 pixels are associated to the track. The following quantities were calculated: the number of associated pixels, the r.m.s. of the distance to the track, the track length in the detector plane  $L_d$  (in millimetres). The full 3D track length  $L$  (in millimetre) is estimated as  $L = \sqrt{L_d^2 + 15^2}$ . The track is split into two equal parts and the minimum r.m.s. value of the two parts is calculated. Clusters are formed by stepping along the track and grouping all hits within a distance of 5 pixels. The number of clusters is counted.

The following criteria were applied to select an event:

- the number of associated pixels larger than 5 and the fraction of associated pixels to the track to the total number of pixels hit larger than 80%;
- $L_d$  larger than 2.75 mm (i.e. 50 pixels);
- the r.m.s. less than 4;
- the number of associated pixels per millimetre of 3D track length should be less than 4.

In total, 164 events were selected in the data. The distributions of some physical quantities are shown in Fig. 10.

A simulation programme was written generating cosmic minimum ionising particles with an angular distribution  $\propto \cos^2 \theta$ . The muon was tracked through the sensitive volume of the detector. Clusters were generated with an average of 1.4 per millimetre and per cluster 3.16 electrons were generated using a Poissonian distribution [13]. The electrons were drifted toward the MediPix2 detector with a diffusion constant of 220  $\mu\text{m}$  per square root centimetre. Inefficient zones of the MediPix2 detector in the region between the pixels and below the pillars were put in. The detector is

assumed to have an efficiency of 100% in the efficient zones. Note that multiple hits on a single pixel are at present not separated. The same selection cuts were applied to data and simulation.

The distribution of the minimum r.m.s. is sensitive to the diffusion constant. Data give an average value of 2.0 pixels (simulation 2.4). This implies that the diffusion constant is slightly better than 220  $\mu\text{m}$  per square root centimetre. The observed number of pixels hit per millimetre is 1.83 on average (2.70 simulation). The number of clusters per millimetre is 0.52 (simulation 0.60). The average 3D track length is 16.5 mm. The number of clusters per millimetre agrees within 15% with the simulation, and the number of electrons within 35%. Note that a 100% efficiency is assumed for the detector. Inefficiencies have also more impact on the number of electrons than on the number of clusters. If we take into account systematic uncertainties on the expected number of clusters and electrons per millimetre, uncertainties on the efficiency and operating conditions of the detector, we find the agreement reasonable. Later experiments will focus on a more precise quantitative understanding of the detector.

#### 4.2. Moiré effects

Fig. 11 shows an image, obtained after irradiating the chamber with  $\beta$ 's from a  $^{90}\text{Sr}$  source. The top-left corner of the image is clearly less efficient. This is due to the non-flatness of the Micromegas in its frame. Apparently, the electrostatic force could not entirely eliminate the warp in the Micromegas foil. Here, the pillars are not in contact with the MediPix2 surface. The gap is wider and the gain is reduced. The dead regions due to the pillars are clearly visible as well.

Fig. 12 shows the image, taken with a non-modified MediPix2 sensor, after irradiating the drift volume with the  $^{90}\text{Sr}$  source. Band-shaped regions with a reduced efficiency are clearly visible. Note that these bands are present in two perpendicular directions. The same effect is visible in an image (Fig. 13) which is the sum of all cosmic rays obtained during one night of data taking, again with a non-modified MediPix. The corresponding image from a modified MediPix2 is shown in

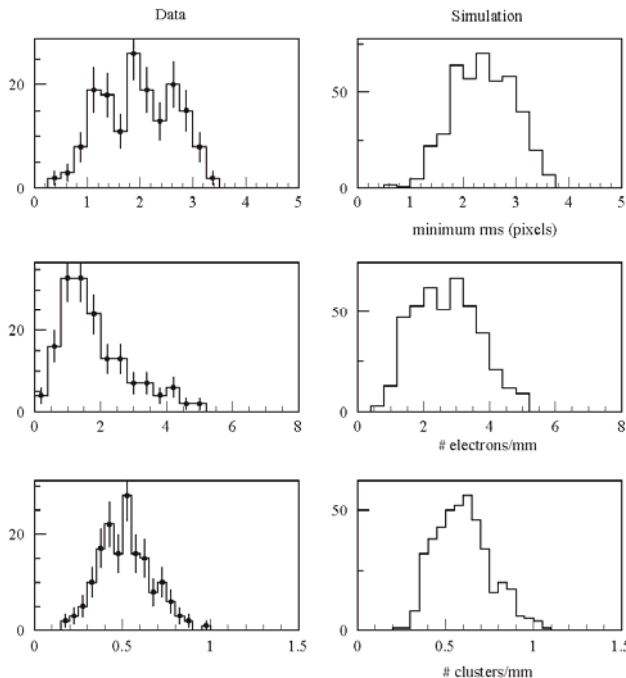


**Fig. 10.** Distributions of some quantities used in the analysis for selected cosmic data (left) and in the simulation (right). Top: the minimum of the two r.m.s. values for a track. Centre: the number of reconstructed electrons per millimetre of 3D track length. Bottom: the number of reconstructed primary clusters per millimetre of 3D track length.

**Fig. 14**, where bands are still present, but much less pronounced. The bands can well be explained in terms of a Moiré effect: the pixel size of the MediPix2 sensor ( $55 \times 55 \mu\text{m}^2$ ) does not match the pitch of the holes in the Micromegas ( $60 \times 60 \mu\text{m}^2$ ). Consequently, the hole position with respect to its nearest pixel centre, shifts when one follows a pixel row or pixel column. The relative hole position repeats after  $60/(60-55) = 12$  pixels.

The Moiré effect can be understood in terms of the pixel signal amplitude being dependent on the relative position of a Micromegas hole and the pixel pad. Such a variation could not be explained

by the charge sharing between 2 or 4 pixels for avalanches (with a certain width), located in the region near a pixel edge, because we did not observe the consequent effect of having significantly more clusters with 2, 3 or 4 hit pixels in the same less efficient regions.

Instead, the less efficient regions can be explained by the partly insulator-covered anode. If a Micromegas hole is located above the joint of 2 pixels, or above the 4 adjacent corners of 4 pixels, the drifting electron will be pulled towards 1 pad which is relatively far away. Along this drift path the electric field is less strong, and the gain is smaller. This effect explains the difference in the

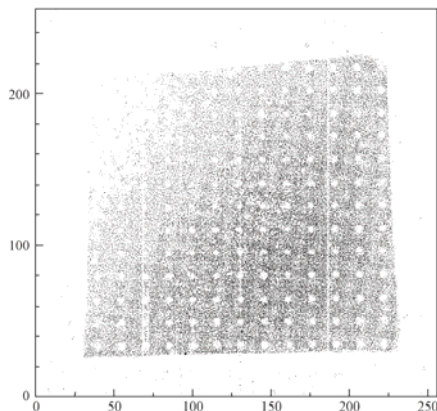


Fig. 11. Superimposed images recorded from the MediPix2/Micromegas prototype TPC after irradiation with  $\beta$ 's from a  $^{90}\text{Sr}$  source.

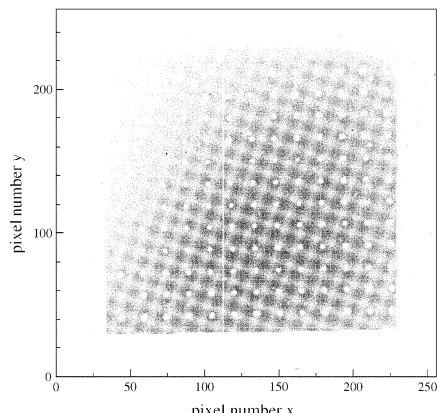


Fig. 12. Superimposed images recorded with a non-modified MediPix2 sensor after irradiation with  $\beta$ 's from a  $^{90}\text{Sr}$  source.

amplitudes of the Moiré effect when using modified or non-modified MediPix2 sensors.

The probability for 2-fold clusters was found to be homogeneous, and not subject to the Moiré

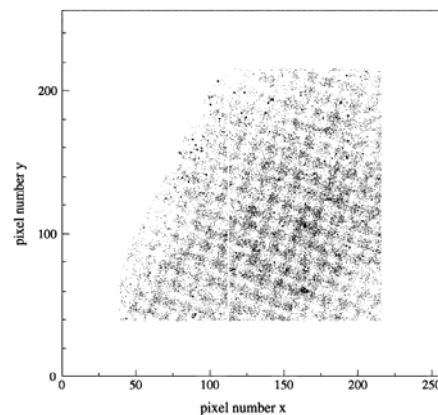


Fig. 13. Superimposed images recorded with a non-modified MediPix2 sensor during one night of cosmic data taking.

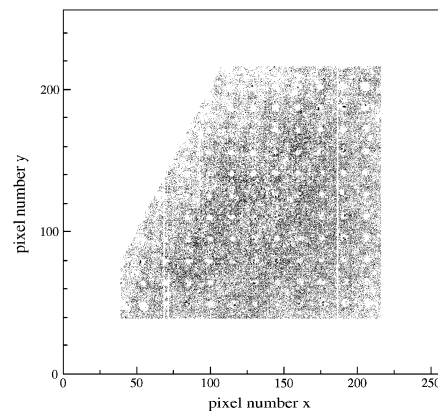


Fig. 14. Superimposed images recorded with a modified MediPix2 sensor during one night of cosmic data taking.

effect, but the measured value was found to be significantly higher than the Monte Carlo simulation (30% and 10%, respectively). We explain this by the occurrence of very large but not rare

avalanche charges, following the distribution shown in Fig. 5. A neighbouring pixel can be hit due to capacitive crosstalk, in spite of the (positive) induced charge.

### 5. Conclusions and outlook

We have demonstrated that single electrons can be detected with an assembly of a CMOS pixel chip and a Micromegas foil, with an efficiency larger than 0.9, in a He-based gas mixture. Bubble chamber-like images of cosmic ray tracks have been obtained and even  $\delta$ -electrons could be observed. The device allowed one to reconstruct the number of primary ionisation clusters per unit of track length, giving the possibility of a measurement of the ionisation loss  $dE/dx$ .

For the future *TimePixGrid*, the grid holes are precisely centred above the pixel pads, eliminating the non-homogeneity of the efficiency. The fact that the non-modified MediPix could stand the strong electric field, together with its strong Moiré effect, makes us confident that we can apply a pixel circuit with small pads, provided that the grid holes are well centred above the pads. The pad capacity can be kept small, simplifying the pixel input circuit. The inter-pad capacity is then also small, reducing the crosstalk between neighbouring pixels. A very small pad may reduce the maximum radiation dose, due to ageing, and an optimum must be found.

The combination of a pixel sensor and a Micromegas offers an instrument capable of giving a full 2D image of all single electrons in a gaseous volume. By replacing the MediPix2 sensor with a *TimePix* chip, a full 3D image is expected to be within reach. These circuits will open new possibilities for particle detection, in terms of position resolution, track separation and energy loss measurements. As another example, the polarisation of X-ray quanta can be measured [14], after its interaction with gas, from the direction of the photo-electron, which is registered accurately with the new device. Applied with a thin drift space of

1 mm, the device could be used as a fast vertex detector in high radiation environments.

### Acknowledgements

We thank the MediPix Collaboration for providing us with several wafers with MediPix2 chips, for the readout software and hardware. We would like to thank Arnaud Giganon, Wim Gotink, Joop Rövekamp and Tom Aarnink for their creative and essential contributions to the realisation of the test detectors.

### References

- [1] P. Colas, A.P. Colijn, A. Fornaini, Y. Giomataris, H. van der Graaf, E.H.M. Heijne, X. Llopard, J. Schmitz, J. Timmermans, J.L. Visschers, Proceedings of the 10th Vienna Conference on Instrumentation, Vienna, 2004; Nucl. Instr. and Meth. A 535 (2004) 506; See also Ref. [14].
- [2] Y. Giomataris, et al., Nucl. Instr. and Meth. A 376 (1996) 29.
- [3] X. Llopard, M. Campbell, R. Dinapoli, D. San Segundo, E. Pernigotti, IEEE Trans. Nucl. Sci. NS-49 (2002) 2279.
- [4] M. Conti, M. Maiorino, G. Mettivier, M.C. Montesi, P. Russo, IEEE Trans. Nucl. Sci. NS-50 (2003) 869.
- [5] D. San Segundo Bello, M. van Beuzekom, P. Jansweijer, H. Verkooijen, J.L. Visschers, Nucl. Instr. and Meth. A 509 (2003) 164.
- [6] Mesa + Research Institute, University of Twente, The Netherlands.
- [7] The Micromegas has been made by the CERN EST Workshop.
- [8] Particle Data Group, Phys. Rev. D 66 (2002) 010001.
- [9] F. Sauli, Principles of operating of multiwire and proportional drift chambers, CERN Yellow Report 77-09, 1977.
- [10] M. Hauschild, in: J.S. Kang, S.K. Oh (Eds.), Proceedings of the International Workshop on Linear Colliders, Jeju, Korea, 2002, pp. 464–469.
- [11] H.S. Snyder, Phys. Rev. 72 (1947) 181.
- [12] W. Riegler, C. Lippmann, R. Veenhof, Nucl. Instr. and Meth. A 500 (2003) 144.
- [13] S. Biagi, Nucl. Instr. and Meth. A 421 (1999) 234.
- [14] R. Bellazzini et al., Proceedings of the 10th Vienna Conference on Instrumentation, Vienna, 2004; Nucl. Instr. and Meth. A 535 (2004) 477.

## PAPER X

***Timepix, a 65k programmable pixel readout chip for arrival time, energy  
and/or photon counting measurements***

P a p e r X



# Timepix, a 65k programmable pixel readout chip for arrival time, energy and/or photon counting measurements

X. Llopart, R. Ballabriga, M. Campbell, L. Tlustos, W. Wong

*CERN, Geneva, Switzerland*

---

## Abstract

A novel approach for the readout of a TPC at the future linear collider is to use a CMOS pixel detector combined with some kind of gas gain grid. A first test using the photon counting chip Medipix2 [1], with GEM [2] or Micromegas [3] demonstrated the feasibility of such an approach. Although this experiment demonstrated that single primary electrons could be detected the chip did not provide information on the arrival time of the electron in the sensitive gas volume nor did it give any indication of the quantity of charge detected. The Timepix chip uses an external clock with a frequency of up to 100 MHz as a time reference. Each pixel contains a preamplifier, a discriminator with hysteresis and 4-bit DAC for threshold adjustment, synchronization logic and a 14-bit counter with overflow control. Moreover, each pixel can be independently configured in one of four different modes: masked mode: pixel is off, counting mode: 1-count for each signal over threshold, TOT mode: the counter is incremented continuously as long as the signal is above threshold, and arrival time mode: the counter is incremented continuously from the time the first hit arrives until the end of the shutter. The chip resembles very much the Medipix2 chip physically and can be read out using slightly modified versions of the various existing systems. This paper presents the main features of the new design, electrical measurements and some first images.

---

## 1 Introduction

The Medipix2 chip [1] has shown great potential in different applications requiring single photon counting approach. Successful tests using the chip for the readout of a TPC prototype for the ILC showed very promising results when coupled to GEM [2] or Micromegas [3] gain grids. Although these experiments demonstrated that single primary electrons could be detected, the chip did not provide information on the arrival time of the electron in the sensitive gas volume nor on the quantity of charge deposited. The Timepix chip

is an evolution from the Medipix2 chip which allows for measurement in arrival time, “time-over-threshold” (TOT) and/or event counting independently in each pixel. An external reference clock (*Ref.Clk*) is used to generate the clock in each pixel that increments the counter depending in the selected operation mode. The chip has the same size, readout architecture and floorplan as the Medipix2 chip allowing almost a full backward compatibility with all the existing Medipix2 readout systems [4,5]. The architecture and functional behavior of the Timepix chip are described in this paper together with first electrical measurements and first images.

## 2 The Pixel Cell

Fig. 1 shows the schematic of the Timepix pixel cell. Although the cell clearly resembles to the Medipix2 pixel it has three main differences: there is a single threshold with 4-bits threshold adjustment, each pixel can be configured in 3 different operation modes, and the counting clock is synchronised with the external clock reference (*Ref.Clk*). The pixel is divided into two large blocks: the analog side formed by the preamplifier, the discriminator (with polarity control pin) and 4 bit threshold adjustment, and the digital side formed by the Timepix Synchronization Logic (*TSL*), the 14-bit shift register, the overflow control logic, the *Ref.Clk* pixel buffer and an 8-bit Pixel Configuration Register (*PCR*). The *PCR* contains 4 bits for the pixel threshold equalization, 1 bit for Masking (*MaskBit*), 1 bit for enabling the test pulse input (*TestBit*) and 2 bits for selecting the pixel operation mode (*P0* and *P1*). The pixel cell contains  $\sim 550$  transistors, its dimensions are  $55 \times 55 \mu\text{m}^2$  and the static power consumption is  $\sim 13.5 \mu\text{W}$  (in acquisition state and *Ref.Clk*=80 MHz). Fig. 2 shows the Timepix pixel cell layout.

The pixel has two working states, depending on the *Shutter* signal. This signal is applied to all the pixels of the matrix simultaneously with a precision of  $\sim 5\text{ns}$ . If the *Shutter* signal is high, an external clock is used to shift the data from pixel to pixel. Either the 8-bit configuration register (*PCR*) is programmed or the 14-bit shift register is read out. When the *Shutter* is low the 14-bit shift register behaves as a linear feedback shift register counter with a single XOR tap with a dynamic range of 11810 counts. In this state the pixel counter is incremented by the *Ref.Clk* depending on the settings of the pixel operation mode bits (*P0* and *P1*):

- (1) Event counting mode (*P0*=0 and *P1*=0): Each event above threshold increments the counter by 1.
- (2) TOT mode (*P0*=1 and *P1*=0): The counter is incremented continuously while the input charge is over threshold.
- (3) Arrival Time mode (*P0*=1 and *P1*=1): The counter is incremented from

the moment the discriminator is activated until the global *Shutter* signal is set high.

### 2.1 Pixel Analog Section

Any charge collected by the octagonal 20  $\mu\text{m}$  width pixel anode is integrated and compared to a global threshold. If the preamplifier output voltage crosses the threshold the output of the discriminator generates a pulse whose width corresponds to the length of time the preamplifier output voltage remains over threshold. The preamplifier follows the scheme proposed by Krummenacher [6] based on a cascaded differential CMOS amplifier. Some global DACs control the front end. The peaking time can be set from 90 ns to 180 ns by the *Prcamp* DAC. The return to zero of a  $\sim 10 \text{ ke}^-$  input charge can be adjusted from 500 ns to 2500 ns depending on *Ikrum* DAC settings. The DC output level of the preamplifier is controlled by the *Vfbk* voltage DAC and it is used to maximise the output voltage dynamic range depending on input charge polarity. The configuration permits the amplification of positive or negative charges and the compensation for detector leakage currents in both polarities, of up to *Ikrum*/2 per pixel. The amplifier gain in the default DAC settings is  $\sim 16.5 \text{ mV/ke}^-$  with a linear voltage dynamic range up to  $\sim 50 \text{ ke}^-$ . The preamplifier output is DC coupled to the discriminator. The discriminator contains an input multiplexer (controlled by the *Polarity* CMOS input to ensure that the discriminator output has the right polarity when a hit crosses the threshold for both input polarities), a differential amplifier (configured to work as an OTA<sup>1</sup>), four independent selectable current sources (used for threshold equalisation); and a current discriminator with hysteresis. The total analog power consumption in nominal conditions is  $\sim 6.5 \mu\text{W}$  and its layout area is 55 x 25  $\mu\text{m}^2$ .

### 2.2 Pixel Digital Section

The analog output from the discriminator (*Hit*) is buffered and gated with the *Maskbit* at the entrance of the Timepix Synchronization Logic (*TSL*). The pixel operation mode bits (*P0* and *P1*) configure each pixel *TSL* in three different modes. In the acquisition state (i.e. *Shutter* is low) the *TSL* synchronizes the *Hit* and the *Shutter* with the *Ref.Clk* to generate a glitch free counting clock signal depending on the operation mode. The counter is stopped if the number of counts reaches the overflow limit of 11810 counts. The *TSL* core uses an asynchronous network of SR flip-flops with race-free state assignment designed with controlled initialization. To minimize the digital power

---

<sup>1</sup> OTA=Operational Transimpedance Amplifier

consumption the *TSL* core is only active when a *Hit* is present. The pixel digital part contains  $\sim 500$  minimum-sized transistors and occupies an area of  $55 \times 30 \mu\text{m}^2$ .

### 3 The Reference Counting Clock

The Timepix chip uses an externally generated tunable clock reference (*Ref\_Clk*) as its counting clock which is distributed throughout the pixel matrix. To minimise the capacitive coupling and to maximise the digital power balance of the *Ref\_Clk* distribution into the full matrix, each pixel includes a minimum-sized inverter to buffer the *Ref\_Clk* to the next pixel up in the column. Furthermore, to minimise the digital coupling and to uniformly distribute the digital power, the *Ref\_Clk* phase is alternated between columns. Assuming a simulated typical propagation delay of  $\sim 195$  ps per pixel inverter/buffer the *Ref\_Clk* is distributed to all the pixels in less than 50 ns. With a *Ref\_Clk* of 80 MHz the measured digital power consumption due to clock distribution into the pixel matrix is  $\sim 450$  mW. The Timepix chip shows no detectable increment of the minimum threshold when compared to the Medipix2 chip, which has no distributed clock and each pixel generates its own asynchronous counting clock.

### 4 Chip Description

Fig. 3 shows the floorplan of the Timepix chip. To minimise non-sensitive area when butting together several chips, the periphery is placed at the bottom of the chip and the sensitive area is placed at the top, with less than  $50 \mu\text{m}$  of non-sensitive area between the last pixel and the chip edge. The sensitive area (top box) is arranged as a matrix of  $256 \times 256$  pixels of  $55 \times 55 \mu\text{m}^2$  resulting in a detection area of  $1.98 \text{ cm}^2$  (87% of the entire chip area). The analog part of the periphery contains one band-gap circuit [7] which internally generates a stable reference voltage which is used by the 13 on-chip global DACs. This reference voltage has a temperature sensitivity of  $-0.22 \text{ mV}/^\circ\text{C}$  and a power supply sensitivity of less than  $1 \text{ mV/V}$ . There are eight 8-bit current DACs, four 8-bit voltage DACs and a single 14-bit voltage DAC which is used for the precise setting of the global threshold. At default settings the threshold DAC LSB<sup>2</sup> corresponds to  $\sim 25 e^-$  with a INL<sup>3</sup> of less than 1.5 LSB in 10-bits. The digital part of the periphery contains all the Input/Output control logic, the IO wire-bonding pads and a 24-bit fused blown registry for unique chip

---

<sup>2</sup> LSB=Least significant Bit

<sup>3</sup> INL=Integral non linearity

identification. Using a 100 MHz readout clock the chip can be read out serially through the on-chip LVDS drivers in less than 10ms, or in parallel through the 32-bit CMOS port in less than 300  $\mu$ s. Both the analog and digital circuitry have been designed to operate with independent 2.2 V power supplies with a total analog power consumption of  $\sim$ 440mW and a digital power consumption of  $\sim$ 450 mW (in acquisition state and  $Ref\_Clk=80$  MHz). The chip contains approximately 36 million transistors and is fabricated in a commercial 6 metal CMOS 0.25  $\mu$ m technology.

## 5 Pixel Electrical Characterisation

Initial electrical measurements were done with a Timepix chip mounted on a standard Medipix2 PCB, using the Medipix2 serial readout system with an updated MurosV2.1 readout board [4] and a modified version of the Pixelman software [5]. The electrical characterization was carried out using an external test pulse with a gain of  $46.875 e^-/\text{mV}$ . The test pulse linear range extends to  $\sim$ 40 ke $^-$ . Since the test pulse gain was extracted from simulations, it should be understood that all the following measurements are preliminary. In all measurements the  $Ref\_Clk$  has been set to 60 MHz unless otherwise indicated.

### 5.1 Measurements in Counting Mode

The electronic noise and effective threshold can be measured using the s-curve method [8] when the pixel is set in counting mode. This method gives information on the noise of the front-end chain. Using a fixed threshold, an input charge is swept from a level where there are no counter counts (i.e. under threshold) to a level where the 100% of the test pulses are counted, creating an s-shaped curve. The effective threshold is at 50% of this s-curve. The charge difference between the 97.75% and 2.25% of the s-curve is four times the RMS noise of the front-end assuming a gaussian distributed noise. Fig. 4 shows an example of four s-curves in electron collection mode. The gain can be calculated as the distance from the measured effective threshold to the noise floor for a given input charge. Fig. 5 shows the linearity (up to 20 ke $^-$ ) of a single pixel at the centre of the matrix for both polarities. The measured electronic noise is  $99.4 \pm 3.8 e^- \text{rms}$  for hole collection and  $104.8 \pm 6 e^- \text{rms}$  for electron collection. The measured DAC step gain is  $24.7 \pm 0.7 e^-/\text{step}$  for hole collection and  $25.4 \pm 1.2 e^-/\text{step}$  for electron collection.

## 5.2 Measurements in TOT Mode

In TOT mode the counter is incremented continuously with *Ref\_Clk* while the preamplifier output is above the threshold. Although the preamplifier output voltage pulse is only linear up to  $50 \text{ ke}^-$  (due to the limited power supply range [0-2.2 V]), and the relative high gain [ $\sim 16.5 \text{ mV/ke}^-$ ], the discriminator output pulse width is linear up to much larger input charges because of the constant current return to zero, which is controlled by the *Ikrum* DAC. Simulations have shown that the linear TOT dynamic range extends up to  $\sim 200 \text{ ke}^-$ . However this could not be electrically confirmed due to the limited test pulse linear range (up to  $\sim 40 \text{ ke}^-$ ). The left hand plot of Fig. 6 shows the relationship between the input charge and the measured time at three different thresholds. The measured response is linear if the input charge is 3-4  $\text{ke}^-$  above threshold. On the right hand side of Fig. 6 the resolution measured as  $\Delta\text{TOT}/\text{TOT} [\%]$  is shown. The resolution is better than 5% when the input charge is  $\sim 1 \text{ ke}^-$  above threshold. As the input charge increases the  $\Delta\text{TOT}/\text{TOT}$  tends to 0 because the  $\Delta\text{TOT}$  is kept constant independently of the increase of the detected charge.

## 5.3 Measurements in Arrival Time Mode

When programmed in arrival time mode, the pixel behaves as a TDC<sup>4</sup>. During acquisition, the counter is incremented from the first time the discriminator output goes high to the closing of the *Shutter*. The quantization error can be up to two *Ref\_Clk* periods since the start and end of the counting clock is synchronized to *Ref\_Clk*. In the MUROSV2.1 readout system the test pulse timing is synchronized to *Ref\_Clk*, therefore it is not possible to measure the quantization error at the pixel level. The time-walk is defined as the difference between the time measured from an input charge that is  $1 \text{ ke}^-$  over threshold and an infinite input charge. The faster the preamplifier peaking time, the better the time-walk value, since there is less time difference from a small charge to a big one crossing the same threshold level. The preamplifier peaking time is controlled by the *Preamp* current DAC. Fig. 7 shows the time-walk measured in a single pixel at the centre of the matrix for five different thresholds and two *Preamp* DAC settings. The measured time-walk is  $\leq 50 \text{ ns}$  for the high *Preamp* current DAC setting. In systems where the charge deposition of a single event spreads over multiple pixels (i.e. GEMs), the matrix could be arranged in a kind of chess pattern, whereby some pixels could be configured in TOT mode and others in arrival time mode, in order to compensate off-line the time-walk through knowledge of the input charge deposited in the neighboring pixels.

---

<sup>4</sup> TDC=Time to Digital Converter

## 6 Threshold Equalisation

Threshold equalisation is used to compensate the pixel to pixel threshold variations due to local transistor threshold voltages and current mismatches [9] or more global effects like on-chip power drops. This compensation is done by means of a 4-bit current DAC placed in the discriminator chain of each pixel. The current range of this DAC is controlled by the *Ths* global DAC with a LSB range of 0-40 nA. The measured INL of this 4-bit DAC in the full pixel matrix is less than 0.8 LSB. To calculate the equalisation mask the threshold distribution for each of the 16 threshold adjustment codes is found. Then the adjustment code is selected for each pixel to make its threshold as near as possible to the average of the threshold distribution mean values. Fig. 8 shows an example of a threshold equalisation of a Timepix chip in both collection modes. The threshold variation before equalisation is  $\sim 240$   $e^-$ rms and after equalisation the achieved noise free threshold variation is  $\sim 35$   $e^-$ rms for both polarities. The minimum detectable charge is defined as the smallest input charge which all pixels are able to resolve when the global threshold is set just over the noise. The minimum detectable charge can be calculated by quadratically adding the measured electronic noise and the threshold variation because both measurements are uncorrelated. Before equalisation the minimum detectable charge for the full matrix is  $\sim 1600$   $e^-$  and after equalisation is  $\sim 650$   $e^-$  for both polarities.

## 7 Fixed Pattern Correction in TOT Mode

The preamplifier output of all pixels can be reconstructed by scanning the threshold over 1 test pulse per *Shutter* period in arrival time and TOT mode consecutively. In arrival mode the peaking time of the preamplifier is reconstructed as a fixed test pulse is scanned by the global threshold. The preamplifier fall time is calculated by subtracting the previously measured arrival time to the TOT measurement for each threshold. Fig. 9 shows an example of the preamplifier output pulse reconstruction of three pixels along the central column. It can be seen that the peaking time and the peak value is unchanged, but the return to zero shows a certain dispersion for the three tested pixels. The return to zero variation from pixel to pixel generates in TOT mode a pixel to pixel variation for the same global threshold, while in the other two modes the effect is undetectable. In each pixel the constant current discharge feedback loop is controlled by the global *Ikrum* DAC which has a nominal range of few nA. Given the small pixel area and the small current value the transistor size of the *Ikrum* current source is not big enough to compensate the pixel to pixel *Ikrum* current mismatch. Extrapolating to the full matrix pixel to pixel current mismatch generates a fix pattern noise in TOT mode. A

correction mask for this effect can be found by calculating the transfer function of each pixel by scanning the test pulse over a fix global threshold. Once the correction mask is found it can be applied to any raw image to compensate for the *Ikrum* current mismatch. Fig. 10 shows an example of the full matrix being in TOT mode after sending in each pixel 1 test pulse of  $18.75 \text{ ke}^-$ ; on the top left is the raw image, at the top right is the corrected image and at the bottom is shown the histogram of both 2D images. The FWHM of the full corrected matrix is  $\sim 1300 \text{ e}^-$ .

## 8 First Images

Fig. 11 shows a 2D image of an equalised chip after sending 10 test pulses of  $\sim 2.3 \text{ ke}^-$ . This images shows the possibility of having simultaneously each pixel working in any of the three operation modes. In counting mode all the pixels count 10 and the masked pixels are at 0 counts. In TOT mode there is a certain spread due to the pixel to pixel TOT variation. In arrival time mode all the counts are between 8827 and 8829. Fig. 12 shows two images obtained with the two gas grain grid systems (GEM and Micromegas) which use a single naked Timepix as collection anode. On the left is shown a measurement in TOT mode of a single cosmic background particle interacting on a gas volume of a triple GEM detector. The maximum number pixel value of 1929 counts corresponds after calibration to  $\sim 120 \text{ ke}^-$ . This image was taken during an EUDET testbeam in DESY with the collaboration of A.Bamberger and U.Renz, Freiburg (Germany). The right of Fig. 12 shows a measurement in arrival time of a cosmic background particle obtained with a Micromegas gas gain grid coupled to the Timepix chip. The measured counts difference is 56 which indicates an arrival time difference of  $1.4 \mu\text{s}$  (with *Ref.Clk*=40 MHz). A triple scintillator is used as coincidence system to generate the *Shutter* trigger. This image was taken in Nikhef (The Netherlands) by J.Timmermans, H. van der Graaf and M.Chefdeville.

## 9 Conclusions

The Timepix chip has been designed using a commercial  $0.25 \mu\text{m}$  technology, with a pixel cell of  $55 \times 55 \mu\text{m}^2$ . Each pixel can be programmed independently in counting, energy or arrival time modes. The chip has been characterised using an external test pulse. Initial measurements show an electronic pixel noise of  $\sim 100 \text{ e}^-$  rms and a full matrix threshold variation  $\sim 35 \text{ e}^-$  rms after equalisation. The minimum detectable charge is  $\sim 650 \text{ e}^-$ . In TOT mode the energy resolution ( $\Delta\text{TOT}/\text{TOT}$ ) is better than 5% if the input charge is

$\geq 1 \text{ ke}^-$  above threshold. The measured time-walk per pixel is  $\leq 50 \text{ ns}$ . The first Timepix bump-bonded to a  $300 \mu\text{m}$  Si semiconductor detector will be available shortly. At this point it will be possible to make an absolute calibration using a radiation source in order to confirm the figures presented here.

## 10 Figure captions

Fig. 1: Timepix pixel cell schematic.

Fig. 2: Timepix pixel cell layout. 1) Preamplifier, 2) Discriminator with 4-bit threshold equalisation, 3) 8-bit PCR, 4) *Ref\_Clk* buffer and TSL and 5) 14-bit shift register and overflow control.

Fig. 3: Timepix floorplan: on the top square there is the  $256 \times 256$  pixel matrix, on the bottom square there is the Timepix IO periphery and DACs.

Fig. 4: An example of measured s-curves at four different thresholds. There are a total of 5000 test pulses sent in counting mode.

Fig. 5: Linearity plot up to  $\sim 20 \text{ ke}^-$  for both polarities (holes on top and electrons on the bottom).

Fig. 6: Linearity of TOT measurements for three different thresholds. On the left is shown the measured energy resolution ( $\Delta\text{TOT}/\text{TOT} [\%]$ ) with 1% and 5% markers.

Fig. 7: Time-walk of 1 pixel of the centre of the matrix. The thick line curves are for *Preamp*=255 (Preamp=1.8  $\mu\text{A}$ ) and the thin line curves are with *Preamp*=127 (Preamp=900 nA).

Fig. 8: Threshold equalisation result for both polarities. On the left for electron collection and on the right for hole collection.

Fig. 9: Reconstructed preamplifier output pulse of three pixels along the central column of the matrix. Injected test pulse charge was  $\sim 9.3 \text{ ke}^-$ .

Fig. 10: An example of the full matrix programmed in TOT mode after sending in each pixel 1 test pulse of  $18.75 \text{ ke}^-$ . On the top left is the raw image, on the top right is the corrected image and at the bottom is shown the histogram of both 2D images. The FWHM of the full corrected matrix is  $\sim 1300 \text{ e}^-$ .

Fig. 11: On the left is a full matrix 2D image response of an equalised chip after sending 10 test pulses of  $\sim 2.3 \text{ ke}^-$ . The matrix is split into three different working modes and the pixels that form the names are masked. On the right

the histogram for each area (operation mode) is shown. The *Ref\_Clk* is set to  $\sim 50$  MHz.

Fig. 12: On the left: TOT mode measurement of a single cosmic background particle interacting on a gas volume of a triple GEM detector. The maximum number pixel value of 1929 counts corresponds after calibration to  $\sim 120$  ke $^-$ . On the right: Arrival time measurement of a cosmic background particle obtained with a Micromegas gas gain grid coupled to the Timepix chip.

## References

- [1] X. Llopert et al, “Medipix2, a 64k pixel readout chip with 55  $\mu\text{m}$  square elements working in single photon counting mode”, IEEE Trans. Nucl. Sci., vol.49, iss. 5 ,(2002), pp.2279-2283.
- [2] P. Colas et al, “The readout of a GEM or Micromegas-equipped TPC by means of the Medipix2 CMOS sensor as direct anode”, Nuclear Instruments and Methods in Physics Research, A53, iss. 1-2, (2004) pp. 506-510.
- [3] H. van der Graaf et al, “Detection of single electrons by means of a Micromegas-covered Medipix2 pixel CMOS readout circuit”, Nuclear Instruments and Methods in Physics Research, A540, iss. 2-3, (2005),pp. 295-304.
- [4] D. San Segundo et al, “An interface board for the control and data acquisition of the Medipix2 chip”, Nuclear Instruments and Methods in Physics Research, A509, Issues 1-3, (2003), pp.164-170.
- [5] T. Holy et al, “Data acquisition and processing software package for Medipix2”, Nuclear Instruments and Methods in Physics Research, A563, Issue 1, (2006), pp.254-258.
- [6] F. Krummenacher, “Pixel Detectors with Local Intelligence: an IC Designer Point of View”, Nuclear Instruments and Methods in Physics Research, A305, (1991), pp.527-532.
- [7] K.E.Kuijk, “A precision reference voltage source”, IEEE Journal of Solid-State Circuits, vol. Sc-8, iss. 3, (1973), pp.222-226.
- [8] F. Anghinolfi et al., “A 1006 element hybrid silicon pixel detector with stobed binary output”, IEEE Trans. Nucl. Sci. vol. 39, Issue 4, (1992), pp.654-661.
- [9] M. Pelgrom, et al., “Matching Properties of MOS Transistors”, IEEE Journal of Solid-State Circuits, vol. 24, no. 5, (1989), pp.1433-1440

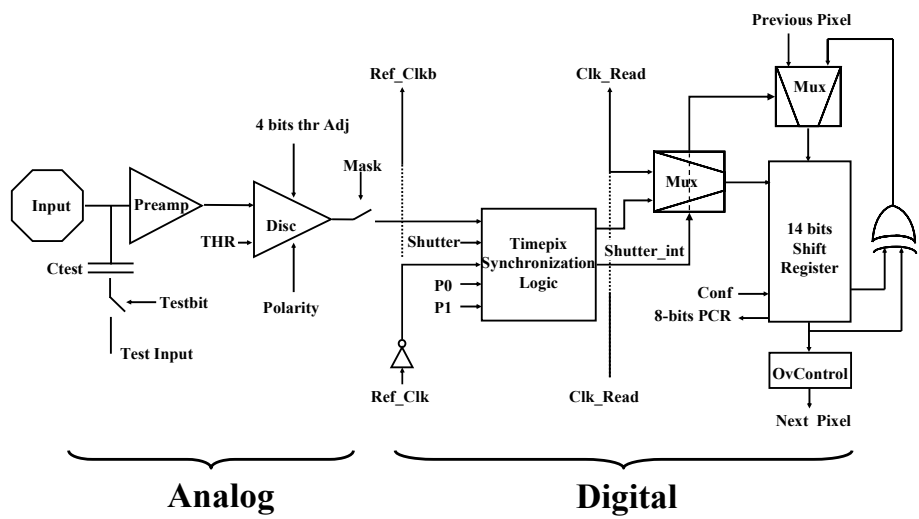


Fig. 1.

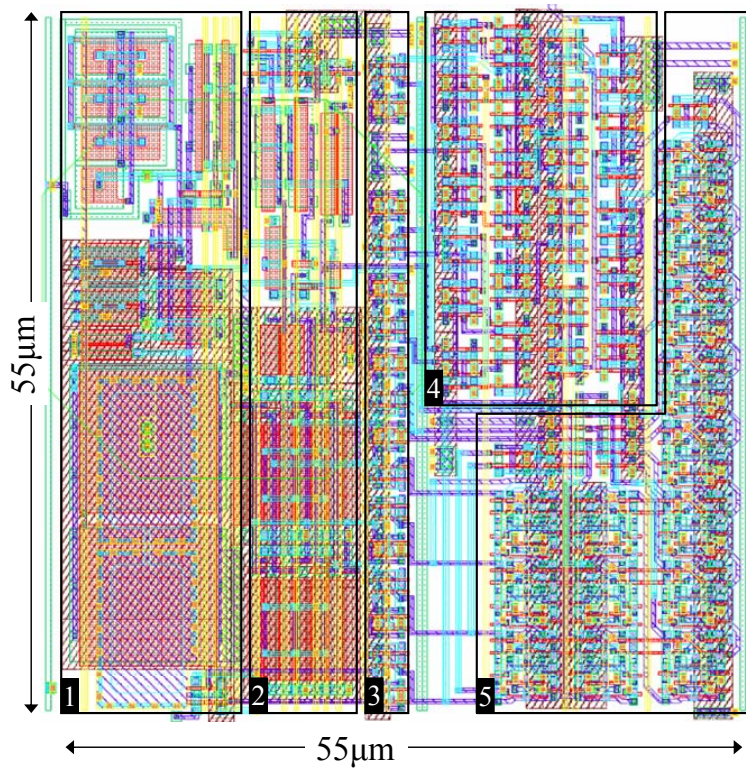


Fig. 2.

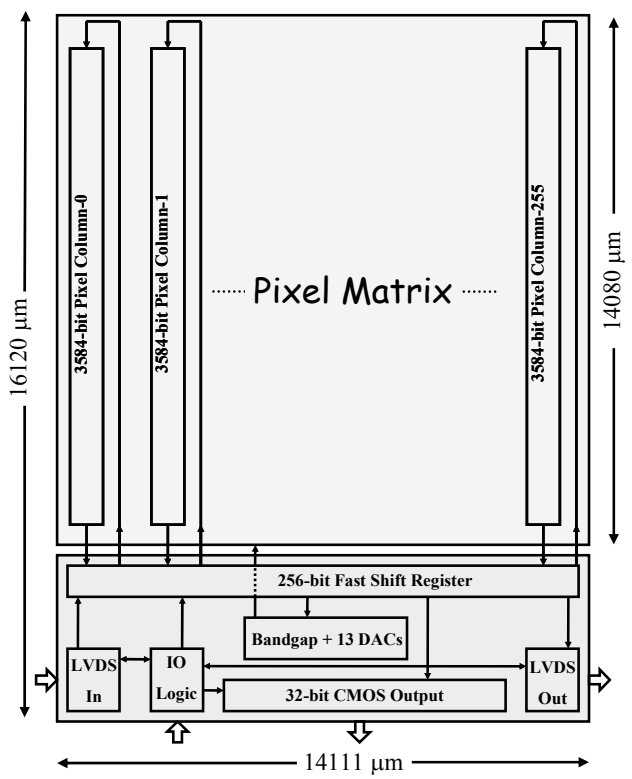


Fig. 3.

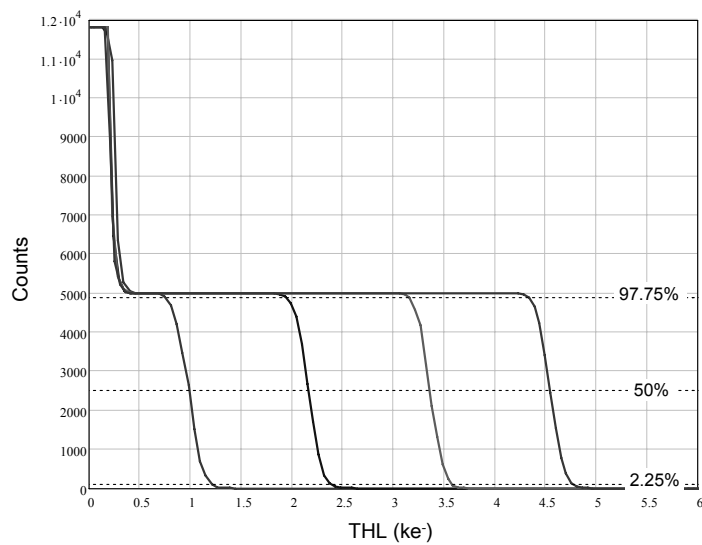


Fig. 4.

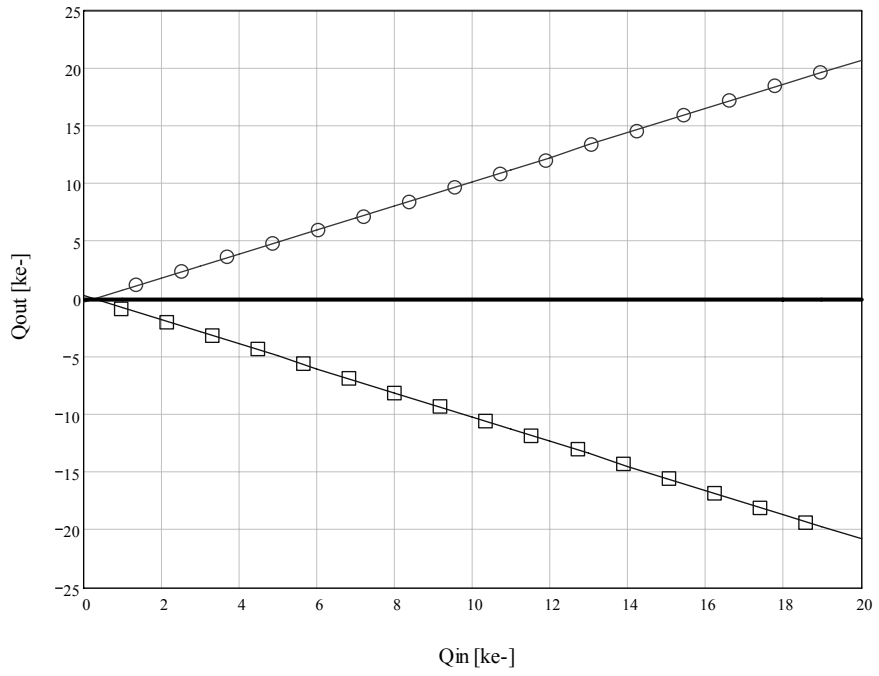


Fig. 5.

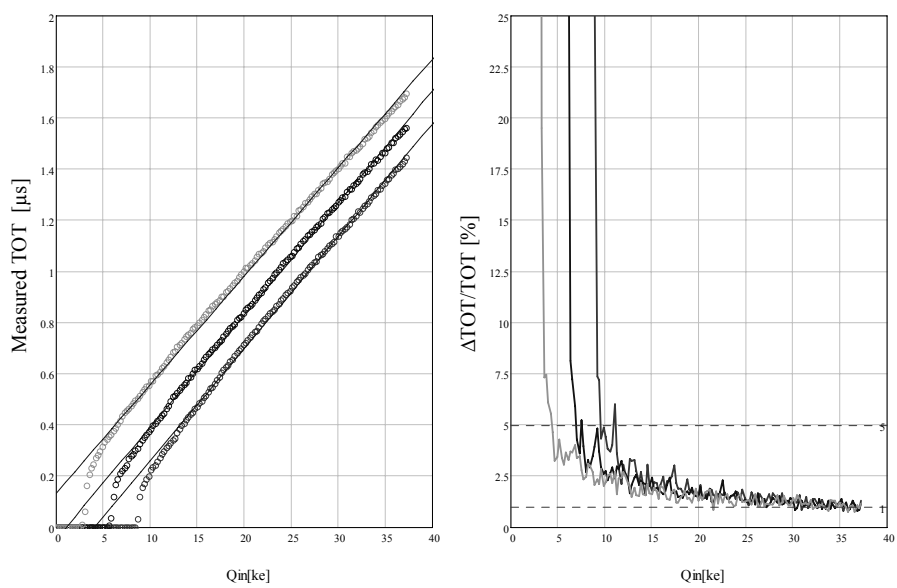


Fig. 6.

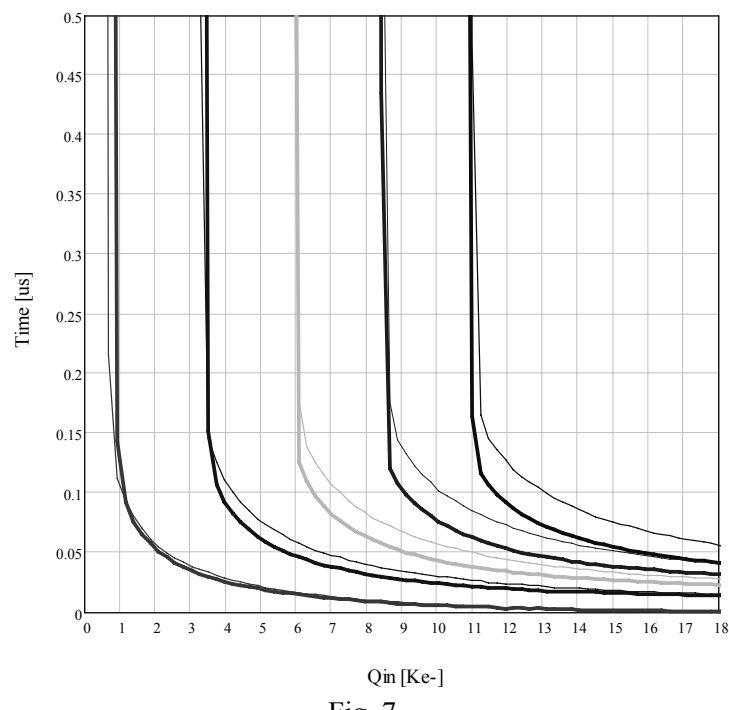


Fig. 7.

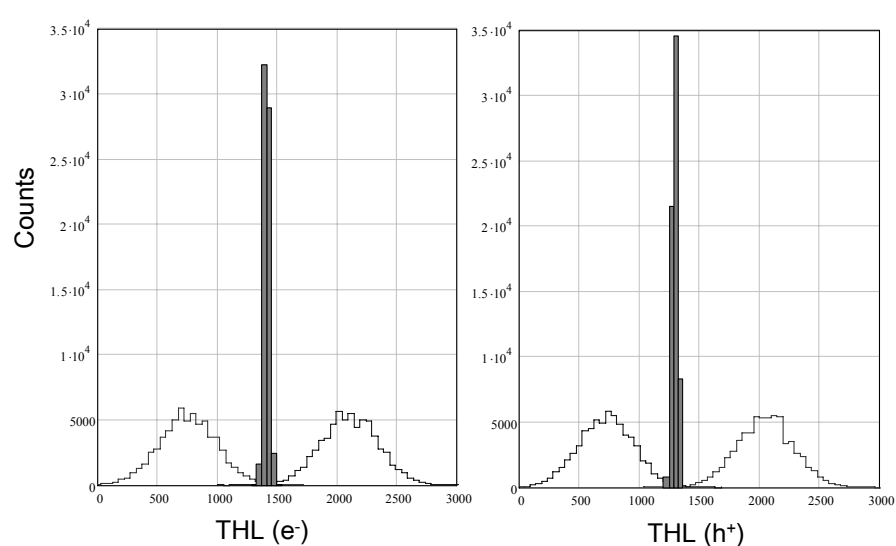


Fig. 8.

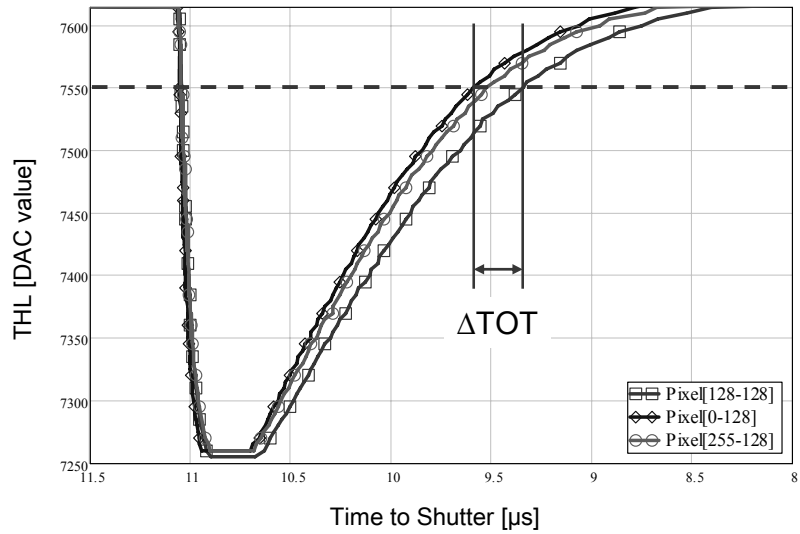


Fig. 9.

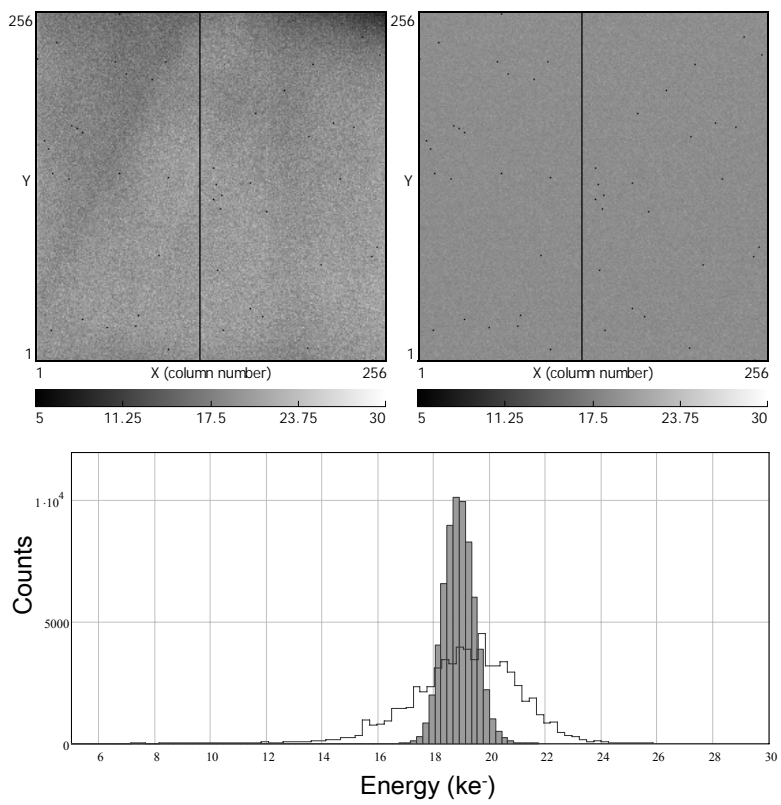


Fig. 10.

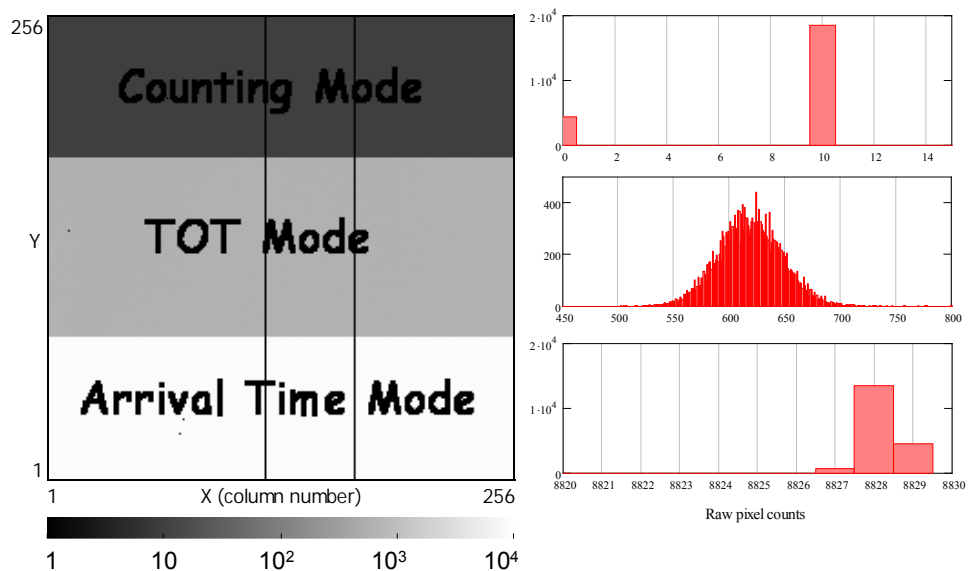


Fig. 11.

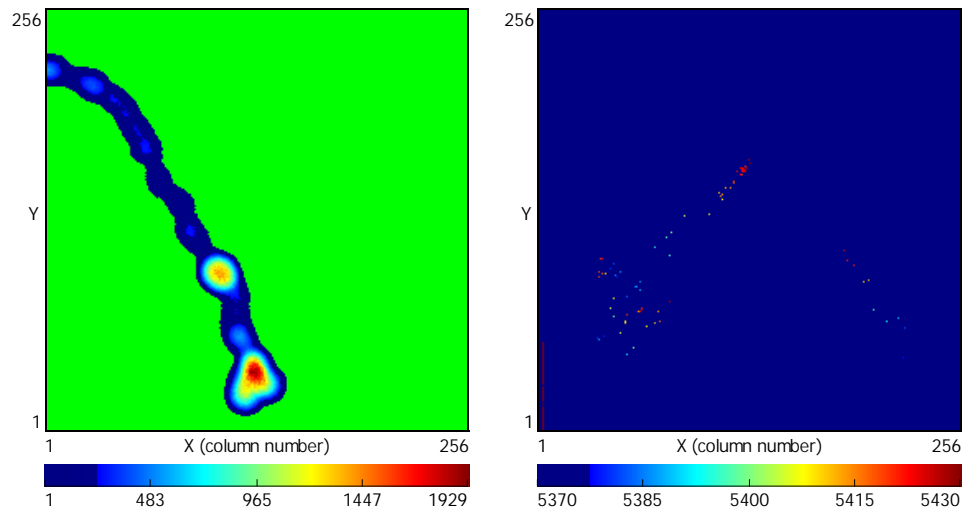


Fig. 12.

## PAPER XI

**The *Medipix3* Prototype, a Pixel Readout Chip Working in Single Photon  
Counting Mode with Improved Spectrometric Performance**

P a p e r XI



# The Medipix3 Prototype, a Pixel Readout Chip Working in Single Photon Counting Mode with Improved Spectrometric Performance

R. Ballabriga, M. Campbell, E. H. M. Heijne, *Fellow, IEEE*, X. Llopart, L. Tlustos

**Abstract**—A prototype pixel detector readout chip has been developed with a new front-end architecture aimed at eliminating the spectral distortion produced by charge diffusion in highly segmented semiconductor detectors. In the new architecture neighbouring pixels communicate with one another. Charges can be summed event-by-event and the incoming quantum can be assigned as a single hit to the pixel with the biggest charge deposit. In the case where incoming X-ray photons produce fluorescence – a particular issue in high-Z materials – the charge deposited by those fluorescent photons will be included in the charge sum provided that the deposition takes place within the volume of the pixels neighbouring the initial impact point. The chip is configurable such that either the dimensions of each detector pixel match those of one readout pixel or detector pixels are 4 times greater in area than the readout pixels. In the latter case event-by-event summing is still possible between the larger pixels.

As well as this innovative analog front-end circuit, each pixel contains comparators, logic circuits and two 15-bit counters. When the larger detector pixels are used these counters can be configured to permit multiple thresholds in a pixel providing spectroscopic information.

The prototype chip has been designed and manufactured in an 8-metal 0.13 μm CMOS technology. First measurements show an electronic pixel noise of ~ 72 e- rms (Single Pixel Mode) and ~ 140 e- rms (Charge Summing Mode).

## I. INTRODUCTION

PIXEL detector advances open up new possibilities in many fields of science. Modern High Energy Physics (HEP) experiments use pixel detectors for tracking systems where excellent spatial resolution, precise timing and high signal-to-noise ratio are required for accurate track reconstruction. Many groups are working worldwide to adapt the hybrid pixel technology to other fields such as medical X-ray radiography, protein structure analysis or neutron imaging. A comprehensive overview is provided in [1].

The innovation in monolithic and hybrid semiconductor ‘micropattern’ pixel detectors for tracking in particle physics was actually to fit pulse processing electronics and associated digital circuitry on a pixel area of much less than 1 mm<sup>2</sup>, with a power consumption in the μW range while retaining the

characteristics of a traditional nuclear amplifier chain [1]. The evolution of hybrid pixel detectors is intimately related to CMOS technology advances following Moore’s Law [3]. The driving force behind this close relationship is continuously improving performance, high integration density, low power consumption and reasonable cost using an industry standard technology. This allows pixel detector Application Specific Integrated Circuit (ASIC) designers to implement more functionality per pixel while maintaining the compact pixel area when a more down-scaled process is used.

Two generations of the Medipix chip have been successfully developed. The Medipix1 chip [4] demonstrated the principle of the photon counting approach, which provides a high dynamic range and images which are practically free of non-photon noise. The pixel dimensions were 170 μm x 170 μm and each pixel contained approximately 400 transistors. It was implemented in a 1 μm CMOS process. The Medipix2 [5] pixel dimensions are 55 μm x 55 μm. It is implemented in a 0.25 μm CMOS technology. It contains approximately 500 transistors per pixel.

The performance of the Medipix2 imaging system is limited by the sharing of charge between neighbouring pixels. The Medipix3 prototype chip implements an architecture aimed at eliminating the spectral distortion produced by the charge sharing process. It has been developed in an 8-metal 0.13 μm CMOS technology. The chip includes a matrix of 8 x 8 pixels. Each pixel contains around 1100 transistors and occupies a total area of 55 μm x 55 μm.

Section II discusses the motivation to develop a new Medipix architecture and presents simulation results that validate the new system. Section III shows the architecture in detail. Section IV presents the measurements and electrical characterization of the chip.

## II. MOTIVATION

Charge diffusion in segmented semiconductor detectors produces a distortion in the energy spectrum seen by an individual pixel [6]. The influence of this effect on the spectrum increases as the pixel pitch is decreased with respect to the thickness of the detector material. As a consequence, there is a trade-off between spatial resolution and energy resolution in single particle counting systems. Fig. 1 shows the simulation of the spectrum seen by a single pixel of a 300 μm thick silicon sensor with a 55 μm pitch pixel. The

Manuscript received November 17, 2006. This project has been undertaken in the framework of the Medipix2 Collaboration, <http://www.cern.ch/MEDIPIX>.

R. Ballabriga, M. Campbell, E. H. M. Heijne, X. Llopart and L. Tlustos are with the European Organization for Nuclear Research (CERN), Geneva 23, Switzerland (e-mail: rafael.ballabriga@cern.ch).

simulation has been done with a 10 keV monochromatic photon beam. The spectrum seen by one pixel using a traditional readout architecture with a front-end electronics noise of 100 e<sup>-</sup> rms is shown in blue. Many photons deposit charge at or near the pixel borders. This charge then diffuses during collection and is shared between adjacent pixels resulting in a low energy tail that limits the energy resolving potential of the system. The spectrum seen by one pixel with the new architecture is shown in red. In this new architecture, the charge information is reconstructed by grouping pixels into clusters of four, summing the charge collected in each cluster, and associating the photon with the summing circuit with the largest charge deposition.

The "charge sharing" tail means that any residual threshold variation between pixels produces a fixed pattern image noise which varies dependent on energy spectrum [7].

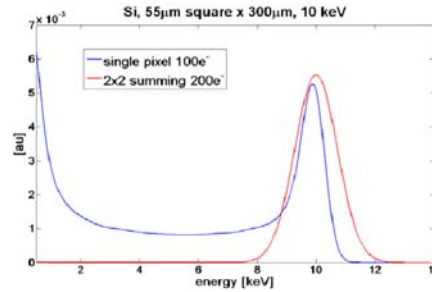


Fig. 1. Simulation of a 300  $\mu\text{m}$  thick Si sensor bump bonded to a 55  $\mu\text{m}$  pixel pitch detector readout. The spectrum seen by one pixel in a traditional system (pixel front-end with 100 e<sup>-</sup> rms noise independent of neighbouring pixels) is shown in blue. In red, the spectrum observed with the new electronics whereby 4 pixels contribute to the total charge sum is shown. The noise of the individual pixels is added in quadrature.

When high-Z materials are used to detect X-rays in the 10's of keV region, fluorescent photons are often produced and they deposit charge at some distance from the primary interaction [8]. Fig. 2 shows simulation results of a 300  $\mu\text{m}$  thick GaAs sensor bonded to a 55  $\mu\text{m}$  pixel pitch detector readout circuit. The simulation in this case has been done with a 20 keV monochromatic photon beam. The influence of the fluorescence photons of Ga (9.2 keV) and As (10.5 keV) in the spectrum is evident in the blue curve. The mean free path of these is comparable to the pixel pitch being 42.62  $\mu\text{m}$  for Ga, and 15.62  $\mu\text{m}$  for As. The spectrum seen using the new architecture (in red) includes the reconstructed energy, the charge deposited by the fluorescence photons provided the deposition takes place within the sensor volume of the pixels neighbouring the impact point.

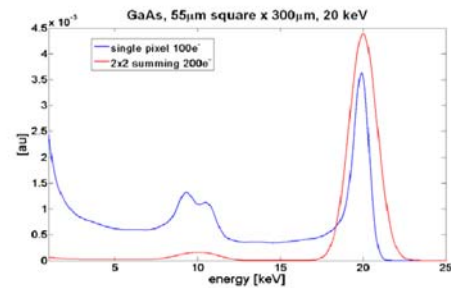


Fig. 2. Simulation of a 300  $\mu\text{m}$  thick GaAs sensor bump bonded to a 55  $\mu\text{m}$  pixel pitch detector readout. The two bumps in the spectrum for the traditional architecture show the effect of the fluorescence photons: Ga (9.2 keV) and As (10.5 keV). The mean free path of these is comparable to the pixel pitch being 42.62  $\mu\text{m}$  for Ga, and 15.62  $\mu\text{m}$  for As. In the new architecture the charge deposited by the fluorescence photon will be included in the charge sum provided the deposition takes place in the sensor volume of the pixels neighbouring the initial conversion.

### III. CHIP AND PIXEL DESCRIPTION

The Medipix3 prototype chip (Fig. 3) has been designed and manufactured in 0.13  $\mu\text{m}$  CMOS technology with eight metal layers. This allows a high degree of interconnectivity between pixels and the implementation of more functionality while maintaining a compact pixel area. Two pixel matrices have been implemented: an 8  $\times$  8 pixel matrix and a small test matrix for circuit debugging purposes. Two pixels with a different layout design have been implemented to test special transistors offered by the foundry. The analog and the digital circuitry have been designed to operate with independent 1.5 V power supplies.

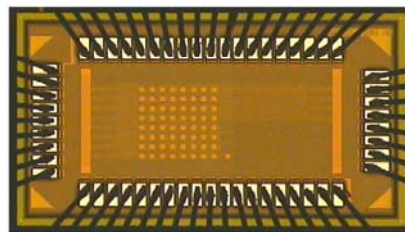


Fig. 3. Medipix3 prototype chip die. The 8  $\times$  8 matrix is implemented in the left hand side of the die. In the right hand side of the chip a small matrix for digital debug is implemented.

The block diagram of the pixel schematic is shown in Fig. 4. The charge collected on a pixel is integrated by a Charge Sensitive Amplifier (CSA) on a feedback capacitance whose

design value is 14 fF (gain of 11.44 mV/ke<sup>-</sup>). The CSA is based on the Krummenacher architecture [9] and can handle both positive and negative input charges. A test injection capacitance of 4.8 fF is provided in each pixel in order to permit full testing of the chip functionality. Seven different test pulses are available to allow injection of different charges in adjacent pixels. Those allow the testing of all the modes of operation of the system. The output of the CSA is filtered by means of a first order semi-gaussian shaper with a time constant of ~100 ns, which acts both as a transconductance and as a noise filter. The shaper also AC couples the output of the preamplifier to the rest of the circuit (eliminating the offset produced by the mismatch of the transistors in the preamplifier feedback loop and thus relaxing the dimensions of those transistors) and makes the system less sensitive to the variations of the preamplifier characteristics. Furthermore the shaper generates eight currents whose amplitudes are proportional to the charge collected on the input electrode.

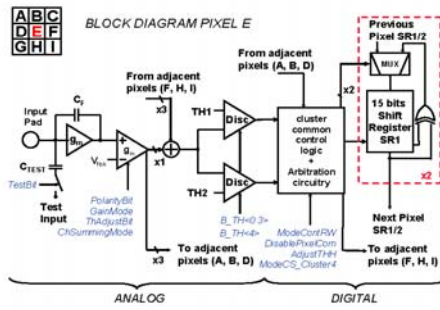


Fig. 4. Medipix3 pixel cell schematic.

The currents generated in the shaper are sent to nodes common to a cluster of four pixels, the adding nodes being located effectively at each pixel corner. As there are two discriminators associated with each pixel, there are two adding nodes per pixel corner.

Note that the chip can be used either in *Fine Pitch Mode* (where the pitch of the detector pixels matches the 55 µm pitch of the readout) or in *Spectroscopic Mode* (where the detector pitch is 110 µm.) Each of these modes can work in *Single Pixel Mode* (*SPM*) whereby the pixel processes the induced charge independently of the operation of the neighbouring pixels, or in *Charge Summing Mode* (*CSM*) whereby the charge deposited in every cluster of 4 pixels is reconstructed and assigned to a single circuit (Table I). In practice this means that the summing nodes are fed with the output of a single pixel only when *Single Pixel Mode* is selected.

The discrimination process is done by applying an offset (threshold) to the output of the summing nodes. Each

discriminator has a 4+1-bit Digital-to-Analog Converter (DAC) to reduce the threshold dispersion caused by mismatch in the transistors that provide the threshold and the summing currents. When *CSM* is used and the discriminator signal is active the charge is assigned to the summing circuit with the largest charge sum in the local neighborhood. The charge assignment decision is based on the operation of a system of arbitrators. Arbiter circuits decide between two requests (inputs), activating an acknowledgement for only one request even when they arrive simultaneously. The typical arbiter structure is based on a RS flip-flop with a simple structure to eliminate glitches at the output and filter the metastable state caused when two inputs arrive closely spaced in time. The arbitration circuits are not used in *SPM*.

TABLE I  
FRONT END OPERATING MODES

Front End Operating Mode	Pixel Size	Area of charge collection	Number of Thresholds
Fine Pitch Mode (Single Pixel Mode)	55µmx55µm	55µmx55µm	2 (1 in SRW)
Fine Pitch Mode (Charge Summing Mode)	55µmx55µm	110µmx110µm	2 (1 in SRW)
Spectroscopic Mode (Single Pixel Mode)	110µmx110µm	110µmx110µm	8 (4 in SRW)
Spectroscopic Mode 110µmx110µm (Charge Summing Mode)	110µmx110µm	220µmx220µm	5

When a given discriminator wins the arbitration decision in *CSM* or when it passes threshold in *SPM*, a pulse is fed to a shift register which is controlled by the *Shutter* signal. When the *Shutter* is high the shift register is configured as a 15-bit pseudo-random counter which counts the discriminator pulses (with a dynamic range of 32768 counts). When the *Shutter* is low the data can be shifted from pixel to pixel and read out externally.

Because the pixel contains two shift registers (one associated with each threshold) the pixel readout can be configured for either *Simultaneous Read-Write* operation or *Sequential Read-Write*.

As the detector pitch is 110 µm x 110 µm in *Spectroscopic Mode* and there are 2 thresholds and counters per readout pixel up to 8 thresholds are provided allowing colour imaging<sup>1</sup>.

Using *Spectroscopic Mode* and *Single Pixel Mode* and *Simultaneous Read-Write* operation up to 4 levels of energy discrimination are available together with dead-time free readout (Table I).

The pixel contains 19 configuration bits to provide a highly flexible system.

The layout of the pixel cell is shown in Fig. 5.

<sup>1</sup> In the prototype chip, only 5 thresholds were implemented but the full 8 thresholds will be available in the complete Medipix3 imaging system.

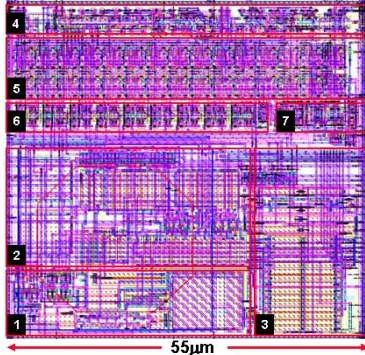


Fig. 5 Medipix3 pixel cell layout. 1. Preamplifier. 2. Shaper. 3. Two discriminators containing a 4-bit DAC each for threshold adjustment. 4. Control Logic. 5. Two 15-bit counters. 6. Nineteen configuration bits. 7. Arbitration logic for charge allocation.

#### IV. MEASUREMENTS

Measurements have been performed using an *IMSL ATS* digital IC tester [10]. Special routines have been programmed in LabVIEW in order to test the chip functionality. Two of the pixels (one in the regular matrix, the other in the test matrix) contain analog buffers which permit external monitoring of the preamplifier output, the two differential nodes of the shaper and the discriminator output. Fig. 6 shows the single shot oscilloscope traces of the analog part of one pixel to an input charge of  $3.7 \text{ ke}^-$ .

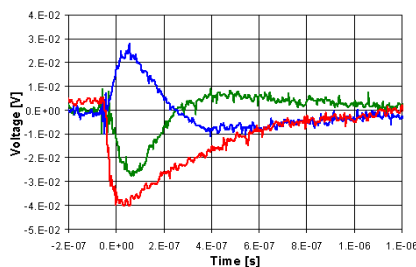


Fig. 6 Oscilloscope screen with the monitored waveforms for a  $3.7 \text{ ke}^-$  input charge. The preamplifier output is shown (red). Two nodes of the differential shaper are also monitored (blue and green). Operation in nominal conditions.

The noise has been measured electrically using the s-curve method. In this method a threshold scan is done through the signal passing from no counts (signal below the threshold) to 100% counts. The resulting shape is fitted with the error function providing information about the effective charge

collected (mean) and the signal noise (sigma). The measured Electronic Noise Charge is  $\sim 72 \text{ e}^- \text{ rms}$  in *Single Pixel Mode* and  $\sim 140 \text{ e}^- \text{ rms}$  in *Charge Summing Mode*. The same results are obtained by scanning the threshold through the noise and fitting the pedestal with a Gaussian probability distribution (no signal is injected in the preamplifier). Measurements show that the operation in *Simultaneous Read-Write* does not degrade the noise performance of the pixel. This is due in part to the relatively high resistivity substrate of the deep submicron technology used.

The threshold dispersion in the matrix has also been measured. It is caused mainly by the mismatch between transistors in the shaper. The measured value for the threshold dispersion is  $1875 \text{ e}^- \text{ r.m.s.}$  before adjustment when the system is working in *Charge Summing Mode*. A 4+1 bit DAC is implemented per summing circuit in order to correct for this dispersion. After tuning the threshold variation falls to  $\sim 110 \text{ e}^- \text{ r.m.s.}$  When the system operates in *Single Pixel Mode* the threshold dispersion after adjustment is  $\sim 55 \text{ e}^- \text{ r.m.s.}$

TABLE II ELECTRICAL MEASUREMENTS	
Front End Operating Mode	Single Pixel Mode      Charge Summing Mode
CSA Gain ( $G_3$ )	$11.4 \text{ mV/ke}^- (G=14F)$
CSA-Shaper Gain	$65 \text{nA/ke}^- (\text{High Gain Mode})$ $30 \text{nA/ke}^- (\text{Low Gain Mode})$
Non linearity	$<5\%$ $9 \text{ ke}^- (\text{High Gain Mode})$ $<2\%$ $22 \text{ ke}^- (\text{Low Gain Mode})$
Peaking time	$\sim 100 \text{ ns}$
Return to baseline	$<1 \mu\text{s}$ for $4 \text{ ke}^-$ (nominal conditions) $<300 \text{ ns}$ (tuning 10)
Electronic noise (High Gain Mode)	$72 \text{ e}^- \text{ r.m.s.}$
Electronic noise (Low Gain Mode)	$105 \text{ e}^- \text{ r.m.s.}$
Threshold spread (adjusted)	$55 \text{ e}^- \text{ r.m.s.}$
Analog power dissipation	$16.2 \mu\text{W}$ (nominal conditions)

Some tests reproducing the effects of a charge shared event have been performed. Fig. 7 shows the results of a test in which a total of 4000 pulses are sent simultaneously to four pixels. The charge is correctly reconstructed and assigned to the summing circuitry (1,1). The total number of counts recorded in the nine summing circuits is also plotted. Fig. 8 shows the reproduction of a charge sharing event in which the signal is induced in two pixels. The hits are assigned to the summing circuits (1,1) and (2,1). Fig. 9 represents the worst case for this architecture where the charge is deposited completely within one pixel. In this case the charge should be assigned randomly to one of the four corners. However one observes an increase in the total number of counts at low energy thresholds. This comes from charge being injected into sensitive analog nodes as a result of arbitrator activity. Extensive simulations using parasitic components have demonstrated that the falling edges of the digital lines can inject some current into the charge summing nodes due to coupling from metal to metal parasitic capacitances. This effect is seen as double counting for the same hit and finds its worst case in the situation where the full charge is induced in a single pixel. There is also some evidence of the same phenomenon in Fig. 7. Design techniques can be applied to

minimize the effect. Shielding of the analog sensitive lines and current starving techniques for the digital circuitry are possible solutions to eliminate the coupling.

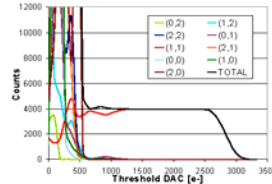


Fig. 7. Reproduction of a charge shared event by means of controlled charge injection in adjacent pixels. The sum of the hits on all counters is shown in black. The reconstructed charge is assigned to the summing circuit (1,1). The small increase in the number of total counts is an effect of the coupling from digital lines to the analog node where the charge summing is performed.

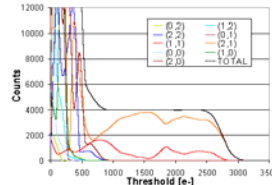


Fig. 8. Reproduction of a charge shared event. The reconstructed charge is randomly assigned to the summing circuits (1,1) and (2,1).

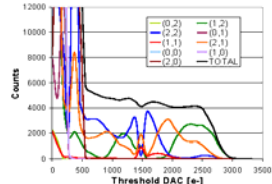


Fig. 9. The charge is fully injected in one of the pixels. This is the worst case of the arbitration circuits operation which have to randomly assign the charge to summing circuits (1,2), (2,2), (1,1) and (2,1). The coupling from the digital to the analog lines produces the shapes which represent the number of

counts of each summing circuit. Layout design techniques can solve the effect of the coupling.

## V. CONCLUSION

The Medipix3 prototype chip has been designed using a commercial  $0.13\mu\text{m}$  CMOS technology. The prototype chip implements a novel architecture aimed at eliminating the spectral distortion produced by charge diffusion. Measurements show an electronic pixel noise of  $\sim 72 \text{ e}^- \text{ rms}$  in *Single Pixel Mode* and  $\sim 140 \text{ e}^- \text{ rms}$  in *Charge Summing Mode*. The threshold dispersion is  $\sim 55 \text{ e}^- \text{ rms}$  for the pixel operating in *Single Pixel Mode* and  $\sim 110 \text{ e}^- \text{ rms}$  in Charge Summing Mode.

The prototype chip has provided very useful information for the design of the full Medipix3 imaging chip.

## ACKNOWLEDGMENT

The authors would like to thank the support and encouragement of the Medipix2 and Medipix3 collaborations.

## REFERENCES

- [1] B. Mikulec, "Development of segmented semiconductor arrays for quantum imaging," NIM-A 510 (2003) 1-23.
- [2] E. H. M. Heijne, "Semiconductor micropattern pixel detectors: a review of the beginnings," NIM-A 465 (2001) 1-26.
- [3] G.E. Moore, "Cramming More Components onto Integrated Circuits", Electronics, Vol. 38, No. 8, p. 114, 19 April 1965.
- [4] M. Campbell, E. H. M. Heijne, G. Meddeler, E. Pernigotti and W. Snoeyen "Readout for a  $64 \times 64$  Pixel Matrix with 15-bit Single Photon Counting," IEEE Trans. Nucl. Sci., vol. 45, pp. 751-753, June 1998.
- [5] X. Llopart, M. Campbell, R. Dinapoli, D. San Segundo and E. Pernigotti, "Medipix2: a 64-k Pixel Readout Chip With 55-mm Square Elements Working in Single Photon Counting Mode" IEEE Trans. Nucl. Sci., vol. 49, No.5, October 2002.
- [6] B. Mikulec, "Single Photon Detection with Semiconductor Pixel Arrays for Medical Imaging Applications", CERN-THESIS-2000-021.
- [7] L. Thustos, M. Campbell, E.H.M. Heijne and X. Llopart, "Signal variations in high granularity Si pixel detectors," IEEE Trans. Nucl. Sci., Vol. 51(6), 2004.
- [8] L. Thustos, "Performance and limitations of high granularity single photon processing X-ray imaging detectors", CERN-THESIS-2005-032.
- [9] F. Krummenacher, "Pixel Detectors with Local Intelligence: an IC Designer Point of View", Nuclear Instruments and Methods in Physics Research, A305, 1991, pp.527-532.
- [10] <http://miccdigital.web.cern.ch/miccdigital/tester/tester.htm>